

Studies of crystal collimation for heavy ion operation at the LHC

Présentée le 2 mai 2024

Faculté des sciences de base
Laboratoire de physique des accélérateurs de particules
Programme doctoral en physique

pour l'obtention du grade de Docteur ès Sciences

par

Rongrong CAI

Acceptée sur proposition du jury

Prof. F. Carbone, président du jury
Prof. M. Seidel, Dr R. Bruce, directeurs de thèse
Dr R. Assmann, rapporteur
Dr J. Jowett, rapporteur
Prof. L. Shchutska, rapporteuse

Acknowledgements

This completion of this thesis work would have not been possible without the valuable help from many people.

I would like to first thank my CERN supervisor Roderik Bruce and my university thesis director Prof. Mike Seidel. They have accompanied and guided me through every step of the process. I am especially grateful for the infinite patience and availability of Roderik Bruce. Thank you for providing a nourishing environment with challenges and opportunities for me to grow academically. Thank you for always supporting me. I will never forget your dedication while reviewing my thesis at midnight. I would also like to thank Prof. Seidel for watching out for my best academic interests and for giving me some key advice.

I would also like to thank the entire collimation team for the constant support. In particular, I would like to thank Stefano Redaelli for all the on-point guidance and tips that helped me through some of the more important occasions. I'd like to thank Pascal Hermes, Andrey Abramov, and Luigi S. Esposito for helping me extensively at the beginning of my PhD and the friendly availability afterwards. A special thanks also to Marco D'Andrea, who helped me with a myriad of things, including the basic small things that I was too embarrassed to ask anyone else! I would like to thank Daniele Mirarchi for all the clarifications on crystals. Above all, I would like to thank my family and my partner for supporting me all the way.

Lausanne, February 21, 2024

R. C.

Abstract

At CERN's Large Hadron Collider (LHC), proton and heavy-ion beams are accelerated to multi-TeV energies to be collided for the needs of the scientific community around the world. The total stored beam energy of tens to hundreds of MJ creates potential threats to the hardware around the collider in case of uncontrolled beam loss. Energy deposited by lost particles may damage impacted elements or cause the LHC magnets to lose their superconducting state, creating unnecessary downtime and decreasing physics production efficiency. To protect the machine a multi-stage collimation system was installed, designed primarily for proton operation but to be used also for heavy ions. However, with the upgrades for High-Luminosity LHC (HL-LHC), the total stored beam energy is to increase from 13 MJ to around 20 MJ. This demands an upgrade also from the collimation side to safely intercept higher beam losses that are to be expected due to higher intensity. Because of the fragmentation of heavy ions inside the collimators, which causes a significant leakage out of the collimators of particles with a charge-to-mass ratio that is different from the main beam, the collimation for heavy ions is more challenging than for protons. Hence, based on the studies performed in the past, it was decided to introduce a new collimation method with a potential for increased performance, called *crystal collimation*, in the operational baseline, already in 2023, when also the beams from the injectors with higher intensity became available.

The imminence of ion operations with crystal collimation presses for a more thorough understanding of this novel method applied on heavy ions. For this reason, this thesis describes a complete simulation framework that has been built for ion crystal collimation. This tool allows a better understanding of the characteristics of crystal collimation for ions, probe for collimation optimizations, and perform predictive analysis for future collimation configurations. The simulation framework is based on the existing SixTrack-FLUKA coupling.

This thesis presents the construction of the simulation framework, the benchmark with old and new data, detailed simulation studies of the LHC collimation performance in various configurations, including the one of the first heavy-ion physics run with crystal collimation in 2023, and other alternative setups.

Key words: heavy ion, crystal, particle accelerator, collimation

Résumé

Au Grand Collisionneur de Hadrons (LHC) du CERN, des faisceaux de protons et d'ions lourds sont accélérés à des énergies de plusieurs TeV afin d'être soumis à des collisions pour les besoins de la communauté scientifique du monde entier. L'énergie totale stockée dans les faisceaux, de l'ordre de dizaines à centaines de MJ, constitue une menace potentielle pour le matériel situé autour du collisionneur en cas de perte incontrôlée de faisceau. L'énergie déposée par les particules perdues peut en effet endommager les éléments touchés ou faire perdre aux aimants du LHC leur état supraconducteur, ce qui entraîne des temps d'arrêt inutiles et donc une efficacité de production moindre. Pour protéger la machine, un système de collimation à plusieurs étages a été installé, conçu principalement pour le fonctionnement des protons, mais pouvant également être utilisé pour les ions lourds. Cependant pour ces derniers, avec les améliorations apportées au LHC à haute luminosité, l'énergie totale stockée dans le faisceau doit passer de 13 MJ à environ 20 MJ. Cela nécessite également une amélioration de la collimation afin d'intercepter en toute sécurité les pertes de faisceau plus importantes auxquelles il faut s'attendre en raison de l'augmentation de l'intensité. En raison de la fragmentation des ions lourds à l'intérieur des collimateurs, qui entraîne une fuite importante de particules dont le rapport charge/masse est différent de celui du faisceau principal, la collimation des ions lourds est plus difficile que celle des protons. C'est pourquoi, sur la base des études réalisées par le passé, il a été décidé d'introduire une nouvelle méthode de collimation potentiellement plus performante, appelée *collimation cristalline*, dans la ligne de base opérationnelle, dès 2023, lorsque les faisceaux provenant des injecteurs à plus forte intensité seront également disponibles.

L'imminence des opérations sur les ions avec la collimation par cristal nécessite une compréhension plus approfondie de cette nouvelle méthode appliquée aux ions lourds. Pour cette raison, cette thèse décrit un cadre de simulation complet qui a été construit pour la collimation d'ions par cristal. Cet outil permet de mieux en comprendre les caractéristiques, de sonder les optimisations de la collimation et d'effectuer des analyses prédictives pour les futures configurations de collimation. Le cadre de simulation est basé sur le couplage existant SixTrack-FLUKA.

Cette thèse présente la construction du cadre de simulation, le benchmark avec des données anciennes et nouvelles, des études de simulation détaillées des performances de la collimation du LHC dans différentes configurations, y compris celle du premier run de physique des ions

lourds avec la collimation cristalline en 2023, et d'autres configurations alternatives.

Mots clefs : ion lourd, cristal, accélérateur de particules, collimation

Contents

Acknowledgements	i
Abstract (English/Français)	iii
Introduction	1
1 Accelerator Physics	5
1.1 Transverse dynamics	6
1.1.1 Equation of motion	6
1.1.2 Transfer matrix notation	9
1.1.3 The inhomogeneous solution and dispersive effects	9
2 Crystal Channeling	11
2.1 Crystal structure and the Miller index	11
2.2 Planar channeling	12
2.2.1 Straight crystals	12
2.2.2 Thermal considerations	16
2.2.3 Bent crystals	18
2.3 Other crystal phenomena	20
2.3.1 Volume Reflection	20
2.3.2 Dechanneling	21
2.3.3 Volume capture	22
3 The Large Hadron Collider	25
3.1 LHC design	25
3.1.1 LHC layout	26
3.1.2 Operational cycle	28
3.2 LHC heavy-ion operation and the High Luminosity LHC	29
4 Collimation in the LHC	31
4.1 Particle loss in the machine	32
4.2 Present collimation system	33
4.2.1 Collimator settings	36
4.3 Particle-matter interaction	36
4.4 Collimation performance	41

4.4.1	Cleaning inefficiency	41
4.4.2	Main limitation and quench limit	43
4.5	Crystal Collimation	43
4.6	LHC crystal collimation upgrade for Pb ions	46
5	Simulation tools	49
5.1	MAD-X	49
5.2	FLUKA	49
5.2.1	Development of crystal coherent effects	50
5.3	SixTrack	50
5.3.1	Development of crystal coherent effects	51
5.4	SixTrack-FLUKA coupling	51
6	Building of the simulation framework	55
6.1	Main input files for crystal collimation simulation	55
6.2	Changes made to include the crystal	56
6.2.1	Creation of the crystal geometries in FEDB	57
6.2.2	Addition of the crystal block in include_custom_assignmat.inp	59
6.2.3	Inclusion of the crystal in CollDB	61
6.2.4	Crystal blocks in the prototypes.lbp	62
6.2.5	Crystal tilt addition in the collgaps file	63
6.2.6	Addition of the crystal output file in include_custom_scoring.inp	64
7	Simulation framework benchmark	65
7.1	Collimation simulation method	66
7.2	Proton benchmarks	68
7.2.1	Single pass	68
7.2.2	Loss Pattern	71
7.2.3	Angular scan	75
7.2.4	Linear Scan	78
7.3	Heavy-ion benchmark	80
7.3.1	Single pass	81
7.3.2	Loss pattern	82
7.3.3	Collimation improvement using crystals	85
7.3.4	Angular scan	99
7.3.5	Linear scan	110
8	Crystal collimation studies with Pb ions in the LHC	113
8.1	Characteristics of crystal collimation	113
8.1.1	Black absorber study	113
8.1.2	Trackback study	114
8.2	Sensitivity studies	117
8.2.1	Crystal miscut	117

8.2.2	Crystal orientation	121
8.2.3	Collimator imperfections	122
8.2.4	Impact parameter study	125
8.3	Configuration optimization	126
8.3.1	TCLA scan	126
8.3.2	Skew TCSG comparison	129
8.3.3	Upstream open	130
8.4	Asynchronous dump simulation	132
8.5	Run 3 Proposed configuration	140
8.6	Operational experience with crystals in the 2023 Pb ion run	141
9	Standard ion collimation optimization	153
9.1	Standard system ion impact parameter scan	153
9.2	Single jaw collimation performance	154
9.3	Collimator jaw tilt study	157
9.4	Optics improvement	158
9.5	Tilted TCP configuration and optics improvement	159
10	Simulations of future runs	163
10.1	Simulation at higher energy	163
10.2	Crystal collimation performance with various ion species	164
	Conclusion	171
A	Appendix	179
	List of figures	199
	List of tables	207
	Bibliography	209
	Acronyms	230
	Curriculum Vitae	231

Introduction

Since the dawn of time, mankind has been drawn to explore its surroundings in the attempt to understand it. This continuous effort is not only driven by curiosity or utility, but also by some of the most fundamental questions of existence: Where does life come from? How did the Universe start? What are we made of? . . .

As our understanding deepened throughout the centuries, our attention has also been drawn to smaller and smaller things, from molecules to atoms, from atoms to nuclei, and from nuclei to the fundamental particles and opening the field of particle physics. Advances in technology have also made great leaps to accelerate and facilitate new scientific pursuits and pave the way for fundamental scientific discoveries. The beginning of particle physics was marked by the observation of cosmic rays. However, our ambition and vision have lead us to bring the cosmic down to Earth. Hence, around the 1950s the era of the great particle accelerators started. Since then, particle accelerators and colliders have managed to not only serve the particle physics community, but they are used also in cosmology, medicine, archaeology and more. The capabilities of particle accelerators have also grown significantly in a matter of decades, up to the realization of one of the most complex machines built by man, the Large Hadron Collider (LHC).

The LHC [1] at the CERN is the world largest and highest-energy particle accelerator. It is conceived to accelerate and collide counter-rotating beams of protons and heavy ions up to an energy of 7- Z -TeV, and so far 6.8- Z -TeV has been achieved. The LHC heavy-ion program relies mainly on collisions between fully stripped Pb ions, or collisions between protons and Pb [2, 3]. The LHC hosts four main experiments: ATLAS [4], ALICE [5], CMS [6], and LHCb [7, 8]. Behind the creation of heavy-ion colliders in particular, there is the aim to study strongly interacting matter and to probe the Standard Model. For example, some of the aspects that can be studied are the quark-gluon plasma (QGP), anti-matter states, and strong force interactions [9, 10]. Apart from the LHC, the only other operational heavy-ion collider in the world is the Relativistic Heavy-Ion Collider (RHIC) [11] at the Brookhaven National Laboratory (BNL), although it is operated at significantly lower energy. The ion collider community seeks continuously to improve the performance of the machines and expand in physics reach. It is planned to upgrade RHIC to an electron-ion collider (EIC) [12, 13]. At CERN, an upgrade of the LHC is also foreseen in order to provide significantly higher luminosity in hadron-hadron collisions, with High Luminosity LHC (HL-LHC) [14], approved by the CERN council in 2016.

For heavy ion operation, the fundamental upgrades have already been implemented in the last long shutdown from end of 2018 to start of 2022.

The upgrade involves a higher luminosity target and higher stored beam energy. In particular, for Pb-Pb operation in the LHC, the transition is from a stored beam energy of around 13 MJ to approximately 20 MJ. This amount of energy poses great risks to hardware and availability of the machine, as there are many beam dynamics processes and equipment failures that could cause high-energy particles to be lost on the machine aperture and deposit energy on the devices around the ring. Some of the most delicate elements in the LHC are the superconducting magnets. These are cooled down to 1.9 K to exploit their superconducting capabilities [1]. Regular or irregular beam losses around the ring may cause heating of the magnets that makes them lose their superconducting properties, also referred to as a magnet quench, or even damage impacted elements. To safely intercept any beam losses and protect the machine aperture, a multi-stage beam collimation system is put in place [15, 16, 17, 18, 19, 20].

In past studies it was found that beam collimation in the LHC is more challenging for heavy ions than for protons. The beam cleaning performance, in terms of relative leakage of initial beam losses intercepted by the collimators to the cold aperture, is around two orders of magnitude worse for ions than for protons [21, 22, 23] due to the out-scattering of ion fragments. This existing challenge together with the future higher stored beam energy makes an improvement on the collimation system necessary for efficient operations with Pb ion beams.

A very promising method for ion collimation is called *crystal collimation*. It exploits materials that have a crystalline structure and are able to trap the incoming particles with certain characteristics within the potential generated by the crystalline planes, so-called planar channeling. The crystal can then be bent so that trapped particles follow the bending and acquire an angular kick. In a collimation system a crystal would be inserted as the closest aperture to the beam core and work in conjunction with a collimator that acts as an absorber, which intercepts the channeled particles exiting the crystal. This method could be used to increase the collimation performance for heavy ions in the LHC, because particles going through the crystal would have a significantly reduced probability to interact with the material while trapped in the channel between the planes. When the channeled particles hit the absorber, they hit deeply enough that the leakage out of the absorber is very small, hence potentially increasing the efficiency of the system.

The first crystal setup was installed in the LHC from 2015 to 2017 [24, 25, 26]. Four crystals have been inserted, one per beam and plane. Between 2015 and 2018 there have been many experimental studies of crystal collimation in the LHC [25, 27, 28, 29, 26, 30, 31, 32, 33, 34], including tests with ion beams. During these tests it was found that in optimal conditions, crystal collimation is able to improve the performance of Pb ion collimation by a factor of 1.5–8, depending on beam and plane [27, 35, 36]. Hence, crystal collimation has been set to be the baseline for heavy-ion operation in Run 3, starting already with the 2023 ion run, and in

HL-LHC.

With crystal collimation set to be operational imminently in the heavy-ion runs, it is essential to have a simulation tool that can be used to reliably study its performance and give a firm understanding of what could be expected. All past simulation studies related to crystal collimation have been carried out for protons. However, nuclear fragmentation of ions could make the collimation process very different, as in previous simulation studies of ion collimation with the standard collimation system [37]. Therefore, this thesis work has been devoted to the construction of a robust and well-benchmarked simulation framework for ion crystal collimation in particle accelerators, and its applications to the LHC. A reliable simulation framework opens the possibility to study the measurements collected in the past and gain a deeper understanding of them, probe specific configurations to understand the ion crystal collimation characteristics, optimize and design for future runs, perform collimation diagnostics during operations, etc. This setup also lays the foundation for more sophisticated crystal collimation scenarios for a variety of particle species.

The main goals of this work are to build an ion crystal simulation framework, benchmark it with old and new data, study the ion crystal collimation itself, design optimal collimation configurations to be used in LHC operation, simulate the performance in future scenarios, and study possible backup plans in case of unforeseen problems with the crystal collimators. This thesis presents relevant aspects of the theoretical foundations of accelerator physics and crystal physics in the Chapters 1 and 2. Then it goes to outline the essential information regarding the LHC and its collimation system in Chapters 3 and 4. The short chapter that follows explains the existing simulation tools that are used in the construction of the simulation framework. From Chapter 6 and onwards, work original to this PhD is presented. Chapters 6 and 7 revolve around the technical setup of the simulation framework and all the benchmarks performed. Chapter 8 looks at first the characteristics of ion crystal collimation, and subsequently explores various ways to optimize the setup leading to the final proposal for the 2023 Pb run, which was subsequently used in operation. A short summary of the 2023 operation with crystal collimation is also given, with strong focus on the parts that are part of this thesis work. Then, Chapter 9 presents studies in search of backup plans using the standard ion collimation system without the use of crystals. The final chapter before the conclusion is about simulations for future hypothesized scenarios, such as the HL-LHC case at higher energy and operational scenarios with other ion species than Pb. The last chapter summarizes all results laid out in the previous chapter and reflects on possible future developments.

1 Accelerator Physics

This chapter provides the essential concepts and fundamental theoretical background in particle accelerator physics needed to understand this work. For a more detailed discussion, [38] can be consulted. As the focus of this project is on the Large Hadron Collider (LHC), which is a circular synchrotron, this chapter will mainly cover the notions most relevant to this type of machine. Certain equations are also written with ion beams in mind, as they are also the focus in this thesis.

Before entering into the details of particle motion, it is important to define the reference frame used, the Frenet-Serret reference system, which follows a reference particle. It will have a closed orbit that constitutes the reference or ideal orbit. The position of the reference particle can be defined by a vector, $\vec{r}(s)$ with the parameterization s , which in this case is the longitudinal position along the orbit. From here, the position \vec{R} of any arbitrary particle can be defined as

$$\vec{R}(x, y, z, s) = \vec{r}(s) + x\vec{e}_x(s) + y\vec{e}_y(s) + z\vec{e}_z(s), \quad (1.1)$$

where $\vec{e}_{x,y,z}$ are the orthogonal unit vectors of the moving coordinate system (\vec{e}_z is tangential to the nominal orbit). The reference system is illustrated in Fig. 1.1

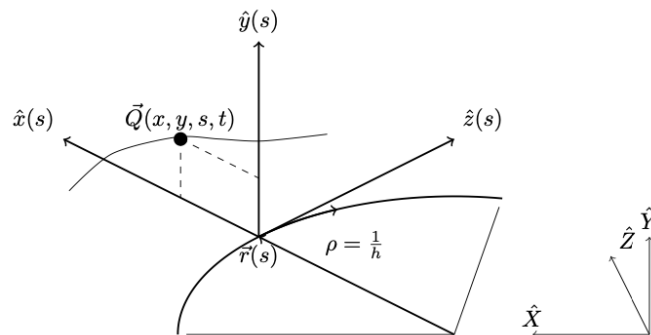


Figure 1.1 – Illustration of the Frenet-Serret coordinate system [39].

1.1 Transverse dynamics

The main purpose of a circular particle accelerator is to accelerate particles to high energies, while guiding them on a nominal orbit and keeping them focused within the beam. This is achieved through a series of beam line elements, the most important ones are

- Radiofrequency (RF) cavities, devices used to provide energy to the particles and accelerate them.
- Dipole magnets: the main dipoles are used to bend the trajectory of charged particles to keep them within the acceptable orbit. They use a uniform transverse magnetic field. There are also kicker magnets which are used among other things to bring counter-rotating beams into a common beam pipe.
- Quadrupole magnets, which are magnets with four poles that provide a transverse magnetic field gradient, g (in T/m), as a function of transverse space:

$$B_x = -gy, \quad \text{and} \quad B_y = gx, \quad (1.2)$$

where B_x and B_y are the magnetic fields in x and y respectively. Quadrupole magnets focus the beam in one transverse plane and defocus it in the other plane. Another quantity used instead of the field gradient is the focusing strength, $k = \frac{q}{P}g$, where q is the particle charge and P is the momentum.

- Higher-order magnets (e.g. sextupoles and octupoles) for higher-order orbit corrections.
- Drift space, region where the particles are left to travel freely.

1.1.1 Equation of motion

As the accelerator lattice is composed of elements which induce electromagnetic fields, the particle motion is determined by the Lorentz force,

$$\frac{d\vec{P}}{dt} = q(\vec{E} + \vec{v} \times \vec{B}), \quad (1.3)$$

where $\vec{P} = \gamma m \vec{v}$ is the particle momentum, q is the electric charge, \vec{E} is the electric field, \vec{v} is the velocity, m is the mass, $\gamma = 1/\sqrt{1 - v^2/c^2}$ is the Lorentz factor, and \vec{B} is the magnetic field. If $\vec{E} = 0$, then for a particle to stay in orbit, the centrifugal force must be equal to the magnetic part of the Lorentz force. This equilibrium gives an important quantity called magnetic rigidity.

$$B\rho = \frac{P}{q}, \quad (1.4)$$

From here the reference magnetic rigidity can be defined as

$$B\rho_0 = \frac{P_0}{q_0} = \frac{m_0 p_0}{Z_0 e}, \quad (1.5)$$

where the P_0 is the design momentum, q_0 the designed charge, m_0 the designed mass, $p_0 = P_0/m_0$ the momentum per designed mass, Z_0 the atomic number of the main beam for ions, and e the elementary charge. It is possible to express the magnetic rigidity of an arbitrary ion with a different $p = p_0 + \Delta p$ [37]:

$$B\rho = \frac{m(p_0 + \Delta p)}{Ze} = \frac{m}{m_0} \frac{q_0}{q} B\rho_0 \left(1 + \frac{p - p_0}{p_0}\right) = B\rho_0 \frac{1 + \delta}{\chi}, \quad (1.6)$$

where we have defined δ and χ as

$$\delta = \frac{P \frac{m_0}{m} - P_0}{P_0} = \frac{p - p_0}{p_0}, \text{ and } \chi = \frac{q}{q_0} \frac{m_0}{m}, \quad (1.7)$$

Equation 1.6 allows us to directly compare any particle with the reference particle. Commonly speaking, since many reference literature only consider particles of the same species as the reference particle (mono-isotopic), δ is usually defined as $\delta = (P - P_0)/P_0$. If we consider only dipoles and quadrupoles, while ignoring higher order multipoles, then starting from Eq. 1.3 it can be shown that the equation of motion in the x plane for the reference particle is

$$\ddot{x} + \left(\frac{1}{\rho(s)^2} + k(s) \right) x = 0, \quad (1.8)$$

where $\ddot{x} \equiv \frac{d^2 x}{ds^2}$. Here, $1/\rho^2$ describes the dipole force, and k is the (de)focusing strength.

Having written the equation in x, a similar equation can be derived for the vertical plane. Particles usually only bend in one plane in circular accelerators and it is often chosen to let this be the x-z plane. The dipole component then disappears for the y plane,

$$\ddot{y} + k(s)y = 0. \quad (1.9)$$

The solution to Eqs. 1.8 and 1.9 is of the form

$$u(s) = \sqrt{\epsilon_u \beta_u(s)} \cos(\psi_u(s) + \phi). \quad (1.10)$$

where $u = x, y$. $\beta_u(s)$ is called the betatron function and it modulates the transverse amplitude of the beam, and the transverse oscillating motion described by this equation is called betatron motion. By combining Eq. 1.10 with Eq. 1.8 and 1.9 we find a differential equation that can be solved for β_u ,

$$\frac{\ddot{\beta}_u(s)}{2} + K_u(s)\beta_u(s) - \frac{1}{\beta_u(s)} \left[1 + \frac{\dot{\beta}_u(s)^2}{4} \right] = 0, \quad (1.11)$$

where $K_u(s) = \left(\frac{1}{R(s)^2} - k(s)\right)$ and $K_y(s) = k(s)$ for the case considered. However, in a collider ring the magnet strengths can be seen as a piecewise function that repeats periodically:

$$K(s) = K(s + C), \quad (1.12)$$

with C being the circumference. Therefore, $\beta_u(s) = \beta_u(s + C)$.

The betatron phase, $\psi_u(s)$, is defined as:

$$\psi_u(s) = \int_0^s \frac{ds'}{\beta_u(s')}, \quad (1.13)$$

while ϕ depends on initial conditions.

It is possible to parameterize Eq. 1.10 with $\beta_u(s)$ and two other quantities:

$$\alpha_u(s) = -\frac{\beta'_u(s)}{2}, \quad (1.14)$$

$$\gamma_u(s) = \frac{1 + \alpha_u^2(s)}{\beta_u(s)}. \quad (1.15)$$

$\alpha_z(s)$, $\beta_z(s)$ and $\gamma_z(s)$ are called *Twiss parameters* (or *Courant-Snyder parameters*). They can be used to describe the particle at any position in phase space and depend only on the machine. As the beam transformations due to magnetic devices are akin to those in classical optics, the Twiss parameters are also referred to as optical functions, and the lattice configuration as beam optics.

Lastly, ϵ_u is a Courant-Snyder invariant, which is a constant of the motion:

$$\epsilon_u = \gamma_u u^2 + 2\alpha_u u u' + \beta_u u'^2. \quad (1.16)$$

This equation shows that the particle draws an ellipse in the phase space just as in other harmonic oscillators. The area it encloses is sometimes referred to as the *single particle emittance*.

To study beam dynamics it is useful to define some statistical quantities. We assume in first approximation Gaussian beams.

Firstly, the betatronic r.m.s size, $\sigma_u(s)$, and beam divergence, $\sigma'_u(s)$, can be defined as

$$\sigma_u(s) = \sqrt{\epsilon \beta_u(s)}, \quad \sigma'_u(s) = \sqrt{\epsilon \gamma_u(s)}. \quad (1.17)$$

with ϵ_u being the emittance of an entire beam. Due to the a process called *adiabatic damping*, higher momentum will give rise to a lower emittance and beam size. To avoid dependence on

momentum, the normalised emittance is often used:

$$\epsilon_n = \beta\gamma\epsilon, \quad (1.18)$$

where β and γ are the relativistic factors of the beam particles.

Lastly, to assess the stability of motion, an essential parameter to consider is *the tune*. It represents the number of betatron oscillations per turn in the machine:

$$Q_u = \frac{1}{2\pi} \int_{s_0}^{s_0+C} \frac{ds}{\beta_u(s)}, \quad (1.19)$$

where C is the machine circumference. Many multi-turn processes depend on it.

1.1.2 Transfer matrix notation

To allow a more convenient way of designing and simulating accelerators, a matrix notation can be used. The solution given in Eq. 1.10 can be written as:

$$u(s) = a\sqrt{\beta_u(s)} \sin \psi_u(s) + b\sqrt{\beta_u(s)} \cos \psi_u(s). \quad (1.20)$$

Here a and b are constants. Knowing the coordinates (u, u') in a certain location s_1 , a and b from Eq. 1.20 the particle coordinates in another location s_2 can be obtained as follows:

$$\begin{pmatrix} u(s_2) \\ u'(s_2) \end{pmatrix} = M(s_1|s_2) \begin{pmatrix} u(s_1) \\ u'(s_1) \end{pmatrix}, \quad (1.21)$$

where M is the transport matrix from s_1 to s_2 . Its elements can be written in terms of the Twiss parameters and phase advance ψ_{21} between the two locations:

$$M(s_1|s_2) = \begin{pmatrix} \sqrt{\frac{\beta_2}{\beta_1}}(\cos \psi_{21} + \alpha_1 \sin \psi_{21}) & \sqrt{\beta_2 \beta_1} \sin \psi_{21} \\ -\frac{1+\alpha_1 \alpha_2}{\sqrt{\beta_2 \beta_1}} \sin \psi_{21} + \frac{\alpha_1 - \alpha_2}{\sqrt{\beta_2 \beta_1}} \cos \psi_{21} & \sqrt{\frac{\beta_1}{\beta_2}}(\cos \psi_{21} - \alpha_2 \sin \psi_{21}) \end{pmatrix}. \quad (1.22)$$

1.1.3 The inhomogeneous solution and dispersive effects

In a real machine it is unlikely that all particles will have the same momentum and in this section we consider the motion for particles that have a momentum different from the main beam, but still close enough that higher orders of δ can be neglected. In this section we

consider the effects linked to the dipole magnets. The general case with non-isotopic ions is considered.

When considering a beam with a finite δ (Eq. 1.7), it can be shown that Eq. 1.8 becomes

$$\ddot{x} + \left(\frac{1}{\rho(s)^2} + k(s) \right) x = \frac{\delta}{\rho(s)}, \quad (1.23)$$

The solution can be expressed as

$$x(s) = x_\beta(s) + D(s)\delta, \quad (1.24)$$

$$x'(s) = x'_\beta(s) + D'(s)\delta, \quad (1.25)$$

with $x_\beta(s)$ describing the betatron motion of the on-momentum particle, aka the solution to the homogeneous equation in Eq. 1.8, and $D(s)$ being a function called *dispersion function*, which determines the offset from the on-energy orbit that is caused by the momentum deviation δ . The dispersion function is defined as

$$D_x(s) = -\frac{\beta_x(s)}{2 \sin(\pi Q_x)} \int_{s_0}^{s_0+C} h_x(s) \sqrt{\beta(s)} \cos \left[2\pi \left(\psi(\tilde{s}) - \psi(s_0) - \frac{Q_x}{s} \right) \right] ds. \quad (1.26)$$

2 Crystal Channeling

Crystal channeling refers to the confinement of particles in crystal structures. This is possible thanks to the ordered placing of atoms in the crystalline lattice. This chapter starts with a brief description of the basics of crystallography, continues with the physics of crystal channeling, and ends with the most important coherent phenomena experienced by particles propagating through a crystal.

2.1 Crystal structure and the Miller index

According to [40], *a crystalline solid is a material whose atoms have a regular arrangement that exhibits translational symmetry*. A crystal has translational symmetry if given an arbitrary set of integers, m_1, m_2, m_3 , there exists a set of three linearly independent vectors that is able to translate a point to another equivalent point in the crystal. The three vectors are called basis vectors and the set is not unique, as any linear combination can give another set. All the translations from all the possible linear combinations $\vec{T} = m_1 \vec{a}_1 + m_2 \vec{a}_2 + m_3 \vec{a}_3$, constitute a group. The volume $V = \vec{a}_1 (\vec{a}_2 \times \vec{a}_3)$ gives the unit cell. By stacking the unit cells, we can fill the whole space. The smallest unit cell is a primitive cell, which is also not unique [40]. By drawing straight lines to represent the crystal lattice we can find the intersections. These are called lattice nodes, which can be a single atom or or a group of atoms.

When using crystals, it is often essential to specify a plane or a set of planes of the crystal. The Miller indices are designed to achieve this. To find the Miller indices, we need to first find the points of interception of the desired plane with the basis vectors. Then, the three numbers found must be divided by their greatest common divisor. The results, (h, k, l) , are the Miller indices for the plane [40]. If the plane is parallel to a basis vector, then its corresponding Miller index is 0 [41].

The crystals used in this work all use the (110) plane for channeling. The crystal in this orientation is also known as a *strip* crystal. In a simplistic cubic cell, this would mean that the it intercepts \vec{x} and \vec{y} at 1, and is parallel to \vec{z} . The (110) plane along with some other planes are

Channeling orientation	interplanar spacing
(100)	1.63 Å
(110)	1.92 Å
(111) _{narrow}	0.78 Å
(111) _{wide}	1.54 Å

Table 2.1 – Interplanar spacing of silicon for different planes. The (111) spacing can be *narrow* or *wide*, since the planes are positioned on two alternating spacings.

illustrated in Fig. 2.1.

The interplanar spacing of the most relevant channeling orientations in silicon are given in Table. 2.1.

2.2 Planar channeling

2.2.1 Straight crystals

We start the physics description of crystal channeling with planar channeling, in particular with straight planes. Generally speaking, defining the potential that defines the interaction between charged particles and atoms is a difficult task that should take into account several factors, including the relative speeds or the atomic number. The Thomas-Fermi model provides a good approximation. For a particle with charge, Z_i , impinging on a material with charge, Z , the potential will be

$$V(r) = \frac{Z_i Z e^2}{r} \phi\left(\frac{r}{a_{TF}}\right), \quad (2.1)$$

where r is the relative distance between the impinging particles and the plane direction, $a_{TF} = \left(\frac{9\pi^2}{128}\right)^{1/3} a_0 (Z^{2/3} + Z_i^{2/3})^{-1/2}$ is the Thomas-Fermi screening radius, a_0 is the Bohr radius, and $\phi\left(\frac{r}{a_{TF}}\right)$ is the Molière screen function [42]. It takes into account the atom charge distribution:

$$\Phi\left(\frac{r}{a_{TF}}\right) = \sum_{i=1}^3 \alpha_i \exp\left(-\frac{\beta_i r}{a_{TF}}\right), \quad (2.2)$$

where $\{\alpha_i\} = \{0.1, 0.55, 0.35\}$ and $\{\beta_i\} = \{6.0, 1.2, 0.3\}$ for $i = \{1, 2, 3\}$ respectively.

According to Lindhard's hypothesis successive scatterings of particles approaching a lattice-preferred direction at small angles cannot be regarded as independent events and the potential that the particle sees is a continuous sum of all the lattice nodes of a plane or line [43]. By choosing x to be perpendicular to the channeling planes, we can write the average continuous

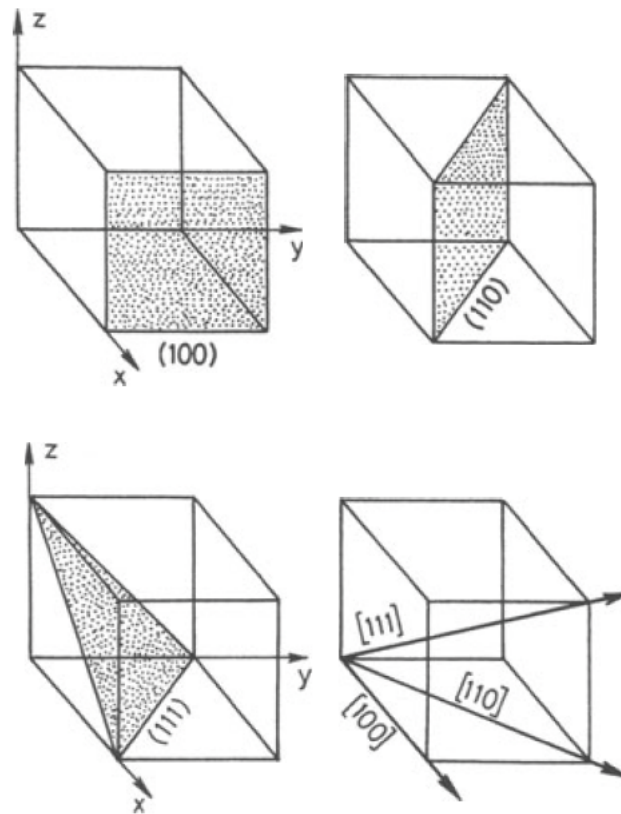


Figure 2.1 – Example of simple planes and their Miller indices for a cubic unit cell [41].

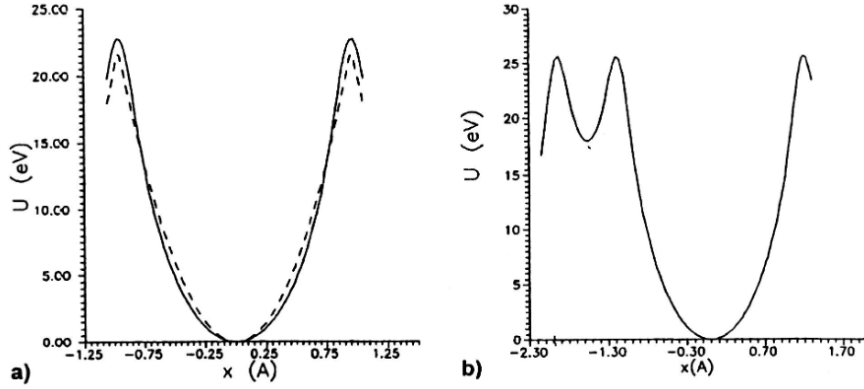


Figure 2.2 – Interplanar potential for Si crystals for a) (110) planes and b) (111) planes

potential, $U_p(x)$, that the particle sees as

$$U_p(x) = Nd \iint_{-\infty}^{+\infty} V(x, y, z) dy dz, \quad (2.3)$$

where d is the distance from the plane, N is the atomic density and V is the potential in Eq. 2.1. Further expanding the potential equation to include Molière's screening function, we obtain

$$U_{pl}(x) = 2\pi Nd Z_i Z e^2 a_{TF} \sum_{i=1}^3 \frac{\alpha_i}{\beta_i} \exp\left(-\frac{\beta_i x}{a_{TF}}\right), \quad (2.4)$$

Having found the potential for one plane, the total potential of the channeling well made of two adjacent crystalline planes can be built by summing the two plane potentials:

$$U(x) \approx U_p\left(\frac{d_p}{2} - x\right) + U_p\left(\frac{d_p}{2} + x\right), \quad (2.5)$$

where d_p is the interplanar distance. The exact potential is shown in Fig. 2.2. The potential could then be approximated with a harmonic function:

$$U(x) \approx U_{\max} \left(\frac{2x}{d_p}\right)^2. \quad (2.6)$$

We now proceed to derive the conditions required for a particle to be channeled in a straight planar crystal. Consider a particle impacting the crystal with a small angle. We can write the particle angle θ with respect to the longitudinal direction as

$$\theta = \tan \frac{p_t}{p_l} \simeq \frac{p_t}{p_l} \implies p_t \ll p_l, \quad (2.7)$$

where p_t and p_l are the transverse (perpendicular to the crystalline plane) and longitudinal (parallel to the crystalline plane) components of the particle momentum respectively. An

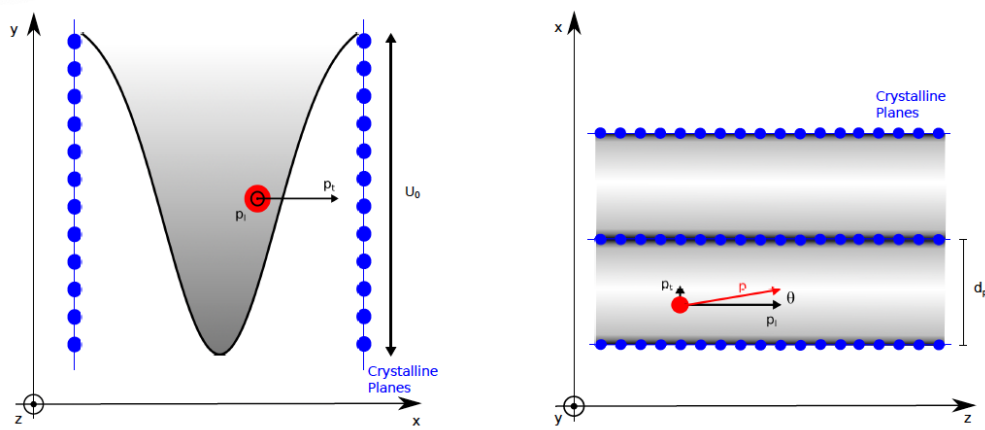


Figure 2.3 – Reference system of a positively charged particle in planar channeling. The red dot represents the particle and the blue dots the crystalline planes. Frontal view is displayed in the left image, and top view in the right image [25].

illustration of the reference frame can be found in Fig. 2.3. Since for the particle to be trapped, its energy must be below the maximum of the potential well, U_{\max} , we can write its energy and define the condition. The total energy is:

$$E = \sqrt{p_t^2 + p_l^2 + m^2 c^4} + U(x) \simeq \frac{p_l^2 c^2}{2E_l} + E_l + U(x). \quad (2.8)$$

Here, the longitudinal energy, $E_l = \sqrt{p_l^2 c^2 + m^2 c^4}$ is conserved because there are no forces acting in the transverse direction. Since both E and E_l are conserved, E_t , the transverse component of energy must also be conserved:

$$E_t = \frac{p_t^2 c^2}{2E_l} + U(x) \simeq \frac{p_l^2 c^2}{2E_l} \theta^2 + U(x) \simeq \frac{p^2 c^2}{2E} \theta^2 + U(x) = \text{constant}, \quad (2.9)$$

where the approximations $\theta \simeq p_t/p_l$, $p_l \simeq p$ and $E_l \simeq E$, are used. For the particle to be in channeling the condition $E_t < U_{\max}$ must be satisfied, which can be written as

$$\frac{p^2 c^2}{2E} \theta^2 + U(x) \leq U_{\max}. \quad (2.10)$$

If the particle enters in the middle of the well, where $U(x)$ is 0, then the inequality can be further simplified to

$$\frac{p^2 c^2}{2E} \theta^2 \leq U_{\max}, \quad (2.11)$$

or

$$\frac{pv}{2} \theta^2 \leq U_{\max}, \quad (2.12)$$

since with v is the particle velocity $pc^2 = vE$ holds. Therefore, for a certain momentum we can obtain a limiting angle, called critical angle (θ_c), beyond which the condition no longer holds. Thus, knowing the particle momentum, the critical angle is:

$$\theta_c = \sqrt{\frac{2U_{\max}}{pv}}. \quad (2.13)$$

Particles with incoming angles larger than the critical angle in absolute value cannot be channeled.

Since, the (110) potential can be approximated to a harmonic potential, the particle motion is also that of a harmonic oscillator. In particular, using $\theta = dx/dz$ Eq. 2.9 becomes

$$E_t = \frac{pv}{2} \left(\frac{dx}{dz} \right)^2 + U_{pl}(x). \quad (2.14)$$

By differentiating in the direction of motion, z , we yield

$$pv \frac{d^2x}{dz^2} + U'(x) = 0, \quad (2.15)$$

$$pv \frac{d^2x}{dz^2} + \frac{8U_{\max}}{d_p^2} x = 0. \quad (2.16)$$

The solution of this equation is

$$x(z) = \frac{d_p}{2} \sqrt{\frac{E_t}{U_{\max}}} \sin\left(\frac{2\pi z}{\lambda} + \phi\right), \quad (2.17)$$

where $\lambda = \pi d_p \sqrt{\frac{pv}{2U_{\max}}}$ is the wavelength of the sinusoidal motion and ϕ is the oscillation phase, which depends on initial conditions.

2.2.2 Thermal considerations

Before proceeding to inspecting the bent crystals, it is important to point out that thermal agitations may play an important role in modifying the potential. The atomic oscillation has a mean square amplitude of [44]:

$$u_T^2 = \frac{\hbar^2}{MK\Theta_D} \left[1 + 4 \frac{T}{\Theta_D} \Gamma\left(\frac{\Theta_D}{T}\right) \right] \quad (2.18)$$

where M is the atomic mass of crystal atoms, K is the Boltzmann constant, Θ_D is the Debye temperature at the absolute temperature T and

$$\Gamma\left(\frac{\Theta_D}{T}\right) = \frac{T}{\Theta_D} \int_0^{\Theta_D/T} \frac{t}{e^t - 1} dt. \quad (2.19)$$

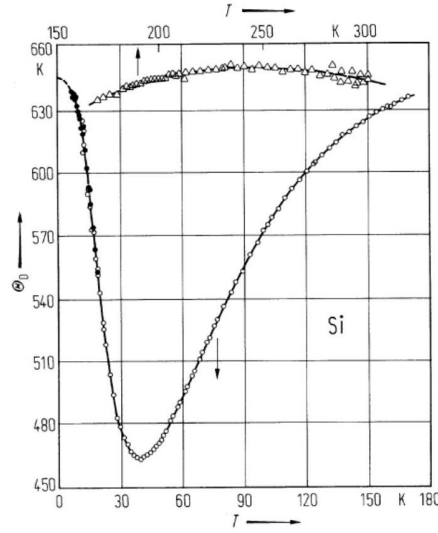


Figure 2.4 – Debye temperature Θ_D in Silicon as a function of the absolute temperature T : bottom curve – $0 < T < 170$ K (bottom scale), top curve – $170 < T < 300$ K (top scale) [45].

Figure 2.4 shows the values of the Debye temperature as a function of absolute temperature.

Since the atoms oscillate independently from each other, we can model the transverse position with a Gaussian function

$$P_T(x) = \frac{1}{\sqrt{2\pi u_T^2}} \exp\left(-\frac{x^2}{2u_T^2}\right). \quad (2.20)$$

By summing up all the contributions $V(|x - x'|)$ from all the infinitesimal atomic layers $(x', x' + dx')$, we get the planar potential as the convolution product:

$$U_{pl,T}(x) = \int_{-\infty}^{\infty} V(|x - x'|) P_T(x') dx'. \quad (2.21)$$

After expanding all the calculations (details can be found in [46]), the planar potential is:

$$U_{pl,T}(x) = 2\pi N d_p Z_c Z_p e^2 a_{TF} \times \sum_{i=1}^3 \frac{\alpha_i}{2\beta_i} \exp\left(\frac{\beta_i^2 u_T^2}{2a_{TF}^2}\right) \left\{ \exp\left(-\frac{\beta_i x}{a_{TF}}\right) \operatorname{erfc}\left[\frac{1}{\sqrt{2}}\left(\frac{\beta_i u_T}{a_{TF}} - \frac{x}{u_T}\right)\right] + \exp\left(\frac{\beta_i x}{a_{TF}}\right) \operatorname{erfc}\left[\frac{1}{\sqrt{2}}\left(\frac{\beta_i u_T}{a_{TF}} + \frac{x}{u_T}\right)\right] \right\}. \quad (2.22)$$

The evolution of the potential due to thermal fluctuations is shown in Fig. 2.5. From this figure

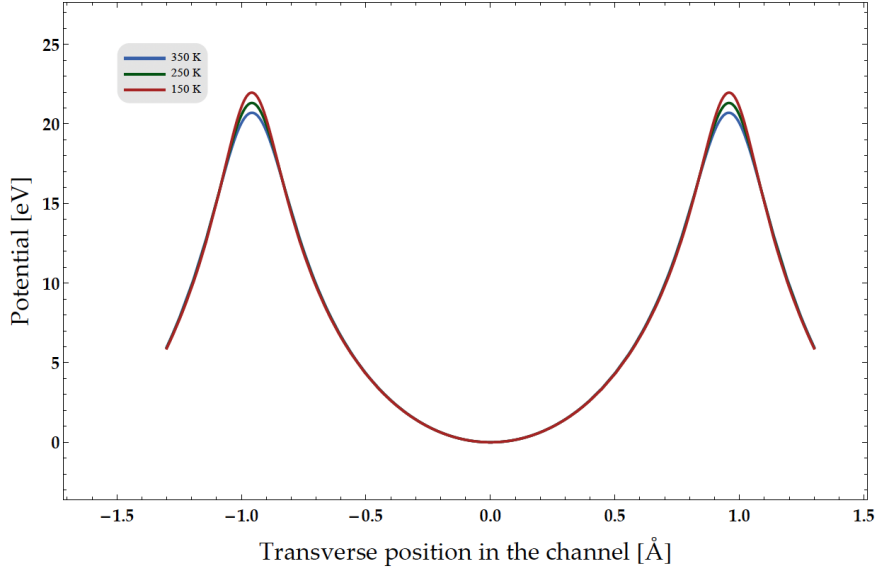


Figure 2.5 – Planer potential of a Si crystal at different temperatures: blue – 350 K, green – 250 K, red – 150 K [46].

we can see that planar potential does not vary significantly at different temperatures, only the maximum changes by a few eV.

2.2.3 Bent crystals

One of the most prominent uses of crystals is in the deviation of particles. For this, it is necessary to bend the crystal to have bent crystalline planes. However, to guarantee the continuity of the potential the bending should be small, i.e. the curvature radius, R , should be much larger than the crystal thickness, w . The bending angle of a crystal is defined as $\theta_b = l/R$, with l being the length of the crystal. The working principle of the channeling and deviation of a particle is illustrated in Fig. 2.6.

The potential of a bent crystal can be found by extending the potential of a straight crystal with the addition of a centrifugal component. Therefore, the equation found in Eq. 2.15 can be transformed into:

$$pv \frac{d^2 x}{dz^2} + U'(x) + \frac{pv}{R} = 0, \quad (2.23)$$

where pv/R is the term of centrifugal force. The extra contribution can be combined with the existing potential to form a new effective potential:

$$U_{\text{eff}}(x) = U(x) + \frac{pv}{R} x. \quad (2.24)$$

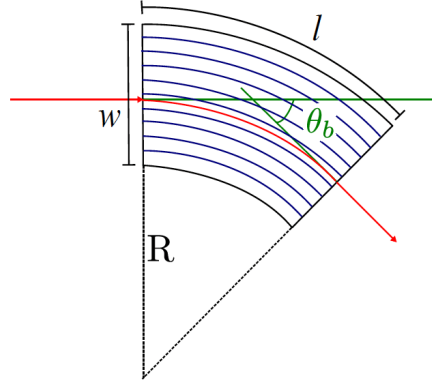


Figure 2.6 – Illustration of the working principle of a bent crystal. The red line indicates the particle trajectory.

Here, due to the finite atomic charge distribution, Eq. 2.6 becomes

$$U(x) \approx U_{\max} \left(\frac{x}{x_{\max}} \right)^2, \quad (2.25)$$

where $x_{\max} = d_p/2 - a_{TF}$ instead of $d_p/2$.

By using a $U_{\text{eff}}(x)$, we can see that channeled particles will still perform harmonic motion. The differences lie in a different equilibrium position corresponding to an off-centered minimum potential and different values in the potential maxima on the two sides (Fig. 2.7). It is also clear from Eq. 2.23 that if the R keeps decreasing, at some point the centrifugal potential will be equal to maximum straight crystal potential, i.e. $\frac{pv}{R_c} = U'(x_{\max})$. This value of R is referred to as the critical radius, R_c :

$$R_c = \frac{pv}{U'(x_{\max})} = \frac{pvx_{\max}}{2U_{\max}}. \quad (2.26)$$

This is the limiting bending radius of the crystal beyond which the particle with momentum p and velocity v can no longer be channeled. The new minimum position is at:

$$x_{\min} = -\frac{pvx_{\max}^2}{2RU_0} = -x_{\max} \frac{R_c}{R}. \quad (2.27)$$

As mentioned previously, the actual depth of the potential well is also reduced. The new one will be at

$$U_{\max}^b = U_{\text{eff}}(x_{\max}) - U_{\text{eff}}(x_{\min}) = U_{\max} \left(1 - \frac{R_c}{R} \right)^2. \quad (2.28)$$

The new bending angle can also be expressed as a function of the straight crystal critical angle:

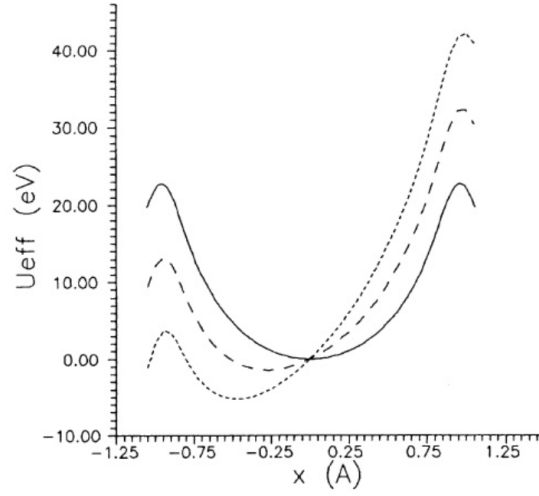


Figure 2.7 – Effective potential of channeling well of a Si crystal: continuous line represents a straight crystal, dashed line represents the effective potential with $p\nu/R = 1$ GeV, and for the dotted line $p\nu/R = 2$ GeV.

$$\theta_c^b = \theta_c \left(1 - \frac{R_c}{R}\right). \quad (2.29)$$

Finally, the solution of the equation of motion of a particle in a bent crystal is

$$x = -x_{\min} + x_{\max} \sqrt{\frac{E_t}{U_{\max}^b}} \sin\left(\frac{2\pi z}{\lambda} + \phi\right), \quad (2.30)$$

where λ is the oscillation period [24].

2.3 Other crystal phenomena

In addition to planar channeling, there are other phenomena that can occur in a crystal. This is because all particles entering the crystal may still interact with the crystal lattice, and consequently gain or lose energy. These effects, similar to channeling, occur at specific incoming angles. We have found that the channeling condition of a particle in a bent crystal is that its impinging angle, θ_i , is smaller than the critical angle of the bent crystal, θ_c^b . Now we explore what happens when the θ_i is outside these limits.

2.3.1 Volume Reflection

For bent crystals, we start from considering the incoming particle range of $\theta_c^b < \theta_i < \theta_b$. This means that the E_t is large enough to traverse at least the first layer of crystalline plane. However,

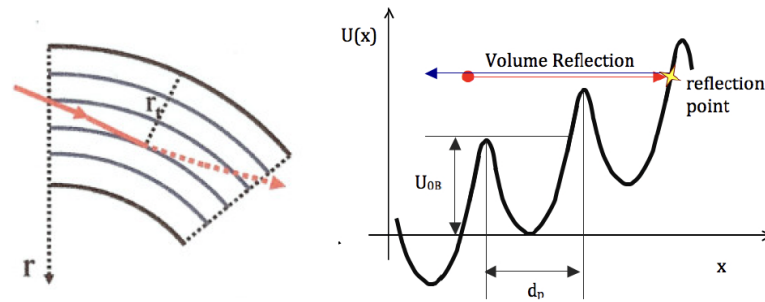


Figure 2.8 – Schematic illustration of the volume reflection process in a bent planar crystal.

the "deeper" the particle travels, the relative angle between the particle travel direction and the next crystalline plane decreases. Since the bending angle is θ_b , the difference in inclination between the first and the last crystal plane is θ_b . Hence, as long as $\theta_i < \theta_b$, the particle will eventually encounter a plane with respect to which the relative angle is zero, i.e. $U_{eff} = E_t$. At this point the particle will be literally reflected towards the center of the channeling well by the potential barrier due to conservation of energy. This phenomenon is called Volume Reflection (VR). A graphical representation of this process is given in Fig. 2.8.

Previous studies have found that in certain cases, particles entering a crystal can go through VR more than 95 percent of the times [47, 48]. However, these particles also need to cross many crystalline planes and this increases the probability of nuclear interactions. Furthermore, the deflection provided by VR (on the order of $1.6\theta_c^b$) tend to be smaller than that from Channeling (CH). Hence, when the goal is to reduce interactions with nuclei, the channeling mode is preferred.

In conclusion, VR is essentially elastic scattering of the particle due to the crystal plane's potential barrier.

2.3.2 Dechanneling

Dechanneling (DC) is the process that takes place when particles in the channeling regime exit channeling and it occurs within the same incoming angle window as for channeling, i.e. $|\theta_c^b| < \theta_i$.

Particles that are channeled may still interact with the lattice nuclei, especially if the oscillation amplitude is big [49]. Due to the inelastic interactions that occur, the particle's transverse energy may exceed the value of the maximum potential and lose channeling condition [50]. Since particles may interact at any point of the crystal well, there will be a distribution of total deflection that ranges from no deflection up to θ_b .

We can imagine that the longer a particle has traveled in the potential well, the less likely it is to find it still in channeling mode. Therefore, we can model the population change of the

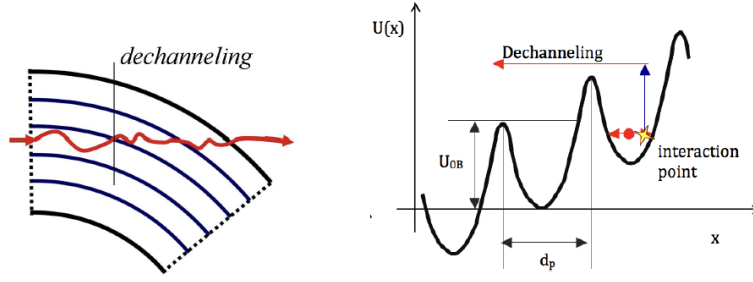


Figure 2.9 – Schematic illustration of the dechanneling process in a bent planar crystal.

initially channeled particles due to dechanneling as an exponential decay:

$$N(z) = N_0 e^{-z/L_D}, \quad (2.31)$$

where z is a path length in the crystal and L_D is the dechanneling length. According to [41] the dechanneling length for straight crystal is:

$$L_D = \frac{256}{9\pi^2} \frac{pv}{\ln(2m_e c^2 \gamma I^{-1})} \frac{a_{TF}}{Z_i r_e m_e c^2}, \quad (2.32)$$

where I is the ionization potential, m_e and r_e are the rest mass and the classical radius of the electrons, respectively.

Additional precaution should be taken for bent crystals, as the two walls of the potential well are not equal and the center of oscillation is shifted. The dechanneling length of a bent crystal is related to that of the straight crystal as follows,

$$L_D^b = L_D \left(1 - \frac{R_c}{R}\right). \quad (2.33)$$

An illustration of the dechanneling process in bent crystals is shown in Fig. 2.9.

2.3.3 Volume capture

Volume Capture (VC) is the opposite process to dechanneling. As interactions within the crystal can increase the transverse energy, they can also decrease it. Volume capture can occur in both the channeling range and the volume reflection range, i.e. $-\theta_c^b < \theta_i < \theta_b$. As with DC, VC can occur at any point, as a consequence the range of possible angular deflections a particle can receive is the same as the one for DC. The process of volume capture is shown in Fig. 2.10.

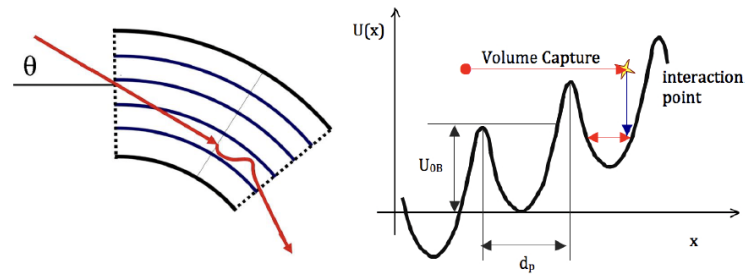


Figure 2.10 – Schematic illustration of the volume capture process in a bent planar crystal.

3 The Large Hadron Collider

The entirety of the thesis work is based on the Large Hadron Collider at CERN [51]. This chapter gives an overview of the LHC design and operation.

3.1 LHC design

The Large Hadron Collider is the world's largest and most powerful particle accelerator, designed to store and accelerate proton and heavy-ion beams. It operates at unprecedented energies, with the design energy being 7 Z TeV. So far, 6.8 Z TeV has been reached. The LHC is located in an underground tunnel at the CERN research center near Geneva, Switzerland. It is a synchrotron with a length of 26.7 km and was originally built in the tunnel that previously housed the Large Electron-Positron Collider (LEP).

The LHC is one of the ion colliders ever built and operated. Others include the Relativistic Heavy-Ion Collider (RHIC) at the Brookhaven National Laboratory and the former CERN Intersecting Storage Rings (ISR) with light ions. During its first operational period (Run 1, 2010–2013), the LHC reached energies of up to 4 Z TeV with proton and $^{208}\text{Pb}^{82+}$ beams, while during the second period (Run 2, 2015–2018) the energy went up to 6.5 TeV for protons and $p\text{-}^{208}\text{Pb}^{82+}$, and to 6.37 Z TeV in $^{208}\text{Pb}^{82+}\text{-}^{208}\text{Pb}^{82+}$. In July 2012, the discovery of the long sought Higgs boson was announced based on the data collected.

From 2019 to 2021, the LHC underwent a phase of machine and detector upgrades. Operation restarted again in 2022 for Run 3, and the LHC achieved even higher energy levels. Proton beams were accelerated to 6.8 TeV, and $^{208}\text{Pb}^{82+}$ beams reached an unprecedented energy of 6.8 Z TeV in 2023. The continuous upgrades and improvements to the performance are crucial for exploring new frontiers in particle physics.

The LHC operates as the final link in chain of accelerator. The injectors pre-accelerate and prepare the beam to meet the requirements of the LHC. The collection of accelerators used at CERN is collectively referred to as the CERN accelerator complex.

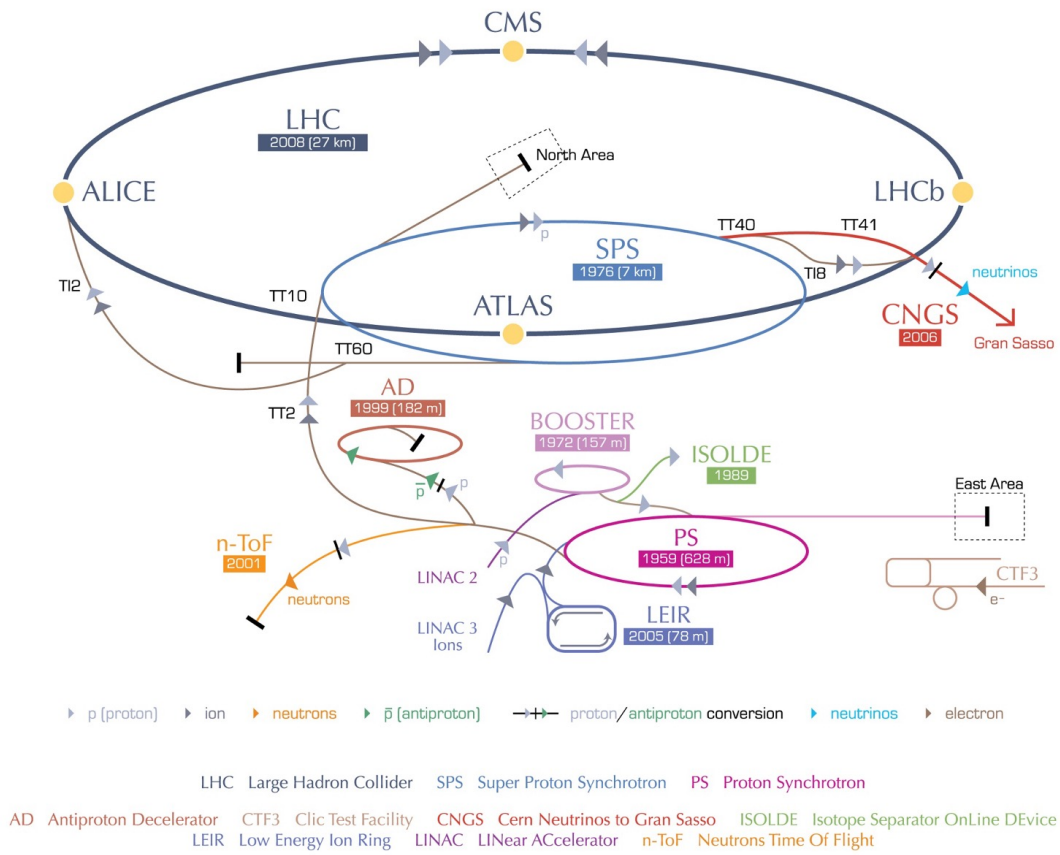


Figure 3.1 – Schematic illustration of the CERN complex [52].

The injector chain for the LHC begins with two separate sources, each producing proton or heavy-ion beams. Proton beam generation starts with a hydrogen ion source that supplies beam to a linear accelerator that accelerates it to a momentum of 50 MeV and then injects it into the Proton Synchrotron Booster (PSB). The PSB further accelerates the beam to 1.4 GeV, which serves as the injection energy for the Proton Synchrotron (PS). The PS provides acceleration up to 25 GeV. After that, the beam is injected into the Super Proton Synchrotron (SPS) where it is brought to a momentum of 450 GeV, which serves as the injection energy for the LHC. A schematic representation can be found in Fig. 3.1.

3.1.1 LHC layout

The overall layout of the LHC (Fig. 3.2) consists of eight arcs and eight straight sections. The latter ones are known as the Insertion Region (IR). Four of these regions, namely IR1, IR2, IR5, and IR8, are dedicated to hosting the main experiments: ATLAS, ALICE, CMS, and LHCb, respectively. The remaining four IRs serve specific operational functions: betatron and momentum cleaning take place in IR7 and IR3 respectively, acceleration occurs in IR4, and the beam dump is located in IR6. These straight insertion regions are separated by the LHC arc

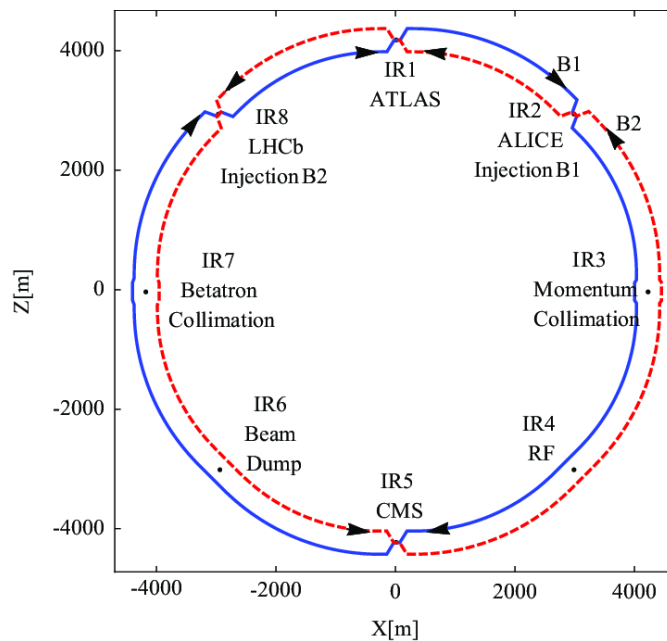


Figure 3.2 – LHC layout. The blue line is beam 1 and the red line is beam 2 [21].

regions, where a combination of superconducting dipole and quadrupole magnets provides the necessary guiding and focusing forces to transport the beam between the insertion regions.

The LHC operates with two counter-rotating beams: Beam 1 (B1) circulating in a clockwise direction and Beam 2 (B2) circulating in a counterclockwise direction when viewed from the top. The longitudinal position within the LHC, typically denoted s , is most of the time measured from IP1 in a clockwise direction, following B1. The two beams circulate in different beam pipes everywhere except around the interaction points of the four experiments.

Each experimental IR has the Interaction Point (IP) in the middle of the section and the configuration of the other machine element is symmetric around the IP. The layout can be found in Fig. 3.2. In the direction of the beam, the section typically starts with the main arc region, which carries the beams from the previous IR to this one. Then, there is the Dispersion Suppressor (DS) region, which is responsible for reducing the periodic dispersion function. This is achieved by omitting one of the three regular dipoles in the arc lattice. Following the DS region, the matching section adjusts the β functions to meet the requirements of the subsequent sections. The separation/recombination dipoles guide the beams from separated beam pipes into a common beam pipe. Finally, the superconducting triplet magnets provide the final focusing at the IP, where the beams collide. However, due to the beams being in the same pipe, there may be undesired collisions. To prevent these secondary collisions in parasitic bunch encounters, crossing angles are applied. Furthermore, separation bumps can also be applied when it is not desired to have collisions.

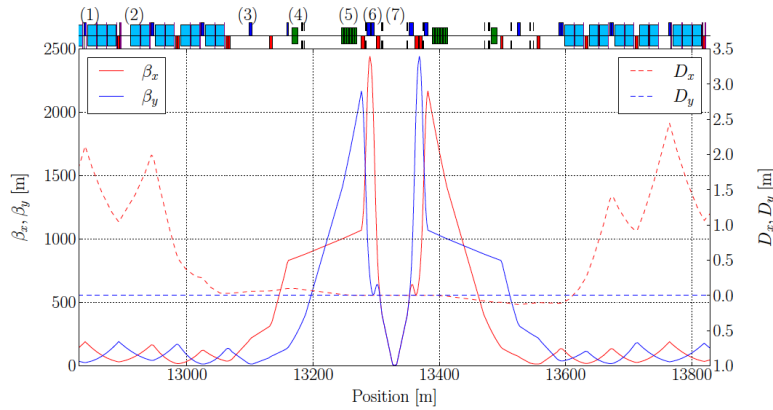


Figure 3.3 – Schematic layout and optical functions of an experimental IR: (1) main arc; (2) DS; (3) matching section; (4) and (5) separation and recombination dipoles; (6) Triplet magnets; (7) IP [37].

3.1.2 Operational cycle

The LHC follows a well-defined operational cycle that ensures safe operation and minimizes uncertainties in magnetic fields that may arise from hysteresis.

The operational cycle begins with the *injection* mode at a beam energy of 450 Z GeV, where particle bunches, or trains of bunches, are injected into the LHC from the injectors. In this configuration, the optics at the collision points are not squeezed but stay at a larger β^* to comply with tight aperture restrictions. The optics in the injection insertions IR2 and IR8 are optimized to achieve the ideal phase advance between the injection septum and the injection protection collimators.

Once the LHC is filled with beam, the mode transitions to the *prepare ramp* phase, during which the injection protection collimators are retracted in preparation for the subsequent energy ramp, which involves accelerating the beams to the top energy. Throughout the *ramp*, power converters, radio frequency (RF) systems, and collimators are adjusted synchronously to match the increasing beam energy and accommodate the decreasing beam size. The stage at the end of *ramp* is called *flat-top* [53].

Following the ramp, the *squeeze* phase is initiated, which is a gradual optical sequence that reduces the β^* value in the high luminosity insertion regions thus reducing the transverse beam size, gradually reaching the final value for collision. In recent years, a first part of the squeeze has been incorporated in the ramp. Then, the beam mode transitions to the *adjust* phase, where the separation bump is collapsed, and small additional bumps are introduced to correct deviations in the closed orbit and maximize the luminosity in the experiments. The end of this phase is called *physics* [22]. Once stable collisions are established in the experimental insertion regions, the beam mode is change to *stable beams*. This beam mode is maintained for several hours until the luminosity decreases below a certain level. At that point, the beams

are intentionally dumped, the magnetic fields are ramped down to match the injection energy, and the cycle restarts. To eliminate hysteresis effects before the subsequent injection mode, the magnet currents are gradually reduced during the ramp down phase to a level below the injection level.

3.2 LHC heavy-ion operation and the High Luminosity LHC

One of the first attempts in history to collide nuclei instead of protons and anti-protons was made at the Relativistic Heavy-Ion Collider (RHIC) at Brookhaven National Laboratory [54]. Then, in 2010, the LHC saw the first collisions of fully stripped lead ions [55]. At the beginning, the ion operation was requested mainly by the ALICE experiment, which aimed to study strongly interacting matter at the highest energy densities. However, in addition to ALICE, the experiments ATLAS and CMS soon joined the heavy-ion programme and took part at the time of the first Pb-Pb run in 2010. In 2012, the asymmetric experiment LHCb joined and participated in the first p-Pb collisions [56]. Further runs with Pb-Pb or p-Pb were carried out in Run 2, with the latest one being the Pb-Pb run in 2018 [57, 58]. Gradual improvements were put in place, reaching a very performing machine setup in 2018. Among others, the bunch spacing was shortened from 100 ns to 75 ns, and thanks to optimizations in the injector chain the achieved average bunch was a factor 3 higher than the design value [58].

In the effort to further improve the machine capabilities, in 2016 the CERN Council approved the HL-LHC project with the aim to significantly increase the machine luminosity for both protons and Pb ions [59, 14]. The operational phase of HL-LHC is planned to start in Run 4, at the time of writing foreseen for 2029. For heavy-ion operation, all main upgrade have been completed already in the Second Long Shutdown (LS2) for the start of Run 3 [60, 27]. Hence, heavy-ion operation has the potential to reach the HL-LHC performance already in Run 3 [61].

To achieve the HL-LHC target performance, several systems of the LHC and the injectors have been, or will be, upgraded. For Pb ions, upgrades in the injectors enable a new production scheme that makes it possible to produce bunch trains with a 50 ns spacing. Thanks to this scheme, 1240 bunches can be injected in the LHC, as opposed to 733 bunches used in 2018. This scheme was put in operation in the first operational period with Pb ions in Run 3, in 2023. The full number of bunches could be achieved in the LHC, however, the HL-LHC targets for bunch intensity and emittance have not yet been fully met. The achieved and targeted parameters are illustrated in Table 3.1. It shows the design parameters for Pb ion operation at the LHC design stage and for HL-LHC, together with the achieved values in 2018 and 2023. It should be noted that some of the 2023 values are preliminary, pending a detailed analysis.

One of the crucial parts is the handling of beam losses when the stored beam energy is increased, which poses great challenges to the collimation beam cleaning system, which is presented in Chapter 4. In brief, the collimation system is in place to keep the beam losses around the ring under control and protect sensitive elements, in particular superconducting magnets that risk to quench due to beam losses. This is more difficult with higher stored beam

	LHC design	2018	2023	HL-LHC
Beam energy (Z TeV)	7	6.37	6.8	7
Total no. of bunches	592	733	1080–1240	1240
Bunch spacing (ns)	100	75	50	50
Bunch intensity (10^7 Pb ions)	7	21	1.5–1.7	18
Stored beam energy (MJ)	3.8	12.9	17.5	20.5
Total beam current (mA)	6.12	22.7	27.1	33.0
Normalized transverse emittance [μm]	1.5	2.3	2.0	1.65
Longitudinal emittance (eVs/charge)	2.5	2.33	2.4	2.42
RMS energy spread (10^{-4})	1.1	1.06	1.02–1.1	1.02
RMS bunch length (cm)	7.94	8.24	8.2	8.24
Peak RF voltage (MV)	16	14	14	14
β^* at IP1/5 (m)	0.55	0.5	0.5	0.5
β^* at IP2 (m)	0.5	0.5	0.5	0.5
β^* at IP8 (m)	10.0	1.5	0.5	1.5
half crossing, IP1/5 [μrad]	160	160	170	170
half crossing, IP2 (external,net) [μrad]	110,40	137,60	170,98	170,100
half crossing, IP8 (external,net) [μrad]	—	160	-135,-274	-170,-305
Peak luminosity, IP1/2/5 ($10^{27} \text{ cm}^{-2}\text{s}^{-1}$)	1.0	6.1	6.4	—
Levelled luminosity, IP1/5 ($10^{27} \text{ cm}^{-2}\text{s}^{-1}$)	—	—	3.5	6.4
Levelled luminosity, IP2 ($10^{27} \text{ cm}^{-2}\text{s}^{-1}$)	—	1.0	3.5	6.4
Levelled luminosity, IP8 ($10^{27} \text{ cm}^{-2}\text{s}^{-1}$)	—	1.0	1.5	1.0

Table 3.1 – Pb beam parameters at the start of collisions in the LHC, as foreseen in the LHC design report (two experiments illuminated) [51], as achieved in 2018 [58, 62] and in 2023, and as envisaged for HL-LHC [63, 61]. The 2018 parameters refer to typical in the fills with 75 ns. Several of the 2023 values are preliminary, pending a systematic and detailed analysis. It should be noted that values for both peak and levelled luminosity are given for 2023, since the luminosity was levelled in the second half of the run but not in the first half.

energy. Therefore, upgrades to the LHC collimation system have been put in place. It is crucial that the collimation works well, in order to avoid magnet quenches and pre-mature beam dumps due to high losses, which is a strong motivation for this thesis work. The aspects of the collimation system and its upgrades are discussed in the next section.

4 Collimation in the LHC

In the LHC hundreds of MJ of energy are stored in the circulating proton beams and more and more ambitious targets are envisioned of the future. For Pb ions, 12.9 MJ were achieved in 2018 and 17.5 MJ in 2023, while the future target is above 20 MJ. The high stored beam energy makes even a small beam loss potentially problematic, in particular for the superconducting magnets, which use type-II superconductors [64]. To maintain their superconducting state, the temperature, applied magnetic field, and current density in the NbTi coils must be such that the material state is kept below a critical surface. When considering a specific pair of parameters among these ones, a critical value for the third parameter can be determined. This critical value marks the transition of the magnet from a superconducting state to a normal conducting state, also known as a quench.

The superconducting LHC magnets are vulnerable to beam losses, as the induced showers reaching their coils cause heating. If the energy deposited by beam particles and their secondary showers exceeds a defined threshold, the magnets can quench. This threshold is referred to as the quench limit. Three distinct time regimes for losses can be identified [65]. Different physical mechanisms come into play for the risk of quench in each time scale. More details can be found in [65].

In order to protect the superconducting magnets and other parts of the machine, a multi-stage collimation system was built [15, 16, 17, 18, 19, 20], where each collimator typically consists of two movable jaws with the beam passing in the centre. The collimation system has several purposes, which can be summarised as:

- Effectively **manage and dispose of particle losses** to minimize the occurrence of magnet quenches.
- Serve as the **primary line of defense** for the entire machine, providing passive protection.
- **Clean the debris generated by collisions** at the interaction points to keep the particle power deposition below the quench limit in the DS.

- **Concentrate radiation** in specific locations of the machine to facilitate easier maintenance access to other parts of the accelerator.
- **Locally protect critical elements** from damage during fast beam failures to enhance the longevity of sensitive apparatus, which would otherwise experience significant degradation if exposed to high radiation levels.
- Probe, scrape, and shape the beam tails, thus **mitigating beam halo issues and enabling accurate diagnostics**.
- **Optimize background levels** at the experimental point for certain colliders. This issue is typically not critical for the LHC but was very important in the 2023 Pb ion run, as discussed more in Sec. 8.6.

4.1 Particle loss in the machine

Particle loss refers to a large enough deviation of a particle from the wanted beam orbit that it eventually leads to the particle hitting the machine aperture. There are two main types of particle loss that may need studying: regular and accidental beam loss.

Continuous beam loss

Since an accelerator is not an ideal conservative system, the motion of the particles is bound to become unstable. Diffusion mechanisms cause the particles to drift from the central region of the beam to its tail. The central part of the beam can be approximated by a Gaussian function and beam core refers typically to everything that is within 3σ . The particles that have drifted out will contribute to populate and replenish what is called the *primary halo*. These halo particles may eventually be lost in the machine. The main causes of the emittance growth and the increase in halo population are [66, 67]:

- Intra-beam scattering.
- Scattering in rest gas in the beam pipe [68, 69].
- Beam instabilities, collective effects, single-bunch instabilities, beam-beam interactions.
- Collisions at the IP.
- Feedback noise.
- Longitudinal drifts out of the RF bucket.

Accidental beam loss

Accidental losses are sudden and unpredictable losses, often due to a malfunctioning of some accelerator element. These can be extremely destructive. Some main causes are:

- Beam injection errors [70].
- Beam extraction errors [71].
- Power converter failures
- Quench heater failures
- General accidents.

4.2 Present collimation system

Typically, the lifetime of the beam in the machine should be at least several hours, but operational conditions in the LHC sometimes result in a drop below 1 hour, with corresponding loss rates of the order of hundred kilowatts or more, which is several orders of magnitudes above the quench limit. Hence, even at the injection energy stage, the LHC cannot be operated without a collimation system.

Given the need for robustness to withstand the highly energetic particles and minimize the leakage out of the collimation insertion, the collimation system of the LHC is designed as a complex multi-stage system to effectively absorb the beam halo and ensure coverage of the phase space under any machine condition. There are two IRs around the ring dedicated to collimation:

- IR3 is used to clean particles with large momentum offsets (momentum cleaning) and sets the energy cut-off threshold. Here, the dispersion should be large, so that the transverse amplitude is dominated by the off-energy component.
- IR7 is the region for the controlled cleaning of the continuous beam loss (betatron cleaning). To target the particles with large betatron amplitudes, the β -function and dispersion are matched so that the transverse offsets are dominated by the betatron offset.

The collimators are categorized into different families based on their usage and consist of two symmetric and independent jaws (blocks of various material), except for the dump collimators, Target Collimator Dump Quadrupole (TCDQ). The layout of the all the collimators is shown in Fig. 4.2. The jaws operate in the horizontal, vertical, and skew planes, utilizing different lengths and materials [17]. To ensure optimal cleaning, the collimators are precisely arranged in a predefined hierarchy in units of the transverse beam size σ , so that every stage is positioned

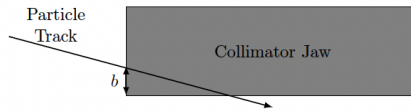


Figure 4.1 – Representation of the impact parameter, b , on a collimator jaw [37].

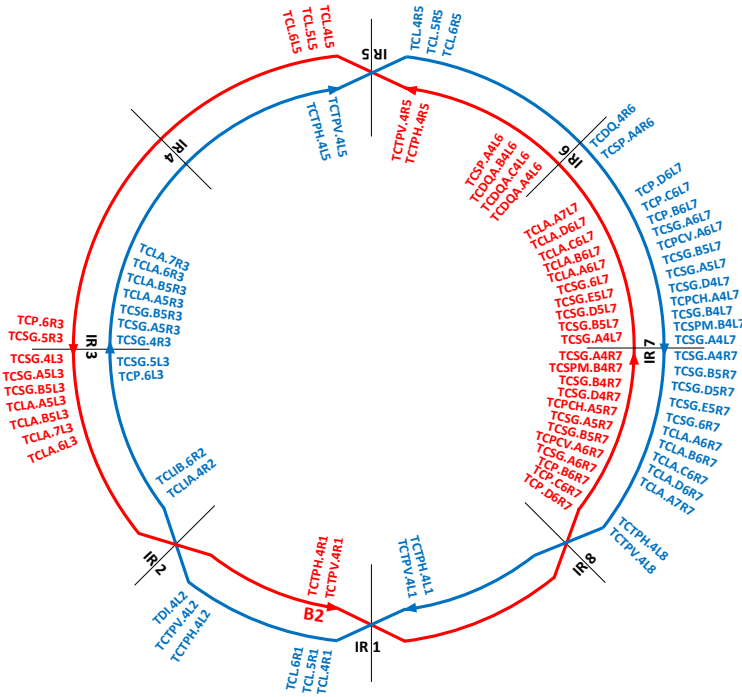


Figure 4.2 – Schematic layout of all collimators in the LHC. The blue line represents Beam 1, and the red line represents Beam 2.

further away from the beam than the previous stage. The need for a multi-stage collimation system comes from the fact that particles usually impact the collimator jaws at very small depths (from a few nm to a few μm [72, 73]) that do not allow the particle to interact with the full length of the collimator due to jaw flatness and surface roughness errors. This depth is called impact parameter, b (Fig. 4.1). This means that many particles will be out-scattered with a simple single-stage collimation. The particles exiting the first stage constitutes the secondary particle halo. A multi-stage collimation would ensure to capture secondary and tertiary particles. The working principle of the collimation system is depicted in Fig. 4.3.

The primary halo is intercepted at the first stage by the Target Collimator Primary (TCP)s, which are the closest to the beam and represents the global aperture bottleneck, i.e. the part of the beam pipe where the circulation is the smallest. These collimators cover the entire transverse space with jaws in the horizontal, vertical and skew planes in IR7. In IR3, only the coverage of the horizontal plane is necessary.

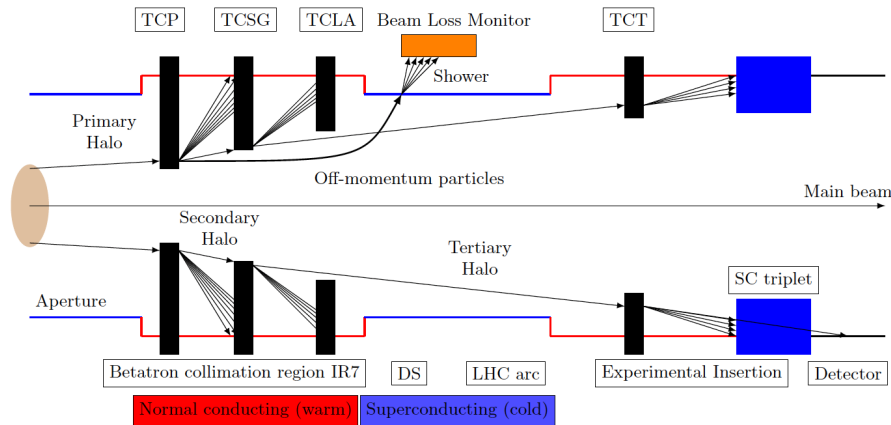


Figure 4.3 – Illustration of the collimation cleaning hierarchy from [37] adapted from [76].

If the particles are scattered out of the TCPs to sufficiently large amplitudes, they will reach the Target Collimator Secondary Graphite (TCSG), which are further from the beam compared to the TCP. Another layer of protection, Target Collimator Long Absorber (TCLA), is added just before the DS to protect the superconducting magnets. These collimators are designed to intercept the electromagnetic showers from the TCSG and some tertiary halo. The TCPs and TCSGs need to be robust, and they are made of carbon-based materials in the LHC (originally carbon-fibre-composite, while later upgraded devices are made of molybdenum-graphite, possibly with a thin Mo coating to reduce impedance [74]). The absorbers should not be exposed directly to high-energy impacts and are instead made of a tungsten alloy (Inermet180) with better absorption that is however less robust.

Sometimes, despite the multi-layered protection, particles may not have received a scattering angle that is large enough to make them captured, and these particles may be lost in the DS section just downstream of IR7. The main reason for particle loss in the DS is the change in magnetic rigidity of the particles mentioned in Section 1.1, where protons from single-diffractive scattering and fragmented ions are particularly affected. The particles lost there are called *collimation debris*.

In the event where the particles are neither intercepted by the TCLA nor lost in the DS, they can likely pass the arcs and then risk to hit the triplet magnets around the IP where there are very large β -functions, making them an aperture bottleneck [75]. To protect the triplet magnets and reduce background for experiments, the Target Collimator Tertiary (TCT)s made of Inermet180 are installed.

Apart from the collimators in IR3 and IR7, there are also other collimators targeted to tackle specific risks [15]. Due to the high luminosity in IR1 and IR5, it is necessary to protect the surrounding machine from the physics debris. This is achieved through the installation of Target Collimator Long (TCL). Another high-risk position is in the section around the beam dump in IR6, which is due to the potentially severe damage in case of dump failure. To protect

the magnets and detector components, the TCDQ and Target Collimator Secondary with Pick-up (TCSP) have been installed. Finally, protection collimators have been put in place also for injection. These are the Target Dump Injection (TDI) and Target Collimator Long Injection Protection (TCLI) in IR2 and IR8. Finally, there is the Target Collimator Long Dispersion (TCLD) mentioned in Section 3.2. An overview of the LHC collimators is given in Table 4.1.

4.2.1 Collimator settings

The movable collimator jaws' locations may be independently changed. The collimator openings are typically provided as the half gap between the jaws in normalised RMS beam size units. The parameters are the same for all collimators in a particular family and can be tweaked to improve collimation efficiency. The following restrictions must be met by the settings:

- Must always minimise the risk of damage to the machine parts, including the collimators themselves.
- The parameters must guarantee that the collimation hierarchy is maintained even when there are drifts in the orbit or optics [77].
- The triplet aperture must always be protected by the tertiary collimators. This means the existence of an upper limit to the maximum applicable TCT setting.
- The impedance due to the collimators should not exceed the instability thresholds.
- To prevent damage during an asynchronous dump, all tungsten collimators and apertures must be sufficiently retracted with respect to the TCDQ/TCSP [71].

The position of the two collimator jaws in their plane is expressed in terms of beam size, σ , in that plane:

$$n_\sigma = \frac{h}{\sigma}, \quad (4.1)$$

where h is the physical distance from the beam center. While the primary collimator defines the geometrical cut of the beam, the secondary collimators should be positioned with an amplitude such that it is able to capture the halo from the primary collimator. The illustration of this multi-stage scattering is given in Fig 4.4. From the longitudinal motion point of view, it is important to ensure that the longitudinal positions of the collimators gives the proper phase advance.

4.3 Particle-matter interaction

To determine whether a halo particle impacting on the primary collimator will be absorbed or scattered to a secondary collimator, and subsequently possibly to an absorber, it is necessary

Collimator name	IR	Plane	Length [m]	Material
TCL.4[R/L][1/5].B[1/2]	1/5	H	1	CU
TCL.5[R/L][1/5].B[1/2]	1/5	H	1	CU
TCL.6[R/L][1/5].B[1/2]	1/5	H	1	INERMET
TCTPH.4[L/R][1/2/5/8].B[1/2]	1/2/5/8	H	1	INERMET
TCTPV.4[L/R][1/2/5/8].B[1/2]	1/2/5/8	V	1	INERMET
TDI.4[L/R][2/8].B[1/2]	2/8	V	1.565	CU
TCLIA.4[L/R][2/8].B[1/2]	2/8	V	1	C
TCLIB.6[L/R][2/8].B[1/2]	2/8	V	1	C
TCP.6[L/R]3.B[1/2]	3	H	0.6	C
TCSG.5[L/R]3.B[1/2]	3	H	1	C
TCSG.4[R/L]3.B[1/2]	3	H	1	C
TCSG.A5[R/L]3.B[1/2]	3	S	1	C
TCSG.B5[R/L]3.B[1/2]	3	S	1	C
TCLA.A5[R/L]3.B[1/2]	3	V	1	INERMET
TCLA.B5[R/L]3.B[1/2]	3	H	1	INERMET
TCLA.6[R/L]3.B[1/2]	3	H	1	INERMET
TCLA.7[R/L]3.B[1/2]	3	H	1	INERMET
TCDQ.4[R/L]6.B[1/2]	6	H	3	C
TCSPA.4[R/L]6.B[1/2]	6	H	1	C
TCP.D6[L/R]7.B[1/2]	7	V	0.6	C (MoGR coated)
TCP.C6[L/R]7.B[1/2]	7	H	0.6	C (MoGR coated)
TCP.B6[L/R]7.B[1/2]	7	S	0.6	C
TCSG.A6[L/R]7.B[1/2]	7	S	1	C
TCPCV.A6[L/R]7.B[1/2]	7	V	0.004	Si
TCSG.B5[L/R]7.B[1/2]	7	S	1	C
TCSG.A5[L/R]7.B[1/2]	7	S	1	C
TCSG.D4[L/R]7.B[1/2]	7	V	1	C (MoGR coated)
TCPCH.A[4L/5R]7.B[1/2]	7	H	0.004	Si
TCSG.B4[L/R]7.B[1/2]	7	H	1	C*
TCSPM.B4[L/R]7.B[1/2]	7	H	1	C (MoGR coated)*
TCSG.A4[L/R]7.B[1/2]	7	S	1	C
TCSG.A4[R/L]7.B[1/2]	7	S	1	C
TCSG.D5[R/L]7.B[1/2]	7	S	1	C
TCSPM.E5[R/L]7.B[1/2]	7	S	1	C (MoGR coated)
TCSPM.6[R/L]7.B[1/2]	7	H	1	C (MoGR coated)
TCLA.A6[R/L]7.B[1/2]	7	V	1	INERMET
TCLA.B6[R/L]7.B[1/2]	7	H	1	INERMET
TCLA.C6[R/L]7.B[1/2]	7	V	1	INERMET
TCLA.D6[R/L]7.B[1/2]	7	H	1	INERMET
TCLA.A7[R/L]7.B[1/2]	7	H	1	INERMET
TCLD.A11[R/L]2.B[1/2]	7	H	0.6	INERMET

Table 4.1 – LHC collimator characteristics for 2022 and 2023 runs. *The collimators TCSG.B4[L/R]7.B[1/2] and TCSPM.B4[L/R]7.B[1/2] are not used simultaneously in a same run. 'H' stands for horizontal, 'V' for vertical, and 'S' for skew.

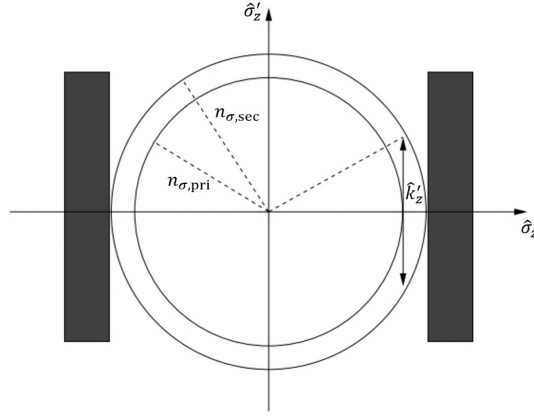


Figure 4.4 – Primary ($n_{\sigma, pri}$) and secondary ($n_{\sigma, sec}$) normalized phase-space plot with the normalized angular kick, \hat{k}'_z , needed from the primary collimator to reach the secondary collimator [78].

to understand its interaction with the collimator material. Therefore, the particle-matter interaction stands as a critical cornerstone in comprehending the theoretical underpinnings of collimation cleaning effectiveness.

Multiple Coulomb Scattering

When a particle is deviated from its original trajectory due to the interaction with the Coulomb field of an atomic nucleus in some material, the particle is going through what is called a Coulomb scattering [79]. This particle can scatter multiple times and accumulate angular deviations over the total number of scatterings to have a large deviation angle at the end. This is the Multiple Coulomb Scattering (MCS) process. The total angular distribution can be described by Molière's formula [79]:

$$\langle \Delta x'_{MCS} \rangle = \frac{13.6 \text{ MeV}}{\beta c P} Z \sqrt{\frac{d}{X_0}} \left[1 + 0.038 \ln \left(\frac{d}{X_0} \right) \right], \quad (4.2)$$

where $\langle \Delta x'_{MCS} \rangle$ is the RMS scattering angle, d is the distance the particle traversed inside the material and X_0 is the radiation length that is a characteristic quantity for the target material.

The radiation length can be accessed through tabulated data or approximated by

$$X_0 = \frac{716.4 \text{ g cm}^{-2} A_m}{\rho_m Z_m (Z_m + 1) \ln(287 / \sqrt{Z_m})}, \quad (4.3)$$

where Z_m is the atomic number, A_m the nucleon number, and ρ_m the density of the target material [79].

Energy Loss from Ionization

Particles at the passage through matter can interact inelastically with the electrons of the atoms constituting the target material. At such encounters, a fraction of the projectile's kinetic energy is disposed into the energy required to liberate an electron from an atom of the target material. While passing through a material, the particle can have inelastic interactions with the electrons of the atoms and deposit kinetic energy into the material. The energy loss per distance travelled, also known as stopping power, can be summarised with the Bethe-Bloch equation [79]:

$$-\frac{1}{\rho_m} \left\langle \frac{dE}{dx} \right\rangle = \frac{4\pi}{\rho m_e c^2} \frac{nq^2}{\beta^2} \left(\frac{e}{4\pi\epsilon_0} \right)^2 \left[\ln \left(\frac{2m_e c^2 \beta^2}{I(1-\beta^2)} \right) - \beta^2 \right], \quad (4.4)$$

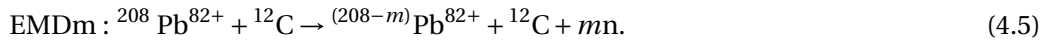
where I is the mean excitation energy (which is tabulated for different materials), m_e is the electron rest mass, q is the particle charge, ρ_m is the density of the traversed material and n is the electron density in the material.

Electromagnetic Interactions

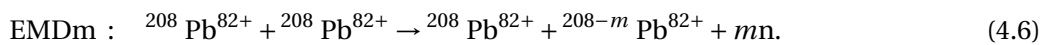
Electromagnetic Dissociation

This process is important for collimation of nuclear beams and not relevant for protons. When the distance at impact between a projectile ion and the target particle is larger than the sum of their radii a photo-nuclear reaction called Electromagnetic Dissociation (EMD) can happen. In these ultraperipheral collisions there can be a large exchange of virtual photon due to the Lorentz contracted electric fields. This can induce the nuclear excitation of both nuclei. The cross section of the EMD process scales proportionally with the square of the atomic number (Z^2) of the impacting nucleus and logarithmically with the relativistic γ factor [80].

The energy gained by the excited nuclei is released as they emit one or more nucleons, with a single-neutron emission exhibiting the highest cross section. Higher order EMD processes with neutron and proton emissions have typically a lower cross section. The neutron (n) emission process of the m -th order, induced by EMD resulting from the interaction of Pb ions in the beam with the carbon material of the LHC collimators, is described by the subsequent reaction equation:



At interaction points, in lead-lead collisions, the same process occurs and the reaction of neutron emission by EMD becomes:



In the context of heavy-ion collimation, the EMD process has a great importance, because the ions that have undergone EMD tend to have a magnetic rigidity rather close to that of the primary beam and without having received a large angular kick. This means that the higher order collimators may not be able to capture them.

Bound-Free Pair Production

The exchange of a virtual photon between two ions in ultra-peripheral collisions may generate a pair of leptons. This process may enable one of the interacting nuclei to capture the negatively charged lepton, resulting in Bound-Free Pair Production (BFPP). Notably, in terms of cross section, BFPP processes involving electron capture are relevant. The BFPP process of m -th order for LHC $^{208}\text{Pb}^{82+}$ ions can be expressed as [81]:

$$\text{BFPP}_m : \quad ^{208}\text{Pb}^{82+} + ^{208}\text{Pb}^{82+} \rightarrow ^{208}\text{Pb}^{82+} + ^{208}\text{Pb}^{(82-m)+} + me^+ . \quad (4.7)$$

To first order, the cross section of the BFPP process with electron capturing is [82]

$$\sigma_{\text{BFPP}} = Z_P^5 Z_T^2 a \log\left(\frac{\gamma_{\text{cm}}}{\gamma_0}\right), \quad (4.8)$$

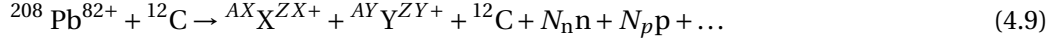
where Z_P and Z_T are the charge numbers of the projectile and target, γ_{cm} is the relativistic Lorentz factor in the center of mass frame and a, γ_0 are tabulated values with a small dependence on Z_T that can be found in [83]. From the dependence on Z_T and the reduced γ_{cm} , we can see that the cross section in collimators is significantly smaller than at IPs.

Nuclear Interactions

Strong force interactions can occur in nuclear collisions when the distance between the centres of the two nuclei is less than or equal to the sum of the radii of the nuclei. The large momentum transfers in gluon exchanges can lead to nuclear excitation and the production of new particles or nuclear fragmentation.

Single Diffractive Scattering (SD) is a crucial nuclear process for protons that interact with the collimator material. During this process, the proton interacts with a nucleus of the collimator material and becomes excited to a higher nuclear state. The proton subsequently decays back from the excited state. As a result of this reaction, the momentum of the outgoing proton is lower in comparison to the initial proton [84]. When this process happens for heavy ions, the fragmentation from the excited projectile and/or target can result in a broader spectrum of residual nuclei compared to the ones produced by EMD processes to cover the entire isotope spectrum (with $A < A_0$) [85]. In addition to a wider spectrum of isotopes, the fragmented particles also have a different angle and momentum with respect to the initial ion. The magnetic rigidities thus differ greatly from the parent particle, which means the loss locations vary greatly. The following formula can be used to describe the disintegration of $^{208}\text{Pb}^{82+}$ ions

in a carbon material:



where A_X, A_Y are the nuclear mass numbers of the fragments X and Y , Z_X, Z_Y are their charge numbers and N_n, N_p are the number of produced neutrons and protons.

Nuclear fragmentation from heavy ion collisions at the IPs does not pose as much of a threat to potential magnet quenches as BFPP due to the smaller cross section [86] and broader magnetic rigidity distribution. On the other hand, high luminosity proton operations can lead to high losses close to the IPs and significant physics debris.

Nuclear Evaporation and Statistical Fragmentation

The residual heavy ions generated from a cascade of interactions may still be in a nuclear charge state higher than the ground level. There are two physical processes of energy dissipation based on the mass of the fragment. Heavy nuclei may decay into their ground state through either by emitting nucleons (nuclear fission) or by emitting δ rays (nuclear evaporation) [87]. The Coulomb barrier suppresses proton emission from nuclear evaporation compared to neutron emission [87]. Light nuclei undergo fragmentation. This can be described statistically using the Fermi breakup model [88]. In this model, significant momentum can be imparted to the residual fragments.

4.4 Collimation performance

4.4.1 Cleaning inefficiency

Since the present collimation system relies on scattering particles to larger amplitudes such that they could be captured by another collimator downstream, it requires that the scattering angular kick $\Delta x'$ is large enough to reach another collimator. Considering as example the TCP and the TCSG, this condition can be expressed as [89]

$$\Delta x' > \sqrt{\frac{(N_S^2 - N_P^2) \epsilon_N}{\gamma \beta_x}}. \quad (4.10)$$

Here, β_x is the horizontal betatron function at the TCP and N_P and N_S are the distances in σ between the one of the collimator jaw and the beam center (also known as half gap) of the TCP and TCSG respectively. This inequality assumes that the betatron phase advance is such that the particle amplitude is maximum at the TCSG. In case this condition is not followed, the particle may keep on circulating in the machine and the loss location becomes difficult to predict.

To evaluate the performance of a collimation system, we can use the local cleaning inefficiency

$\eta(s)$. It quantifies the loss rate in the machine aperture from collimation debris. For proton losses, it is defined as the number of locally lost protons $N_{\text{loc}}(s)$ in an interval $[s, s + \Delta s]$ (a particle is considered lost at a certain location s if it hits the machine aperture/collimator surface s), normalized by the interval length and the total number of protons N_{tot} lost on the collimation system [89]:

$$\eta_p = \frac{N_{\text{loc}}(s)}{N_{\text{tot}} \Delta s}. \quad (4.11)$$

It is possible to merely count the number of protons, as they have similar momenta. However, this definition is less useful for heavy ions because these can fragment into daughter particles with a large momentum spectrum. Hence, a different and more general definition is used for heavy ions, where the different energy contributions are taken into account. In particular, the energy deposited by each ion is used:

$$\eta = \frac{E_{\text{loc}}(s)}{E_{\text{tot}} \Delta s}, \quad (4.12)$$

where E_{loc} is the total amount of energy lost in the interval $[s, s + \Delta s]$ and E_{tot} is the total energy lost in the machine excluding hadronic showers.

These definitions are mostly useful for simulations. In actual measurements, it is not possible to directly obtain the distribution of particles impacting on the vacuum chamber. Instead, what is being measured is the secondary showers created by the particles interacting with the material at the location of impact. Devices used in the LHC to measure the secondary showers are the Beam Loss Monitor (BLM) [90, 91]. There are thousands of BLM in the LHC, typically installed on the outside of the tanks or cryostats, to keep track of particle losses all along the ring around superconducting magnets, collimators and other locations [90, 91]. These are gas filled ionization chambers. These devices monitor the machine continuously to ensure that the quench limit and damage limits, such as plastic deformations limits, are not exceeded, in which case an immediate beam abort is triggered before damage or a quench occurs. Due to the fact that it is the secondary showers that are being measured and due to the limited longitudinal and azimuthal coverage, the BLM signals cannot be directly used to quantitatively deduce energy deposition. To get an estimate of the measured cleaning inefficiency, the experimental equivalent of the η is defined as

$$\eta = \frac{\text{BLM}_{\text{loc}}(s)}{\text{BLM}_{\text{max}}}, \quad (4.13)$$

where BLM_{loc} is the BLM signal at a certain location and BLM_{max} is the maximum BLM signal recorded along the entire ring. BLM_{max} is used as scaling factor because the maximum BLM signal should occur at the TCP in a conventional scattering collimation system and the signal at TCP is proportional to the total number of particles that enters the collimation system. Thus, it is comparable to the normalization in Eq. 4.12 at least in a qualitative sense. Discrepancies by a factor of a few, or up to an order of magnitude can be expected due to the different BLM

responses around the ring [19].

4.4.2 Main limitation and quench limit

With the present collimation system, the main limiting loss location is in the DS of IR7. For protons this is mainly due to SD interactions that modify the particle direction slightly, but the momentum greatly, making its capture by higher order collimators unlikely. For heavy ions, with the fragmentation processes mentioned previously, the particles exiting these reactions may have not only a different momentum per nucleon, but also a different charge-to-mass ratio. When the magnetic rigidity falls out of the rigidity acceptance, the particle can end up in the DS, as the dispersion there is larger.

One of the most important factors to consider in collimation performance is the superconducting magnet quench limit. This is because each quench leads to a considerable machine down time, which is time lost for the physics production. To understand what is the minimum level of collimation performance that is required, we can first model the circulating beam intensity $I(t)$ as

$$I(t) = I_0 \exp^{-\frac{t}{\tau}}, \quad (4.14)$$

where I_0 is the injected intensity and τ is the beam lifetime. During the LHC design, a specification was made that the collimation system should be able to handle $\tau_{\min} = 0.2$ h without triggering a beam dump or quench [92]. The condition for safe operations with the superconducting quench limit being R_q is

$$I_{\max} \leq \frac{R_q \tau_{\min}}{\eta}, \quad (4.15)$$

where η is the highest local cleaning inefficiency. Often, accelerator performance requirements, e.g. on luminosity, set goals for the desired intensity, which together with τ_{\min} and R_q will dictate the maximum possible local inefficiency.

4.5 Crystal Collimation

In a crystal collimation system, the primary aperture bottleneck, where any halo particles should first be intercepted, is no longer the TCPs described above, but instead a bent crystal. If the crystal is oriented such that the crystalline planes are parallel to the incoming trajectory of the halo particles, these are subject to crystal channeling as described in Sec. 2.2. For a bent crystal, the halo particles follow the bending of the crystalline planes and the channeled halo exits the crystal having acquired a large angular kick. Thanks to this kick, the particles hit a downstream absorber, and the impact depth can be made large enough that there is very little out-scattering. An illustration of the working principle can be found in Fig. 4.5. One crystal

and one corresponding absorber is allocated to each beam and plane. The crystals should be placed at a location on the lattice where the divergence of the intercepted halo particles is below the critical channelling angle.

Crystal collimation provides a few advantages over the standard system, especially for heavy-ion collimation. First of all, it gives a more compact system that is easier to control. Secondly, the inelastic interaction rate in the crystals is drastically reduced. This is otherwise a big culprit of losses due to fragmentation in heavy-ion operation. Lastly, the deflection given by the crystal is significantly larger than the one traditionally obtained with amorphous scattering. Hence, it makes absorption in the next collimation stage much more likely, as the particles are more likely to hit the absorber and hit it deeper in the material, thus reducing leakage. Crystal collimation has hence the potential to significantly reduce the cleaning inefficiency in downstream elements.

The method used to evaluate the experimental crystal performance is different than for the standard one in Eq. 4.13. This is because the crystal channels most of the particles it receives and its BLM signal is no longer representative of the total number of particles entering the collimation system. This quantity is thus deduced from the instantaneous change in the total beam intensity, which quantifies the instantaneous number of particles injected in the collimation system:

$$\eta = \frac{\text{BLM}_{\text{loc}}(s)}{dI/dt}, \quad (4.16)$$

where I is the beam intensity. This method can also be used to quantify the cleaning performance with the standard collimation system, in particular when the two systems are compared.

Since the normalization to dI/dt tend to give inefficiencies many orders of magnitude smaller than the simulated one, an alternative normalization of the measured loss maps can be used. This normalization is done with respect to the total BLM energy lost in the ring instead of dI/dt :

$$\eta = \frac{\text{BLM}_{\text{loc}}(s)}{\text{BLM}_{\text{tot}}}, \quad (4.17)$$

where BLM_{loc} is the sum of all BLM signals around the ring. This is normalization has the advantageous of easier comparison with respect to simulated data. For all measured loss maps presented in later chapters where a comparison to simulation is done, a measured loss map with total BLM signal sum can be found in the Appendix.

The first crystal collimators in the LHC were installed in 2015 after extensive studies [26, 24]. These devices were not used for standard operation, but rather for machine studies at low intensity. To compare the efficiency of different bending planes, a (110) crystal was installed for the horizontal plane of Beam 1 and a (111) crystal for the vertical plane of Beam 1. These crystals remained in the machine for the entire duration of Run II. After the successful

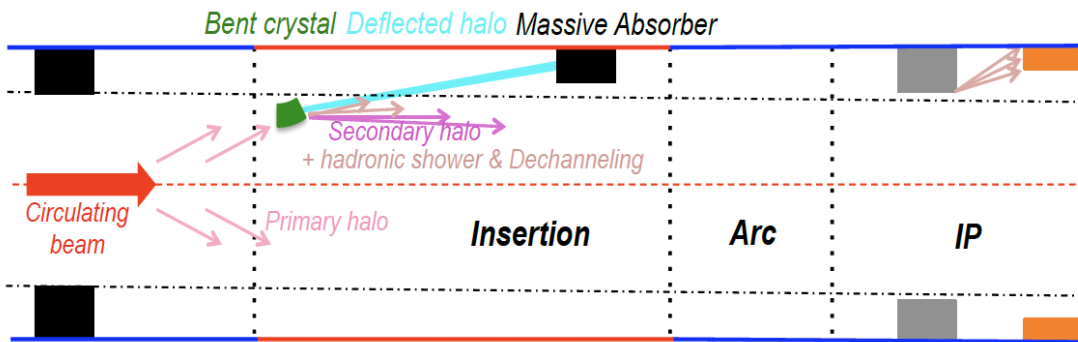


Figure 4.5 – Working principle of crystal collimation [24].

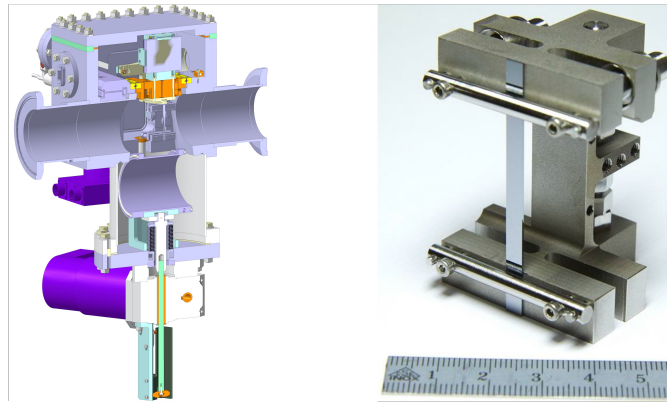


Figure 4.6 – Left – Schematic drawing of a goniometer. Right – (110) crystal in its holder [25].

deployment in 2016 of the first B1H crystals [93], plans were made to install similar crystals in Beam 2. Around the beginning of 2017 one (110) crystal was installed for Beam 2 horizontal plane (B2H) and one (111) for Beam 2 vertical plane (B2V) [25].

All crystals were replaced around the end of the second Long Shutdown (from 2019 to 2022) with (110) crystal for their better performance with respect to the (111) crystal [27]. Both older and newer crystals are featured in this thesis work.

The crystals used for collimation are placed in a holder, which is then mounted on a device called goniometer that is used for linear and rotational motion of the crystal. The assembly of the crystal-goniometer pair is called Target Collimator Primary Crystal (TCPC). The illustrations of a goniometer and a crystal in its holder are shown in Fig. 4.6.

The specifications of all crystals mentioned in this thesis work are displayed in Table 4.5. All crystals mentioned here are of the (110) type and have a width of 2 mm, a height of 50 mm, and a length of 4 mm. The crystals currently present in the LHC at the time of completion of this thesis work have the label "(new)".

NAME	Plane	Installation	Bending	Measured	Energy	Particle
TCPCH.A4L7.B1 (old)	B1H	2015-2016	64.5 μ rad	27.11.2018 [35]	6.37 Z TeV	Pb
TCPCH.A5R7.B2 (old)	B2H	2018	36.4 μ rad	27.11.2018 [35]	6.37 Z TeV	Pb
TCPCH.A4L7.B1 (new)	B1H	6.2023 [94]	49.3 μ rad [95]	26.06.23	450 GeV	p
TCPCV.A6L7.B1 (new)	B1V	12.2021 [96]	46.3 μ rad [97]	11.08.2022	6.8 TeV	p
TCPCH.A5R7.B2 (new)	B2H	2.2023 [98]	45.4 μ rad [99]	15.06.2023	6.8 TeV	p
TCPCV.A6R7.B2 (new)	B2V	12.2021 [96]	51.1 μ rad (Chapter 7) 49.7 μ rad (Chapter 7)	16.06.2023	6.8 TeV 6.8 Z TeV	p Pb

Table 4.2 – Specifications of crystals featuring in this thesis work.

4.6 LHC crystal collimation upgrade for Pb ions

As mentioned in Chapter 3, the increase in I_{\max} by almost a factor 2 for Pb ions envisaged for Run 3 and HL-LHC puts high demands on the cleaning inefficiency of the collimation system, since the requirement on $\tau_{\min} = 0.2$ h is maintained (see Eq. 4.15). In Run 1 and 2 it was also seen that the heavy-ion cleaning performance was 100 times worse than for protons [37, 21, 22, 23]. It was estimated that if nothing is done, the stored beam energy must be kept to around 10 MJ instead of 21 MJ for $\tau_{\min} = 0.2$ h [100, 101].

Since the cleaning performance could not easily be improved with the standard collimation system used in Run 2, it was foreseen earlier to add a new collimator in the IR7 DS, TCLD [102, 103, 59], which would intercept off-rigidity particles. To make space for it, the plan was to install two shorter 11 T dipoles, replacing one standard 8 T dipole, in order to make space for the new collimator. However, this installation has been postponed due to delays in the design and production of 11 T magnets suitable for operation.

In parallel, experimental studies with crystal collimation with Pb ions have been proceeding in the LHC [35]. In these tests standard secondary collimators were used as absorbers in various configurations and a significant improvement in cleaning performance was found with crystal collimation compared to the performance with the standard system [27].

Machine development sessions have been dedicated to crystal collimation studies at low intensity with protons as well [32, 33]. However, the deposited beam power on the absorber would be too high if crystals were to be used in standard physics operation with protons, due to the high intensities (about 400 MJ of stored beam energy has been achieved, and HL-LHC targets almost 700 MJ). This issue is not a concern, on the other hand, for Pb ion operation, even for HL-LHC intensities [104]

Therefore, based on the potential for significantly improved cleaning performance mentioned above and confirmed in initial beam tests, crystal collimation was introduced in the baseline for Pb ion collimation in Run 3 and HL-LHC [27]. It was successfully deployed in physics operation for the first time in 2023, as explained in more detail in Sec. 8.6, which also presents

a few minor problems encountered in operation.

In order to prepare for the 2023 Pb ion run baseline configuration with crystals, it was essential to have a tool that allows one to investigate, understand and explore crystal collimation before the planned operations. Such a simulation tool was not available prior to this thesis work. Multi-turn crystal collimation simulations could only be done for protons. This thesis work builds the framework to simulate the scenarios of interest in the 2023 Pb ion run, as well as future runs, and to simulate other particle species in crystal collimation studies. In particular, with this tool it is possible to study crystal collimation in detail, to identify and mitigate bottlenecks, to optimize present configurations, to make future predictions, and even to follow up operational problems.

5 Simulation tools

Because of the complexity of the LHC apparatus, much of the upgrade studies rely on theoretical simulations. The simulation tools in turn have also become more and more complex and complete over time. For particle collimation it is no different. This chapter gives a short description of all the principal components of the simulation framework used for ion collimation. This framework also lays the foundation for the crystal ion collimation simulation framework, which is part of this thesis work and explained in Chapter 6.

5.1 MAD-X

Methodical Accelerator Design (MAD-X) is a versatile computational tool used for the design and simulation of particle accelerators. Among its capabilities, it is able to simulate beam dynamics, build a computer sequence of the accelerator lattice, and compute and optimize beam optics. The code is written in the languages C, C++, Fortran77 and Fortran90. The tool was first introduced in 2002 as the successor of MAD-8 [105]. For collimation studies, MAD-X is used to produce a beam optics file, which contains magnet strengths and other information that are used as input to particle tracking.

5.2 FLUKA

FLUKA [106, 107, 108, 109] stands for FLUktuierende KAskade in German, i.e., fluctuating cascade. FLUKA is a general purpose Monte Carlo code. Its applications range widely from accelerator design to radiation protection, medical physics, and more. It is a complete package that allows the user to define initial particle distributions, which would then be transported through complex 3D geometries with wide range of material possibilities [106, 108].

FLUKA is important for collimation from the particle-matter interaction point of view, as it is able to simulate detailed interactions between the primary particle and the material nuclei, together with the electromagnetic and hadronic showers.

5.2.1 Development of crystal coherent effects

One of the most important developments in recent years, which enabled the realization of this thesis, is the addition of crystal effects.

Presently, the crystal routine in FLUKA limits itself to (110) crystals. For a bent crystal, a particle that has the right conditions is tracked to follow the channeling well by the use of a virtual magnetic field [46]. Particles are propagated within the crystal in a microscopic step-by-step approach, accounting for modified physical processes compared to an amorphous material. For particles that satisfy the channeling condition, interaction probabilities are reduced. Dechanneling happens via multiple microscopic treatments of single scattering. Quasi-channeled particles are also tracked in single scattering mode [110]. The routine allows user to specify any crystal properties, such as bending, miscut, torsion, etc [46, 110].

This thesis work did not contribute to the development of the FLUKA crystal routine itself, but only uses its functionalities in collimation studies.

5.3 SixTrack

SixTrack is a 6D symplectic particle tracking code originally designed for long-term dynamic aperture studies [111, 112]. At a later stage, particle-matter interactions for protons were added so that SixTrack could be used for proton collimation studies during the LHC design stage [113, 111, 114, 115]. It is able to perform multi-turn high-energy single particle tracking. It does so by efficiently computing trajectories using 6D symplectic maps, or scattering elements [111]. It is able to handle both thick and thin elements. Originally designed for protons, with later upgrades, now it is also capable of handling arbitrary ion species in the tracking part [116], while the particle-matter interactions are still limited to protons only.

It has been used extensively for collimation studies with protons and heavy-ions for multi-turn magnetic tracking. In order to model the interaction of protons with the collimator material, SixTrack includes a Monte-Carlo module and a collimation subroutine [114]. Particle tracking starts with an initial distribution that can be defined in the SixTrack input files. The element-by-element tracking then alternates between magnetic tracking and particle-matter interaction in collimators. Protons are considered lost when an inelastic interaction occurs or when they hit the machine aperture. The check of losses on the aperture is done with a detailed aperture model and a sophisticated loss location computation algorithm [111]. Particles are tracked turn after turn until they are all lost in the machine. The main goal of these collimation studies is typically to obtain the final particle loss distribution around the ring resulting from impacts of the beam halo on the collimation system.

5.3.1 Development of crystal coherent effects

Crystal interactions have been included in the SixTrack for protons. The implementation of the crystal routine began a few years ago [117]. The physics of the model then has been gradually refined throughout the years with more benchmark to experimental data [24, 27]. The model is largely an analytical model combined with interaction probabilities constants derived from experiments [117, 24]. Hence, the fundamental operational principles are different from that in the FLUKA crystal routine, where a microscopic treatment is done and the crystal physics are mainly based on the reduction of the probability of certain interactions.

5.4 SixTrack-FLUKA coupling

The SixTrack-FLUKA Coupling [118] is a simulation framework that actively couples SixTrack 4 and FLUKA. The two codes are run in parallel and exchange information one with another using a special interface called FLUKAIo [119]. For beam collimation purposes SixTrack is used for the magnetic multi-turn tracking, while FLUKA handles the particle-matter interactions in the collimators. This exploits the advantages of both sides.

Presently, this tool is the state-of-the-art of the heavy-ion collimation simulations in the LHC. Heavy-ion simulations began with ICOSIM [89, 120], which used a highly simplified model, where scattering and changes in momentum were not included. Subsequently, to resolve these limitations, the Ion-Equivalent Rigidities (STIER) [37] method was introduced. With this upgrade, the first interactions between particle and collimator are simulated with FLUKA. The particles which survived are then tracked with equivalent magnetic rigidities within SixTrack. This code was able to increase simulation accuracy. A further development came with heavy-ion SixTrack (hiSixTrack), which was able to track arbitrary ion species with the relevant species information. A new Hamiltonian was also implemented for a more accurate tracking of particles with different masses and charges [37, 116]. This SixTrack version was then later coupled to FLUKA for a full online exchange of particle coordinates [121, 37].

For the SixTrack-FLUKA Coupling, during execution, an initial particle distribution is started in SixTrack, which tracks the particles along the ring. When a particle reaches a collimator, all relevant information linked to the particle is sent to FLUKA. FLUKA then performs the necessary particle transport through the collimator in a full 3D geometry. If the particle survives the interactions with the material, the new coordinates and attributes of the original particle and any additional particle that was created are sent back to SixTrack to continue with the particle tracking. Typically, only protons and ion fragments are sent back to SixTrack. The tracking of a particle stops when it gets lost either in a collimator or on the aperture (i.e. on a non-collimator surface). A schematic representation of this process is shown in Fig. 5.1. More details on the input files and customization are explained in Chapter 6.

On the SixTrack side, markers corresponding to the start and to the end of the FLUKA regions are added to the standard optics input file. On the FLUKA side all the 3D collimator geometries

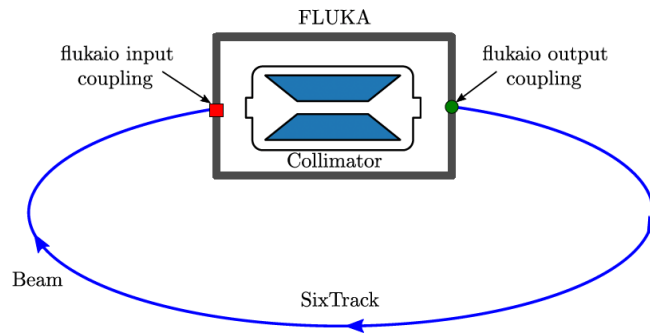


Figure 5.1 – Working principle schematic of the SixTrack-FLUKA Coupling

are places in an ordered line, and a mapping is done between the start and end markers in SixTrack and the start and end of each FLUKA geometry. Each collimator cell contains a detailed 3D model of the collimator, a vacuum region surrounding the collimator and a layer of "black absorber" outside. This is an artificial material in FLUKA, acting as a perfect absorber, which directly stops and kills any particles reaching it. All collimator geometries are stored in a repository called FLUKA elements database (FEDB) (FLUKA element database) for easy retrieval. A frontal view of some of the FLUKA collimator models is given in Fig. 5.2.

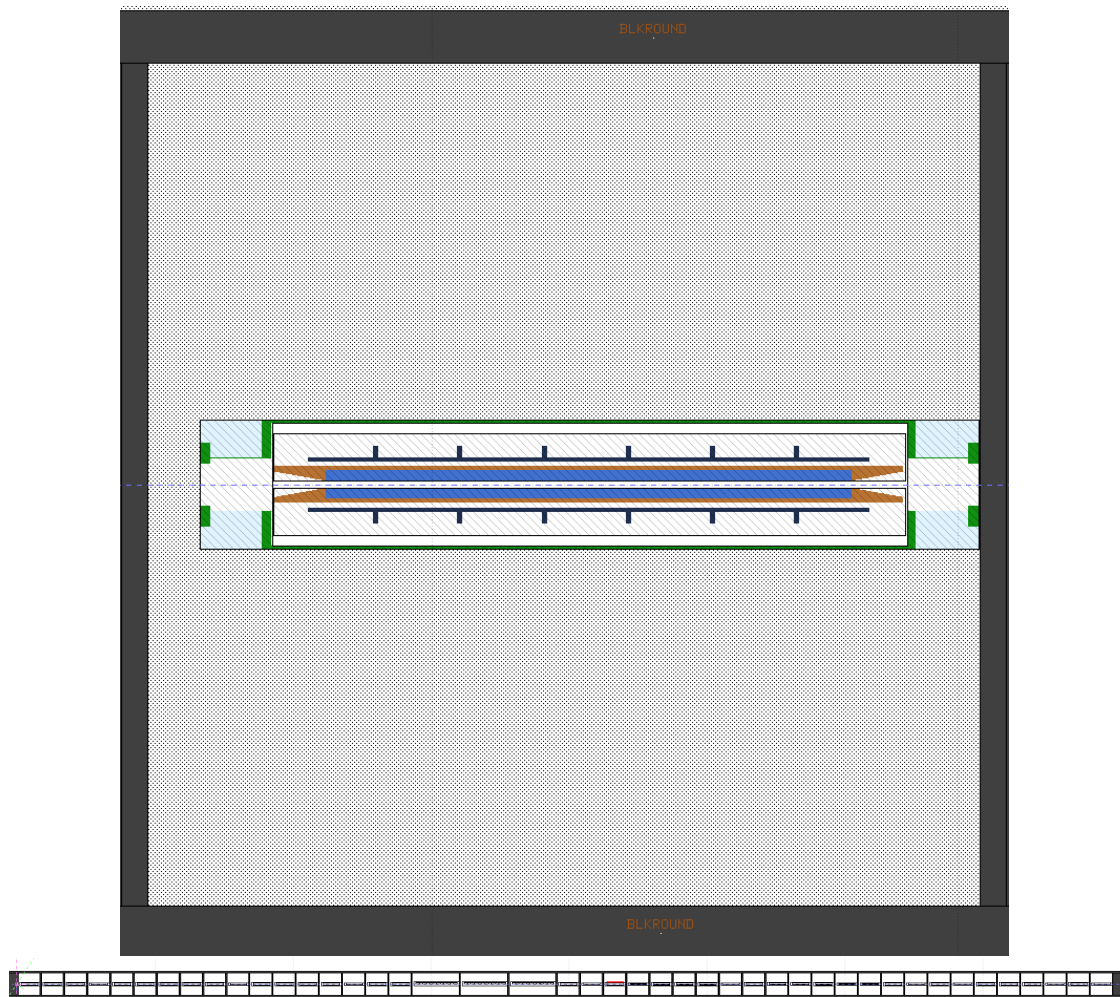


Figure 5.2 – Example of the transverse projection in the x-z plane of the FLUKA 3D geometry of a collimator (TCT - top) and of the geometry of a FLUKA collimator lattice, including many different collimators (bottom).

6 Building of the simulation framework

Because of the challenges outlined in Section 3.2, crystal collimation has been included in the heavy-ion collimation baseline starting from 2023. With this upgrade, it becomes necessary to have a reliable simulation framework to understand, mitigate, and optimize particle loss in accelerators using crystal collimation. Presently, the program SixTrack is used for many collimation studies and activities. However, its crystal collimation capabilities are limited to protons. In an effort to expand the simulation toolkit and set up a more general tool, able to handle also heavy ions and benefiting from the more detailed physics implementation in FLUKA, a new simulation framework is created as part of this thesis work. It relies on the existing SixTrack-FLUKA Coupling, used already for simulations of heavy-ion collimation with the standard collimation system, but with the addition of the new crystal physics recently included to FLUKA. The new simulation tool hence handles combined magnetic tracking and particle matter interactions including both standard collimation and crystal collimation, for both proton and ion beams.

6.1 Main input files for crystal collimation simulation

The SixTrack-FLUKA Coupling, the basis of the crystal simulation setup of this thesis work, requires the active coupling between the particle-matter interactions of FLUKA, the particle tracking of SixTrack, and the optical parameters from MAD-X. Hence, it has a series of complex input files with all the necessary initial information to carry out a simulation. On the other hand, the complexity allows great flexibility in simulation scenarios. This section is dedicated to the description of the compulsory input files, of the SixTrack-FLUKA Coupling, such that the modifications made to include crystals can then be understood.

Typically, for a simple (crystal) collimation study the necessary files to start a simulation are:

- **fort.2:** input file for SixTrack, generated by MAD-X, including the machine lattice and all element strengths that is used by SixTrack to build the machine optics used for magnetic tracking. It has to be modified to include the start and end markers of the FLUKA

regions. Many parameters, such as orbit bumps and crossing angles, can be customized according to one's needs in the generation of fort.2.

- **fort.3:** input file for SixTrack that contains the main parameters of the simulation, e.g. the particle energy, total number of particles, maximum number of turns, particle species, list of collimators for FLUKA, initial external distribution file, etc. It is mostly manually written.
- **fort3.limi:** input file for SixTrack containing a list of aperture definitions around the ring. It is typically generated by an auxiliary tool (`generate_sixtrack_apertures.py`).
- **gpdist_config.txt:** input file for an auxiliary Coupling tool (`gpdist.exe`) that creates the initial particle distribution to be tracked. It is mostly manually written.
- **insertion.txt :** list of injection and extraction roto-translations to make coordinate transformations between the SixTrack coordinate system, at start and end markers of the FLUKA elements, and the FLUKA reference system.
- **lhCFtion.inp:** input file for FLUKA, built as pre-processing by a code within the SixTrack-FLUKA coupling package, called *FLUKA_builder.py* from the FEDB from several separate FLUKA input files, which contains
 - All collimator geometries and roto-translations.
 - Beam information and some of the FLUKA output files to generate, such as information on particles lost and impacts (taken from `include_settings_beam.inp`).
 - Custom variables and scoring (taken from `include_custom_scoring.inp`).
 - Physics settings in FLUKA such as the cutoff energy for transport (taken from `include_settings_physics.inp`).
 - Custom material assignments (taken from `include_custom_assignmat.inp`).
 - Etc.

Beyond these, the program also requires a file with collimator setting information that allows the pre-processing to automatically construct a FLUKA 3D geometry with the correct mm opening for each collimator (*collgaps* file or old version of Collimator Database *CollDB*), optics file from MAD-X (*twiss* file), and a file called *prototypes.lbp* that specifies how to build the lattice of collimators in FLUKA, and links the FEDB with the twiss collimator names.

6.2 Changes made to include the crystal

This section lays out in detail the changes made to the existing SixTrack-FLUKA Coupling that makes crystal-based simulation possible.

6.2.1 Creation of the crystal geometries in FEDB

To have a crystal element recognisable by FLUKA and automatically generated in the pre-processing as any other collimator, it is necessary to define two different parts: the 3D implementation of the geometrical body and the specifications of crystal effects. We first talk about the geometrical body part.

The *FLUKA_builder.py* uses the conventions in the FEDB to assemble a line of collimators of different components, positions, and materials. For each collimator type, there is a unique raw model in the FEDB, which is copied for each instance of that collimator type in the lattice. For each collimator instance, the raw model is automatically modified through rotations and translations according to the transverse angular orientation (horizontal, vertical, or skew), longitudinal tilt, and mm opening of that instance. Hence, the geometrical body of the crystal has been implemented also following the conventions of FEDB. Typically, collimators are defined in what is called *assemblies*, which is a collection of simpler objects called *prototypes*. Since the crystal is a simple object where the supporting structures are far away from the beam and have no influence on the beam dynamics, only the crystal itself has been implemented without the crystal holder, tank, etc. It is therefore sufficient to define a prototype.

To create the prototype of an ordinary collimator element, it is necessary to define three files:

- **Bodies file:** contains the definition of basic geometrical shapes.
- **Region file:** contains the regions to be used that are defined by applying logical operations to the basic bodies.
- **Material file:** contains the material assigned to each region.

For the crystal, the bodies file is named with the convention [accelerator line]_TCPC[plane][beam].bodies. For example, the vertical crystal for Beam 1 of HL-LHC will be called hilumi_TCPCVB1.bodies. The bodies file contains two concentric cylinders to define a ring, a plane to cut the ring on one side, and a parallelepiped box to cut on the other side. All crystal bodies are designed to curve in the horizontal (x - z) plane (Fig 6.1), including vertical crystals. If the crystal body serves for a vertical crystal, then after all rotations and translations, the FLUKA builder will simply rotate it by 90° around the z -axis. This is done because this is how other collimators are dealt with. An example of a bodies file of a crystal with $46.3 \mu\text{rad}$ bending, 4 mm length, 2 mm width, and 50 mm height is

```

1 RPP TCPCVB1      0.0 0.3 -4.0 4.0 0.0 0.6
2 RCC TCPCVB11    8639. -1.7 0. 0.0 3.4 0. 8639.
3 RCC TCPCVB12    8639. -3.0 0. 0.0 6. 0. 8638.8
4 PLA TCPCVB13    1.0 0.0 21597.499984584578 8639. 0. 0.
```

The first column refers to the type of basic body required, the second to the name of the body assigned, and the values following each body refers to the geometric parameters [106]. The first basic body should also be a *boxing body*, i.e. a basic body that contains the entire

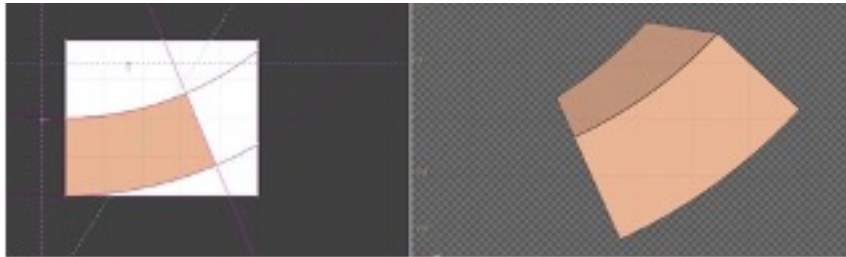


Figure 6.1 – Illustration of the crystal inserted in the LHC with exaggerated proportions: left – x-z side view; right – 3D.

geometric shape defined in this file. The first body in this case is TCPCVB1. Its name then is used by other FLUKA components to refer to the entire geometry defined in this file. Please note that FLUKA uses centimeters as default length unit.

The regions file, called `hilumi_TCPCVB1.regions`, is:

```

1 TCPCVB1R    5 | +TCPCVB1 +TCPCVB11 -TCPCVB12 +TCPCVB13
2 TCPCVB1B    5 | +TCPCVB1 +TCPCVB12
3              | +TCPCVB1 -TCPCVB13
4              | +TCPCVB1 -TCPCVB11

```

The first column defines the name of the region, the number refers to the approximate number of bodies involved, and the terms after “|” are the bodies together with the operations linked to each of them (typically, unions denoted with “+” and intersections denoted with “-” between the basic bodies in order to create more complex geometric shapes). Details can be found on [106].

Finally, the materials file called `hilumi_TCPCVB1.assignmat` is:

```

1 ASSIGNMA    SILICON    TCPCVB1R
2 ASSIGNMA    VACUUM     TCPCVB1B

```

The column indicates the material assignment operation, the second column lists the material, and the last column gives the names of the relevant region.

A visual representation of this kind of geometry with exaggerated proportions is shown in Fig. 6.1. A similar geometry has been defined for all crystals in the LHC. The specification of the crystal always follows the latest measurements. In particular, the 3D model is defined by a segment of a ring formed by two concentric cylinders, where the outer cylinder’s radius and segment length correspond to the measured crystal length and bending radius. However, the measurements using high energy protons and ions are subject to large uncertainties. Hence, the crystal parameters may change from simulation to simulation. In this thesis work, the parameters are defined statically as explained here unless drastic changes in the crystal are found. To account for frequent new measurements and make simulations more robust, it may be beneficial to add the functionality to redefine parameters, such as bending radius, with each simulation in an automated way without editing the prototype definition.

6.2.2 Addition of the crystal block in include_custom_assignmat.inp

The next step is to tell FLUKA that in this prototype there is a crystalline structure, where the dedicated crystal physics processes should be active, and not just amorphous silicon. To do this, it is necessary to add a CRYSTAL card to the FLUKA input for each affected geometry, including the information that is needed to enable coherent effects, e.g., the bending angle, orientation of the crystalline planes in the FLUKA coordinate system, crystal length, torsion coefficient, and the crystal temperature. This has been implemented through a modification of the file include_custom_assignmat.inp, which is used to build the FLUKA input in the pre-processing. It is sufficient to place all the relevant information on all crystal regions in this one file. One example where two crystals are defined (TCPCVB1R is for the hilumi_TCPCVB1 seen above) is:

```

1 * ..+...1....+...2....+...3....+...4....+...5....+...6....+...7..
2 *
3 * Crystal Card
4 *   what(1) = REGNUM (mandatory)
5 *   what(2) = Crystal bending angle [mrad]
6 *   what(3) = A parameter = Crystal length [cm]
7 *   what(4) = B parameter = Torsion coefficient [mrad/cm]
8 *   what(5) = C parameter = Quasi-Mosaic factor [mrad/cm]
9 *   what(6) = D parameter = Crystal temperature [K]
10 *   sdum   = crystal type
11 *   what(7,8,9) = U/V/W of nominal crystal normal to the curvature plane
12 *   what(10,11,12) = U/V/W of nominal crystal channel direction
13 *   what(13,14,15) = X/Y/Z of crystal nominal position
14 * ..+...1....+...2....+...3....+...4....+...5....+...6....+...7..
15 * CRYSTAL  what(1)  what(2)  what(3)  what(4)  what(5)  what(6)  sdum
16 * CRYSTAL  what(7)  what(8)  what(9)  what(10) what(11) what(12) &
17 * CRYSTAL  what(13) what(14) what(15)                                     &&
18 *
19 CRYSTAL    TCPCHB1R    0.054    0.4    0.0    0.0    300.0 110
20 CRYSTAL    0.0    -1.0    0.0    0.0    0.0    1.0 &
21 CRYSTAL    0.00001  -3000.0  10000.0                                     &&
22
23 CRYSTAL    TCPCVB1R    0.0463   0.4    0.0    0.0    300.0 110
24 CRYSTAL    0.0    -1.0    0.0    0.0    0.0    1.0 &
25 CRYSTAL    0.00001  -3000.0  11000.0                                     &&

```

The asterisk sign is the comment sign for FLUKA. The commented lines explains the crystal values shown in the bottom part [46, 106]:

- what(1) the name of the crystal. This must be the same as the name of the first region in the regions file, as defined previously.
- what(2) defines the crystal bending angle in mrad.
- what(3) defines the length of the crystal in cm.
- what(4) defines the torsion coefficient in mrad/cm.
- what(5) defines the quasi-mosaic factor in mrad/cm.

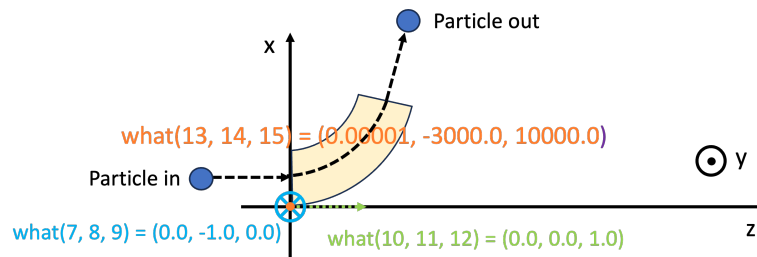


Figure 6.2 – Illustration of the values `what(7, 8, 9)`, `what(10, 11, 12)`, and `what(13, 14, 15)` in context. `what(7, 8, 9)`, in cyan, gives the direction of the equivalent magnetic field for an anticlockwise bending in the x-z plane (dashed black line), which in this case is coming out of the page (i.e. negative y direction). `what(10, 11, 12)` is the dashed green arrow that defines the direction of channeling. `what(13, 14, 15)` is the orange dot and refers to the position from where we want to originate the two previous vectors.

- `what(6)` defines the crystal temperature in K.
- `sdum` defines the type of crystal, i.e. whether it is a 111 or 110 crystal. For the moment, only 110 is possible.
- `what(7, 8, 9)` in the next line are dedicated to the coordinates that define the vector normal to the curved crystalline planes. This parameter can be understood as the direction of an equivalent magnetic field that would give the same deviation. In both crystals taken here as example, the particles would travel in the positive z direction and impact on a face parallel to the x-y plane, to curve their trajectory in the x-z plane anticlockwise. This requires an equivalent magnetic field in the negative y direction.
- `what(10, 11, 12)` are dedicated to the coordinates that define the vector of the crystal channeling direction. This function allows us to set direction of channeling and miscut crystals, that have a channeling direction non-perpendicular to the face that particles impact on. More on miscut crystals can be found in Section 8.2.1.
- `what(13, 14, 15)` refers to the position of where we would like to define the `what(7, 8, 9)` and `what(10, 11, 12)`. This can be seen as the “origin” of the internal channeling reference system. This point can be defined anywhere in the crystal. It is defined in the FLUKA lattice coordinate system, where all the collimators are, and not in the crystal standalone body geometry. It is conventionally defined at the beginning of the crystal, where the particle impacts the body. To avoid numerical computation errors, *x* is set to 0.00001 instead of 0.0.

A schematic illustration of the normal vector, the channeling direction vector and the crystal nominal position is given in Fig 6.2. It is to be noted that it is necessary to break the line in FLUKA after 7 *what*.

6.2.3 Inclusion of the crystal in CollDB

After having defined the crystal element implemented in FLUKA, it is time to tell FLUKA where to put the crystal. Collimator settings are defined both in CollDB and collgaps. Given that there are three dimensions, there are also three possible rotations. CollDB is only able to define the rotation around the z -axis to set if the collimator is in the horizontal, vertical or skew plane. To set crystal orientation with respect to beam direction and allow channeling, it is necessary to rotate in the y -axis (for a crystal in the horizontal plane). This rotation angle is commonly referred to as *tilt*. To do this we need to manually edit the collgaps file. Since the collgaps is not a file that is usually generated by hand because the parameters depend on optics and setting. It is either produced with a short SixTrack simulation or with the *FLUKA_builder.py* both using CollDB. Both methods could be used. The produced collgaps is then modified to include the tilt.

Since the SixTrack-FLUKA Coupling uses SixTrack 4 which is linked to an older version of CollDB, we will also report here an example with the older version of CollDB:

```

1  #
2  TCPCV . A6L7 . B1
3  tcpcv . a6l7 . b1
4  4 . 75
5  CRY - Si
6  0 . 004
7  1 . 5707963267948966
8  0 . 000
9  79 . 62
10 0 . 002
11 0 . 034
12 0 . 0
13 1
14 0 . 000000
15 0 . 000000
16 33 . 41033479
17 255 . 7285437
18 #

```

The first two lines are the name of the crystal for MAD-X and SixTrack in capital and small letters. The second line sets the half-gap of the collimator in beam size, σ . The third line is the crystal material, silicon. Please note that the old version of CollDB and the *FLUKA_builder.py* do not support the direct use of "Si". Only "CRY-Si" is possible. The other lines refer to the other crystal and optics specifications. These are only placeholders and the actual values here are not important, because in the simulation the crystal and optics specifications will be taken from the FLUKA and MAD-X side respectively.

By feeding a CollDB with these settings to *FLUKA_builder.py*, we will be able to obtain a collimator line with the crystal at the correct half-gap, but no tilt. However, we can use the collgaps produced to create the collimator line lattice again after inserting the required tilt. Before we can achieve all this, we must take care of another input file, prototypes.lbp.

6.2.4 Crystal blocks in the prototypes.lbp

The inclusion of the element in the CollDB is not sufficient for the *FLUKA_builder.py* to connect the element the name in the CollDB to the correct prototype geometry, as this is the name used in SixTrack and in MAD-X, but not in FLUKA (it is not always possible to use the same name as FLUKA has specific naming conventions, thus another file is used). To create the link, we need to add extra lines corresponding to the crystal in prototypes.lbp after the lines for the other collimators. Typically the additional crystal lines look like this:

```

1 #
2 PROTOTYPE      CRYHB1
3 FEDB_SERIES    hilumi
4 FEDB_TAG       TCPCHB1
5
6 MAP_ENTRIES    TCPCH.A4L7.B1
7
8 ROT-DEFI        0.0      0.0      0.0      0.0  -3000.0  10000.0 proto
9 ROT-DEFI_FROM_TWISS_SEQUENCE 3  -1.0  rotat  angle
10 ROT-DEFI_FROM_TWISS_SEQUENCE 1  -1.0  trasl  halfgap
11 ROT-DEFI_FROM_TWISS_SEQUENCE 2  -1.0  rotat  tilt1
12 #
13 PROTOTYPE      CRYVB1
14 FEDB_SERIES    hilumi
15 FEDB_TAG       TCPCVB1
16
17 MAP_ENTRIES    TCPCV.A6L7.B1
18
19 ROT-DEFI        0.0      0.0      0.0      0.0  -3000.0  11000.0 proto
20 ROT-DEFI_FROM_TWISS_SEQUENCE 3  -1.0  rotat  angle
21 ROT-DEFI_FROM_TWISS_SEQUENCE 1  -1.0  trasl  halfgap
22 ROT-DEFI_FROM_TWISS_SEQUENCE 2  -1.0  rotat  tilt1

```

Here, there are two crystals reported, each starting with a hash symbol. The prototype CRYVB1 is for the hilumi_TCPCVB1. The non-blank lines from the line 2 to the line 11 are: the name of the prototype; the line of accelerator the prototype belongs to; the FEDB tag or the name of the *boxing body* mentioned previously; the name of the element in MAD-X (and also in SixTrack and CollDB); the position of the prototype in the FLUKA lattice line (cannot overlap with any other collimator); rotation of the raw prototype geometry around the z -axis with the angle taken from the field "angle" of collgaps; translation in the x -axis to set the half-gap taken from the field *halfgap* in collgaps; rotation around the y -axis rotation with the angle taken from the field *tilt1* of collgaps. The crystal is first brought to the designated position in the lattice (Fig 6.3.1) with the line

```
ROT-DEFI        0.0      0.0      0.0      0.0  -3000.0  11000.0 proto ,
```

then *tilt1* rotates it around the y -axis (Fig 6.3.2) with line

```
ROT-DEFI_FROM_TWISS_SEQUENCE 2  -1.0  rotat  tilt1.
```

After the tilt rotation, the line

```
ROT-DEFI_FROM_TWISS_SEQUENCE 1  -1.0  trasl  halfgap
```

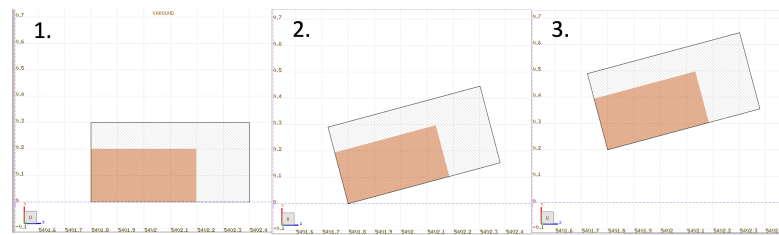


Figure 6.3 – Illustration of the rotational and translational steps of a crystal to be inserted in the collimator lattice. 1. crystal is translated to the designated linear position in the lattice. 2. crystal is tilted around the y -axis for the correct orientation with respect to the beam travelling in the positive z direction. 3. crystal is translated along the x -axis to have the correct half-gap.

applies the half-gap in the x - z plane (Fig 6.3.3) , since all crystals including the vertical plane crystals are defined to curve in the x - z plane. Finally, it is a vertical plane crystal, the line

```
ROT-DEFI_FROM_TWISS_SEQUENCE 3    -1.0    rotat    angle
```

serves to rotate the last setup by 90° around the z -axis.

For normal two-sided collimators there are two jaws, one on the positive axis and the other on the negative axis and "tilt1" refers to the rotation of the positive jaw, and another "tilt2" refers to the rotation of the negative axis. All crystals in the LHC are on the positive side, hence this setting. However, if in the future there should be double sided crystals, this part should be changed to add "tilt2".

6.2.5 Crystal tilt addition in the collgaps file

Since the collgaps file only comes from a simulation of SixTrack or from the *FLUKA_builder.py*, if we choose to use the *FLUKA_builder.py*, then it has to be run twice: the first time with CollIDB to generate the collgaps without crystal tilt, and the second time with the newly generated collgaps and an inserted tilt. Therefore, before running the *FLUKA_builder.py* the second time, the collgaps should be modified to have the tilt in the "tilt1" field and have "Si" instead of "CRY-Si" in the Material field. Hence, the line for the crystal before adding the tilt may look like this:

```
1 # ID name angle[rad] betax[m] betay[m] halfgap[m] Material Length[m] sigx[
  m] sigy[m] tilt1[rad] tilt2[rad] nsig
2 28 TCPCV.A6L7.B1 1.5707963268E+00 3.2325277533E+01 2.5502419737E+02
  1.6669718229E-03 CRY-Si 4.00000E-03 1.24944E-04 3.50941E-04 0.00000E+00
  0.00000E+00 4.75000E+00
```

After inserting the tilt and changing the material, we obtain

```
1 # ID name angle[rad] betax[m] betay[m] halfgap[m] Material Length[m] sigx[
  m] sigy[m] tilt1[rad] tilt2[rad] nsig
2 28 TCPCV.A6L7.B1 1.5707963268E+00 3.2325277533E+01 2.5502419737E+02
  1.6669718229E-03 Si 4.00000E-03 1.24944E-04 3.50941E-04 1.57883206932e
  -05 0.00000E+00 4.75000E+00
```

Using the *FLUKA_builder.py* twice is cumbersome. To circumvent this problem, one may create a higher level script that executes the double compilation automatically, or change the *FLUKA_builder.py* at its source.

6.2.6 Addition of the crystal output file in `include_custom_scoring.inp`

Finally, to add the output dedicated to crystals provided by the FLUKA crystal routine, it is possible to add the line

```
1 * . . . . . 1 . . . . . 2 . . . . . 3 . . . . . 4 . . . . . 5 . . . . . 6 . . . . . 7 . . . . . 8
2 USRICALL          50.0                                CRYSTAL
```

to the file `include_custom_scoring.inp`. This optional scoring creates a file that contains information on the crystal processes that the each particle undergoes in the simulation, in terms of a numeric code for the type of coherent crystal process, incoming angle, kick received, etc. Please note that the particles that experienced inelastic nuclear interaction or EMD or other fragmentation will not be listed, and secondary particles produced are not checked for possible channeling. Thus, by default, secondary particles cannot be subject to any crystal process. This is believed to be a reasonable treatment, as the momentum of secondary and fragmented particles tend to be very different from the parent, thus unlikely to experience channeling.

During the development of this framework, a few inconsistencies were found which triggered updates and changes to the crystal routine itself on the FLUKA side, e.g. a low energy approximation has been removed in simulating the transition region between VR and Amorphous (AM) of high-energy particles without artifacts [106].

7 Simulation framework benchmark

This chapter presents the benchmark works done for the new simulation setup. Previous benchmark studies have been carried out for the two crystal interaction simulation routines, SixTrack and FLUKA, featured here. However, these studies focus on mostly the crystal routine alone and on lower energy particle. Especially for ions, benchmark studies have never been covered in a multi-passage (particle impact the crystal multiple times) collimation setting.

For the SixTrack crystal routine, benchmark results can be found in [122, 24, 123, 25]. In [122], comparisons of the simulated results with detailed single-passage (particles pass through crystal only once) 400 GeV proton data can be found. [24] presents a variety of single-passage and multi-passage benchmark at a few hundreds of GeV with different bending angles. In [123] the background predictions of crystal collimation for 450 GeV protons on a special application for forward experiments [124, 125] compared with measured signals is shown. Finally, proton multi-passage benchmark studies at 6.5 TeV have been carried out in [25] with very encouraging results for most of the studies.

The FLUKA routine benchmarks are presented in [46, 110, 126, 127]. In the publications [46, 110, 126] a series of single-passage benchmark on low energy protons are presented, whereas [127] is a more recent update on single-passage benchmark on low energy ions.

Both tools have limitations in terms of simulation accuracy as reported in the works mentioned above. However, FLUKA has been subject of numerous updates in recent years and benchmark work is not always published. Hence, the limitations discussed in these works may no longer apply to the routine used in this thesis work. Furthermore, since for both simulation routines benchmark has been done at low energies, their performance at higher energies is difficult to predict. This thesis work, therefore, also serves as a first partial benchmark for the individual crystal routines at high energies and not only for the ion-crystal collimation setup.

The benchmark work in this chapter is divided in two parts, one dedicated to protons, and one dedicated to Pb ions. For both species, benchmark investigations cover crystal phenomena alone on a detailed single-pass level as well as multi-turn loss maps using a crystal-based

collimation system.

7.1 Collimation simulation method

With the multitude of particle loss mechanisms outlined in Section 4.1, it is challenging to model particle loss on the collimator system. As it is computationally intensive to simulate the entire beam, including the beam core that typically does not interact with the collimation system, only the beam halo is simulated. The full diffusion process bringing the halo onto the collimator is also not simulated, instead the starting conditions are such that the halo particles have already an amplitude sufficiently large to hit the primary collimators. The starting distribution is typically approximated to either an annular or direct halo, a so-called pencil beam, at an assumed impact parameter, b [17, 18, 19]. A pencil beam is a point-like distribution in the phase space. In the studies presented here a distribution in the horizontal plane would have 1 nm spread in x and a 0.1 μrad spread in x' . In the other plane a Gaussian distribution up to 3σ of beamsize is used. Figure 7.1 shows the example of an annular halo and a direct halo or pencil beam. The impact parameter is usually set to $b = 1\ \mu\text{m}$. This number is consistent with previous diffusion studies [128, 129, 130] but nevertheless carries a large uncertainty. However, the simulation results with the standard collimation system for protons are typically not sensitive to small variations of b , as shown in e.g. [19] for protons. With ion beams, the multi-turn dynamics is more complex and a stronger cleaning dependence on the impact parameter has been observed [37], however, $b = 1\ \mu\text{m}$ gives the worst performance and using this value is therefore conservative. For crystal collimation with Pb ions, the dependence of the cleaning performance on the impact parameter is studied in Sec. 8.2.4 of this thesis. Otherwise, all simulations presented in this thesis use a pencil beam at a 1 μm impact parameter unless otherwise stated.

In FLUKA, ion handling is done with a module called DPMJET within FLUKA and activation is needed for it to be included. Physics processes can be activated based on the user's needs. Some crucial physical interactions for ions, such as EMD, are also activated for ion studies. In order to optimize simulation, there can be cut-off energies and magnetic rigidities, these are the levels beyond which the particles are no longer being transported, but deposited in-situ. For high-energy collimation studies, particles with energies below 1 TeV are not tracked. For the studies discussed in this thesis work, non magnetic cut has been applied. Neutral particles, protons and electromagnetic showers are also not simulated, because similar to the low energy particle, they do not contribute greatly to the overall cleaning result.

The simulation usually starts at the primary collimator, with all particles in the initial distribution interacting with the primary collimation stage already at the first turn. This interaction is handled by FLUKA, and any surviving particles (only the nuclear fragments from the initial ion are typically tracked, and not secondary shower particles) are sent back to SixTrack, where the tracking continues. The particle coordinates are compared with a detailed aperture model with 10 cm precision in each machine element. Particle interactions in any downstream

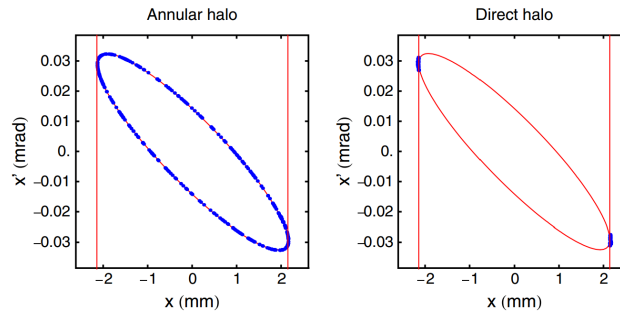


Figure 7.1 – Example of annular halo in the phase space – left and direct annular halo or pencil beam – right. The vertical red lines represent the cut of the relevant collimator [19].

collimator are again simulated in FLUKA in a similar fashion. Each simulated particle is tracked until the particle itself and all its generated daughter particles are absorbed either in the collimation system or the aperture. Particles are considered lost and the tracking stops when they undergo nuclear inelastic interactions inside a collimator or reach the physical aperture in any other element. The coordinates and properties of all lost particles are recorded. In crystal simulations, the beam distribution is one-sided because in each plane there is only one crystal on one side of the beam.

With the beam bending in the x - z plane due to the geometry of the LHC arcs, the dynamics in the two transverse planes, x - z and y - z , are not always the same. Hence, simulations are generally carried out for each beam and transverse plane separately. Independently from the plane simulated collimators from all planes are inserted (exceptions may occur). Beam 1 circulates in the clockwise direction from a topdown view, while Beam 2 circulates in the anticlockwise direction. The planes of simulations are then Beam 1 horizontal plane (B1H), Beam 2 vertical plane (B1V), B2H, and B2V.

To assess and compare collimation studies, one of the most used observables is the so-called loss map. Measured loss maps are acquired usually in low intensity settings (3×10^{11} charges). Losses onto the elements are induced by a transverse damper called Active Transverse Damper (ADT). It excites the beam by introducing white noise. The main targeted section for betatron loss maps, which is the kind studied in this thesis work, is IR7. Beam excitation could also target IR3 for off-momentum loss maps [37]. The signals recorded by the BLMs would constitute a loss map. For simulations, the procedure is as mentioned above.

In a loss map, the local cleaning inefficiency, $\eta(s)$, is plotted as a function of position in the ring, s . η will be as defined in Equation 4.13 if we are investigating a measured loss map without crystal, as in Equation 4.16 if it is a measured loss map with crystal, and as in Equation 4.12 if it is a simulated loss map. The longitudinal bin size used for normalization in simulated loss map inefficiencies is the collimator length for collimator losses as reported in Table 4.1, and 0.1 m for all other elements. It is worth noticing that the crystal collimator with its 4 mm length is shorter than conventional collimators by a few orders of magnitude and due to the

normalization may seemingly intercept very high losses.

In all simulations presented in this thesis work, the assumed crystal temperature is 300 K. This is because the crystal in the LHC is placed in a warm section. Therefore the temperature fluctuation should not deviate from the values plotted in Fig. 2.5 and 300 K is on the pessimistic side for the electromagnetic potential.

7.2 Proton benchmarks

To benchmark the simulation framework, proton beams have first been studied in this Chapter, since the results can be compared against a multitude of experimental data and to standalone SixTrack simulations using its built-in crystal routine [24, 117, 27], which only handles protons. Detailed information on the physics and benchmark of that routine can be found in [24, 122, 131, 117, 25, 132]. Furthermore, it is useful to compare with protons because the channeling condition for positively charged particles only depends on the magnetic rigidity [41], if the interactions with a continuum potential are assumed to be linear.

7.2.1 Single pass

The first type of comparison consists of exploring in detail single-pass studies at high energies (LHC proton energy of 6.5 TeV) independently of multi-turn effects in the accelerator. Comparison has only been done between the simulation tools (SixTrack-FLUKA Coupling and the standalone SixTrack routine) as there are no measurements available at this energy for this kind of study [126]. For this purpose, 6×10^6 6.5 TeV protons uniformly distributed in x and x' have been simulated in both codes to hit the crystal face and pass through it only once. The crystal bends in the $z-x$ plane, while the beam travels in the z direction. The distribution extends from $10 \mu\text{rad}$ to $80 \mu\text{rad}$ in x' and from -1 mm to 1 mm in x . The crystal used is the TCPCH.A4L7.B1 (old) in Table 4.5.

The results in terms of the deflection angle given to any proton as function of its incoming angle from the standalone SixTrack is shown in Fig. 7.2a and from the SixTrack-FLUKA Coupling in Fig. 7.2b. A summary of the efficiency of the various crystal phenomena can be found in Fig. 7.5.

The two codes classify crystal interactions slightly differently (classification categories and codes of the two codes can be found in Tables 7.1, 7.2). This makes quantitative comparisons difficult. As introduced in Chapter 2, different crystal interactions correspond to different incoming angles. Therefore, in the analysis, crystal interactions have been assigned again independently from the tools, where each particle exiting the crystal has been assigned to a given interaction process according to its incoming angle and angular kick. The division boundaries to distinguish the different processes are shown in Figs. 7.2a and 7.2b. The incoming particles are perfectly aligned with the crystal planes when $\theta_i = 0$.

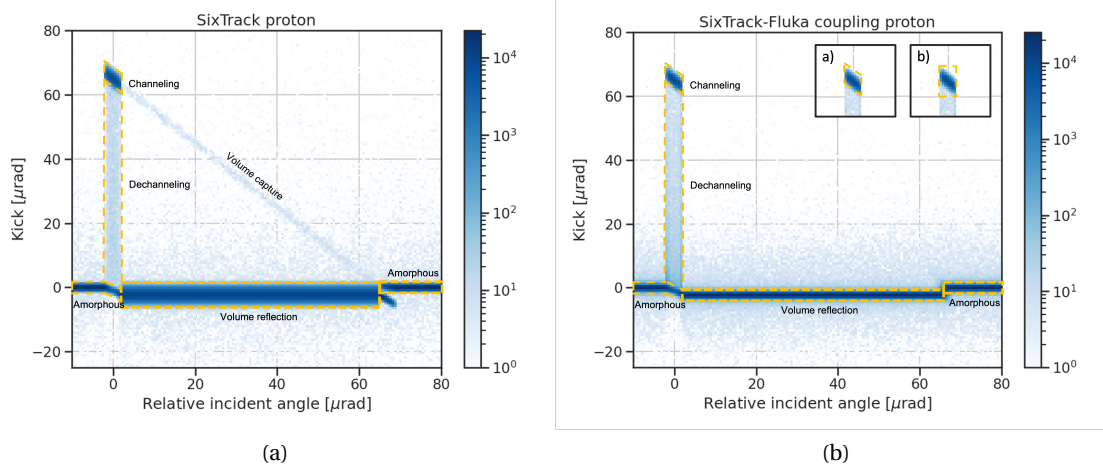


Figure 7.2 – Simulated proton angular kick distribution as a function of relative angle between incoming particles and crystal orientation with SixTrack (a) and SixTrack-FLUKA Coupling (b) after a single pass through the crystal. In figure (b), subfigures a) and b) compare the final CH boundaries between using small histogram slices – a) and a rough section cut – b).

The division boundaries have been found by first dividing the incoming angle axis. The numerical boundaries can be found in Table 7.3. After the division on the horizontal axis, a histogram of received angular kicks for a selected incoming angle window is plotted for each interaction process except for the channeling window. The angular kick distribution is then fitted with a Gaussian function. All particles within the 3 standard deviations are assigned to the process linked to that incoming angle range. An illustration of how the analysis was done is shown in Fig. 7.3, where the VR region is taken from the incoming angle range of $2\mu\text{rad} \leq \theta_i \leq 65\mu\text{rad}$ for SixTrack. In this figure the full range in angular kick is plotted. The Gaussian function is fitted to the VR peak around $-2.32\mu\text{rad}$ with the dashed black line and 3 standard deviations are used. The same method is applied to the SixTrack-FLUKA Coupling.

For the channeling window, smaller sub-slices of the order of 0.2 to $0.4\mu\text{rad}$ in θ_i are taken, because rough rectangular boundaries as the ones shown in Fig. 7.2b subfigure b) would include particles that were not fully channeled. Hence, the approach that gives the boundaries in Fig. 7.2b subfigure a) is preferred. For each slice, a histogram of angular kicks is plotted and one Gaussian curve is fitted for the channeling region and another for the amorphous region. All particles in between the channeling and amorphous curve are counted as dechanneled particles. All particles that do not fall within any of the boundaries found are considered scattered particles. Volume captured particles have not been included in the scattered particles, as the volume capture process has not yet been included in the FLUKA routine for high energy particles, as seen in Fig. 7.2b. The difference between the initial number of particles and the final number of particles is considered as particles absorbed by the crystal. The number of particles is used because we do not expect a big difference in total energy between each particle.

Code	Crystal interaction
1	Amorphous
2	Volume reflection
3	Channeling
4	Volume Capture
5	Absorption
6	Dechanneling
7	Proton-neutron elastic interaction
8	Proton-proton elastic interaction
9	Single diffractive
10	Rutherford Scattering
15	Channeling followed by absorption
17	Channeling followed by proton-neutron elastic interaction
18	Channeling followed by proton-proton elastic interaction
19	Channeling followed by single diffractive
20	Channeling followed by Rutherford scattering
100	Volume reflection in VR-AM transition region
101	Amorphous in VR-AM transition region

Table 7.1 – SixTrack crystal process classification codes.

Overall, the results in Figs. 7.2a and 7.2b agree well between the two codes. The main differences that can be noticed between the two routines are the lack of volume capture in FLUKA, a different distribution for volume reflection in the y-axis (Fig. 7.4a), and a different distribution in the x-axis for the dechanneled particles (Fig. 7.4b). Presently, because there is no experimental data at this energy and precision, it is not possible to determine the correct approach. The accuracy of reproducing the volume processes are, however, not of capital interest to the specific application of LHC operations, as they have a negligible impact on the loss maps when channeling is the chosen regime. The doubt on the DC distribution may also not introduce significant differences in loss maps, discussed in Sec. 7.2.2, as long as the downstream absorber has an aperture small enough to capture most of the dechanneled particles that have smaller angular kicks together with the CH particles. For DC however, the FLUKA approach seems more reasonable, because with larger θ_b particles oscillate with larger amplitudes, and they thus have a higher probability of interacting with the lattice. Nevertheless, VC should only occur to a small fraction of the volume particles.

In conclusion, the process rates agree quite well between the two routines and for the discrepancies seen (different VR and DC distributions) it is difficult to judge the approaches due to the lack of experimental data. Benchmarks for both tools have been done at lower energies [122, 24, 123, 25, 46, 127, 110, 126, 132]. However, any accuracy at lower energy may not reflect the same level of accuracy at high energies. The lack of VC in FLUKA at high energies is known and the FLUKA team is actively working on implementing it in future releases.

Code	Crystal interaction
-1	Amorphous
0	Amorphous
1	Hybrid
2	Dechanneling
3	Channeled (until the end)
4	Captured
5	Reflected

Table 7.2 – FLUKA crystal process classification codes.

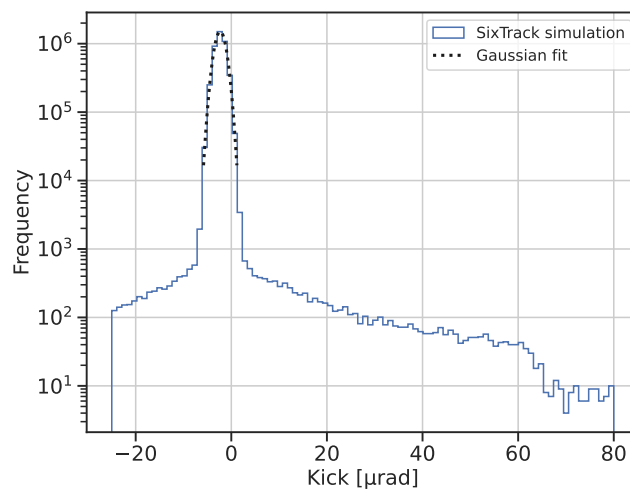


Figure 7.3 – The blue line is the SixTrack simulated B1H crystal angular kick distribution in VR range with 6.5 TeV protons. The black dashed line is the Gaussian fit of the VR peak. The incoming angle range is from 2 μrad to 65 μrad .

7.2.2 Loss Pattern

Having assessed the single-pass crystal treatment of the FLUKA routine, we now assess the crystal as inserted in a multi-turn accelerator, which contains also other collimators.

As an example benchmark case an LHC B1H loss map is selected, with crystal in channeling orientation for 6.5 TeV protons measured on the 12th of September 2018 with a β^* of 1 m. This test was part of a machine development session, described in detail in [33]. The loss map acquisition was part of a larger set of crystal tests. For the entire machine development session, 30 bunches with total intensity below 3×10^{11} protons are injected. Right after injection, crystals are aligned in the transverse planes to the beam size (or beam envelope) to ensure that it is touching the beam core but not scraping, and that it is the closest collimator to the beam. Once the crystals are aligned transversely, they are rotated slowly to find the orientation where they are in optimal channeling. This process is called *angular scan* and it is

SixTrack [μrad]	Coupling [μrad]	Processes
-10 – -2.2	-10 – -2	AM
-2.2 – 2	-2.2 – 2	CH, DC, AM
2 – 65	2 – 66	VR, VC
65 – 80	66 – 80	AM

Table 7.3 – Crystal single pass study incoming angle boundary division for protons.

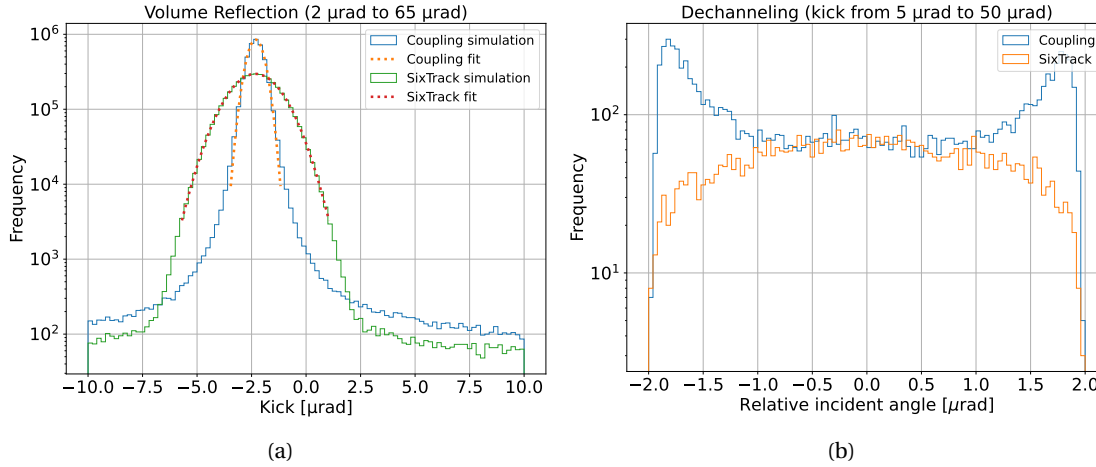


Figure 7.4 – Left: Comparison of simulated VR distribution in angular kick for the B1H crystal with 6.5 TeV protons. The incoming angle range is $2\mu\text{rad} \leq \theta_i \leq 65\mu\text{rad}$. The blue curve is SixTrack-FLUKA coupling simulation and the orange curve the SixTrack simulation, whereas the dashed orange and red lines are their respective Gaussian fits. Right: Comparison of simulated DC in incoming angle for the B1H crystal with 6.5 TeV protons. The range is $-2\mu\text{rad} \leq \theta_i \leq 2\mu\text{rad}$ and $-10\mu\text{rad} \leq \theta_{kick} \leq 50\mu\text{rad}$. The blue curve is SixTrack-FLUKA coupling and the orange curve SixTrack.

described in detail in the next Section. Various measurements are then taken at this energy. For the measurement of interest in this section, the energy is ramped up to 6.5 TeV. During the energy ramp the beam envelop changes in size transversely and the beam divergence, which is essential in having optimal channeling also changes. Hence, since the energy ramp up is an automatic process, to maintain channeling throughout the ramp, a function was produced in advance for both linear and angular position [27]. Once the beam has reached top energy, the loss maps are acquired as described in Section 7.1. The test was done at the machine stage of *flat-top* and the collimator used as absorber was TCSG.B4L7.B1. The collimator settings can be found in Table 7.4.

The method to simulate the loss distribution around the ring is described in Sec. 7.1. As the data were obtained during Run 2 at the *flat-top* stage, the optics used for simulation is the corresponding Run 2 optics [133]. The simulation uses a standard pencil beam at an impact parameter of $1\mu\text{m}$ on the crystal and with an initial population of 60×10^6 protons. Since the

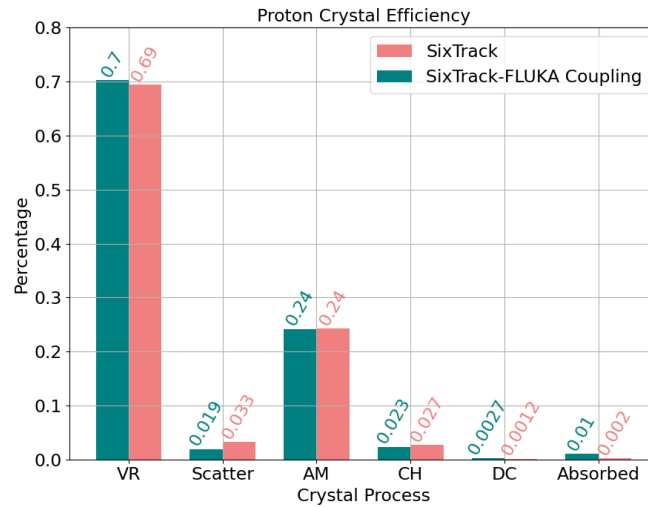


Figure 7.5 – Relative interaction rate of the different coherent crystal processes for 6.5 TeV protons as simulated with the standalone SixTrack and the SixTrack-Coupling.

crystal is only placed on one side of the beam, the beam distribution is also only one-sided. Collimation cleaning efficiency is assessed by plotting the loss map around the entire ring (Fig 7.6). Special attention is paid to the IR7 dispersion suppressor, which is typically the location with superconducting magnets that receives the highest fraction of the collimation losses leaking out of IR7. This location is typically therefore the bottleneck for any limitations on beam intensity and lifetime. For this reason, an IR7 zoomed plot is shown in Fig. 7.7. For ease of comparison the measured loss maps have been plotted also normalizing to the total BLM signal around the ring instead of dI/dt (see Eq. 4.17). This is done whenever there is a comparison between measured and simulated loss maps. They can be found in the Appendix.

Figure 7.6 compares the measured and the simulated loss maps. Black, red, and blue bars represent the losses on the collimators, warm sections and superconducting (cold) sections respectively. The SixTrack-FLUKA coupling shows an excellent agreement with the SixTrack standalone routine, where it should be noted that SixTrack has a higher energy cut (threshold below which a particle is no longer transported) and therefore gives less warm losses around $s = 20150$ m. Above the measurement noise level, a good qualitative agreement of the measured loss pattern with the SixTrack-FLUKA coupling can be observed. A detailed quantitative comparison is not possible here since the simulations show lost particles and the measurements show the energy deposition at the BLMs from the induced shower. Previous studies have shown that an order-of-magnitude discrepancy can be expected due to only the difference in response of BLMs at different locations [19]. Further discrepancies can be expected from the fact that a single particle loss can cause showers that affect several BLMs. The particle shower propagation to the BLMs is more pronounced in the warm regions, which explains these higher measurement values (red bars in Fig. 7.7). With a detailed FLUKA shower propagation simulation as a second step using the SixTrack results as inputs, it is also possible

Collimator	IR	Half gap [σ]
TCPD6L7.B1		123.0
TCPC6L7.B1		91.0
TCSG.B6L7.B1		107.0
TCSG.A6L7.B1		104.0
TCPCV.A6L7.B1		out
TCSG.B5L7.B1	7	87.0
TCSG.A5L7.B1		85.4
TCSG.D4L7.B1		6.5
TCPCH.A4L7.B1		5.0
other TCSGs		6.5
TCLAs		10
TCPs/TCSGs/TCLAs	3	15.0/18.0/20.0
TCTs	1/2/5/8/2	8.5/37.0/8.5/15.0
TCSGs/TCDQ	6	7.4
TCL	1/5	out

Table 7.4 – Collimator settings for 2018 B1H proton angular scan benchmark at 6.5 TeV ($\beta^* = 1$ m) [27].

to simulate power deposition, such as in [134], where inputs from this thesis were used. In past simulations of this type, the typical agreement with measured BLM signals is around a factor of 3 in the DS, while the agreement in the warm sections is even better [19, 135].

Both losses on the IR7 cold magnets and on the rest of the collimators show good agreement, except for a slight underestimation of the simulation compared to data for the collimator cluster around $s = 20100$ m, which may be due to upstream showers. It is worth mentioning that for simulation all losses on one collimator are grouped together in one bar, while despite having only one BLM per collimator, there can be other BLMs close by, thus generating more loss bars. Furthermore, the high simulated loss at $s = 19919.5$ m in Fig. 7.7 representing the crystal cannot be directly compared with the measured data, as the simulation result is normalized to the length of the crystal, which is two orders of magnitude shorter than the other collimators.

Finally, regarding the different treatment of volume processes and dechanneling between the two tools mentioned in the previous paragraph, the good agreement between the two loss maps confirms that the accuracy of reproducing the volume processes is not of capital interest in this kind of operations. Furthermore, in view of the collimation setup, the doubt on the DC distribution may potentially be a small issue as long as the downstream absorber has an aperture small enough to capture most of the dechanneled particles that have smaller angular kick together with the CH particles.

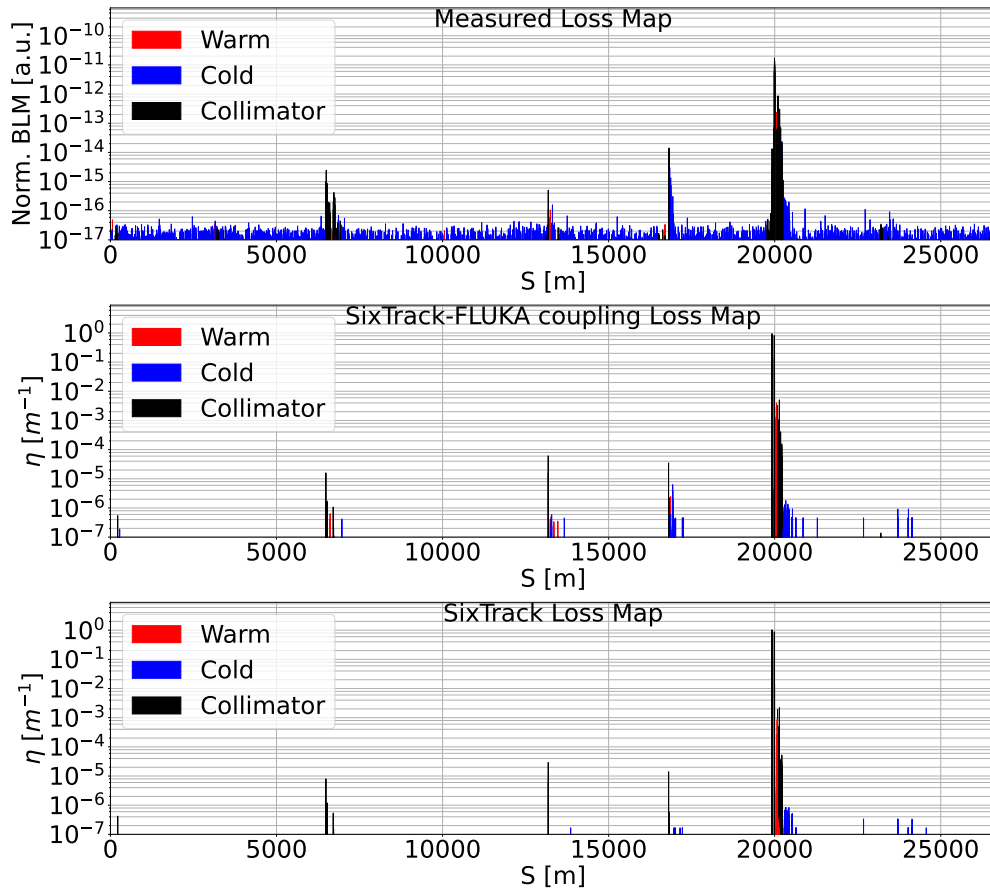


Figure 7.6 – Measured (top), SixTrack-FLUKA coupling simulated (middle) and SixTrack simulated (bottom) loss map from the B1H 2018 proton test at 6.5 TeV ($\beta^* = 1$ m). Measured loss map normalized to total BLM signal can be found in Fig. A.1.

7.2.3 Angular scan

After the multi-turn benchmark with the crystal in channeling orientation, we study so-called angular scans that are performed to assess the loss pattern at other crystal orientations. At constant loss rate, the crystal is rotated with respect to the incoming beam such that the incoming angle changes (a representation is shown in Fig. 7.8), and the BLM signal close to the crystal is recorded as a function of angle. To improve the signal-to-noise ratio and detect clear BLM signals, for each measurement, three bunches are excited with the ADT (the same ADT used in acquiring loss maps, as describes in Section 7.1). The white noise introduced by the ADT increases the diffusion rate and the particle losses in a controlled manner. The signal at different orientation angles is then normalized by the signal acquired at the orientation where the crystal acts as an amorphous material. The scan ranges over angles where the crystal is in the orientations for channeling, volume reflection, or amorphous scattering, giving rise to variations in the rate of inelastic interactions at the crystal, and hence also the local BLM signal [24].

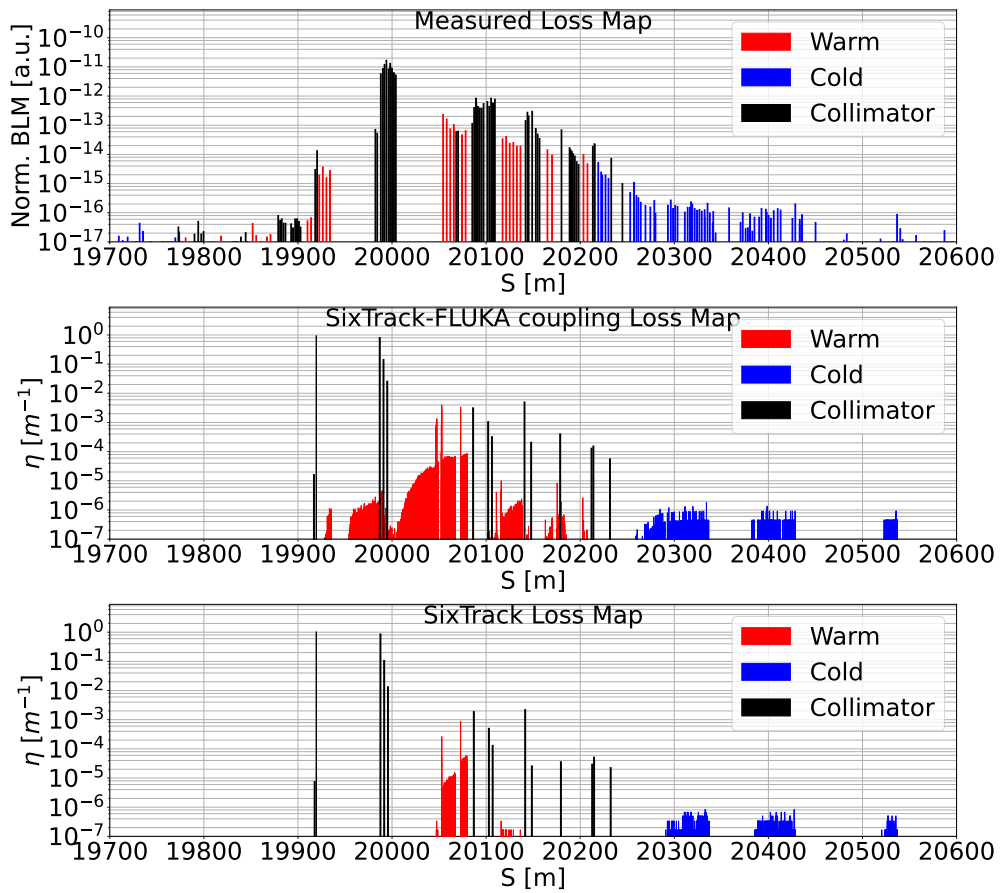


Figure 7.7 – Measured (top), SixTrack-FLUKA coupling simulated (middle) and SixTrack simulated (bottom) loss map from the 2018 proton test at 6.5 TeV, as in Fig. 7.6 but zoomed around IR7. The crystal can be found at 19919.5 m and the absorber at 19987 m. Measured loss map normalized to total BLM signal can be found in Fig. 7.7.

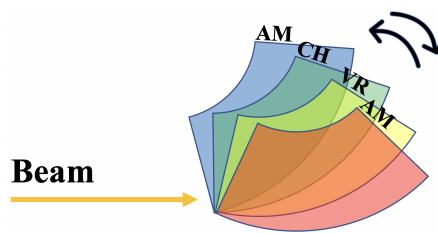


Figure 7.8 – Angular scan illustration.

A comparison of angular scan was made between measured data and the simulation from the two crystal routines. The chosen angular scan has the same machine configurations as the one described in Section 7.2.2, thus at 6.5 TeV in the B1H plane.

The angular scan simulation follows the same method and statistics as for loss maps. However, instead of simulating only the case when the crystal is in optimal orientation, other orienta-

tions are also simulated and other loss maps created. The crystal orientation stretches from one amorphous orientation to the other. Crystal orientation points are chosen strategically to cover all plateaus and dips with an approximate granularity of around $5 \mu\text{rad}$. The energy absorbed in the crystal at every orientation is then normalized to the energy absorbed in the amorphous crystal. This is done both for SixTrack and the SixTrack-FLUKA Coupling. The simulation results, where the normalized BLM signal and energy are plotted against the crystal orientation, are compared to the measured data in Fig. 7.9. The measurement is taken from a machine development session described in [33]. The BLM signals were recorded every second while the crystal was continuously rotating at a speed of $1 \mu\text{rad}$ per second. For the measured data the average value of the BLM signal at the crystal in amorphous orientation is used as normalization factor.

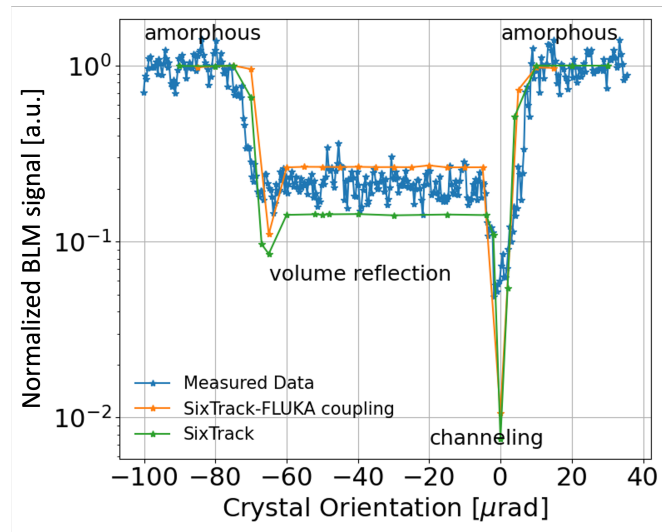


Figure 7.9 – Measured BLM data at the B1H crystal (old) (Table 4.5) from 2018 (blue) [27, 33], SixTrack-FLUKA coupling simulation (orange), and SixTrack simulation (green) of the local losses at the TCPCH.A4L7.B1 crystal during an angular scan in B1H with 6.5 TeV protons.

A qualitatively good agreement among the three sets of data is seen, especially concerning the sharp minimum, which corresponds to the situation where the crystal is in channeling orientation, where the inelastic interactions inside the crystal are reduced to a minimum. The difference in channeling well depth with respect to the measured data can in part be explained by imperfections that are not considered in simulation. Another possibility is that the initial beam angular spread linked to the previously measured impact parameters is not suitable for the particular beam excitation method used in this test.

In the volume reflection section, approximately from $-70 \mu\text{rad}$ to $-10 \mu\text{rad}$ there seems to be a small underestimation of the measurement by SixTrack and a small overestimation by the SixTrack-FLUKA coupling. A similar level of discrepancy was observed in a previous study [25].

7.2.4 Linear Scan

Lastly, a linear scan benchmark is performed. In a linear scan, the crystal is kept in channeling orientation, while the absorber is slowly moved toward the beam starting from an open position (Fig. 7.10) to gradually intercept the channeled halo and reconstruct its profile. The signal acquired by the absorber's BLM at different positions is equivalent to the integral of the beam distribution from ∞ (open position) to the position the absorber is at in that instant. Since the channeled halo has approximately a Gaussian distribution, the BLM signal from the absorber as function of position is approximately an error function. The signal would have described the Gaussian channeled halo after it has passed the inflection point (correspondent to the peak of the Gaussian distribution) in the error function and it is starting to plateau. After the absorber has moved beyond the point where it intercepts the entire channeled halo, however, the BLM signal at the absorber does not remain constant. It continues to rise slowly as the absorber approaches the beam until a spike of high losses occurs at the beam core boundary. This slow rise is caused by particles that are dechanneled at smaller angular kicks or see the crystal as an amorphous material. An illustration of a typical BLM signal and the corresponding beam distribution is shown in Fig 7.10. The same type of ADT beam excitation is also used here.

A linear scan is used to estimate experimentally the multi-turn channeling efficiency and the bending angle of the crystal. The multi-turn channeling efficiency is defined as N_{CH}/N_{tot} , where N_{CH} is the number of particles channeled over all the turns the particles remain circulating and N_{tot} is the total number of the particles impacting on the crystal at the first turn. We can find N_{CH} by looking at the absorber's BLM signal during the linear scan. Since the start of the plateau position of the absorber error function denotes the position where the absorber is capturing all the channeled particles, the BLM signal at that position is proportional to N_{CH} . To find N_{tot} it is sufficient to take the absorber BLM signal when the absorber is at the same σ position as the crystal, since it allows to intercept all particles (except for a small amount of VR particles in the CH regime, which are kicked towards the beam core) from the crystal without intercepting the particles of the beam core. Hence, the ratio between the plateau level of the error function and the level before the absorber attains the beam core represents the multi-turn channeling efficiency, while the inflection point of the error function gives the bending angle.

In the considered example for the comparison, the data taken come from a 2022 machine development session, using TCPCV.A6R7.B2 (new) with 6.8 TeV protons, at the *flat-top* stage. The optics can be found in [136] and the collimator settings are given in Table 7.5. TCSG.D4L7.B1 was used as absorber. The TCPCV.A6R7.B2 was aligned to optimal channeling at 5σ and the absorber started the scan at around 5.5 mm. The absorber moved $50\mu\text{m}$ every 3 s, while the BLM recorded the reading every second. The BLM data are grouped into sets to three data points to have one BLM signal every 3 s to comply to the absorber speed. From each set of three data points, the average and standard deviation are taken. The experimental data are then normalized to the beam loss rate and to the level of the BLM signal just before

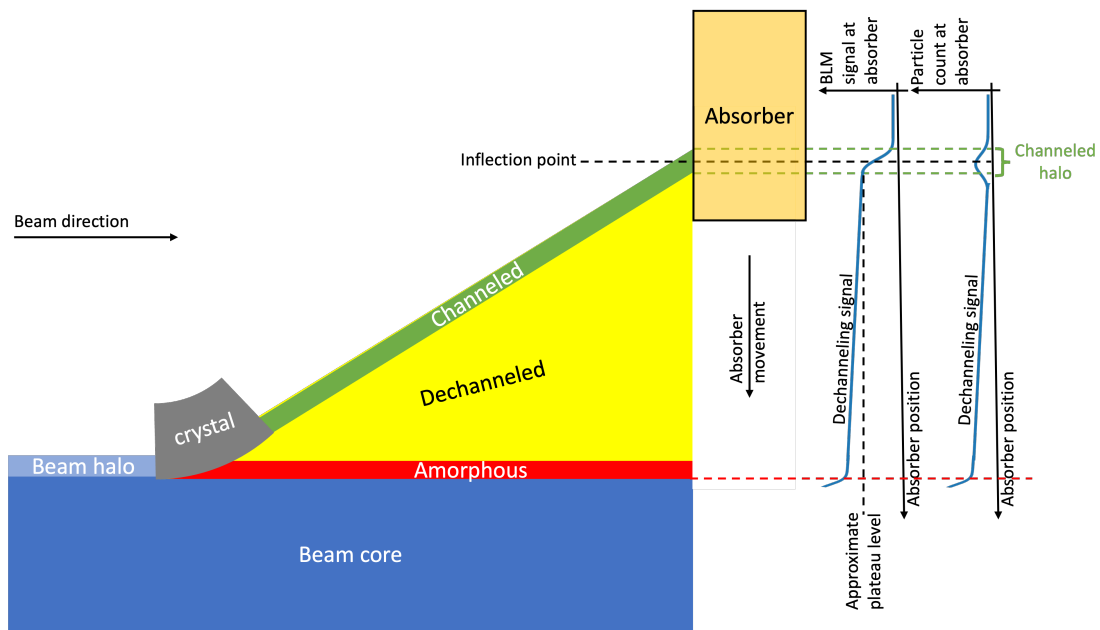


Figure 7.10 – Linear scan illustration: Beam travels from left to right. The beam halo (light blue) hits the crystal (grey) and the particles exiting the crystal can have channeled (green), dechanneled (yellow), or interacted with the amorphous material (red). They can then hit the absorber depending on the position of the absorber. In a linear scan the absorber moved downwards until it reaches the beam core. The BLM signal (right blue curve) recorded as a function of its transverse position and the corresponding beam distribution (left blue curve) are illustrated schematically.

the absorber intercepts the core (occurring with the absorber at the same σ aperture as the crystal), as it gives the intensity of the entire beam halo that impacted the crystal.

To simulate this case, a single simulation was done with each code, using a pencil beam with 3×10^5 protons and $1 \mu\text{m}$ impact parameter on the crystal as starting distribution. The absorber was closed to the same σ aperture of the crystal (5.2σ), and the distribution of the particles on the absorber was recorded. The particle distribution on the vertical axis is then integrated from the open position of the collimator ($+\infty$) to all intermediate points and normalized to the total number of protons impacting the crystal. The results are shown in Fig. 7.11.

The simulated results show a reasonable reproduction of the BLM signal, considering that the sustained loss rate of the beam over time is noisy and that we are simulating a perfect machine. The SixTrack-FLUKA Coupling gives a multi-turn efficiency of approx. 87%, which is a closer reproduction of the measured one at around $70 \% \pm 15 \%$, whereas for SixTrack's simulation this is almost 10% higher. The overestimation of the two simulations with respect to the experimental data may be correlated with the deeper channeling well found in Fig 7.9. In general, this level of agreement is acceptable considering the large uncertainty over the measured signal.

Collimator	IR	Proton Heavy ion	
		Half gap [σ]	
TCP.D6R7.B2		out	10
TCP.C6R7.B		out	10
TCP.B6R7.B2		out	10
TCSG.A6R7.B2		out	10
TCPCV.A6R7.B2		5.2	5
TCSG.B5R7.B2	7	out	10
TCSG.A5R7.B2		out	10
TCPCH.A5R7.B2		5.2	5
TCSG.D4R7.B2		out - 5	
other TCSGs		6.5	
TCLAs		10	
TCPs/TCSGs/TCLAs	3	15.0/18.0/20.0	
TCTs	1/2/5/8	18.0/37.0/18.0/18.0	
TCSPs/TCDQ	6	7.3	
TCL	1/5	± 25 mm	

Table 7.5 – Collimator settings for 2022 B2V the 6.8 TeV proton and the 6.8 Z TeV heavy-ion linear scan benchmark at ($\beta^* = 1$ m) [137].

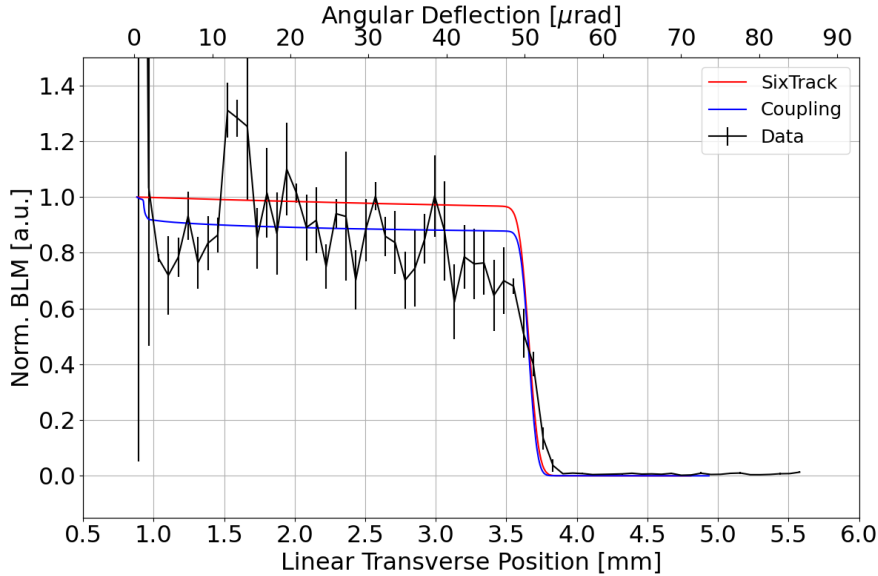


Figure 7.11 – Measured (black) and simulated (SixTrack – red, SixTrack-FLUKA Coupling – blue) 2022 B2V crystal linear scan for 6.8 TeV proton.

7.3 Heavy-ion benchmark

Having performed the benchmark on protons, we now pass on to Pb ions, which are most relevant to the operational applications of the simulations. The types of tests used here are of

the same type as for protons. For relevant parts there is also a comparison to protons.

7.3.1 Single pass

As for protons, a single-pass study has been performed for Pb ions with 6×10^6 primary ions and the same initial distribution. The aim of an ion single-pass study is mainly exploratory and comparative. Unfortunately, as for protons there is no experimental data at this energy and precision. However, some of the key benchmark results at low energy can be found in [122, 24, 123, 25, 46, 127, 110, 126, 132]. Since there is more experience around proton operations with crystals, a comparison with the proton single-pass study may help in understanding more complex studies, such as multi-turn collimation studies. Results from SixTrack cannot be used for comparison, since the built-in crystal treatment in SixTrack only supports protons.

For the single pass simulation, a flat distribution of 6×10^6 6.37 Z TeV Pb ions have been used. The initial distribution goes from -1 mm to 1 mm in x covering the entire surface of the crystal, and from -10 to 80 μrad in x' to cover the whole range from one amorphous section to the other. The crystal used is the same as for protons, TCPCH.A4L7.B1 (old) in Table 4.5.

The results are shown in Fig. 7.12. The same analysis method has been applied to ions with the difference of weighting the heatmap by energy and of an additional amorphous region above the volume reflection region.

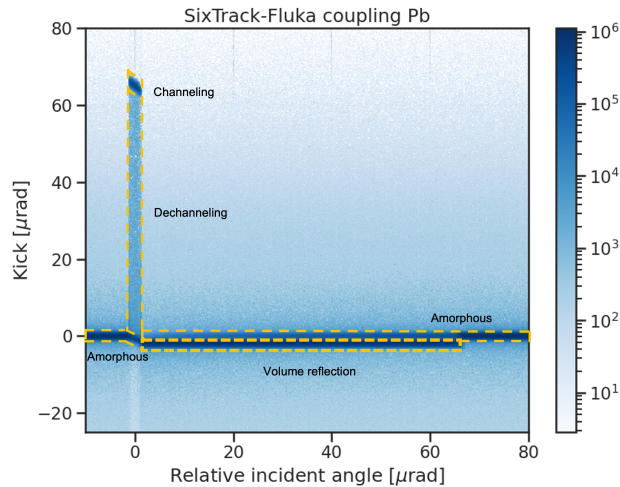


Figure 7.12 – Simulated 6.37 Z TeV Pb angular kick distribution as a function of relative angle between incoming particles and crystal orientation with SixTrack-FLUKA Coupling after a single pass through the crystal.

The summary crystal interaction plot is given in Fig. 7.13. Qualitatively, the results agree with the ones for protons, with clearly defined regions for each of the coherent crystal processes, although there are a few important differences. The main differences compared to protons are the increased amount of amorphous particles, an expected decreased amount of channeled

particles and a slight increase in absorbed particles. There is also an apparent constant background. This is composed of mostly light ion fragments. To the decrease in the number of VR particles there is a corresponding increase in the amount of AM particles. This increase of AM particles occurs in the VR region as we can see the additional AM band in Fig. 7.12, compared to Fig. 7.2b for protons. Qualitatively, this agrees from what is expected, caused by the much higher cross section of nuclear fragmentation of ions in matter compared to inelastic interactions of protons. In the FLUKA crystal routine, channeling stops at the moment of fragmentation and the created fragments are not channeled.

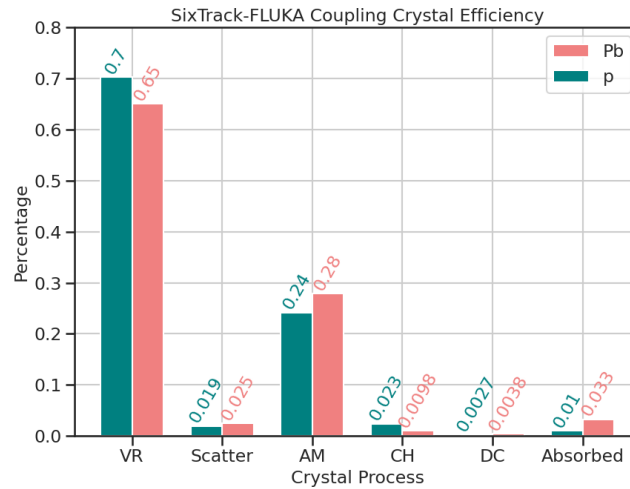


Figure 7.13 – Crystal process efficiency summary for the SixTrack-Coupling with protons and Pb ions.

7.3.2 Loss pattern

Similarly to protons, a comparison to measured loss maps from machine development in 2018 with crystals as primary collimators has been carried out. Here an example is shown for B1H Pb ions at 6.37 Z TeV. The measurement [35] was performed at the *flat-top* stage during the LHC operational cycle. The collimation settings followed the standard *flat-top* settings used in the 2018 Pb-Pb run [22], but the crystals were inserted as the bottleneck in IR7 at 5σ and the collimators upstream of the crystal fully open (details in Table 7.6). More information about the measurement done on the 27th of November 2018, the optical setup and collimation system settings can be found in [27, 35]. The optical and collimation settings reflect the ones used during the data taking. In the SixTrack-FLUKA coupling, an initial pencil beam distribution of 6×10^6 $^{208}\text{Pb}^{82+}$ ions was simulated and an impact parameter of $1\ \mu\text{m}$ was used.

The measured (normalized to the beam flux) and simulated (normalized to the total energy lost) loss maps for B1H are shown in Figs. 7.14–7.15.

Collimator	IR	Half gap [σ]
TCP.D6L7		123.0
TCP.C6L7		91.0
TCP.B6L7		107.0
TCSG.A6L7		104.0
TCPCV.A6L7		5.0
TCSG.B5L7	7	87.0
TCSG.A5L7		85.4
TCSG.D4L7		6.5
TCPCH.A4L7		5.0
other TCSGs		6.5
TCLAs		10
TCPs/TCSGs/TCLAs	3	15.0/18.0/20.0
TCTs	1/2/5/8	15.0/15.0/15.0/15.0
TCSPs/TCDQ	6	7.4
TCL	1/5	out

Table 7.6 – Collimator settings for 2018 B1H Pb ion crystal benchmark at 6.37 Z TeV ($\beta^* = 1$ m) [23].

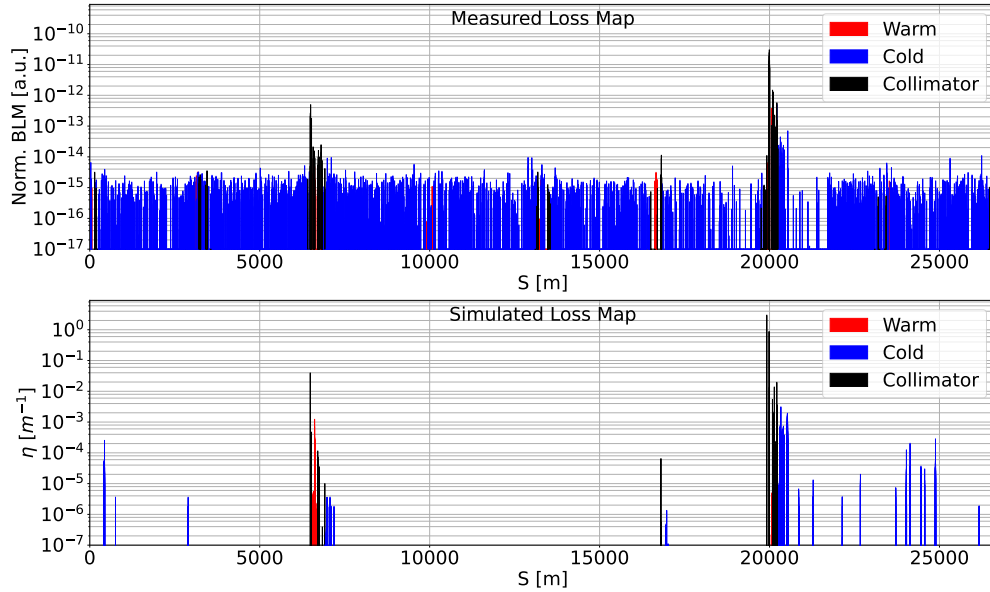


Figure 7.14 – Measured (top) and simulated (bottom) loss map for B1H 2018 Pb run at 6.37 Z TeV. Measured loss map normalized to total BLM signal can be found in Fig. A.3.

When excluding the background noise in the measurement, the simulated loss pattern reflects well what is seen from the measured BLM signals including the losses in insertion region 3 (around $s = 7000$ m). The zoom of IR7 in Fig. 7.15 shows that the highest three clusters in the superconducting region around $s = 20300$ m, $s = 20400$ m and $s = 20530$ m in the measured data plot are reproduced up to the same order of magnitude in simulation. It is important

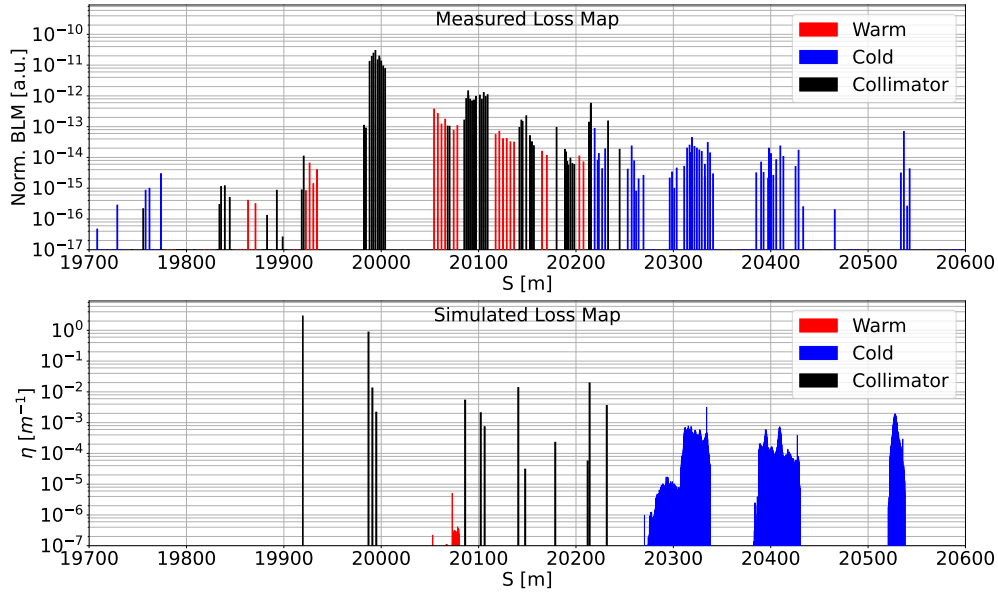


Figure 7.15 – Measured (top) and simulated (bottom) loss map around IR7 for 2018 Pb run at 6.37 Z TeV. Measured loss map normalized to total BLM signal can be found in Fig. A.4.

to recall that these simulations are not fully comparable to the measured data, as they lack the full shower propagation. As in the case of protons, the BLMs on warm elements in the straight section of IR7 intercept showers from upstream elements and it is therefore expected that the warm losses appear more dense in the measurement (top part of Fig. 7.15) than in the simulation (bottom part), where only the impacts of single ions are recorded without their shower development. Furthermore, as for protons, it is expected that the simulated cleaning inefficiency at the location of the crystal appears much higher in the simulation than in the measurement, due to the short 4 mm length to which the losses are normalized.

There are a few individual loss spikes in the simulation that do not appear in the measured loss map, such as the one around $s = 400$ m. Some of them are below the background level. The ones above noise level may be due to orbit and optics imperfection, or the aperture model in SixTrack which includes tolerances that make it slightly tighter. Finally, some transitions in the aperture models are artificially sharp, and this could concentrate losses on certain locations. Concerning the losses on the collimators, for heavy ions there is a small underestimation for the collimators around $s = 20100$ m as seen for protons. However, the same caveats apply as for protons on the short crystal length and that the simulation comparison does not include the shower development, which is particularly important while comparing the BLMs signal at warm magnets and collimators in IR7 with the simulated data. Such a comparison is discussed in [138, 134]. In [134], the particle impacts on the collimators shown in this section have been used to produce detailed beam shower. One of the key figures in the paper where simulated shower propagation in IR7 compared to the measured one is shown in Fig 7.16.

To enhance the robustness of the benchmark and to include the other planes, the loss map

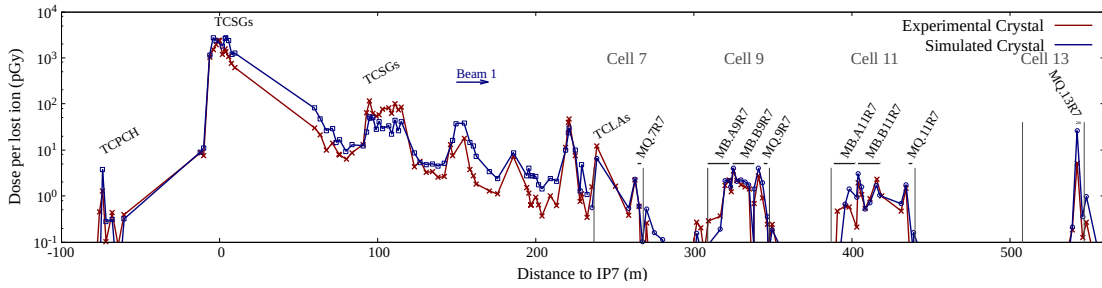


Figure 7.16 – Figure from [134] showing simulated and experimental BLM signals for crystal-based 6.37 Z TeV Pb collimation in IR7 and the downstream DS region for B1H 2018 machine development test. The beam direction is from left to right. The BLM signals are given per ion lost in the collimation system. The acronyms MB, MQ represent the dipoles, and quadrupoles respectively.

benchmark has also been done for the 2022 ion tests [139]. The loss maps were recorded on the 19th of November 2022 during the 2022 ion tests [139] at the *flat-top* stage and the record energy of 6.8 Z TeV. The crystals used for horizontal plane were the old ones, while for the vertical plane there were the new crystals, as reported in Table 4.5. The optics [136] and the initial number of primary particles used are the same as for the previous loss map benchmark. The proton collimator settings [137] were used with the addition of the crystals. The detailed settings can be found in Table 7.7. The comparison loss maps are in Figs 7.17 - 7.20 both in full ring view and zoomed IR7 view. The level of reproduction by simulation is generally satisfactory.

Collimator	IR	Crystal	Standard
		Half gap [σ]	
TCPs/TCSs/TCLAs	7	5.0/6.5/10.0	
TCPCs	7	4.75 (CH/AM)	out
TCPs/TCSGs/TCLAs	3	15.0/18.0/20.0	
TCTs	1/2/5/8	18.0/37.0/18.0/18.0	
TCSPs/TCDQ	6	7.3	
TCL	1/5	± 25 mm	

Table 7.7 – Collimator settings for the 2022 6.8 Z TeV heavy-ion loss map benchmarks for both beams at ($\beta^* = 1$ m) [137]. Configurations include the standard system, crystal collimation in channeling, and crystal collimation in amorphous.

7.3.3 Collimation improvement using crystals

From past experimental results [27], an improvement of the ion cleaning performance is found while using crystal-based collimation with respect to the standard system. In order to design future configurations, it is important to be able to confidently predict the relative improvement

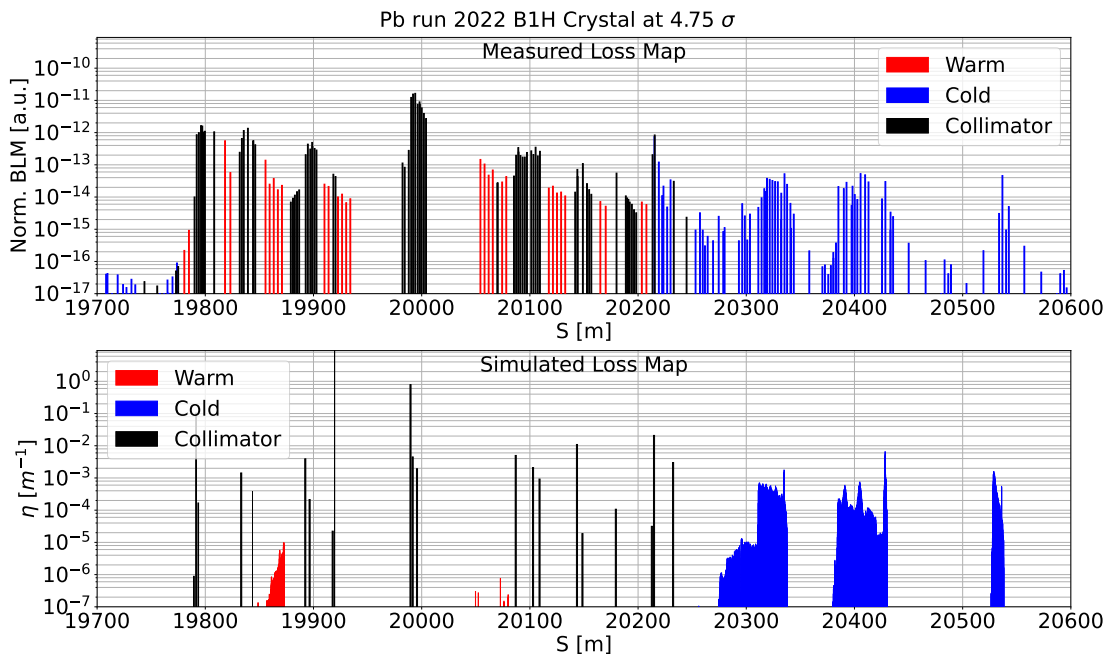
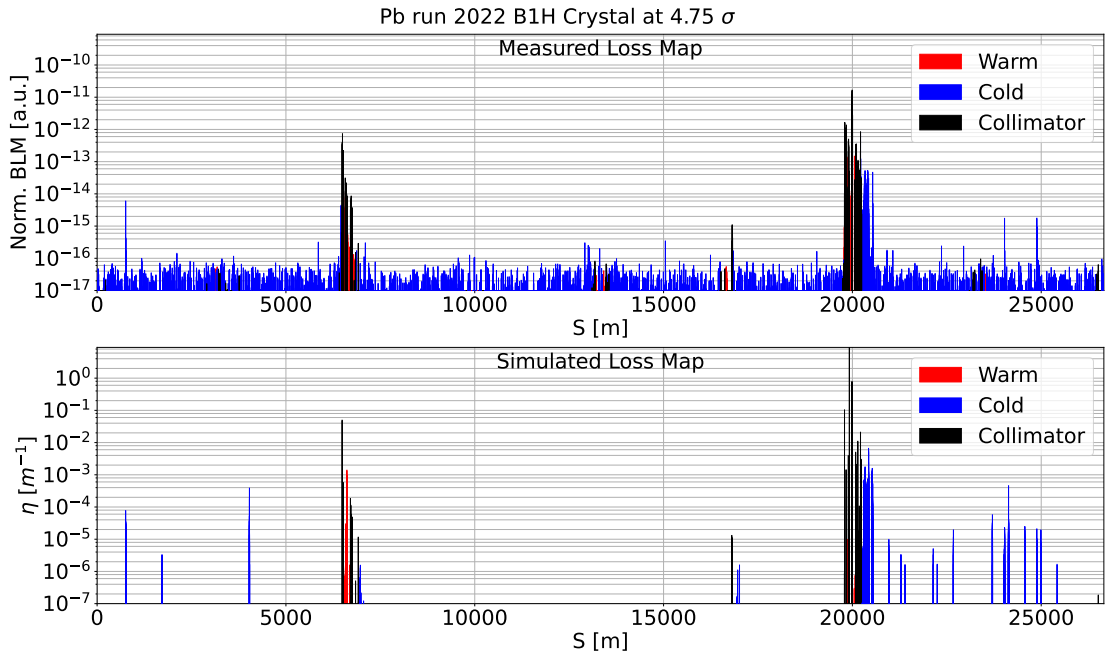


Figure 7.17 – (a): Measured (top) and simulated (bottom) loss map for B1H 2022 Pb test crystal collimation in channeling at $6.8 Z$ TeV *physics*. (b): zoom in IR7. Measured loss map normalized to total BLM signal can be found in Fig. A.5.

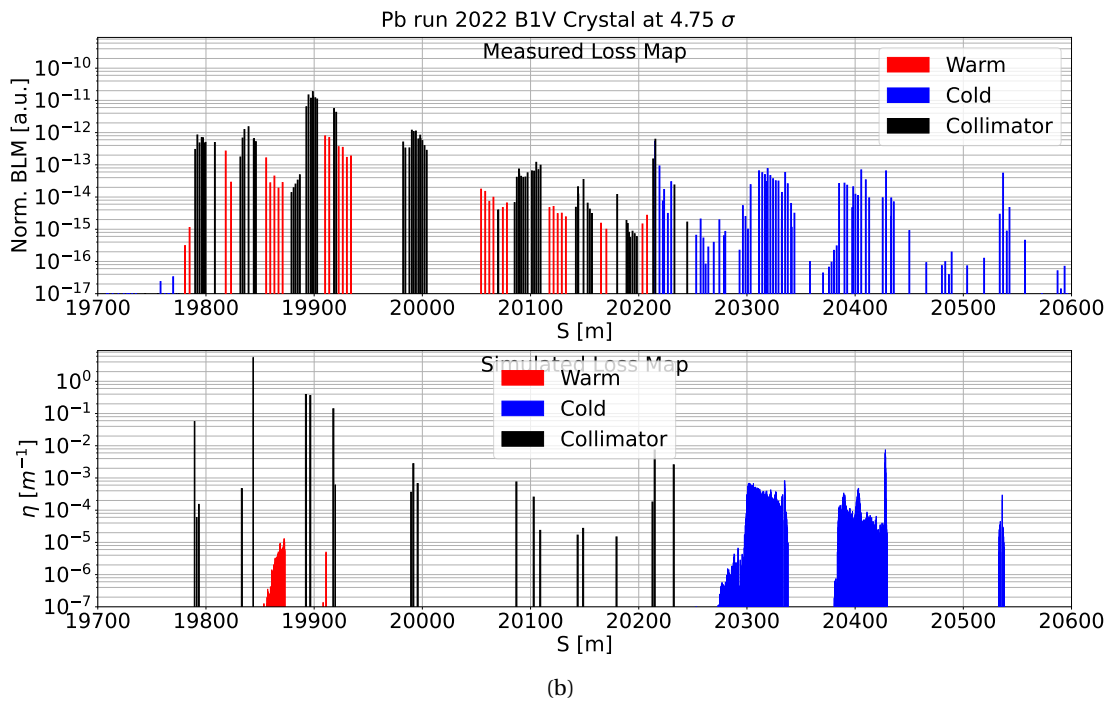
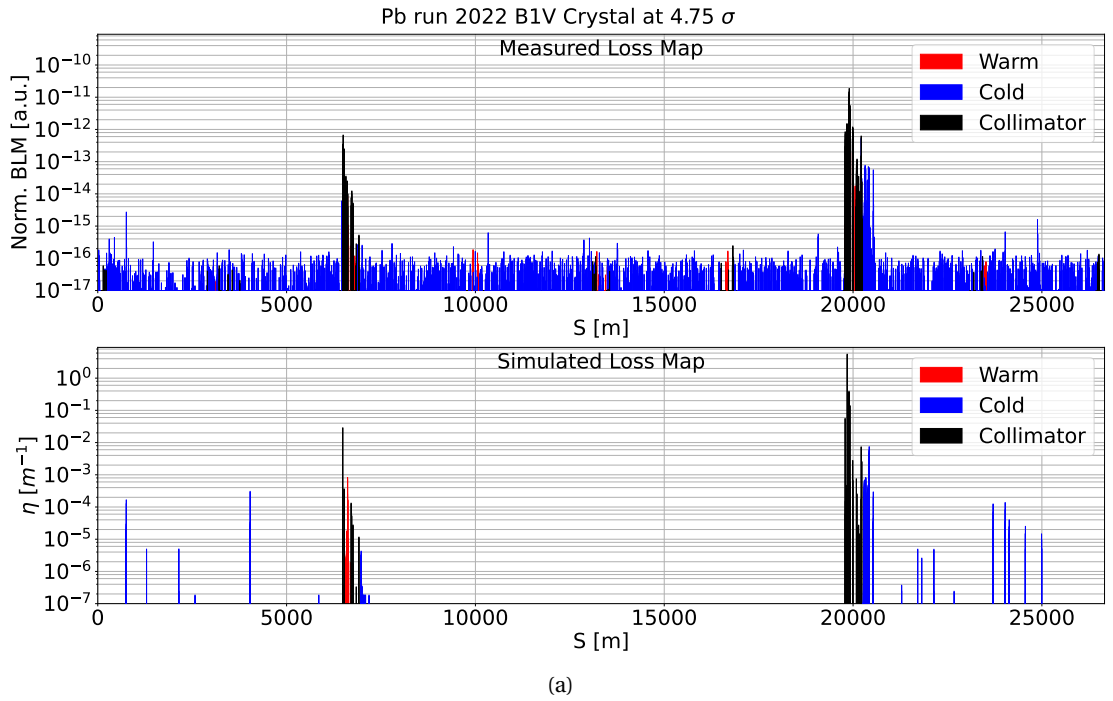


Figure 7.18 – (a): Measured (top) and simulated (bottom) loss map for B1V 2022 Pb test crystal collimation in channeling at $6.8 Z$ TeV *physics*. (b): zoom in IR7. Measured loss map normalized to total BLM signal can be found in Fig. A.6.

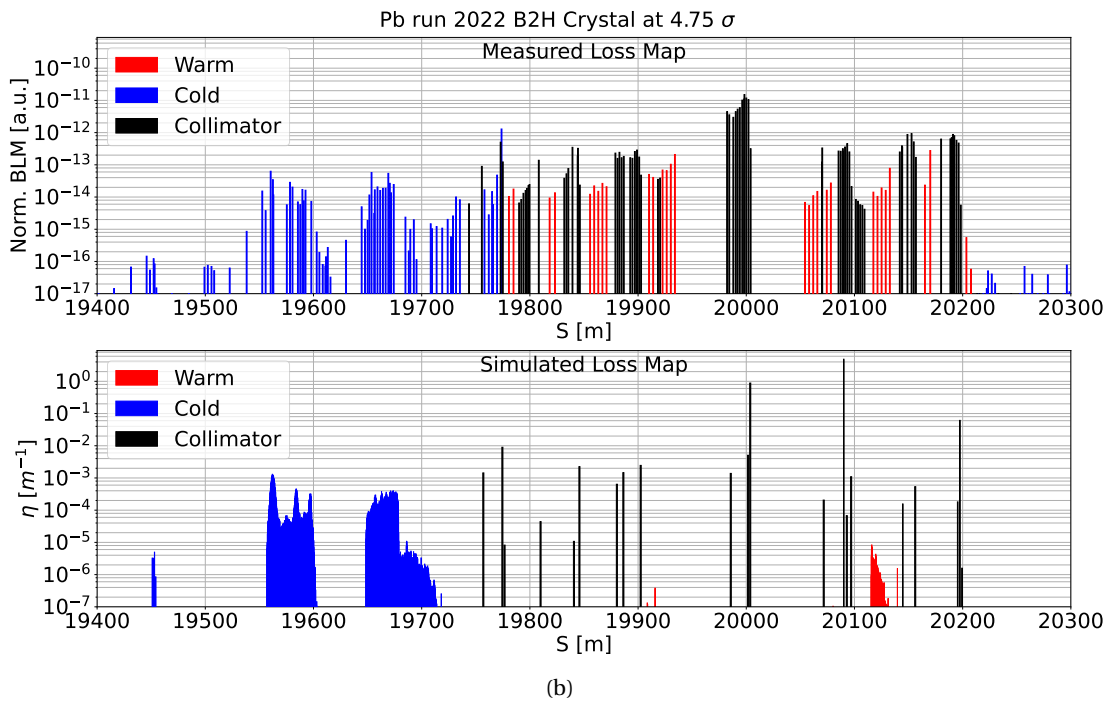
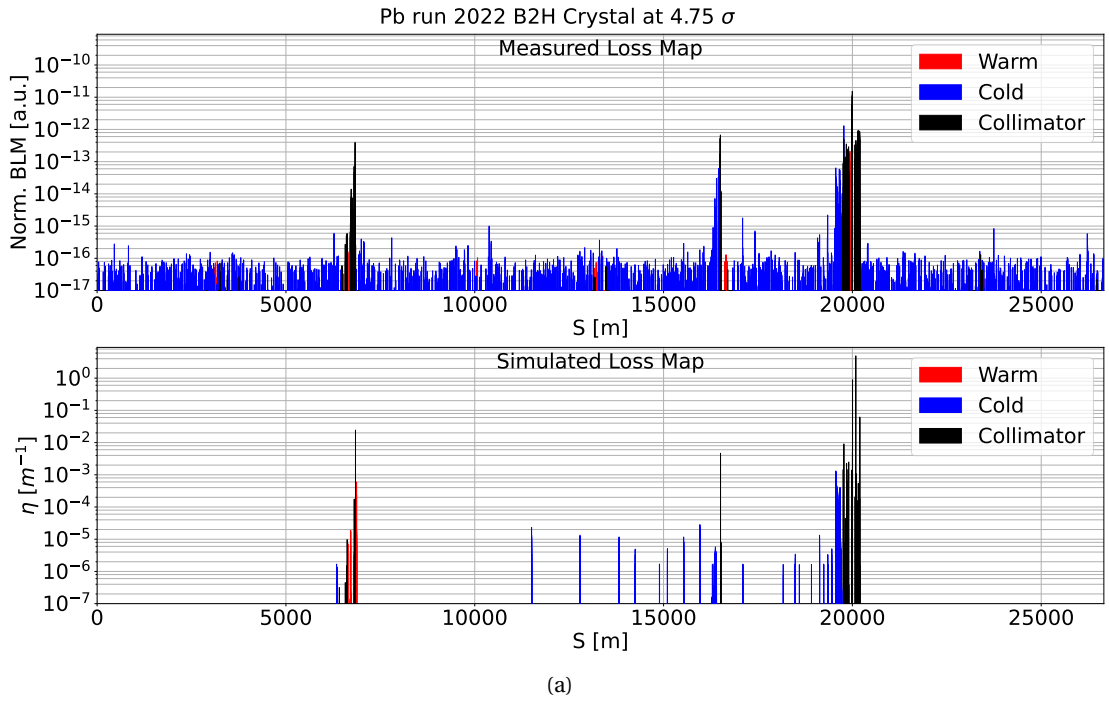


Figure 7.19 – (a): Measured (top) and simulated (bottom) loss map for B2H 2022 Pb test crystal collimation in channeling at $6.8 Z \text{ TeV physics}$. (b): zoom in IR7. Measured loss map normalized to total BLM signal can be found in Fig. A.7.

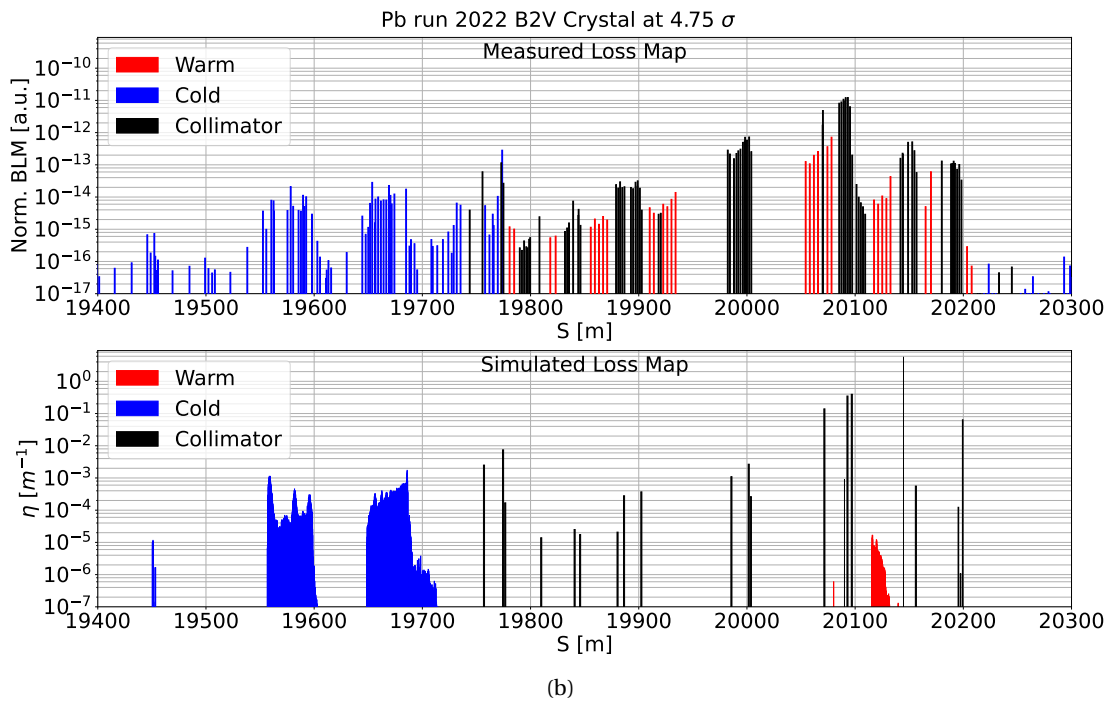
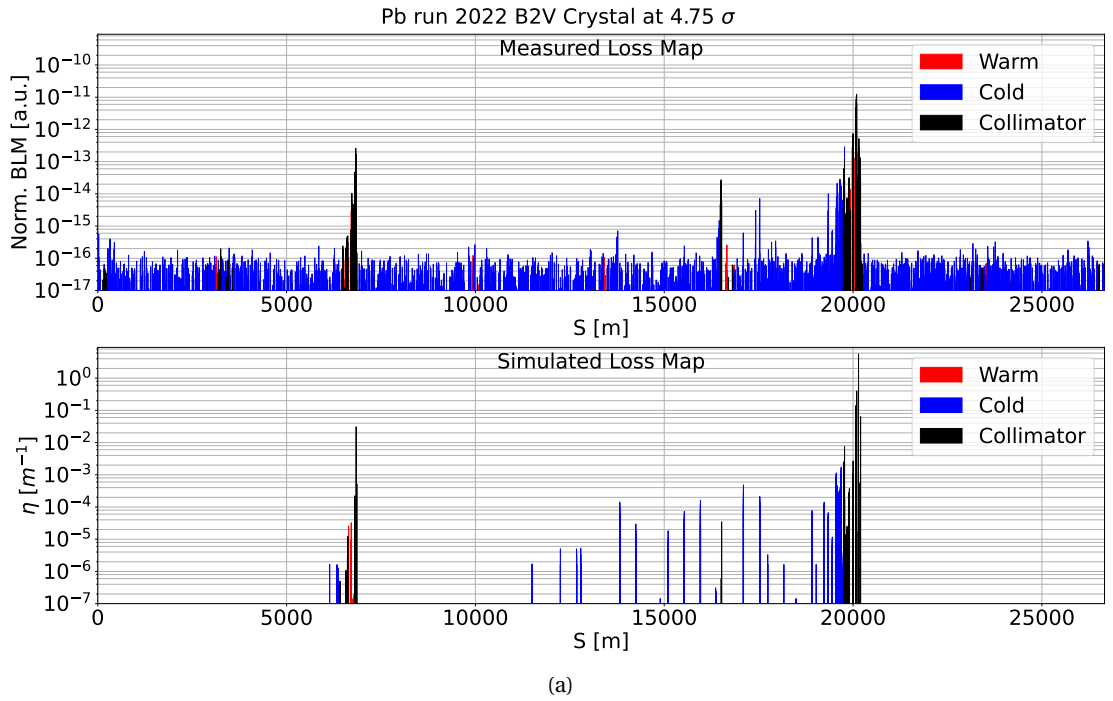


Figure 7.20 – (a): Measured (top) and simulated (bottom) loss map for B2V 2022 Pb test crystal collimation in channeling at $6.8 Z$ TeV *physics*. (b): zoom in IR7. Measured loss map normalized to total BLM signal can be found in Fig. A.8.

with respect to past configurations. In this case the most recent past configuration is the standard collimation. Hence, this section is dedicated to the benchmark against the relative improvement found in machine development measurements. Other than comparing the crystal collimation in channeling with respect to the standard configuration, the crystal in amorphous scenario is also compared, as it represents the other extreme scenario in a crystal-based setup.

In all previous loss maps, distinct clusters of losses can be seen in the DS corresponding to the different cells where the quadrupoles are focusing in the horizontal plane, and the single-pass dispersion hence reaches a maximum. Using the losses in these clusters allows for a more compact representation of the results and an easier comparison of different cases [19], in terms of computed average and maximum values of the inefficiencies in each cluster. The precise regions are highlighted for Beam 1 in Fig. 7.21 (similar divisions are used for B2H). The naming of the clusters follow the LHC quadrupole magnet names. These are, following the beam direction, Q7 (blue), Q8-9 (orange), Q10-11 (green), and Q12-13 (red).

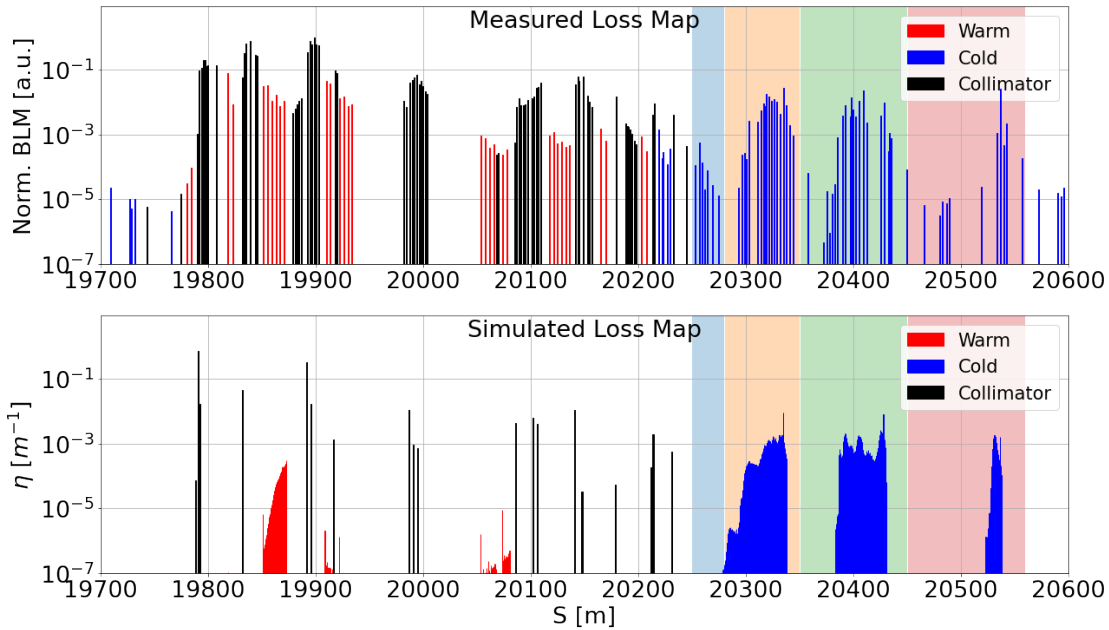


Figure 7.21 – Illustration of cold loss clustering for the B1H 2018 standard *physics* collimation setup [22, 35, 36] with Pb ions at 6.37 Z TeV for measured data (top) and simulation (bottom): Q7 (blue), Q8-9 (orange), Q10-11 (green), and Q12-13 (red). The beam travels from left to right.

During Run 2, crystals in the vertical planes were of quasi-mosaic kind, which means they were using the 111 plane as channeling plane. However, presently it is not possible to simulate 111 crystals in FLUKA, thus those tests could not be benchmarked. The horizontal planes have been benchmarked and the results are presented in this section. The vertical plane crystals have been upgraded with 110 crystals during the Long Shutdown period after Run 2. Machine development tests have been performed in 2022 [139] after the installation. The results allow to benchmark for all planes and show the ion data that have not been presented previously.

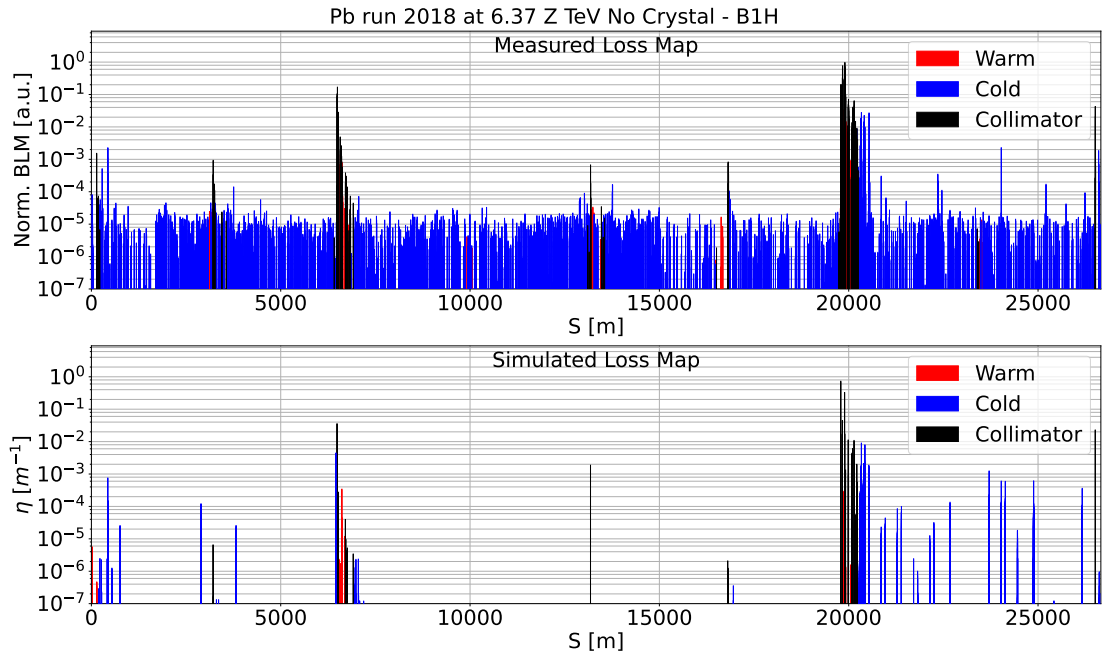
Collimator	Beam	IR	$^{208}\text{Pb}^{82+}$ 2018 Flat Top	$^{208}\text{Pb}^{82+}$ 2018 Physics
			($\beta^* = 100$ cm) Half-gap [σ]	($\beta^* = 50$ cm) Half-gap [σ]
H TCP	B1	7	5	5.5(L)-5.0(R)
V TCP	B1	7	5	5
H/V TCPs	B2	7	5	5
TCSGs/TCLAs	B1/2	7	6.5/10	6.5/10
TCP/TCSGs/TCLAs	B1/2	3	15/18/20	15/18/20
H TCTs	B1	1/2/5	15/15/15	11/9/9
H TCTs	B2	1/2/5	15/15/15	9/9/9
V TCTs	B1/2	1/2/5	15/15/15	9/9/9
TCTs	B1/2	8	15	15
TCDQ / TCSP	B1	6	7.4/7.4	7.4/7.4
TCDQ / TCSP	B2	6	7.4/7.4	7.4/7.4(L)-11.2 (R)
TCL.4/5/6	B1/2	1/5	out/out/out	15/15/out

Table 7.8 – 2018 $^{208}\text{Pb}^{82+}$ ion runs collimator settings for $\epsilon_N^P=3.5$ μm from [22]. L and R indicates the left and right jaw, respectively. H and V correspond to horizontal and vertical planes, respectively.

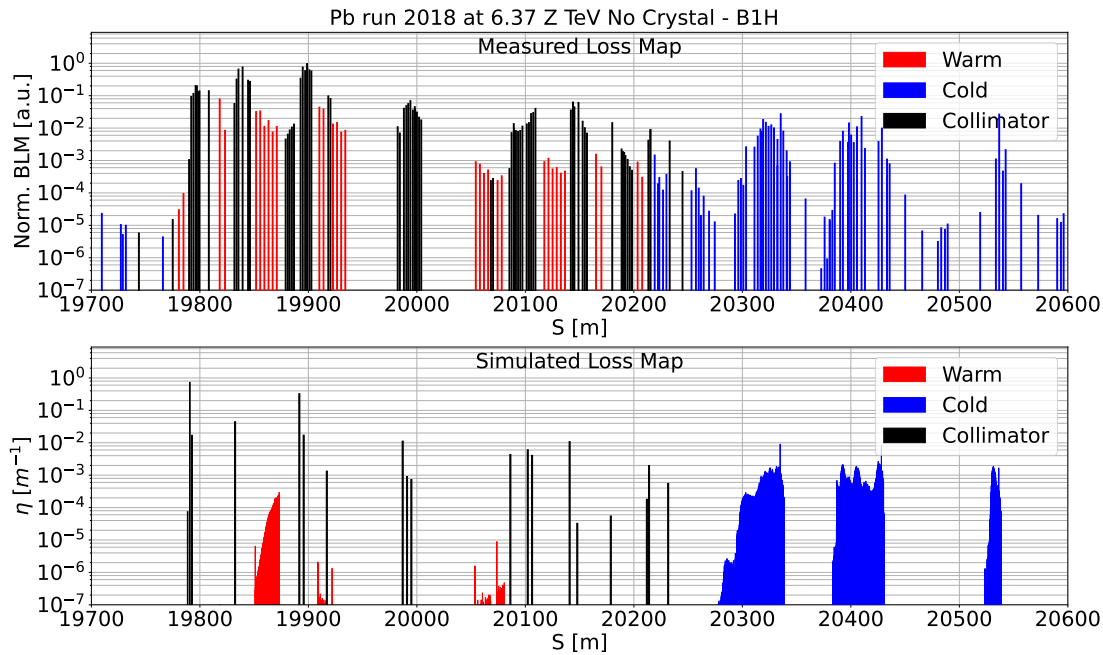
For the 2018 benchmark, three loss maps per plane have been simulated (crystal in channeling, amorphous crystal, standard collimation system). The planes considered are B1H and B2H. The associated crystals are TCPCH.A4L7.B1 (old) and TCPCH.A5R7.B2 (old) from Table 4.5. The scenario considered is the *physics* 2018 setup for the two horizontal beams. This was chosen because the data collected on the 27TH of November 2018 for these scenarios [35, 36] could serve as additional benchmark. For this comparison 6×10^6 $^{208}\text{Pb}^{82+}$ primary ions at 6.37 Z TeV were simulated on the side of the crystal. The collimation settings can be found in Table 7.8. The crystal was placed adiabatically at 4.75σ to be the primary collimator.

The loss maps of the measured and simulated cases are presented in Figs 7.22 - 7.27. All measured loss maps are here normalised to flux to make them comparable, as the signals normalised by flux are generally 10 orders of magnitude smaller. As the aim of this benchmark is to compare the relative improvement factor, as predicted from simulations, with the one found in measurements, a relative plot is created. The results of the simulations are first plotted in terms of average and maximum inefficiencies in the DS clusters. Then, the simulated and measured crystal cases are normalized to their respective standard collimation results. The end results are shown in Fig. 7.28 for B1H and in Fig. 7.29 for B2H.

Generally, the crystal-based system in channeling orientation performs significantly better than the standard system in measurements in all clusters except Q7. It should be noted though that this cluster is very susceptible to particle showers, as it is the closest to the TCLAs, and the signals in the Q7 cluster are also usually very small in absolute for simulations (plot (b) of Figs 7.22 - 7.27) and not a performance bottleneck. It has also been confirmed with FLUKA studies by others [134], using input from this thesis, that the signal on the Q7 BLM



(a)



(b)

Figure 7.22 – Measured (top) and simulated (bottom) loss map comparison for 2018 B1H standard collimation at 6.37 Z TeV *physics*. (a): full ring; (b): zoom in IR7.

is indeed dominated by showers from upstream collimators and not caused by local power deposition in the magnet. The worsening in cleaning performance with crystals at this location

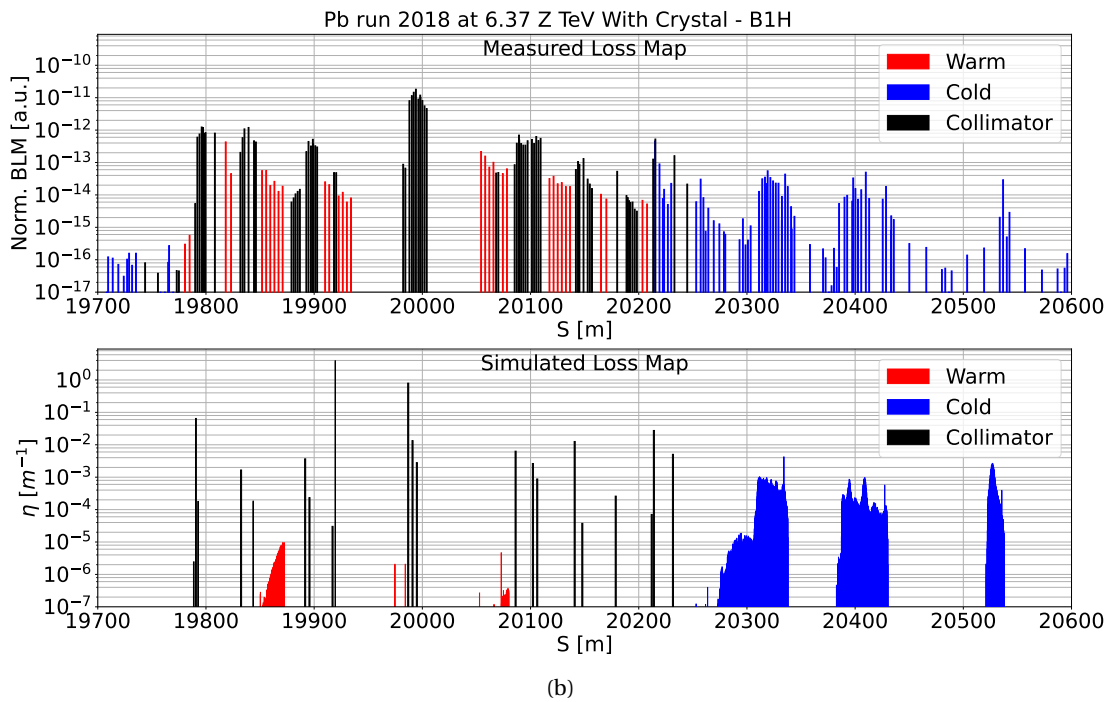
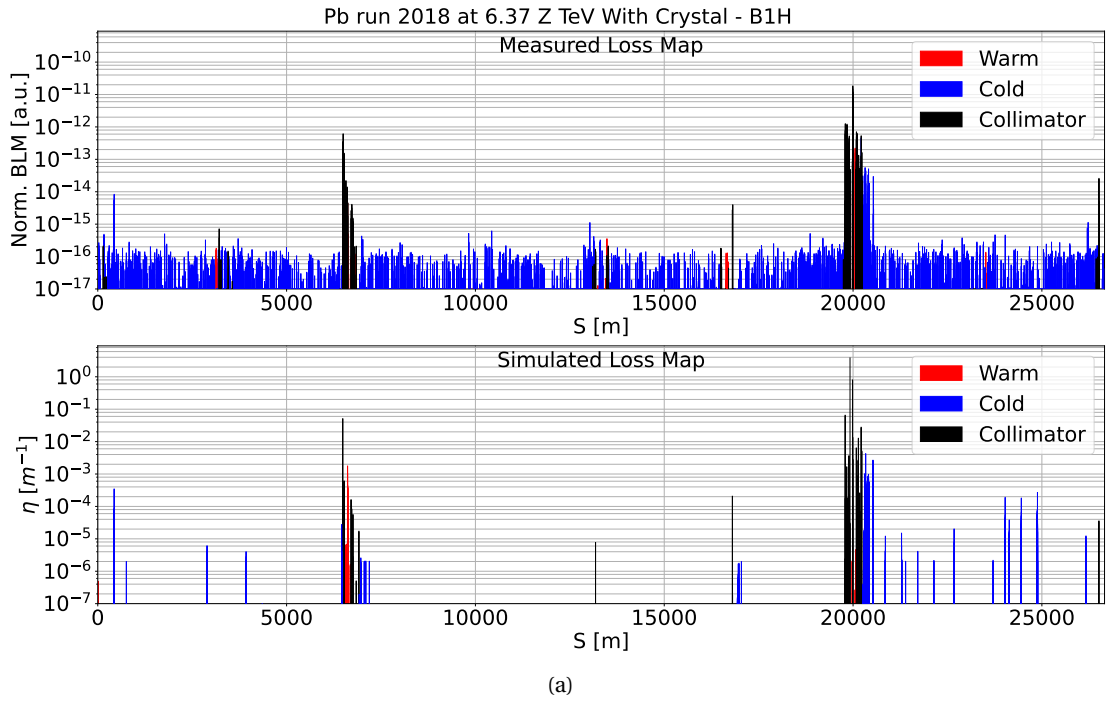
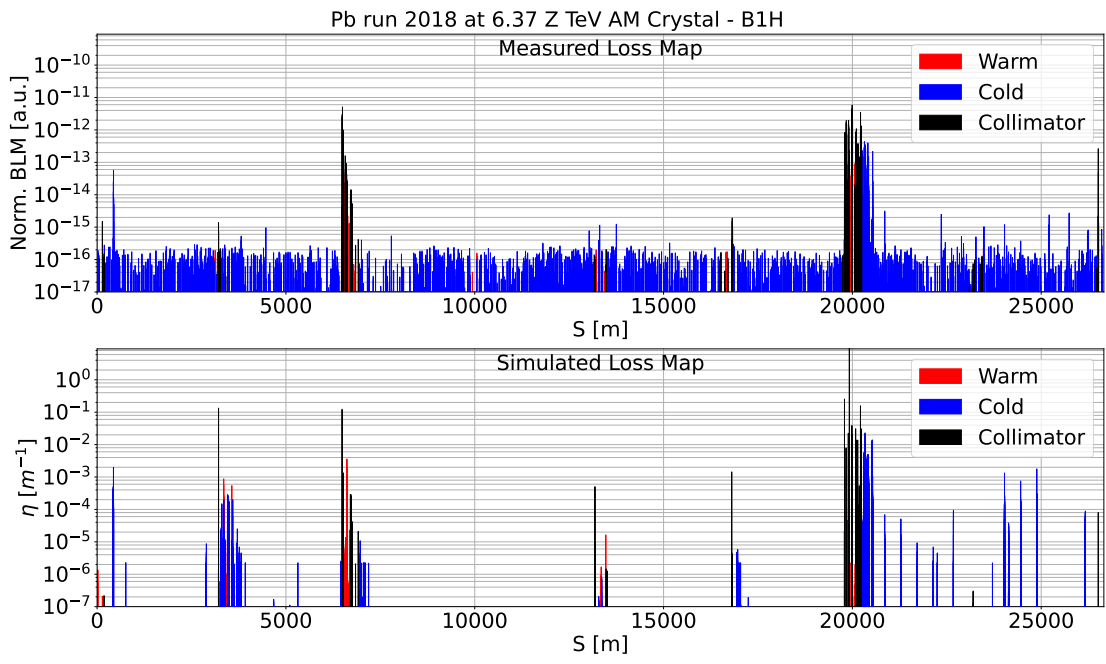
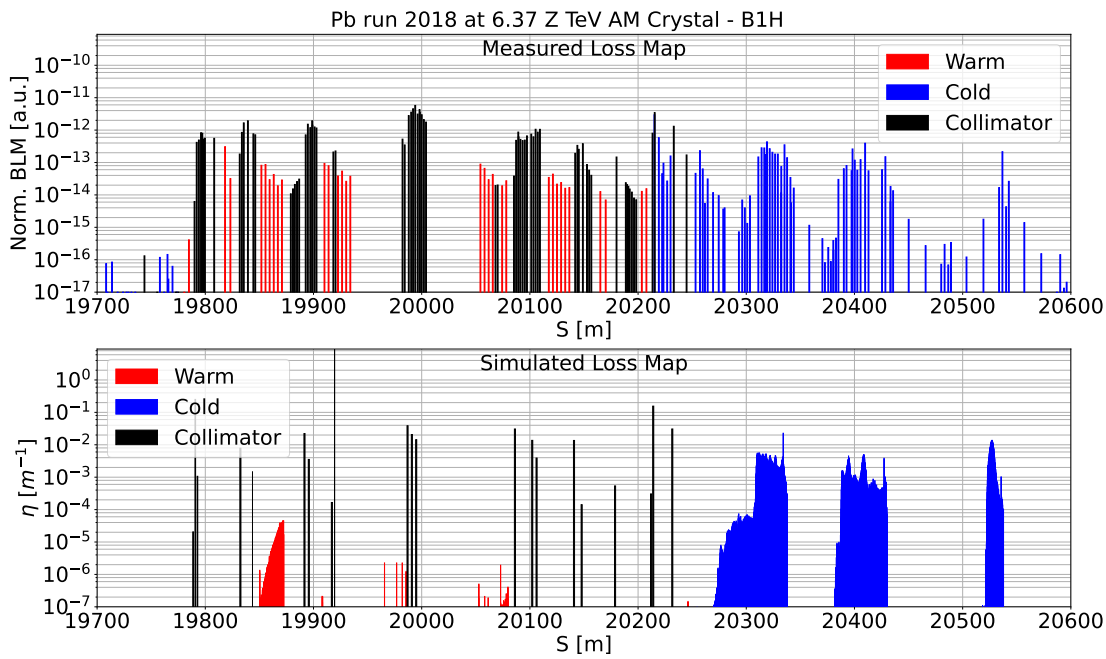


Figure 7.23 – Measured (top) and simulated (bottom) loss map comparison for 2018 B1H crystal collimation in channeling at 6.37 Z TeV *physics*. (a): full ring; (b): zoom in IR7. Measured loss map normalized to total BLM signal can be found in Fig. A.9.



(a)



(b)

Figure 7.24 – Measured (top) and simulated (bottom) loss map comparison for 2018 B1H crystal collimation in amorphous at 6.37 Z TeV *physics*. (a): full ring; (b): zoom in IR7. Measured loss map normalized to total BLM signal can be found in Fig. A.10.

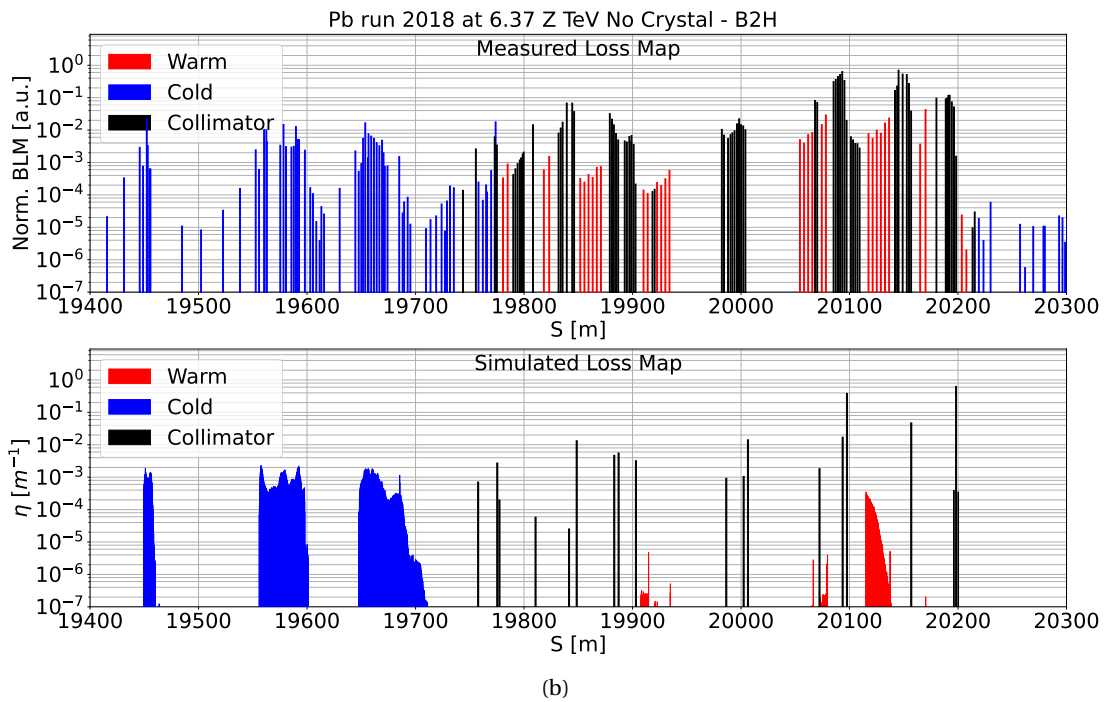
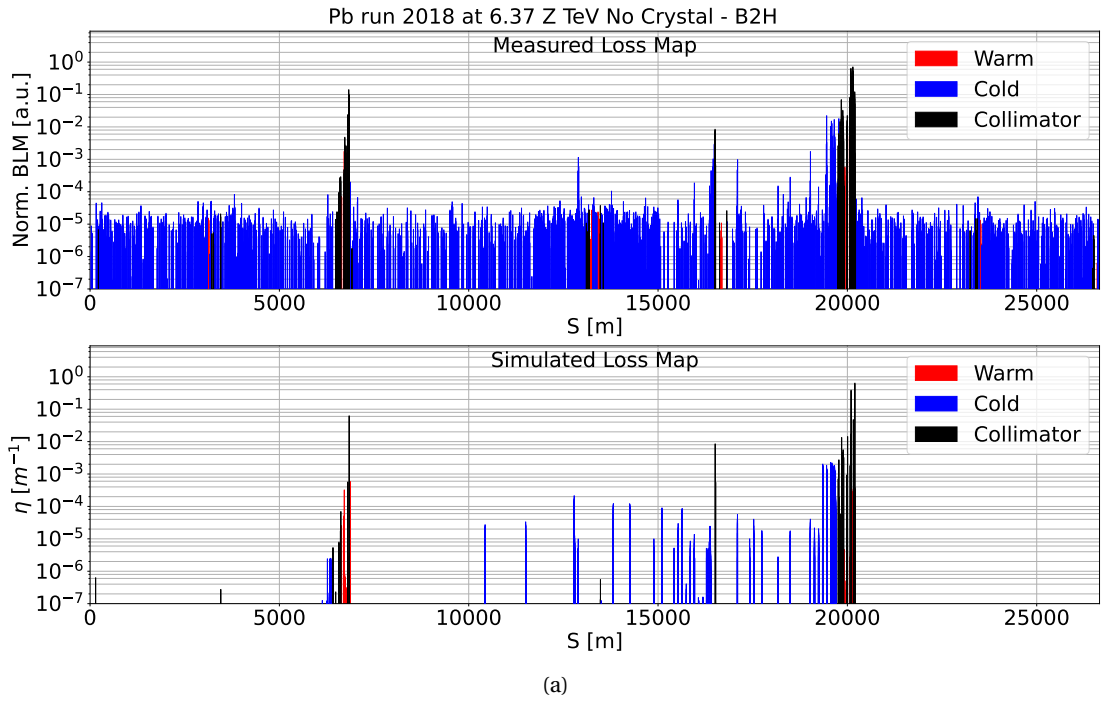
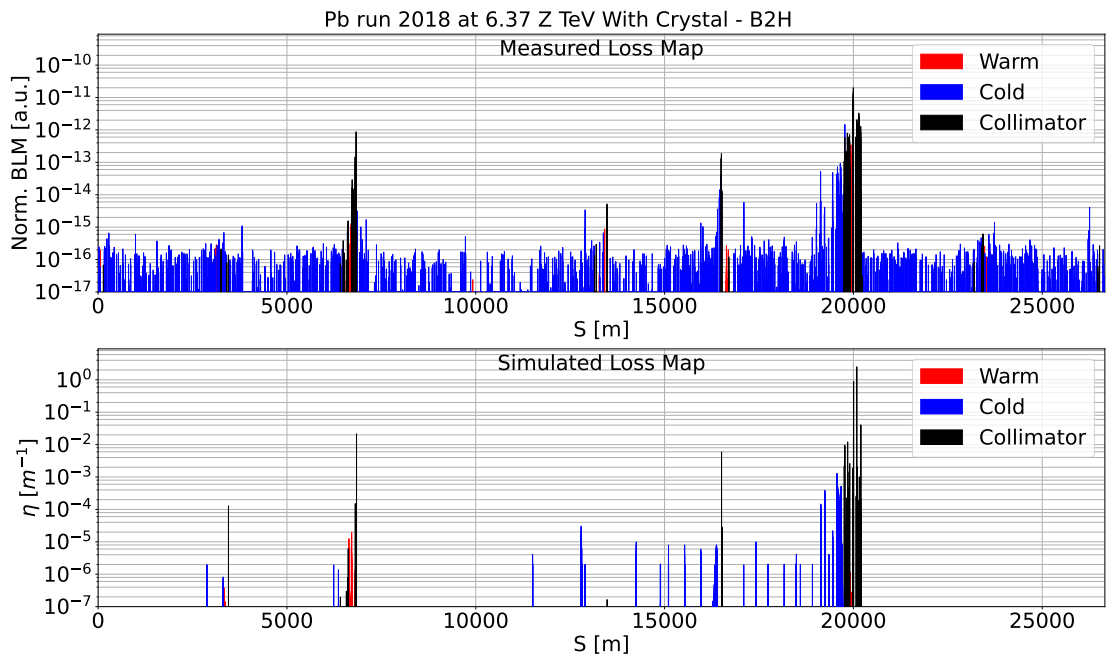
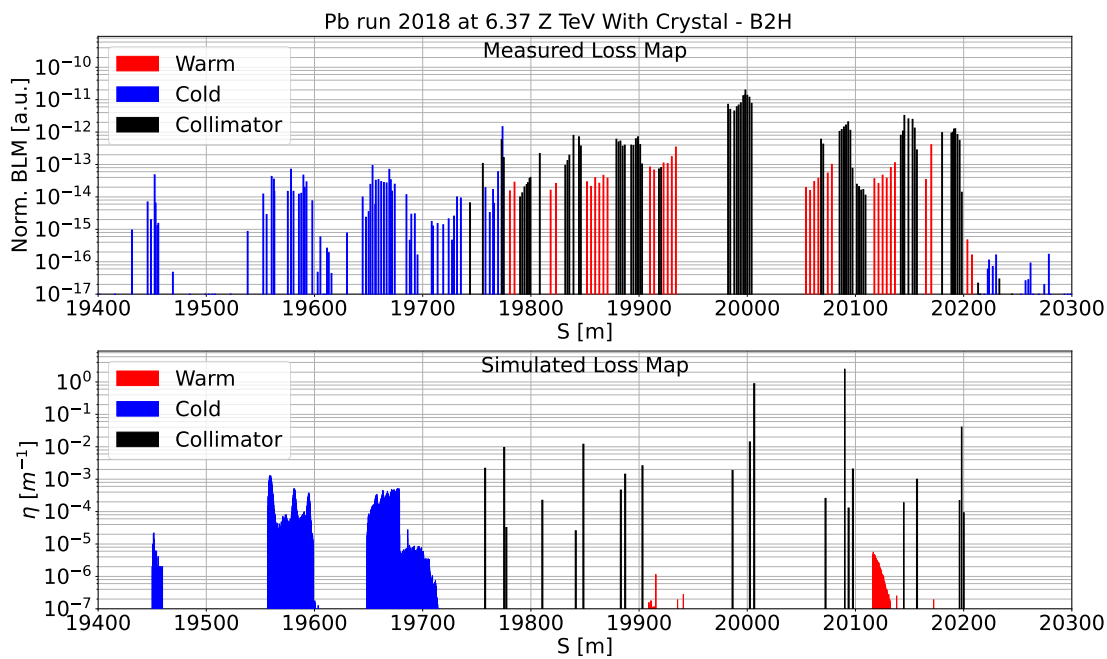


Figure 7.25 – Measured (top) and simulated (bottom) loss map comparison for 2018 B2H standard collimation at 6.37 Z TeV *physics*. (a): full ring; (b): zoom in IR7.

is therefore not problematic. The cleaning performance is reproduced very well in relative in the simulations.



(a)



(b)

Figure 7.26 – Measured (top) and simulated (bottom) loss map comparison for 2018 B2H crystal collimation in channeling at 6.37 Z TeV *physics*. (a): full ring; (b): zoom in IR7. Measured loss map normalized to total BLM signal can be found in Fig. A.11.

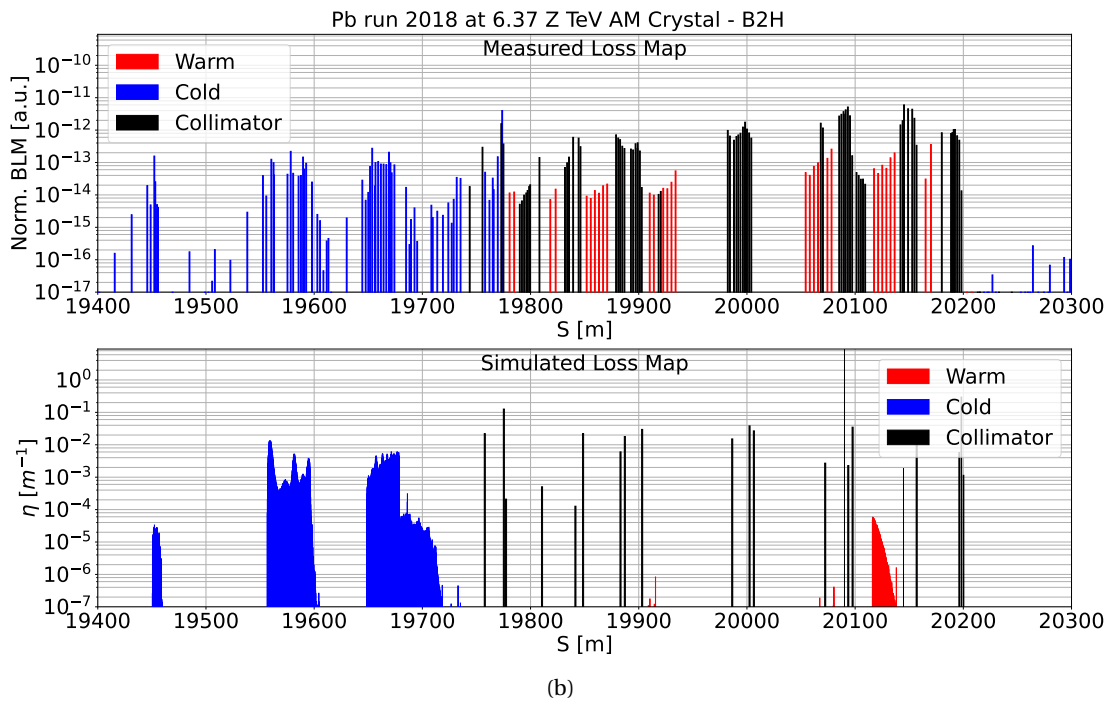
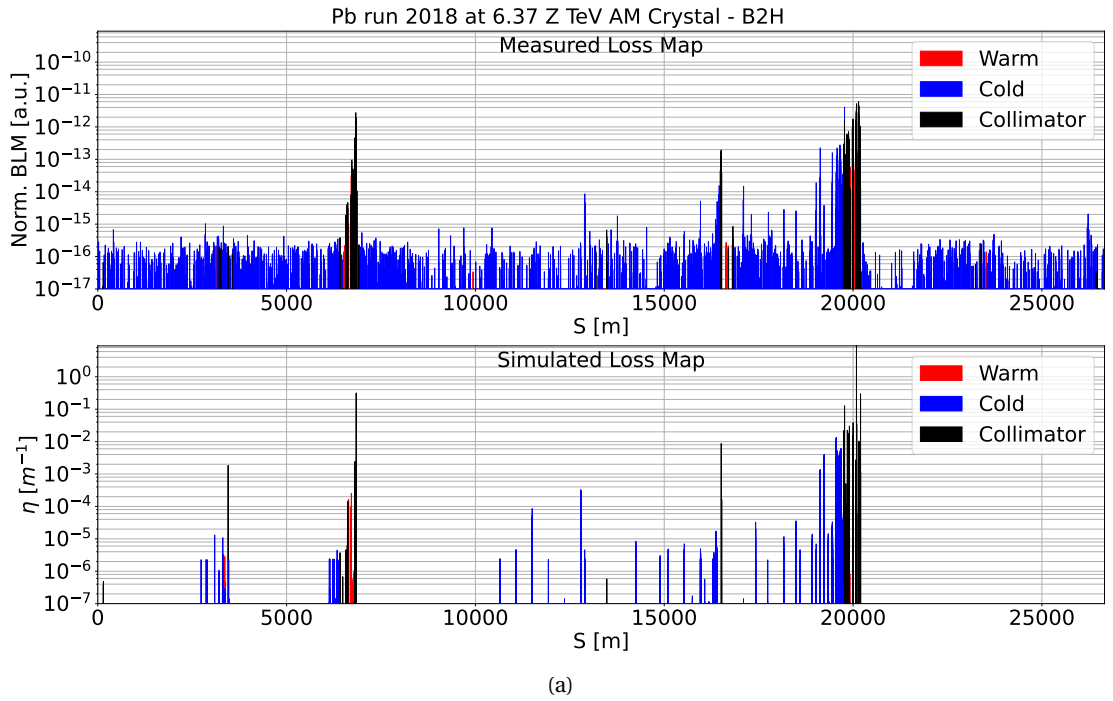


Figure 7.27 – Measured (top) and simulated (bottom) loss map comparison for 2018 B2H crystal collimation in channeling at 6.37 Z TeV *physics*. (a): full ring; (b): zoom in IR7. Measured loss map normalized to total BLM signal can be found in Fig. A.12.

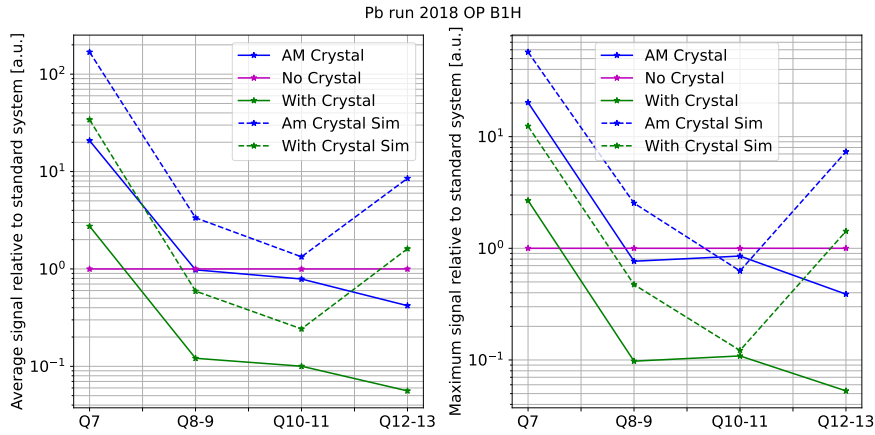


Figure 7.28 – Average (left) and maximum (right) inefficiencies for DS clusters in measured (continuous) and simulated (dashed) data for the B1H 2018 *physics* setup [22] with Pb ions at 6.37 Z TeV. The crystal data and simulations results (amorphous – blue and channeling – green) are normalized to their respective standard-no-crystal setup (purple).

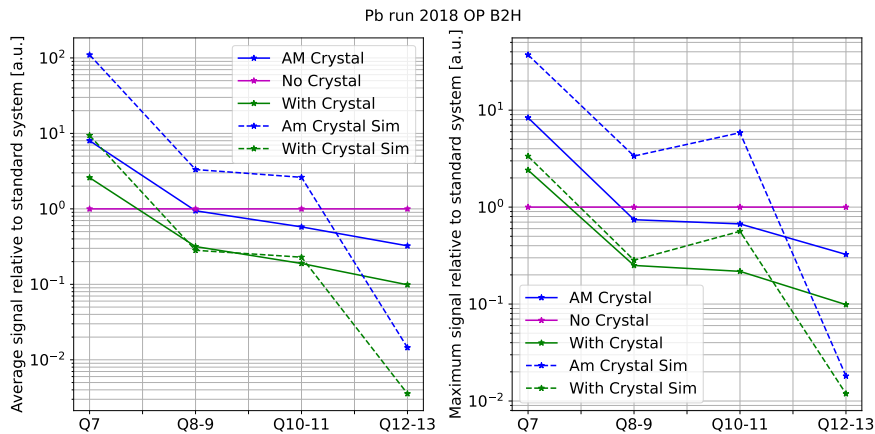


Figure 7.29 – Average (left) and maximum (right) inefficiencies for DS clusters in measured (continuous) and simulated (dashed) data for the B2H 2018 *physics* setup [22] with Pb ions at 6.37 Z TeV. The crystal data and simulations results (amorphous – blue and channeling – green) are normalized to their respective standard-no-crystal setup (purple).

Considering clusters Q8-9 and Q10-11, where the limiting location for the cleaning performance is typically found, it can be seen for both beams that measured data show a factor 4 of cleaning worsening with the crystal in amorphous compared to the standard collimation and an improvement of up to an order of magnitude with the crystal in channeling. Similar results are seen in the simulations. There is a maximum deviation of about a factor of 2 or 3 for simulations from the experimental data for these two clusters.

Finally, the losses in cluster Q12-13 are overestimated by the simulation. These losses are, according to the simulation, made up almost exclusively by the isotope $^{206}\text{Pb}^{82+}$, created

through electromagnetic dissociation, causing the loss of two neutrons by the incoming $^{208}\text{Pb}^{82+}$ halo particles in the crystal. It is, however, unlikely that the cross section in FLUKA for the creation of this isotope is the main cause of the discrepancy, since earlier studies with the standard collimation system instead showed an underestimation of the $^{206}\text{Pb}^{82+}$ losses in Q12-13. Including the effect of the BLM response, through a FLUKA simulation using the studies of this thesis as input [134], the overestimation in absolute at Q12-13 is about a factor 5 between the measurement and the simulation with the crystal in channeling. Considering the complex simulation setup, that the losses span about 7 orders of magnitude, this agreement is considered acceptable.

In conclusion, for this set of benchmark cases, a collimation system with crystals in amorphous orientation has a worse cleaning performance than the standard collimation system and may decrease the cleaning efficiency of more than an order of magnitude from the channeling setup. This means that in case of loss in channeling, it may be better to extract the crystal and revert to the standard system. On the other hand, with the crystals in channeling orientation, significant gains in cleaning performance are observed.

In order to expand to the remaining plane, a similar benchmark has been performed for the 2022 tests. The optics settings and simulation statistics are the ones used in Section 7.3.2 2022 benchmark. The collimation setup for the three cases can be found in Table 7.7. The loss maps of the simulated case compared to the measured data are shown in Figs 7.17 - 7.20 and Figs 7.30 - 7.37 (standard systems loss map inefficiencies are computed with maximum BLM signal as described in Eq. 4.13). The same improvement factor plot has been produced for each plane in the 2022 configuration. In order to bypass simulation artifacts due to aperture, a binning of 2 m has been chosen instead of the usual 0.1 m. The comparison plots are in Figs 7.38 - 7.41.

In the improvement factor plots for 2022, similar conclusions as for the 2018 comparison can be made. One of the differences that can be spotted is the high predicted factor in Q10-11 for the two B1 planes (Figs 7.38, 7.39) both for the channeling and amorphous setup compared to the measured one. This can be attributed to the cold spike loss in simulations at the end of this cluster that we can see in Figs 7.17, 7.18, 7.30, and 7.31 (b).

Lastly, it is worth noting that the improvement factors for the same planes can vary depending on the setup and beam energy, if we compare Figs 7.28 with Fig 7.38. The difference in improvement extends to the various planes as well.

7.3.4 Angular scan

An angular scan comparison between simulations and measurements with Pb ions has been done for the same crystal as the one used in the proton angular scan, i.e. the TCPCH.A4L7.B1 (old) in Table 4.5 in B1H. The beam, optics and collimation settings remain the same as for the loss map study in Sec. 7.3.2. The analysis method remains the same as for protons. The

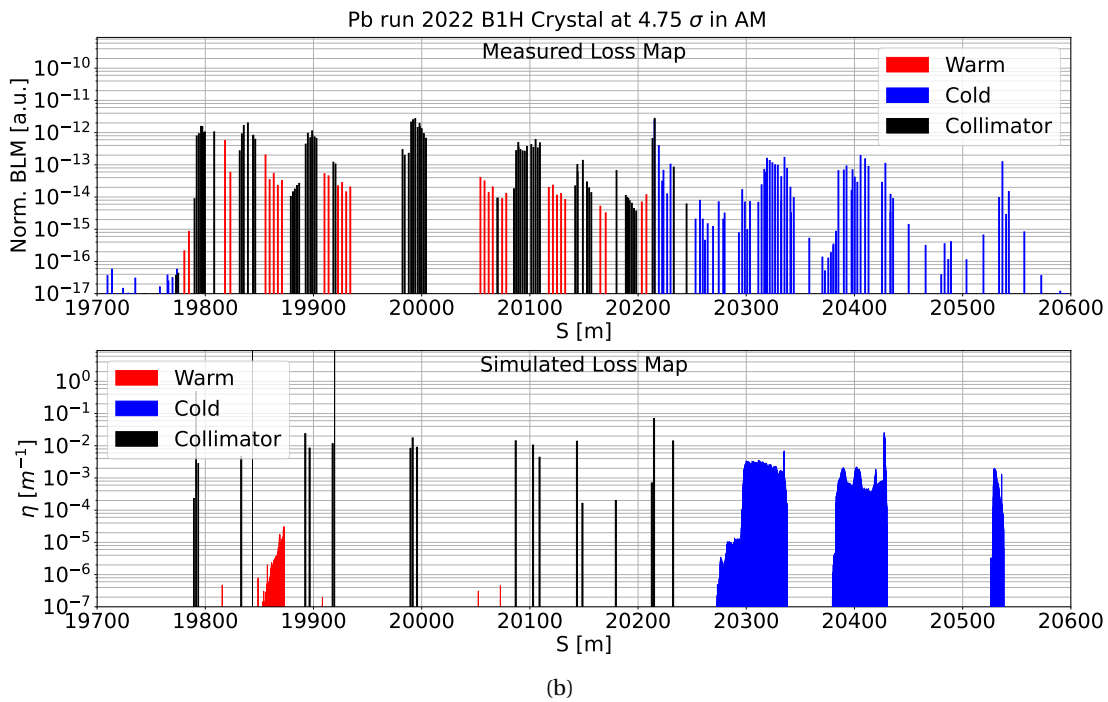
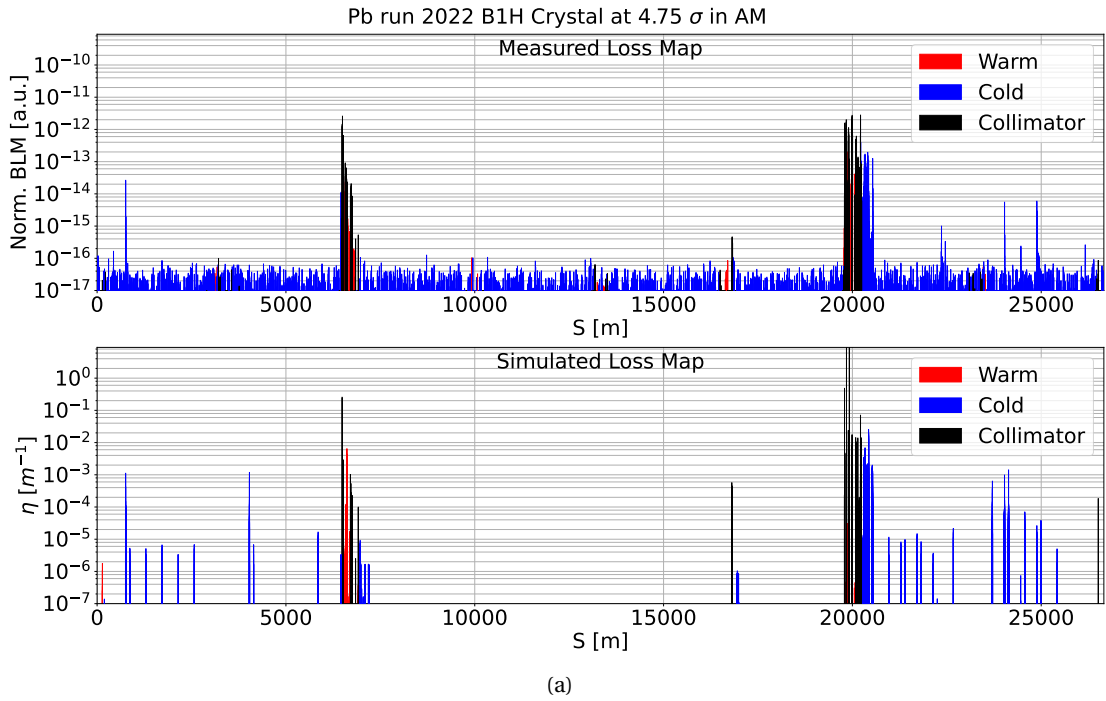


Figure 7.30 – (a): Measured (top) and simulated (bottom) loss map for B1H 2022 Pb test crystal collimation in amorphous at 6.8 Z TeV *flat-top*. (b): zoom in IR7. Measured loss map normalized to total BLM signal can be found in Fig. A.13.

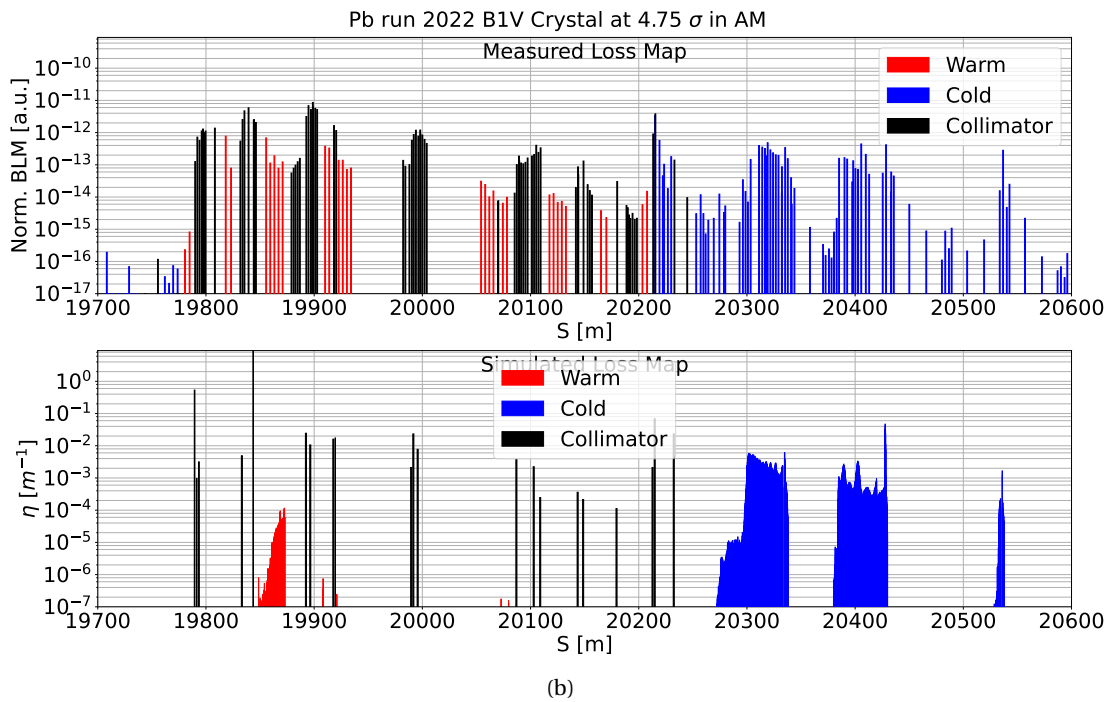
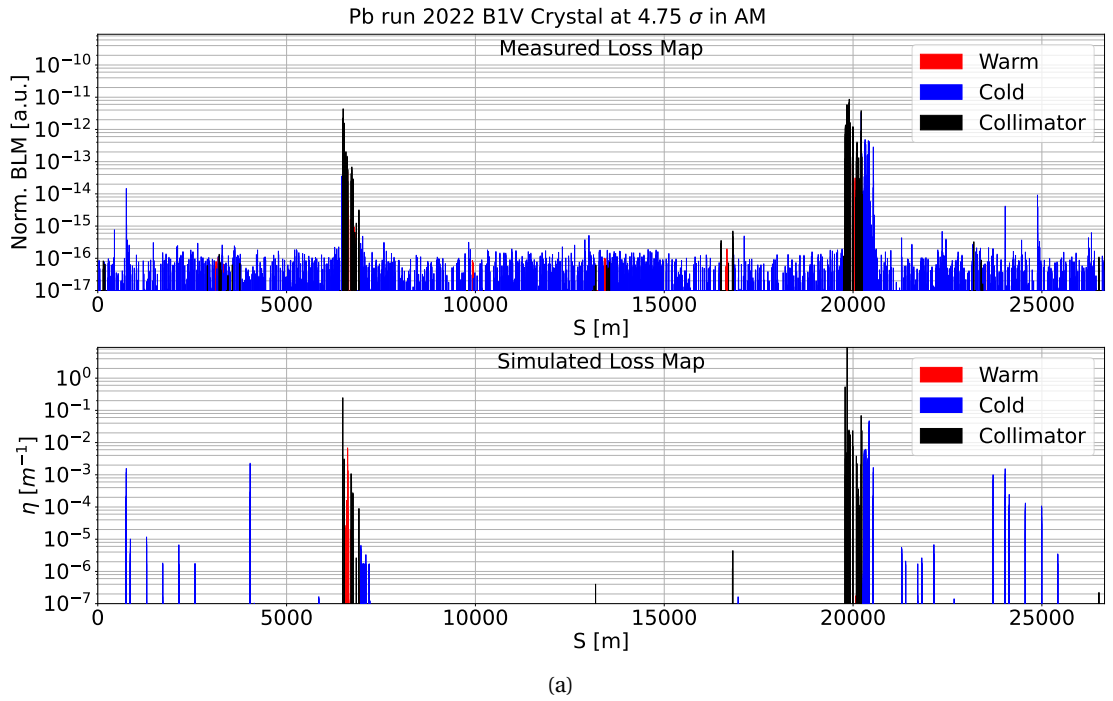


Figure 7.31 – (a): Measured (top) and simulated (bottom) loss map for B1V 2022 Pb test crystal collimation in amorphous at 6.8 Z TeV *flat-top*. (b): zoom in IR7. Measured loss map normalized to total BLM signal can be found in Fig. A.14.

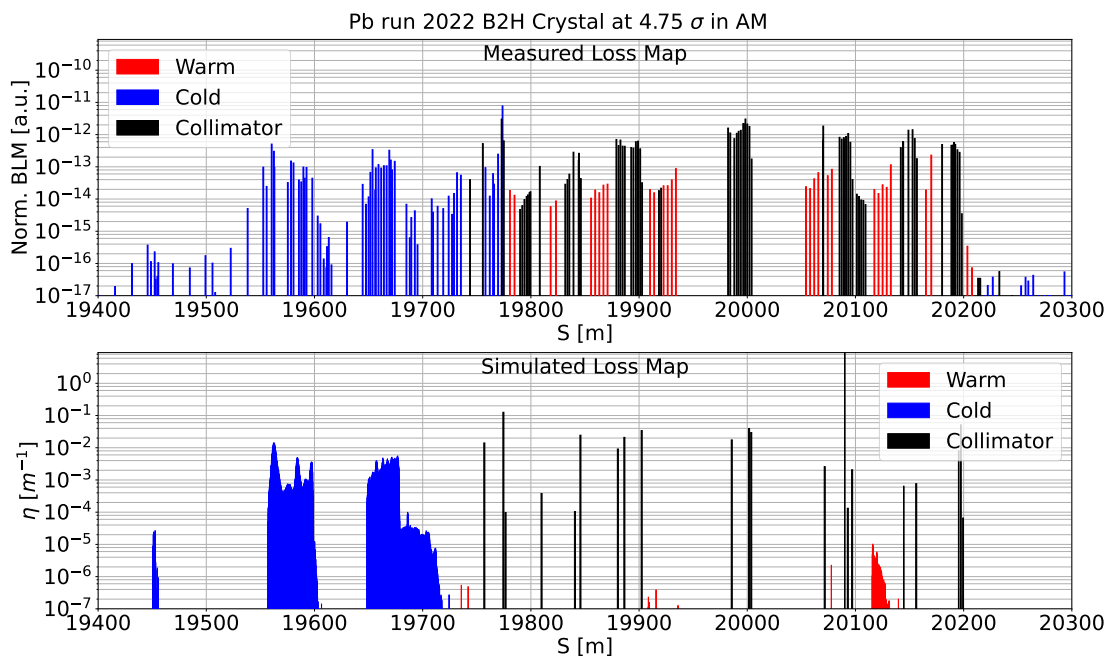
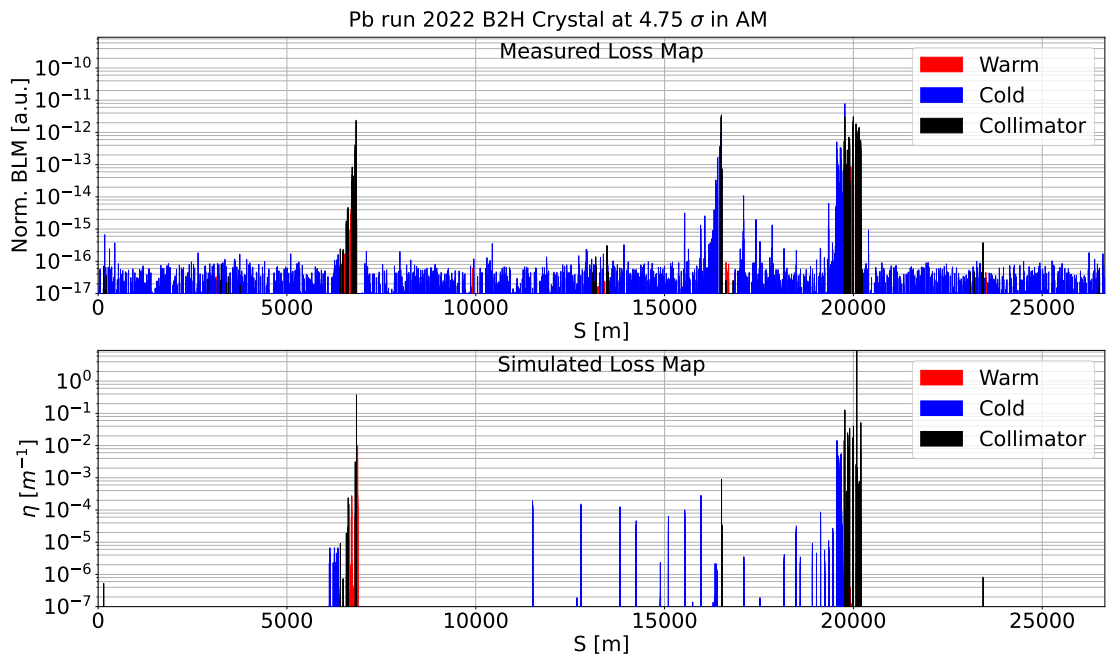


Figure 7.32 – (a): Measured (top) and simulated (bottom) loss map for B2H 2022 Pb test crystal collimation in amorphous at 6.8 Z TeV *flat-top*. (b): zoom in IR7. Measured loss map normalized to total BLM signal can be found in Fig. A.15.

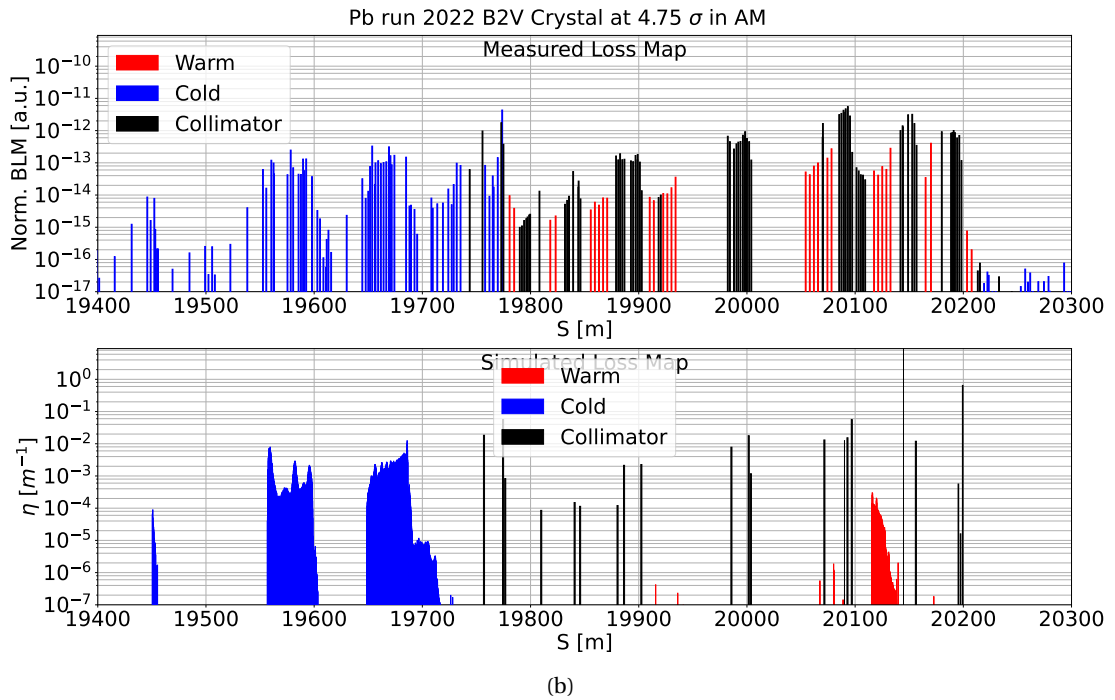
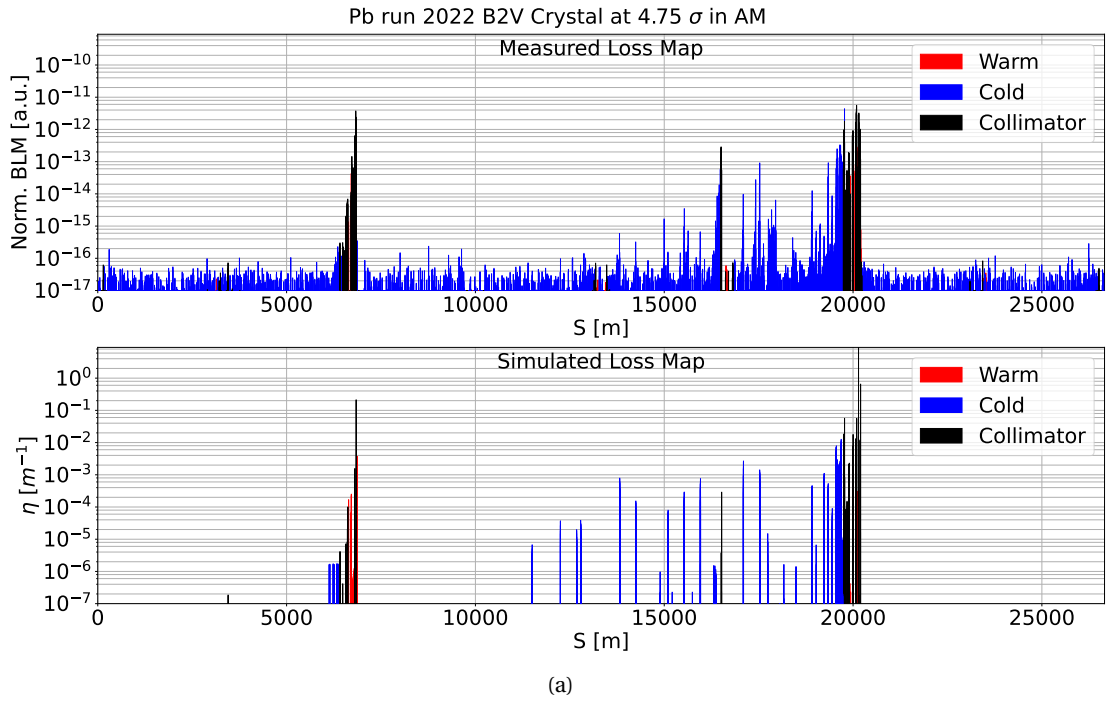


Figure 7.33 – (a): Measured (top) and simulated (bottom) loss map for B2V 2022 Pb test crystal collimation in amorphous at 6.8 Z TeV *flat-top*. (b): zoom in IR7. Measured loss map normalized to total BLM signal can be found in Fig. A.16.

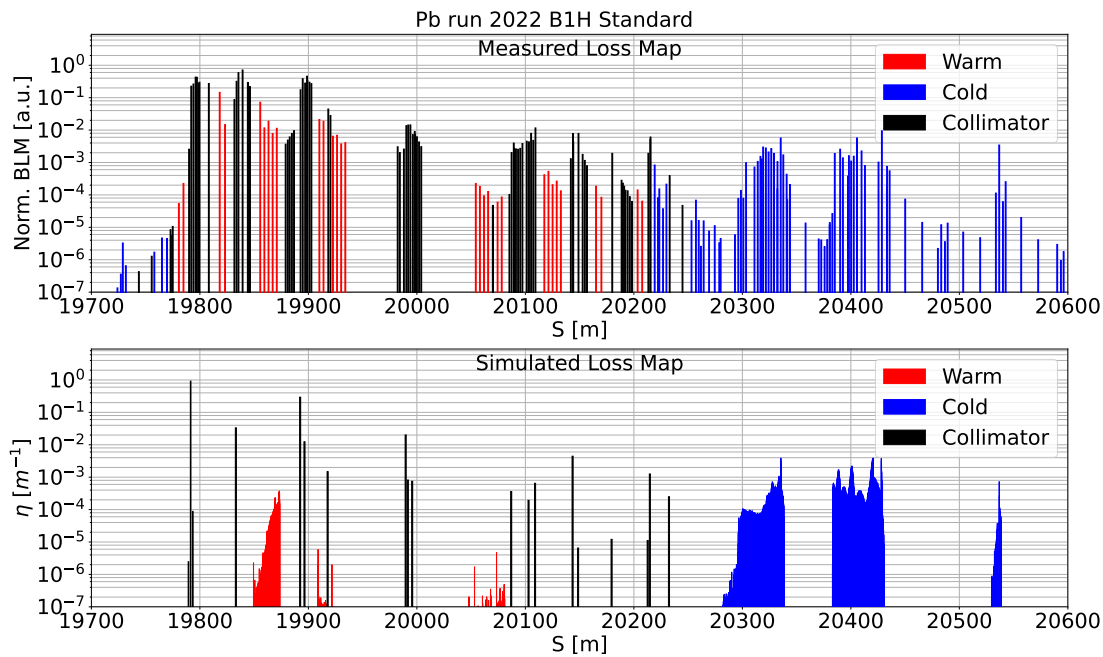
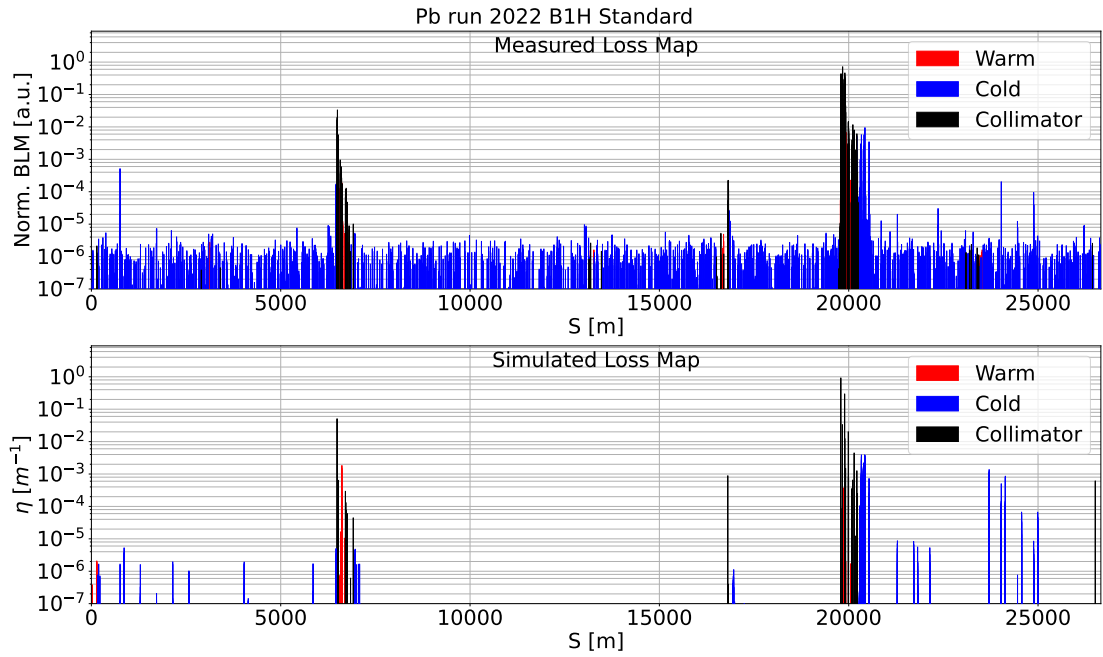


Figure 7.34 – (a): Measured (top) and simulated (bottom) loss map for B1H 2022 Pb test standard collimation at 6.8 Z TeV *flat-top*. (b): zoom in IR7.

measured data are from a machine development session on the 27th of November 2018 [35]. The simulation procedure is the same as the one used for the proton angular scan. The results

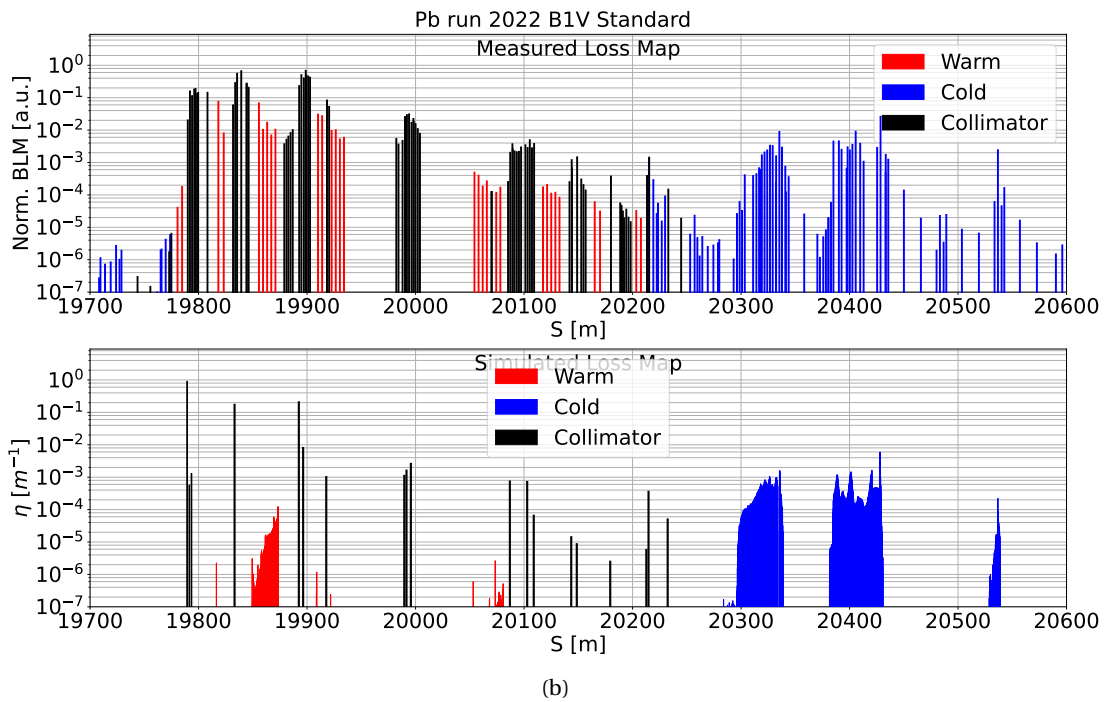
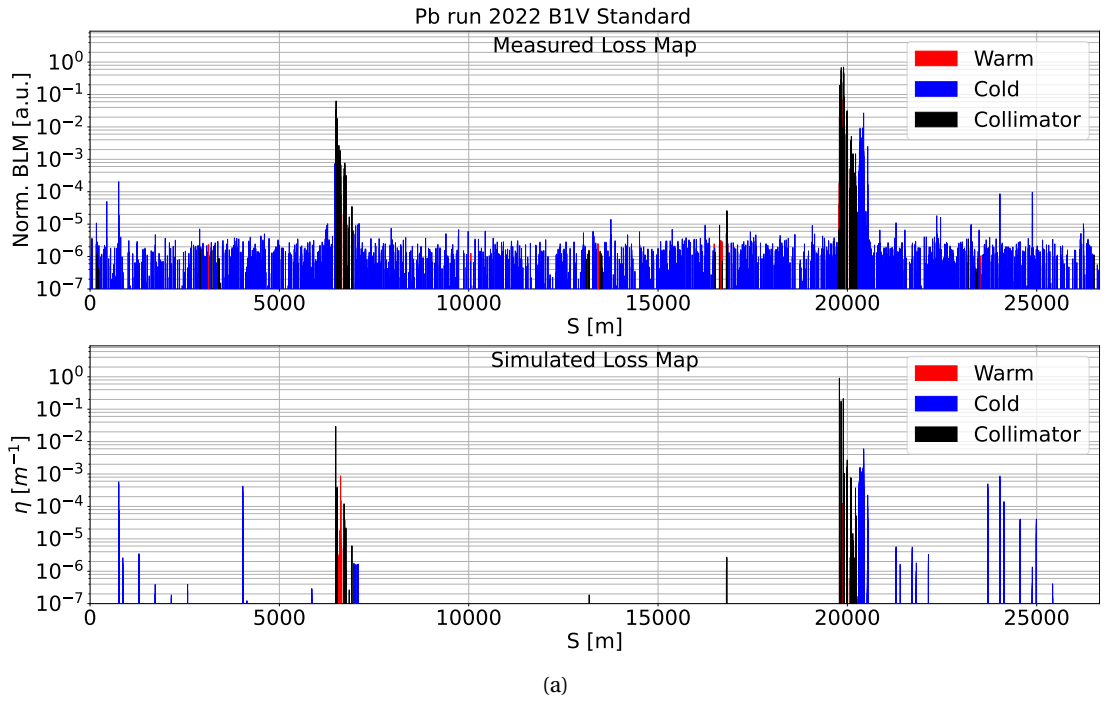


Figure 7.35 – (a): Measured (top) and simulated (bottom) loss map for B1V 2022 Pb test standard collimation at 6.8 Z TeV flat-top. (b): zoom in IR7.

of the comparison are shown in Fig. 7.42.

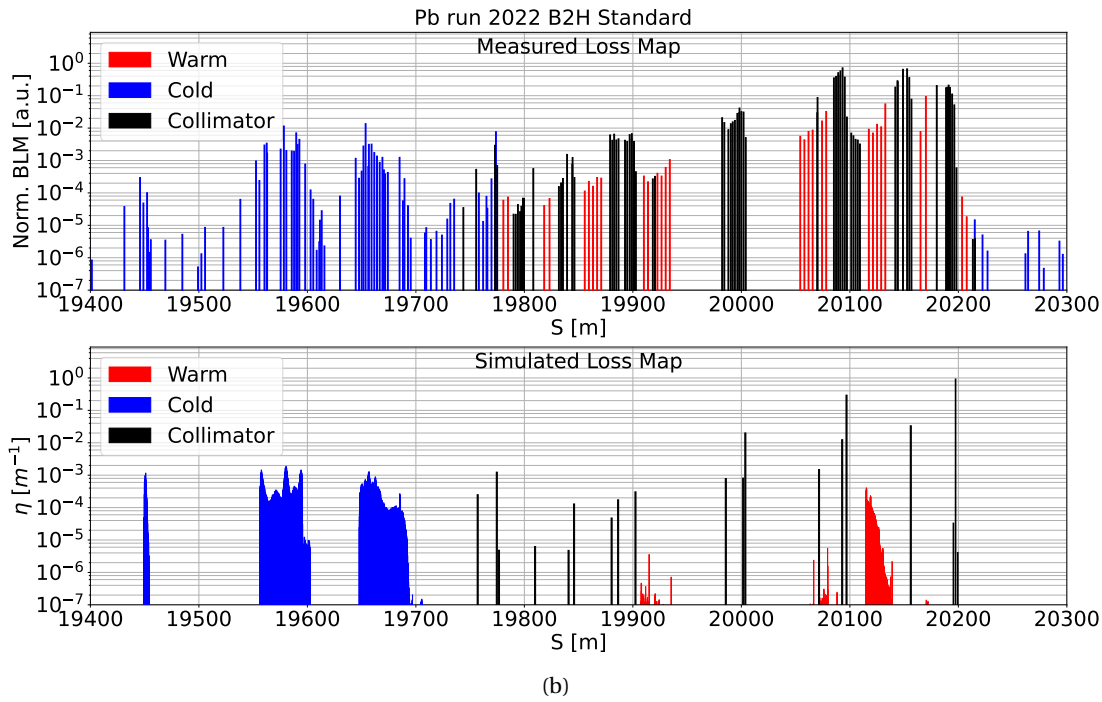
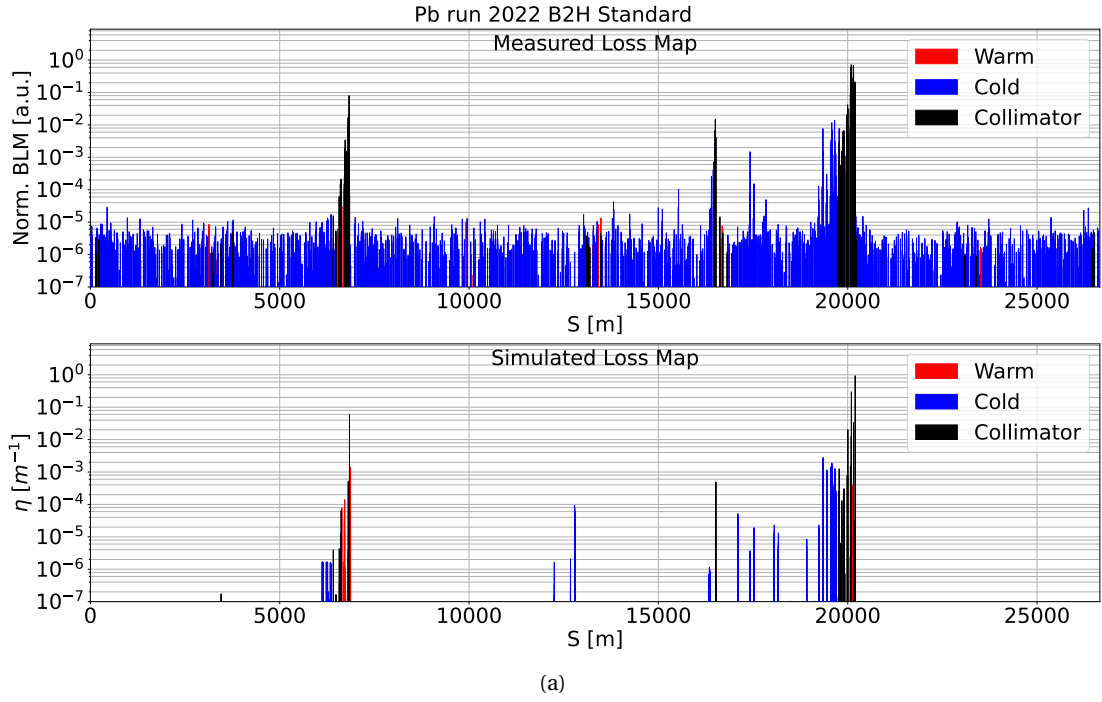


Figure 7.36 – (a): Measured (top) and simulated (bottom) loss map for B2H 2022 Pb test standard collimation at 6.8 Z TeV *flat-top*. (b): zoom in IR7.

The simulation correctly assigns the crystal processes, e.g. CH, AM, VR, to the different crystal orientations. We see the same difference in channeling well depth as for protons, where the

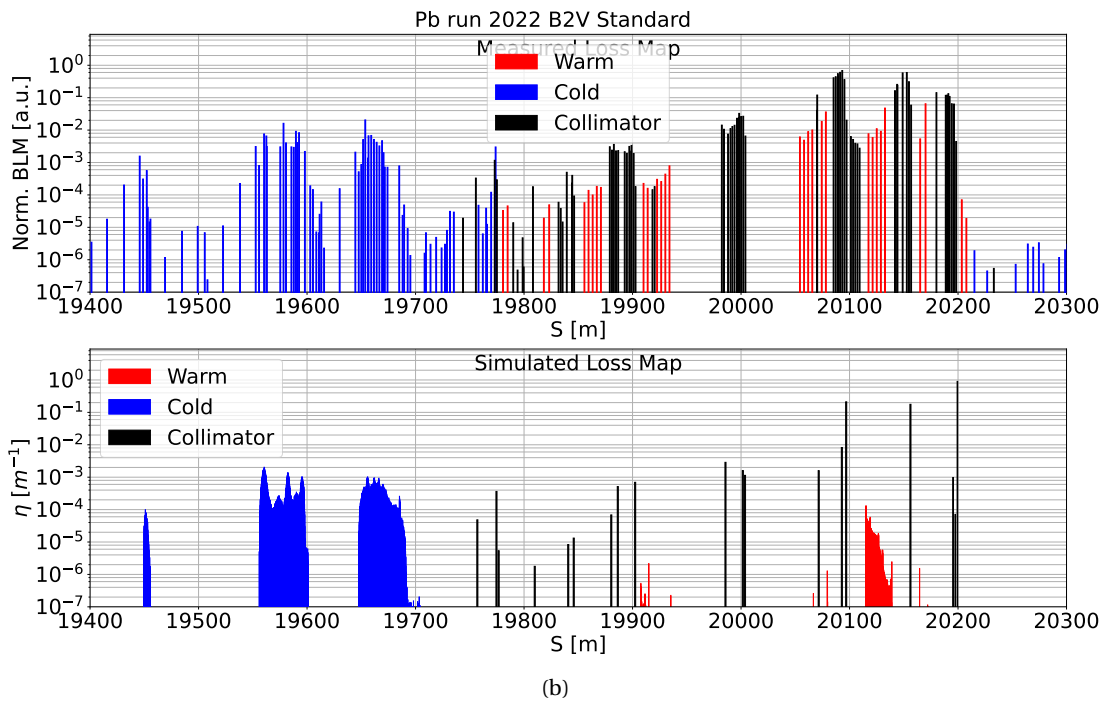
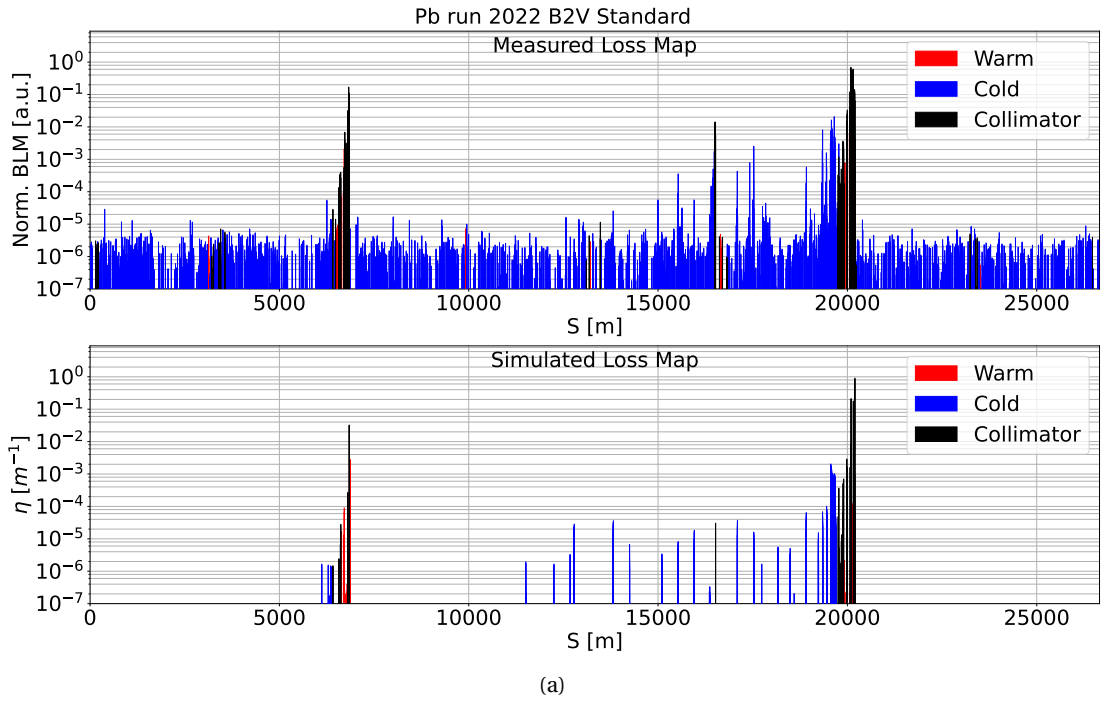


Figure 7.37 – (a): Measured (top) and simulated (bottom) loss map for B2V 2022 Pb test standard collimation at 6.8 Z TeV flat-top. (b): zoom in IR7.

simulated channeling well is much deeper than the measured one. The cause of this difference may still lie in not having included imperfections in the simulations and the fact that BLM

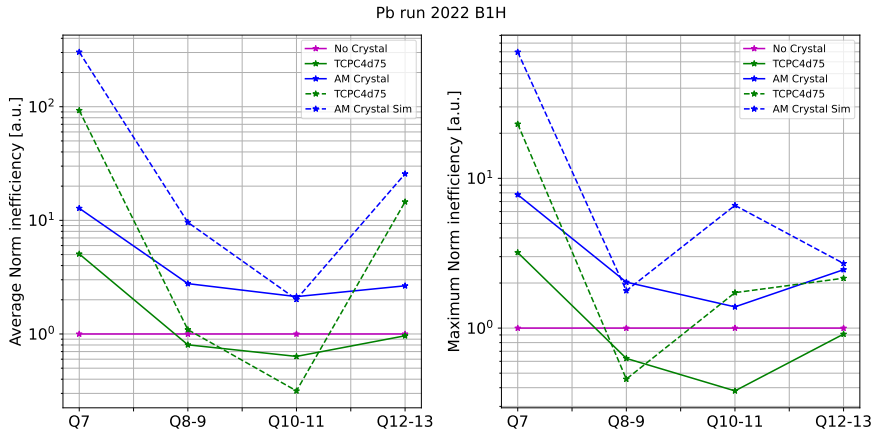


Figure 7.38 – Average (left) and maximum (right) inefficiencies for DS clusters in measured (continuous) and simulated (dashed) data for the B1H 2022 *flat-top* setup (Table 7.7) with Pb ions at 6.8 Z TeV. The crystal data and simulations results (amorphous – blue and channeling – green) are normalized to their respective standard-no-crystal setup (purple).

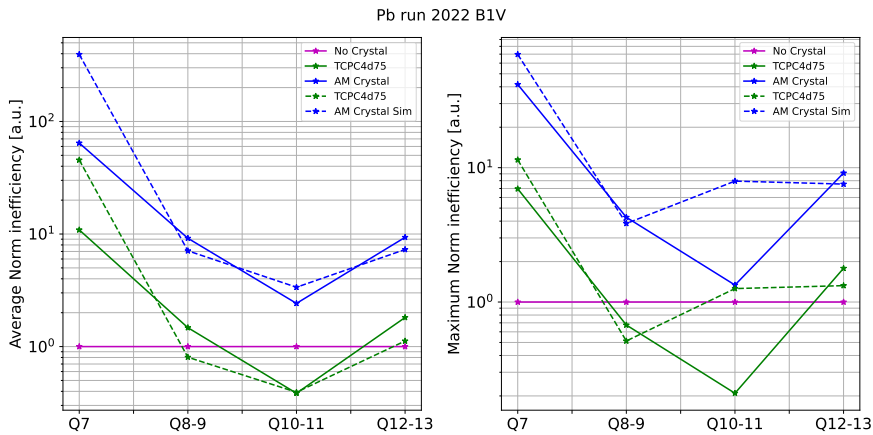


Figure 7.39 – Average (left) and maximum (right) inefficiencies for DS clusters in measured (continuous) and simulated (dashed) data for the B1V 2022 *flat-top* setup (Table 7.7) with Pb ions at 6.8 Z TeV. The crystal data and simulations results (amorphous – blue and channeling – green) are normalized to their respective standard-no-crystal setup (purple).

signals are not directly comparable to the energy lost in the crystal in simulations. The main discrepancy here is in magnitude of the normalized BLM signal in the angular range where volume reflection occurs. An over estimation of the absorption in the VR region was already seen for protons, although for ions this is exacerbated. In this plot, an error bar of the level of VR corresponding to two standard deviations is plotted on both sides to give an estimation of confidence. The error bar is derived from the data fluctuation. Since the VR level is calculated

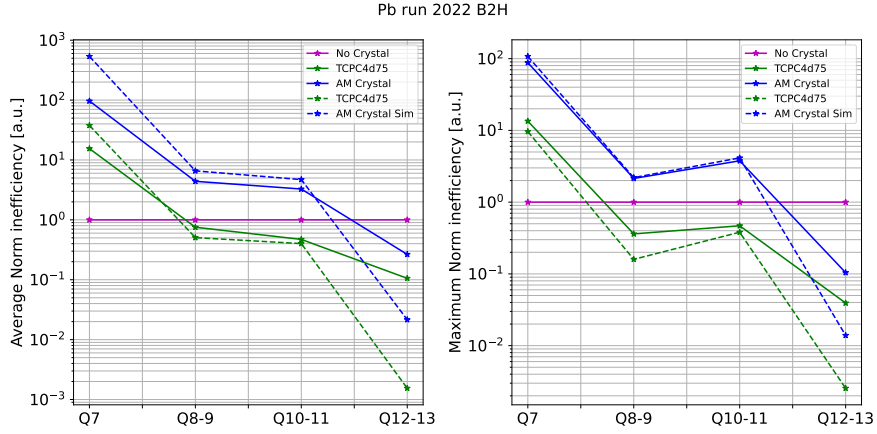


Figure 7.40 – Average (left) and maximum (right) inefficiencies for DS clusters in measured (continuous) and simulated (dashed) data for the B2H 2022 *flat-top* setup (Table 7.7) with Pb ions at 6.8 Z TeV. The crystal data and simulations results (amorphous – blue and channeling – green) are normalized to their respective standard-no-crystal setup (purple).

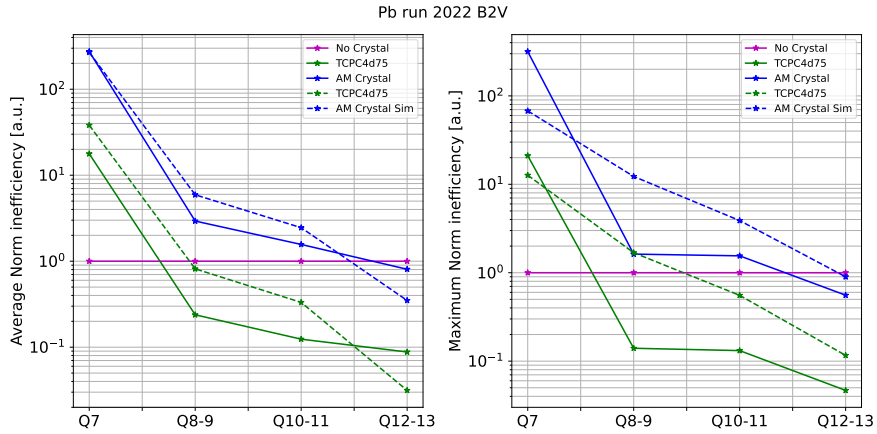


Figure 7.41 – Average (left) and maximum (right) inefficiencies for DS clusters in measured (continuous) and simulated (dashed) data for the B2V 2022 *flat-top* setup (Table 7.7) with Pb ions at 6.8 Z TeV. The crystal data and simulations results (amorphous – blue and channeling – green) are normalized to their respective standard-no-crystal setup (purple).

with $VR_{norm} = \overline{VR}/\overline{AM}$, the error of the normalized VR level is

$$\sigma_{VR_{norm}} = VR_{norm} \sqrt{\left(\frac{\sigma_{AM}}{\overline{AM}}\right)^2 + \left(\frac{\sigma_{VR}}{\overline{VR}}\right)^2} \quad (7.1)$$

where VR_{norm} is the normalized VR level, \overline{VR} and \overline{AM} are the average VR and AM values, and $\sigma_{VR,AM}$ are the standard deviation of the VR and AM signals taken as errors. It is possible that the excessive absorption reflects the amorphous band above the volume reflection stripe shown in the single pass plot (Fig. 7.12) mentioned in the Single pass Section. The found

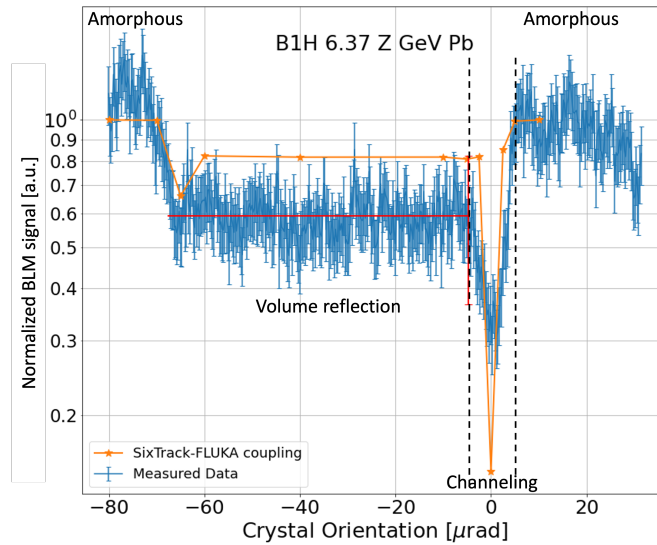


Figure 7.42 – Angular scan for B1H 6.37 Z TeV Pb ions of a $65\mu\text{rad}$ crystal for measured data (blue), simulation (orange), and volume reflection plateau between 2 standard deviations (red).

discrepancy in the range of volume reflection does, however, not have a sizeable impact on the cleaning efficiency in the tracking studies, since the dominating coherent process for this application is the channeling.

7.3.5 Linear scan

Finally, a linear scan benchmark is performed for Pb ions. The crystal used is the same one used in the proton linear scan benchmark, i.e. TCPCV.A6R7.B2 (new) (specifications in Table 4.5). The test was performed on the 19th of November 2022 during the 2022 ion tests [139] at the *flat-top* stage and the record energy of 6.8 Z TeV. The optics [136] and the initial number of primary particles used are the same as for the 2022 B2V proton linear scan benchmark. The collimator settings are the same everywhere as in the proton run [137] except for IR7. Exact settings are reported in Table 7.5.

The analysis is done using the proton linear scan analysis method with the difference that the particle count and the following integral are weighted with the particle energy, in order to account for different contributions from light and heavy secondary nuclei. The results are shown in Fig. 7.43. The simulated results reproduce the measured data satisfactorily. There is a small overestimation of the multi-turn channeling efficiency: around 75% for simulation and 60% for the measured data. However, measurements at this energy tend to be difficult and noisy. It is worth mentioning that due to the very limited time allocated to the ion tests, a shorter method of collimators alignment was used. As a consequence, the measured data may be of worse quality than it could have been. In fact, a 60% channeling efficiency is lower

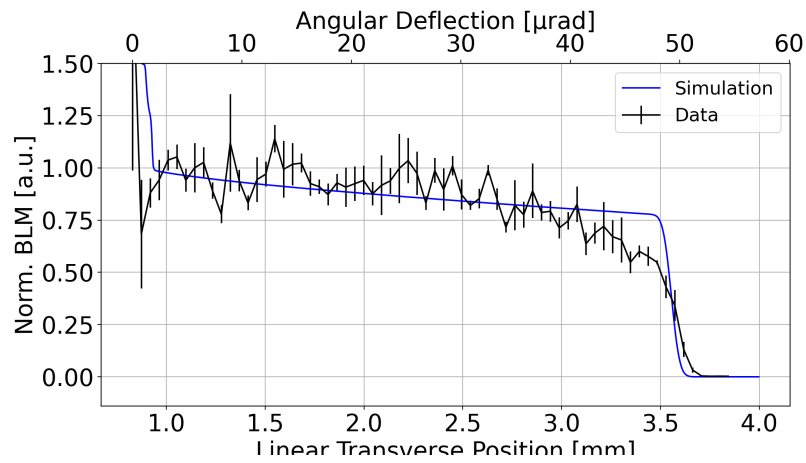


Figure 7.43 – Measured (black) and simulated (blue) 2022 B2V crystal linear scan for 6.8 Z TeV Pb ions.

than what was historically measured for (110) crystal with ions at this energy [27]. Therefore, in view of this shortcoming, it is too soon to dismiss the simulated reproduction as lacking. It would be best to perform more and better measurements and compare again.

8 Crystal collimation studies with Pb ions in the LHC

Crystal collimation is a novel technique for controlling the beam halo in high-energy ion colliders. Many characteristics studied over the years with the standard collimation method cannot be assumed for crystal collimation. This chapter describes the use of the new simulation setup for crystal collimation, as described in Chapter 6 and benchmarked in Chapter 7, in order to characterize and better understand the collimation process of the crystal-based system, as well as to do predictions, define operational settings, and mitigate operational problems.

This chapter starts with dedicated key studies to define the characteristics of crystal collimation with Pb ions in the LHC. The main source of losses leaking to the DS is identified, and the sensitivity of the cleaning performance to different impact parameters, crystal orientation, and various imperfections is investigated. The next part is dedicated to investigations of the cleaning performance with different configurations of the standard collimators being part of the crystal-based system, followed by studies of fast beam failures with a crystal-based collimation system in place. This leads up to a proposal for operational settings, which was successfully implemented in the 2023 Pb ion run in the LHC. Finally, this chapter is closed with a brief summary of the operational experience with crystal collimation in the 2023 Pb ion run, with particular focus on problems that could be mitigated using simulations that are part of this thesis.

8.1 Characteristics of crystal collimation

8.1.1 Black absorber study

As mentioned in previous chapters, the most limiting section of the LHC for collimation performance is the IR7 DS region. Therefore, this section is dedicated to the investigation of the main source of losses with Pb ion beams in this region, when a crystal-based collimation system is used. One of the key elements for this is to understand is the history of the particles lost in the DS, and which collimator or collimators are the main contributors to the losses there, in order to investigate if anything can be done to further decrease these losses. For

crystal collimation, it is possible that the crystal itself is the main source of the DS losses.

To test this hypothesis, two simulations have been conducted to be compared: one is an ion collimation simulation with the crystal in channeling as primary collimator, and all standard collimators in place at larger openings than the crystal. The other simulation has the exact same configuration except that all standard collimators are perfect black absorbers (an artificial material in FLUKA stopping all impacting particles, without any outscattering - see Sec. 5.4). With all collimators made of this material, any out-scattered particles leaving the collimation insertion and lost elsewhere must by definition come directly from the crystal and not from the standard collimators. The machine configuration used is the one from 2018 at the operational stage of *physics* with $\beta^* = 100$ cm. For this comparison 6×10^6 $^{208}\text{Pb}^{82+}$ primary ions at 6.37 Z TeV were simulated. The collimation settings are those used in Run 2 Pb-Pb operation using the standard collimation system, as reported in Table 7.8, but with the crystals inserted in addition at 4.75σ to be the new primary collimator. The simulated loss maps for B1H for the full ring and the zoom in IR7 are shown in Figs. 8.2 and 8.3 respectively.

The two loss maps are very similar. What is different in the black-absorber study is the lack of "tails" in certain clusters of losses. For example, in IR3 we see that in the standard-material simulation there are other losses (warm, cold and collimator) after the first IR3 collimator at around $s = 6300$ (Beam 1 circulates from $s = 0$ to $s = 26659$). Since in the black-absorber simulation there can be no leakage from any non-crystal collimator, we can conclude that the losses after the first IR3 collimator comes from the leakage of that collimator. The same considerations can be made about other IRs. In fact, all losses around the ring observed in the ring in the black-absorber study, both on collimators and the machine aperture, must originate directly from outscattering in the crystal.

When zooming into IR7, we notice that the losses in the DS are also very similar between the results of the two setups, although not strictly identical. This means that any leakage of out-scattered particles from standard collimators does not contribute in a significant manner to the losses in the DS. Since the leakage from the crystal depends on the crystal and the beam impact characteristics, it is not possible to reduce leakage from the source without changing the device. Hence, any further optimization of crystal collimation must be based on blocking as many as possible of the outscattered particles that may reach the DS, by acting on collimator settings or optics, e.g., the single-pass dispersion, instead of trying to make the channeled halo hit in deeper into the standard collimators. With the present LHC hardware, DS losses may be hence be improved only via changes in collimation settings or changes to the magnetic settings of the machine.

8.1.2 Trackback study

To have a quantitative view on what is the contribution from the crystal and other collimators to the DS, the SixTrack-FLUKA Coupling has been modified in collaboration with other team members [140] to assign to newly created particles, i.e. out-scattered ion fragments, numeric

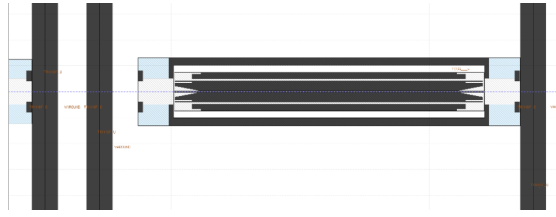
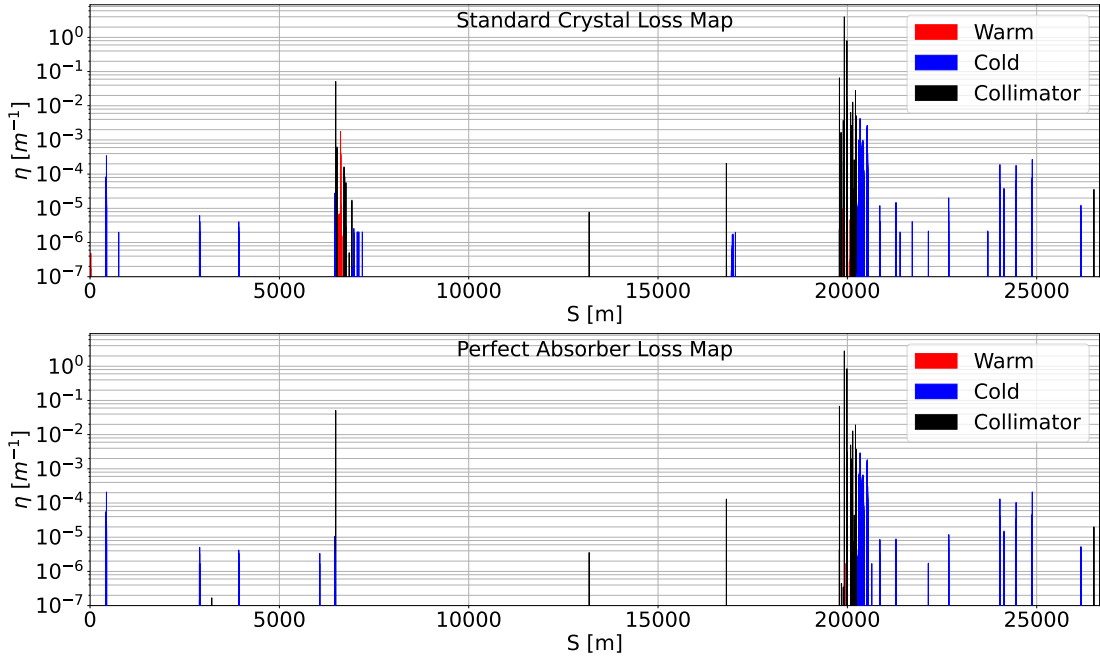


Figure 8.1 – Front view of a collimator set as black absorber.

Figure 8.2 – Simulated crystal collimation for the 6.37 Z TeV Pb ion 2018 *physics* stage with normal collimator materials (top) and black absorber used as material in all standard collimators (bottom) – full ring view.

IDs, as well as in maintaining the same parent-particle numeric ID, so that each particle is uniquely identifiable and can be tracked back with a complete history.

A crystal simulation has been carried out for the 2023 Run 3 ion optics [141] in collision with Pb ions at 6.8 Z TeV, and here the example of B2H is considered. Beam parameters can be found in Table 3.1. The Run 3 ion optics is identical to that of Run 2 with minor modifications. In the following, all simulations use the Run 3 ion optics. The crystal used is the TCPCH.A5R7.B2 (new) in Table 4.5 and the associated absorber is the TCSPM.B4R7.B2. The collimation settings are the same as for the Run 2 *physics* stage for heavy ions (see Table 7.8) with the crystal inserted at 4.75σ . As for previous simulations, 6×10^6 $^{208}\text{Pb}^{82+}$ primary ions were simulated with a pencil beam at $b = 1 \mu\text{m}$. All particles lost in the DS were recorded. The particle IDs were used to track back to the last collimator that each lost particle hit, as well to identify the first crystal process that each particle or its parent particle have undergone, the crystal process

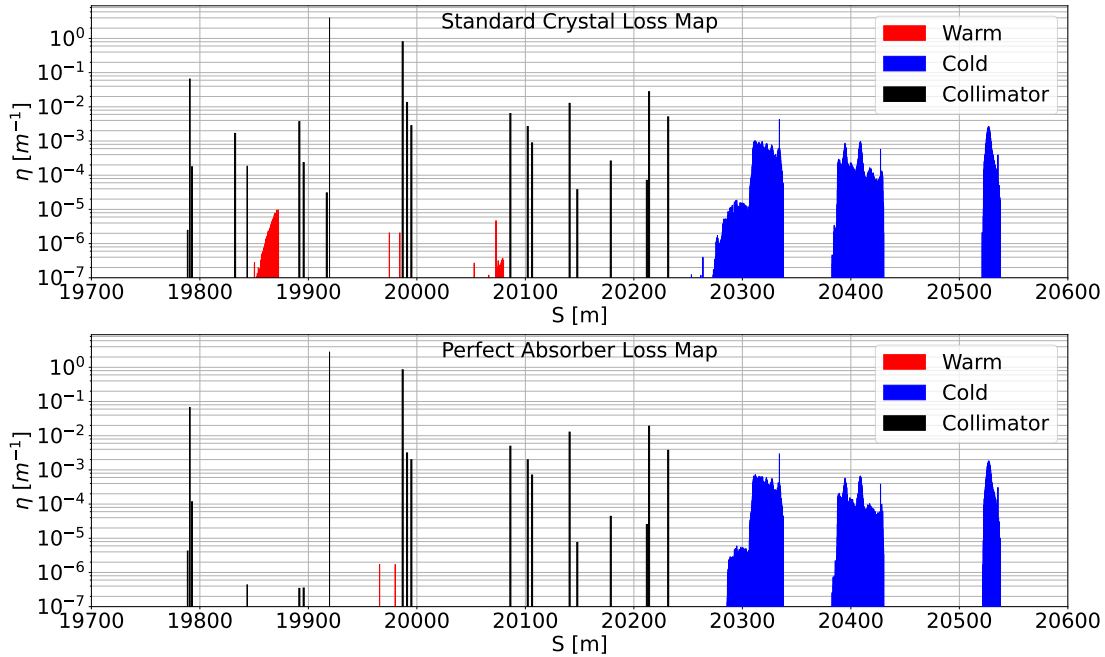


Figure 8.3 – Simulated crystal collimation B1H loss map for the 6.37 Z TeV Pb ion 2018 *physics* stage with normal collimator materials (top) and black absorber used as material in all standard collimators (bottom) – zoom in IR7.

that the particle or the parent particle last went through, the turn the particle was created, and the turn it was lost. The results are presented as bar charts in Figs. 8.4a, 8.4b, 8.5a, and 8.5b (only the 10 turns with the highest count are plotted).

From the collimator leakage plot in Fig 8.4a, we can see that over 80% of the number of particles lost in the DS come from the crystal, while only a small percentage come from other collimators such as the TCP and TCLA. The contribution of the crystal is even more clear if the particle count is weighted with the energy as shown in Fig. 8.4b. In this case, the crystal contributes to almost 100% of the energy deposited in the DS, since practically all lost heavy fragments come directly from the crystal, which is consistent with the black-absorber study.

A certain particle may have gone through the crystal several times before being lost with a crystal interaction through each passage. The plots in Fig. 8.5a show the first and last crystal interaction of each lost particle, where "0" stands for amorphous interaction and "INI" stands for INelastic Interaction with possible fragmentation including also EMD. Please note that the first and last interaction may be one and the same. Here we see that the last crystal interaction is almost 100% inelastic interaction, while in their first interaction inelastic interaction only amounts to a bit more than 60%. This means that the main issue in DS losses come from inelastic interactions and fragmentation, while the particles which have undergone amorphous interactions still have a chance to go through the crystal again. However, it is also important to remember that only particles lost in the DS are investigated here. This is

consistent with results obtained running FLUKA with inputs extracted from the simulations in this thesis [134].

Lastly, most particles lost (approx. 60%) in the DS are both created and lost in the first turn (particles created in the first turn includes also primary particles). Some particles, however, can still circulate in the machine for many turns after exiting the crystal. The second most common turn for losses is the 14th turn. This is most likely due to the fractional tune. Around 84% of their parent particles underwent the amorphous process in the first turn while the rest went through inelastic interaction, and only hit the crystal again 13 turns later. Finally, the two plots suggest that all particles lost in the DS are created and lost in the same turn, in accordance with the expectation that all ions lost in the DS have an effective momentum offset that is so large that they cannot survive the arcs and hence make a full turn before they come back.

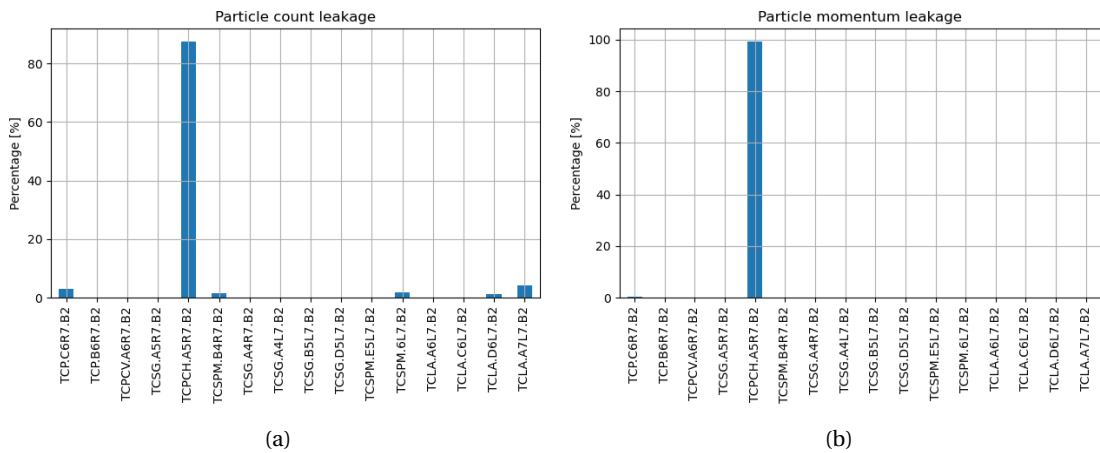


Figure 8.4 – Count of particles that hit a certain collimator as their last collimator hit before being lost in the IR7 DS. Plot (a) is unweighted, and plot (b) is weighted by the particle energy at the DS.

8.2 Sensitivity studies

This section is dedicated to studies related to the sensitivity of crystal collimation performance to various imperfections, in particular miscuts, crystal orientation, impact parameter and collimator imperfections.

8.2.1 Crystal miscut

In the simulations of crystal collimation we usually assume perfectly cut edges in the model of the crystal. However, it is possible that there are small errors so that the upstream edge of the crystal is not perfectly perpendicular to the crystalline planes. As a consequence, there may

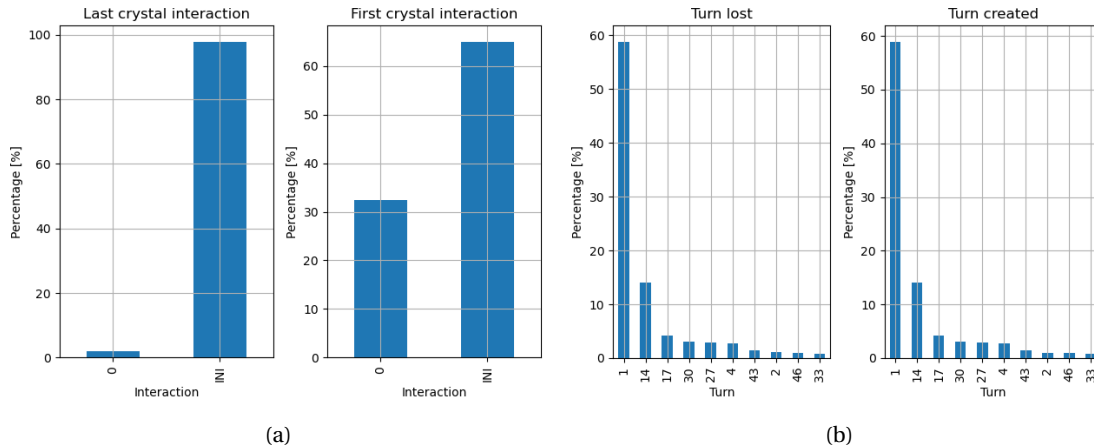


Figure 8.5 – Plot (a): count of the first and last crystal interactions, where 0 is amorphous and INI is inelastic interactions for the particles lost in the IR7 DS. Plot (b): count of the particles lost in the IR7 DS that are created and lost in a certain turn.

be a small non-zero angle, θ_{mc} , formed between the direction perpendicular to the upstream edge and the crystalline planes, as illustrated in Fig. 8.6. This angle is called a miscut angle. Miscut angles can potentially increase or decrease the path a particle travels in a crystal, hence a different final angular kick received. This depends on the miscut angle, impact parameter and crystal length.

Based on previous x-ray measurements [142, 143, 144] done on crystals at CERN, the miscut is typically on the order of tens of μrad and all the presently installed crystals in the LHC have a miscut below $10\mu\text{rad}$ [142]. Hence, simulated miscut angles ranged from $-75\mu\text{rad}$ to $+75\mu\text{rad}$.

When setting up the crystal for machine operation, the crystal is first aligned transversely to have the desired half gap, then the optimal angular orientation is found with an angular scan as described in Chapter 7. In practice this means rotating the crystal until the minimum crystal BLM signal is found, which corresponds to the channeling orientation. With a crystal that has a miscut, the channeling orientation does not correspond to the direction perpendicular to the crystal face and the orientation of the crystal is not parallel to the average beam halo angle. If there is a miscut, the found orientation will then be in a way that it compensates for the misaligned crystalline planes. For a positive miscut, the crystal must be rotated more in the clockwise direction than if the crystal did not have any miscut. This also translates into the longer bent side of the crystal being more inside the beam than the crystal face. Since the impact parameter refers to the depth at which the beam hits an element and should be maintained constant, the impact parameter for a positively miscut crystal must be calculated from the deepest point rather than the crystal edge. A schematic representation of how the impact point and the impact parameter calculation are changed is shown in Fig. 8.6. For a negatively miscut crystal the impact parameter can still be calculated from the crystal edge. The compensation in the crystal orientation is achieved by adding the miscut angle to the

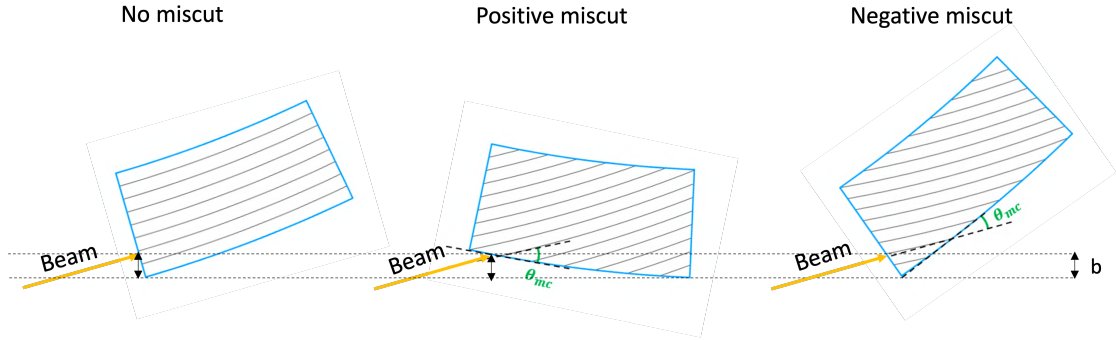


Figure 8.6 – Schematic representation of the change in beam impact point for a bent crystal depending on the miscut value: no miscut (left), positive miscut (middle), negative miscut (right). The yellow arrow represents the beam halo direction, and b is the impact parameter.

existing crystal orientation, i.e. $\phi_{mc} = \phi_0 + \theta_{mc}$, where $\phi_{mc,0}$ is the orientation of the crystal in the machine with and without miscut. A more accurate impact parameter calculation has also been implemented depending on the orientation.

As for previous simulations, to each miscut angle a simulation with a pencil beam of 6×10^6 $^{208}\text{Pb}^{82+}$ primary ions at 6.37 Z TeV is carried out. The crystal used is the TCPCH.A5R7.B2 (old) in Table 4.5. The results are plotted as average DS inefficiencies in Fig. 8.7.

Collimator	IR	Half gap [σ]
TCP.D6R7		
TCP.C6R7		out
TCP.B6R7		out
TCSG.A6R7		
TCPCV.A6L7		5.0
TCSG.B5R7	7	out
TCSG.A5R7		6.5
TCSG.D4L7		5.0
TCPCH.A4L7		6.5
other TCSGs		10
TCLAs		
TCPs/TCSGs/TCLAs	3	15.0/18.0/20.0
TCTs	1/2/5/8	15.0/15.0/15.0/15.0
TCSPs/TCDQ	6	7.4
TCL	1/5	out

Table 8.1 – Collimator settings for B2H Pb ion crystal miscut study at 6.37 Z TeV based on [23] settings.

For all clusters the average inefficiency stays rather constant (the fluctuation in average inefficiency and the error are both approx. 0.02×10^{-4}) independent of the miscut angle. This behaviour is expected as long as the variation in angular kick is small enough that the

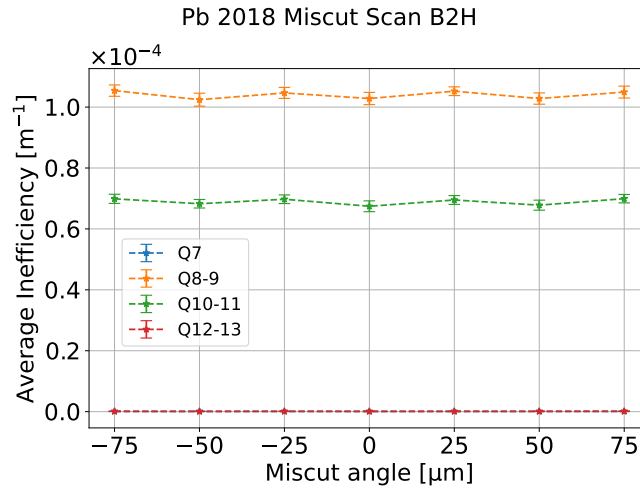


Figure 8.7 – Average inefficiencies of cold loss clusters in the DS region for different crystal miscut values in B2H at 6.37 Z TeV.

channeled particles still impact on the absorber. For both positive and negative miscut angles, with the assumptions of impact parameter stated above, there is a critical miscut angle beyond which the miscut effects of smaller or larger angular kicks may be detected in the rest of the ring, where the difference in angular kick would make particles hit at such a shallow impact parameter on the crystal absorber, or miss the absorber altogether. We can understand the critical miscut angle by approximating the crystal geometry to a parallelepiped. For the negatively miscut crystal, as the miscut increase in absolute value, the distance that the particle travels in the crystal starts from the length of the crystal to gradually larger values until it meets the other edge of the crystal. After that, the path length will start to decrease. This is illustrated in Fig. 8.8. The negative miscut angle that correspond to the maximum distance travelled in the crystal with a set impact parameter is the critical or limiting miscut angle for that impact parameter. The impact on the cleaning performance will then also depend on the difference in collimator half-gap between the crystal and the absorber. For the present settings, the miscut values should be larger than the limiting one, before considerations on whether the channeled particles can still reach the absorber come to play.

For a positively miscut crystal, when the miscut is small is enough, the crystal orientation compensation is also small. Hence, the impact point may still be on the crystal incoming face. As the miscut angle increases, the orientation compensation also increases, until the impact point is exactly on the edge of the crystal. This is the maximum path length possible. With even bigger miscut angles, the impact point will fall on the lateral face. This is the exact same considerations as for the negatively miscut crystal, if we calculate the impact parameter from the outgoing face. A schematic representation is shown in Fig. 8.8.

The critical miscut value is equal to b/l , where b is the impact parameter and l is the crystal length. In the case of $b = 1\mu\text{m}$ and $l = 4\text{mm}$, the critical miscut angle is $250\mu\text{rad}$. The

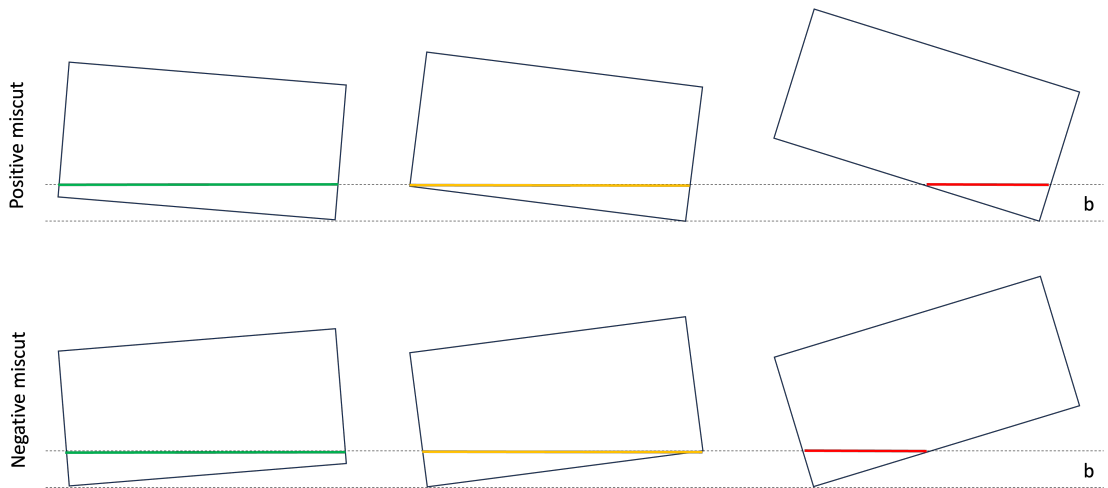


Figure 8.8 – Schematic representation of the particle path length within a miscut crystal (positive – top, negative – bottom) at three different regimes: impact on incoming face (green), impact on edge (yellow), impact on lateral face (red).

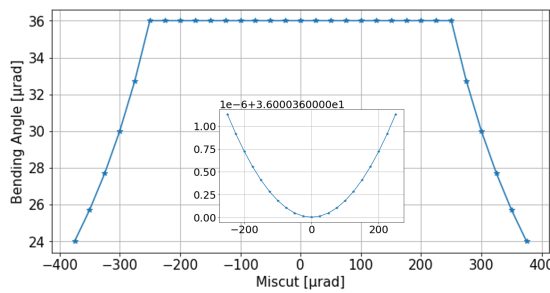


Figure 8.9 – Bending angle of crystals with different miscut at constant impact parameter.

corresponding bending angle, θ_b , would be $\theta_b = \frac{l'}{R}$, where l' is the distance travelled and R is the bending radius. Using simple trigonometry, the evolution of bending angle is calculated and shown in Fig. 8.9. This analytical estimation shows that the change in bending angle for the parameters considered is negligible, as the miscut of all crystals presently installed in the LHC are below $10 \mu\text{rad}$ [142]. Hence, miscuts in crystals are not of great importance unless very large ($\gtrsim 250 \mu\text{rad}$).

8.2.2 Crystal orientation

During operation with crystal collimation it is possible that the beam orientation with respect to the crystal fluctuates over time and exposes the beam to amorphous crystal orientation. Automatic re-alignment tools [145] have been developed to mitigate the crystal drifting out of channeling. However, despite the presence of such tools, it is still advisable to understand the extent of small angular drifts. In this section the effects of these fluctuations in the DS are studied. Small angular offsets from the optimal orientation, ϕ , on the order of the critical

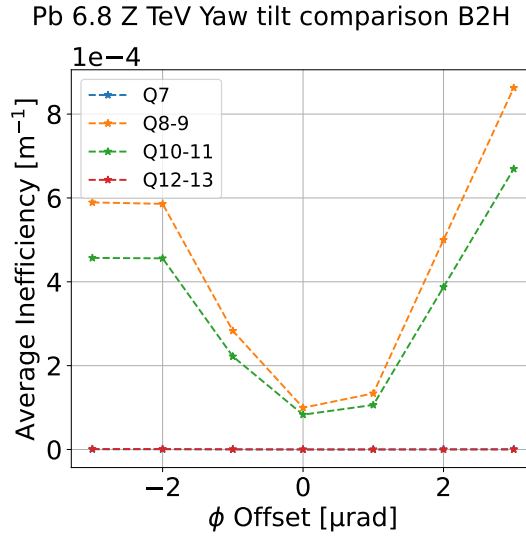


Figure 8.10 – Average inefficiency in the IR7 DS as a function of optimal crystal orientation (ϕ) offset for B2H ion simulation at 6.8 Z TeV. The curve for Q7 and Q12-13 are overlapping.

angle are studied (approximately $2 \mu\text{rad}$). The configuration used is the Run 3 optics with Run 2 collimation settings for B2H *physics* stage for heavy ions 7.8 and the crystal inserted at 4.75σ . 3×10^6 primary $^{208}\text{Pb}^{82+}$ are simulated at 6.8 Z TeV for each offset.

The results are presented as average inefficiencies in the DS region in Fig. 8.10. This simulation resembles the ones done for the angular scan shown in Fig. 7.42. The optimal channeling orientation is at ϕ offset = 0. However, in Fig. 7.42 the losses in the crystal was plotted, while in this section the channeling well is investigated with a finer resolution and the observable is instead the average losses in the DS. By looking at the losses in the Q8-9 and Q12-13 clusters it is possible to notice the start of a plateau associated to the negative angular offsets. This is consistent with the volume reflection plateau seen in Fig. 7.42. There is no plateau on the positive offset side as it is the amorphous side. We can conclude that the performance seen in crystal angular scans is indicative of the performance in the DS. Finally, even within the $\pm 2 \mu\text{rad}$ corresponding to the critical angle, we can expect a cleaning performance fluctuation of up to a factor of 6, which is about enough to cancel out the gains expected from crystal collimation over the standard collimation system. It is therefore very important that the crystal can be kept reliably as close as possible to the optimal channeling orientation all the time in operation.

8.2.3 Collimator imperfections

Conventional collimators may suffer from misalignment errors during beam operation. Two of the most common machine imperfections are studied here: misalignment of the centers and the longitudinal tilt angle of the collimator jaws.

There is a misalignment in the collimator center when the center of the two-jaw system no longer coincides with the center of the beam core. This may happen e.g., due to an imperfect alignment during the setup of the system, orbit drifts with time (during a fill or from one physics cycle to the next), due to small changes in the reproducibility of the machine, etc. It is possible to estimate a possible misalignment with an independent set of readings of the collimator jaw position. These readings are offered by the Beam Position Monitor (BPM)s [146], whose logged signals provide detailed estimates over time of the drift of the centers following the initial alignment. For this study the BPM readings from the 2023 ion run at stable-beam periods with more than 960 bunches were used (sampled every second). In order to stay on the conservative side, misalignments from IR collimators, such as TCTs, have been included in the statistics, although they typically exhibit larger deviations than the collimators in IR7, which are the main driver for the cleaning inefficiency in the IR7 DS. The effect of these imperfections is therefore overestimated.

By computing the standard deviation on the transverse and angular readings of all the available BPMs, it was found that the IR7 collimators equipped have a standard deviation on the alignment of center of $243\ \mu\text{m}$ (Fig. 8.11a) and on tilt angle of $282\ \mu\text{rad}$ (Fig. 8.11b).

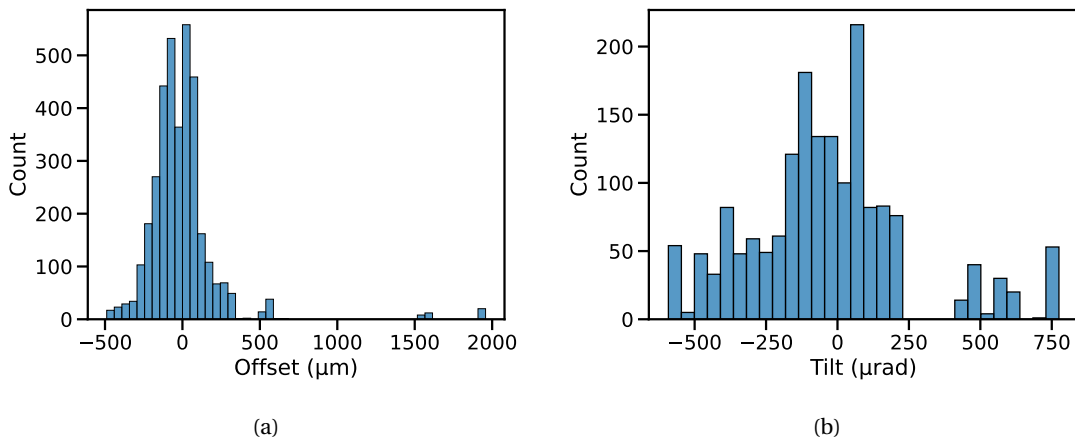


Figure 8.11 – Distribution of misalignment of the collimator system center measured with the BPMs (a) and of the collimator jaw tilt (b) from data collected during the 2023 ion run.

To model the imperfections in the collimator center, random transverse offsets have been generated with a Gaussian distribution that centers around $0\ \mu\text{m}$ and a $\sigma = 243\ \mu\text{m}$. In this way, 15 sets of simulations have been generated from 15 seeds for the B2H plane with Run 3 optics and Run 2 collimator settings (the crystal is set at $4.75\ \sigma$) [22] at $6.8\ \text{Z TeV}$. Each set has 3×10^6 primary $^{208}\text{Pb}^{82+}$. The imperfections have been generated for all collimators except for the crystal, which is still assumed to be the primary collimator, and for which a center error would hence be less important. It is clear that if any drifts in the machine would make another collimator the primary aperture bottleneck of the ring, the full benefit of crystal collimation is lost. Therefore, for operational settings, the $0.25\ \sigma$ margin between the crystal and the

standard TCP should be increased to at least 1σ , since previous studies with protons have highlighted difficulties in maintaining the collimation hierarchy with so small retractions over longer time periods [147].

The modelling of the jaw tilt imperfections is done in a similar manner. The Gaussian distribution used to generate the random tilt angles is centered around $0\mu\text{rad}$ and has a σ of $282\mu\text{rad}$. The results are reported for the center imperfections and tilt imperfections in Figs 8.12a and 8.12b respectively along with the value obtained in the perfect machine without collimator imperfections. Only the average cleaning inefficiencies in clusters Q8-9 and Q10-11 are given, since the losses in the other two clusters are very small.

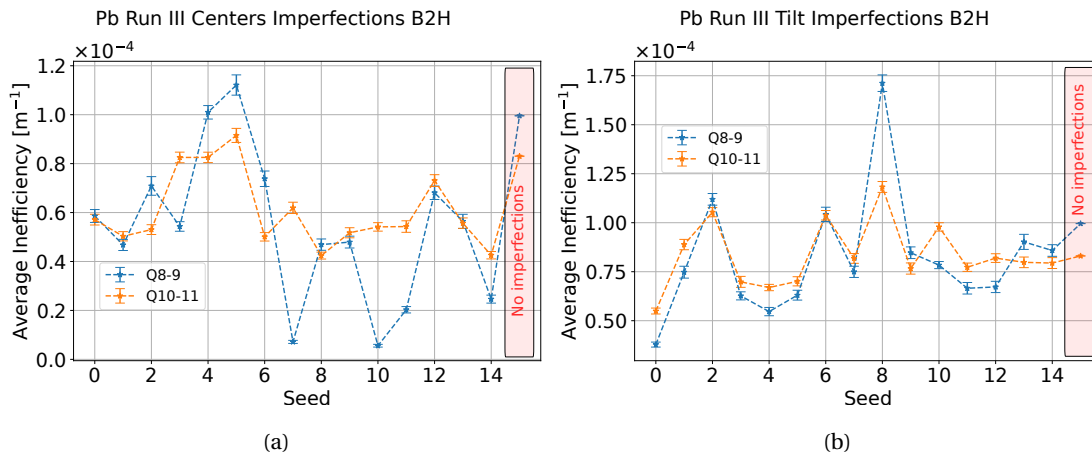


Figure 8.12 – Simulated average inefficiency of DS clusters for different random numbers seeds in collimator center (left) and tilt (right) imperfections for B2H at 6.8 Z TeV. Seed 15 corresponds to the perfect machine without imperfections.

From the plots and the table shown we can see that the simulations of machines with the collimator imperfections considered do not always predict systematic worsening of the cleaning performance, contrary to what is typically found with the standard collimation system [18, 19]. Instead, the average over the studied seeds either oscillates around the perfect case (tilt imperfections) or gives a slightly better cleaning (center imperfections) in the two key DS clusters, Q8-9 and Q10-11, although this is likely a statistical artefact. This is an encouraging result, as it allows us to use simulations to predict the pessimistic scenarios and propose safer operational setups. It may also signify that the crystal system is more robust to imperfections from other collimators with respect to the standard system.

Here, only a couple of collimator imperfections have been explored. The study could be improved by including more sources of imperfection, such as optics and surface imperfections [19]. Furthermore, it could be necessary to investigate the overall effect of all error sources combined, as this scenario may change the conclusions reached in this section.

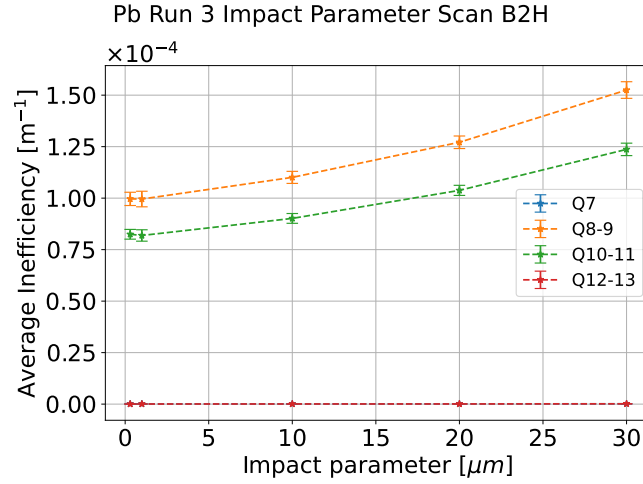


Figure 8.13 – Average inefficiency in the DS of the cold loss clusters represented in Fig. 7.21 for the crystal impact parameter scan for B2H at 6.8 Z TeV.

8.2.4 Impact parameter study

In this thesis work the assumed impact parameter is often $b = 1 \mu\text{m}$ following previous studies [128, 129, 130]. However, the precise impact parameter during operation and during beam tests such as loss maps and angular scans is very difficult to estimate. Moreover, during operations there may be different loss mechanisms, such as orbit movements and beam instabilities that induce larger impact parameters due to, e.g., stronger diffusion of the halo. Hence, in this section, the possible consequences of variations in impact parameter are investigated through an impact parameter scan.

The simulation scenario for the impact parameter scan is the same as the one used in Section 8.1.2 with the B2H crystal inserted at 4.75σ , i.e. 6.8 Z TeV Pb ions with the Run 3 ion optics and *physics* setup. The plane considered is still B2H. The impact values considered range from 0.3 to $30 \mu\text{m}$. The results for the impact parameter scan in terms of average and maximum inefficiencies in the DS are shown in Fig. 8.13.

The resulting average cleaning inefficiency in the clusters at Q8-9 and Q12-13 shows a gradual increase of up to 50% in the studied range of impact parameters, with the worst cleaning at the highest impact parameter. This may be due to the dependency of the interaction rate on the angles of the incoming particles. In these simulations, the crystal is always oriented to match the x' of the particle with the amplitude of $x = N_p$, where N_p is the half-gap of the collimator. However, the larger the amplitude of the incoming halo particle, the larger is the difference in incoming angle with respect to the crystalline planes. Particles with larger oscillation amplitudes and larger angular difference are hence more susceptible to interactions with the lattice and to dechanneling. Since we found in Section 8.1.1 and 8.1.2 that most particles lost in the DS come directly from the crystal, we can hypothesise that the gradual increase we see here is due the increase in interactions between the particle and the material that follows from

angles further away from the optimum angle for channeling, which in turn are a consequence of larger oscillation amplitudes. The increase should continue until x' reaches the critical angle, after which volume processes may take over as in the angular scans. For our case (the crystal at 4.75σ), with a critical angle of $\theta_c \approx 2 \mu\text{rad}$, this would happen at an impact parameter of $b \approx 110 \mu\text{m} \approx 37\%$ of σ_x , where σ_x is the beam size in x .

This result can be compared with impact parameter studies for Pb ions using the standard collimation system, such as the ones presented in [37, 22], which show a very different qualitative behaviour. With the standard system, the losses in the IR7 DS instead decrease with increasing impact parameter. The reason is that ions hitting deeper into the standard primary collimator jaw traverse a longer distance inside it and hence have a higher chance of multiple fragmentation events that would break up the nucleus so much that any surviving fragments have a magnetic rigidity so different from the main beam that they will be lost before reaching the DS.

This comparison highlights a feature that could potentially influence the performance of crystal collimation in the LHC machine. In the LHC, the crystals are aligned angularly using losses created with an ADT excitation. If the diffusion processes for halo particles during strong beam losses in operation would cause significantly larger impact parameters on the crystal, there is a risk that the cleaning performance for strong losses might be worse than with a perfect angular alignment.

This set of simulations shows that the impact parameter plays an important role in crystal collimation, and that it may be worth it to conduct more detailed studies on the most accurate representation of beam diffusion in the future and the most efficient way of commissioning the crystal collimation system for optimal performance with operational losses.

8.3 Configuration optimization

This section is aimed at the exploration of better performing collimation setups using the crystal. In particular, different half gap settings are explored for different types of collimators.

8.3.1 TCLA scan

As seen in Section 8.1.1 and 8.1.2, in order to improve cleaning performance it is needed to block a larger fraction of particles outscattered from the crystal, which may reach the DS. For this reason, the TCLAs have been considered. In previous studies, they were typically placed at 10σ . Here a scan has been carried out through simulations with smaller TCLA half-gaps to assess whether tighter TCLAs can improve cleaning. The apertures range from 10σ down to 7σ . Smaller half-gaps would risk breaking the hierarchy, since the TCSGs are at 6.5σ . Even a 7σ setting is likely too tight for operation, but is nevertheless included in the study for academic purposes.

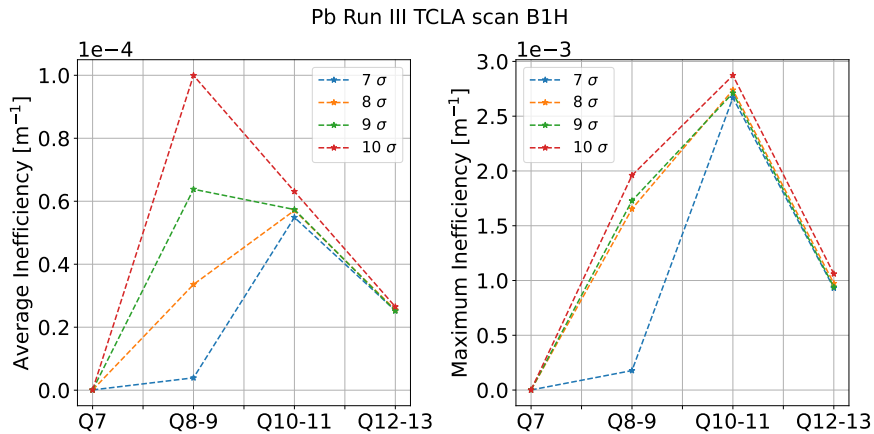


Figure 8.14 – Simulated average (left) and maximum (right) inefficiency in DS clusters for different half-gap settings of IR7 TCLAs (see legend) for B1H at 6.8 Z TeV Pb ions.

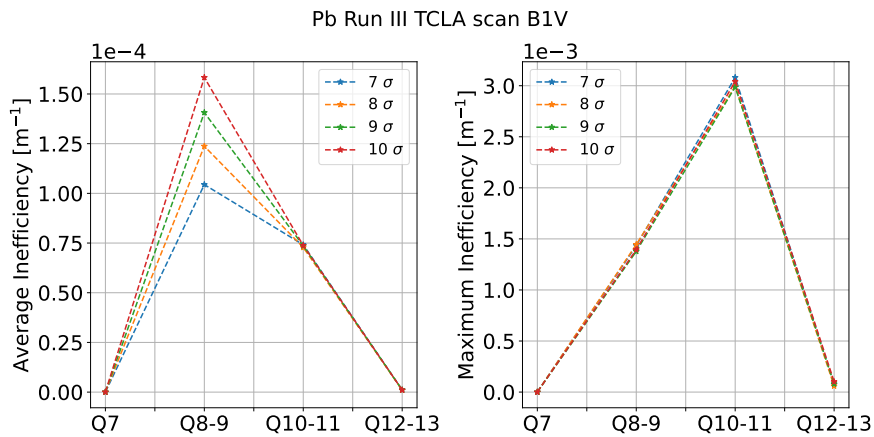


Figure 8.15 – Simulated average (left) and maximum (right) inefficiency in DS clusters for different half-gap settings of IR7 TCLAs (see legend) for B1V at 6.8 Z TeV Pb ions.

The simulation is carried out in all planes and the crystals used are the new ones in Table 4.5. The optics are still the one for ion Run 3 and the collimators are set according the Run 2 *flat-top* stage (see Table 7.8) with the crystals at 4.75σ . 3×10^6 primary ions at 6.8 Z TeV were simulated with an impact parameter of $1\mu\text{m}$. The average and maximum inefficiency in the DS region is plotted in Fig. 8.14, 8.15, 8.16, and 8.17 for B1H, B1H, B2H, and B2V respectively.

For all planes, a tightening of the TCLAs gives a reduction of the losses in cluster Q8-9 when we look at the average values. The maximum inefficiencies are less coherent. This is expected because the maximum is only one point in the loss map and is much less statistically relevant than the average. Hence, we can conclude that if we were to set tighter TCLAs in operations we can expect better cleaning for the cluster Q8-9.

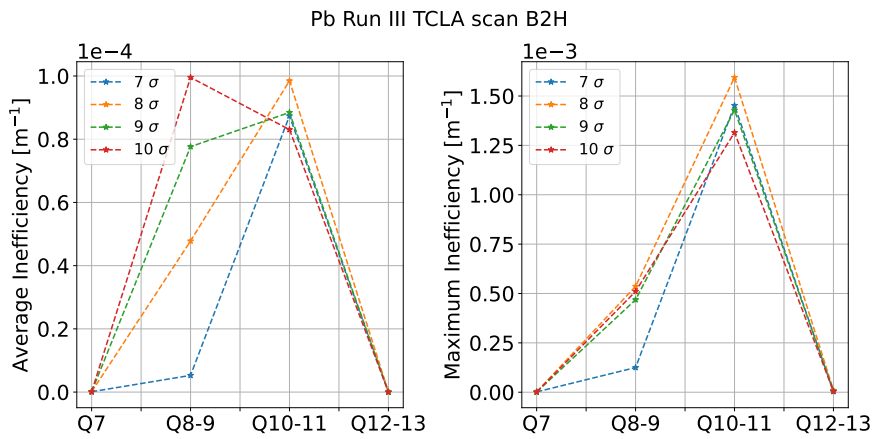


Figure 8.16 – Simulated average (left) and maximum (right) inefficiency in DS clusters for different half-gap settings of IR7 TCLAs (see legend) for B2H at 6.8 Z TeV Pb ions.

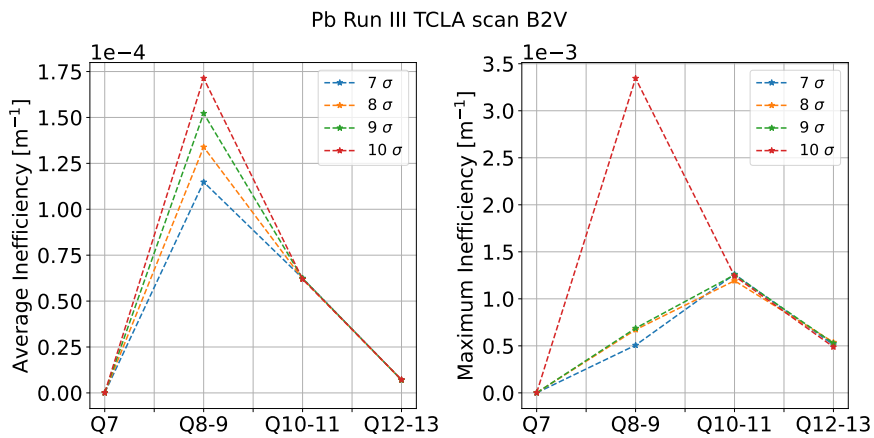


Figure 8.17 – Simulated average (left) and maximum (right) inefficiency in DS clusters for different half-gap settings of IR7 TCLAs (see legend) for B2V at 6.8 Z TeV Pb ions.

8.3.2 Skew TCSG comparison

Chapter 4 explained that the basic principles of crystal collimation consist of having a bent crystal in the channeling orientation with respect to the beam halo and a downstream absorber to absorb the channeled halo. In the vertical plane of the two beams there are two skew TCSGs positioned longitudinally between the crystal and the designated absorber (TCSG.[A/B]5[L/R]7.B[1/2]). The skew collimators do not affect the horizontal planes. It has been seen both in simulation and measurements [148] that they may intercept part of the channeled halo, possibly at shallow, grazing impacts. To illustrate this, the particle trajectory as simulated with MAD-X is shown in Fig. 8.18, together with the collimator openings (crystals at 5σ and TCSGs at 6.5σ) projected onto the vertical plane. A bending of $50\mu\text{rad}$ is chosen as it is the design bending [26]. Trajectories with a $45\mu\text{rad}$ and $55\mu\text{rad}$ bending radius are also shown to allow a margin of error. When the particles are intercepted with a deep enough impact parameter this interference is not an issue, as they are anyway likely to be absorbed. However, when a particle is grazing, it is much more likely to survive and scatter out of the collimator, thus making it difficult to be absorbed at a later stage. Furthermore, the recently added molybdenum graphite coating [74] may be sensitive to energy deposition, and it is preferable to avoid intercepting the full channeled halo on the coating.

Here, a simulation with the SixTrack-FLUKA coupling is done, comparing the current skew collimator setting of 6.5σ and a setting where most of the channeled particles do not hit the skew collimators, found to be 8σ . As for other simulations, 6×10^6 $^{208}\text{Pb}^{82+}$ primary Pb ions at $6.8 Z$ TeV were simulated in the Run 3 *physics* configuration. The collimation setup used is modified according to what was learned in the previous investigations. The modifications include more open TCPs due to the risk of losing collimator hierarchy as explained later in Section 8.5 and tighter TCLAs which gives better cleaning in the Q8-9 clusters. The collimator settings used can be found in Table 8.2. The simulated loss maps of B1V and B2V with the skew collimators at 6.5σ and 8σ are displayed in Figs 8.19, 8.20, 8.21 and 8.22 respectively. A summary plot comparing the average inefficiency of the collimation setup in Run 2, the new setup with tight skews, and the new setup with more open skews is shown in Fig. 8.23 for B1V and B2V.

In the loss maps for B1V the skew collimator losses are the two black bars at around $s = 19895\text{m}$ immediately after the small warm loss cluster. The bar after the skews is the absorber. The losses visibly decrease from Figs 8.19 to 8.20, while the absorber losses increase. This is consistent with previous studies. Studying the losses in the DS, the result confirms the previous hypothesis that there is very little leakage from non-crystal collimators. Overall, the two loss maps do not show any noticeable difference there. More quantitatively, Fig 8.23 shows that the two skew collimator setups give the same average inefficiency. The plot also compares with the collimation setup from Run 2 and the improvement in Q8-9 is due to the tighter settings of the TCLAs. The same considerations can be also made for B2V. We can conclude that from a performance point of view the settings of the skew collimators in the vertical planes do not matter.

During the Run 3 ion beam commissioning, the configurations mentioned in this section have been tested. The data collected on the 23rd of September 2023 with different skew collimator settings show that the difference in half-gap does not influence the level of losses in the DS, consistently with the simulation results presented here. These results are shown for B1V in Fig. 8.24.

Collimator	IR	Skews at 6.5σ		Skews at 8σ	
		Half gap [σ]			
TCPs		6			
TCPCV.A6[L/R]7.B[1/2]		5			
TCSG.B5[L/R]7.B[1/2]		6.5		8	
TCSG.A5[L/R]7.B[1/2]	7	6.5		8	
TCpch.A5[L/R]7.B[1/2]		5			
other TCSGs		6.5			
TCLAs		8			
TCPs/TCSGs/TCLAs	3	15.0/18.0/20.0			
TCTs	1/2/5/8	9.0/9.0/9.0/15.0			
TCSPs/TCDQ	6	7.4			
TCL	1/5	15.0			

Table 8.2 – Collimator settings for the Run 3 optics 6.8 Z TeV Pb ions skew collimator simulations.

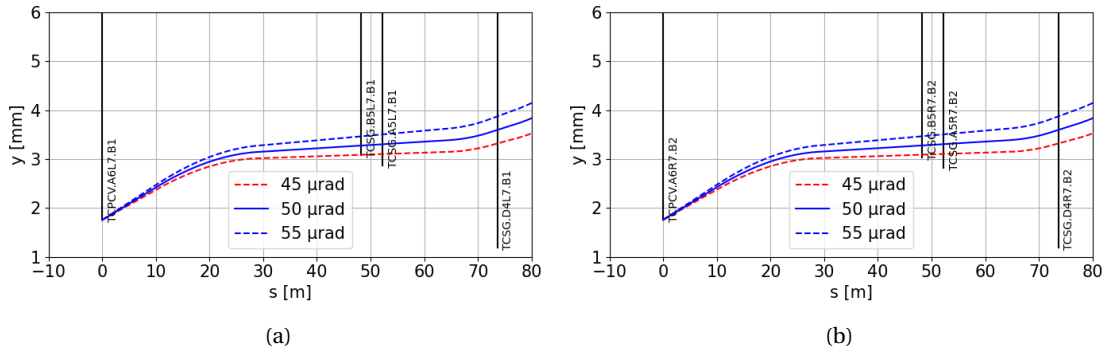


Figure 8.18 – Simulated trajectory of a particle channeled by a $45 \mu\text{rad}$ (red dashed), $50 \mu\text{rad}$ (blue continuous) and $55 \mu\text{rad}$ (blue dashed) at 6.8 Z TeV for B1V (left) and B2V (right) Run 2 collimator settings. Black lines are represent the collimator openings. The skew collimators (TCSG.[A/B]5[L/R]7.B[1/2]) are projected to the vertical plane.

8.3.3 Upstream open

Historically, many measurements were taken with the collimators upstream to the crystal open [32, 33, 29], which made measurement conditions cleaner. In particular, the TCPs are installed upstream of the crystal. After setting the crystal as the primary collimator, the TCPs

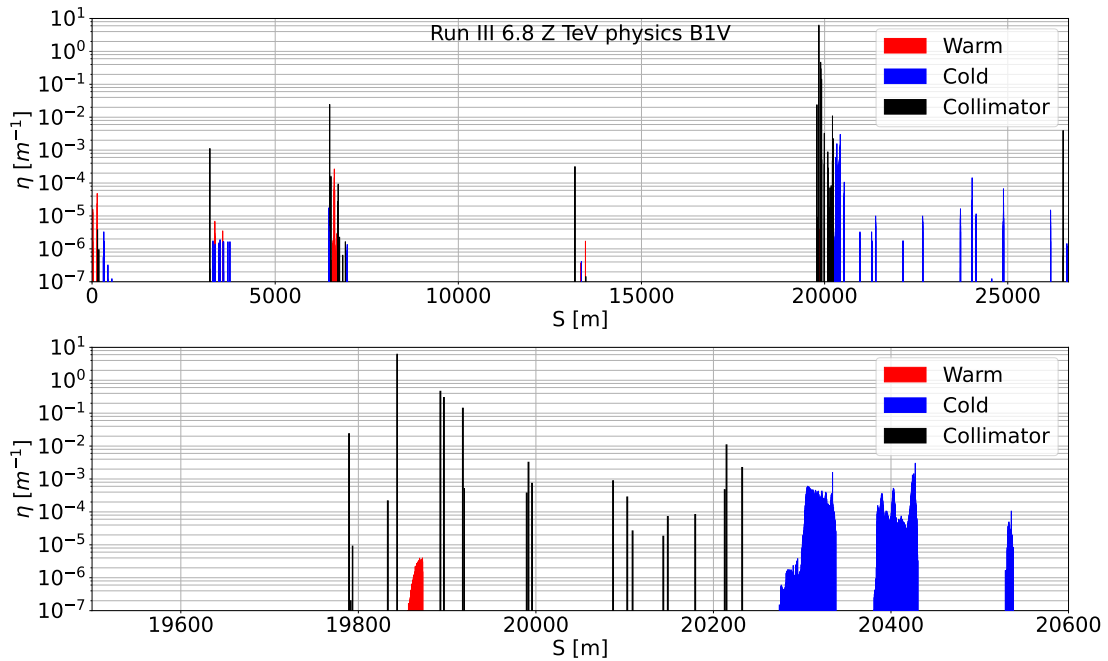


Figure 8.19 – Simulated loss maps of Run 3 B1V with Pb ions at 6.8 Z TeV in the new collimator settings (see Table 8.2) and skew collimators at 6.5σ with their respective zoomed version in IR7 (bottom).

are the closest to it in terms of transverse half gap. It is possible thus that in multi-turn dynamics, particles that have passed the crystal once and come back to IR7 might be scattered by the upstream TCPs instead of hitting the crystal a second time. To find out whether this effect is significant and whether having upstream collimators open improves the cleaning, a simulation comparison is made of the two cases. This is studied for so-called *adiabatic* settings, where the crystal is positioned a quarter of beam σ further in than the TCPs, while all other collimators are at nominal openings.

The scenario chosen is the B2H one used during the 2022 ion tests at *flat-top*. The measurements were performed on the 19th of November 2022. The optics is the one used for protons and can be found in [136] and the collimator settings are as described in Table 8.3. As in previous simulations, a pencil beam of 6×10^6 $^{208}\text{Pb}^{82+}$ primary ions at 6.8 Z TeV was simulated at an impact parameter of 1 μm . The loss maps of the simulations are normalized to the total energy lost in the collimation system. They can be found in Figs. 8.25 and 8.26.

The loss maps obtained from the two setups are very similar. From this we can conclude that there is no cleaning performance advantage from either. Hence, for safety reasons, it may be wiser to keep use the adiabatic setup.

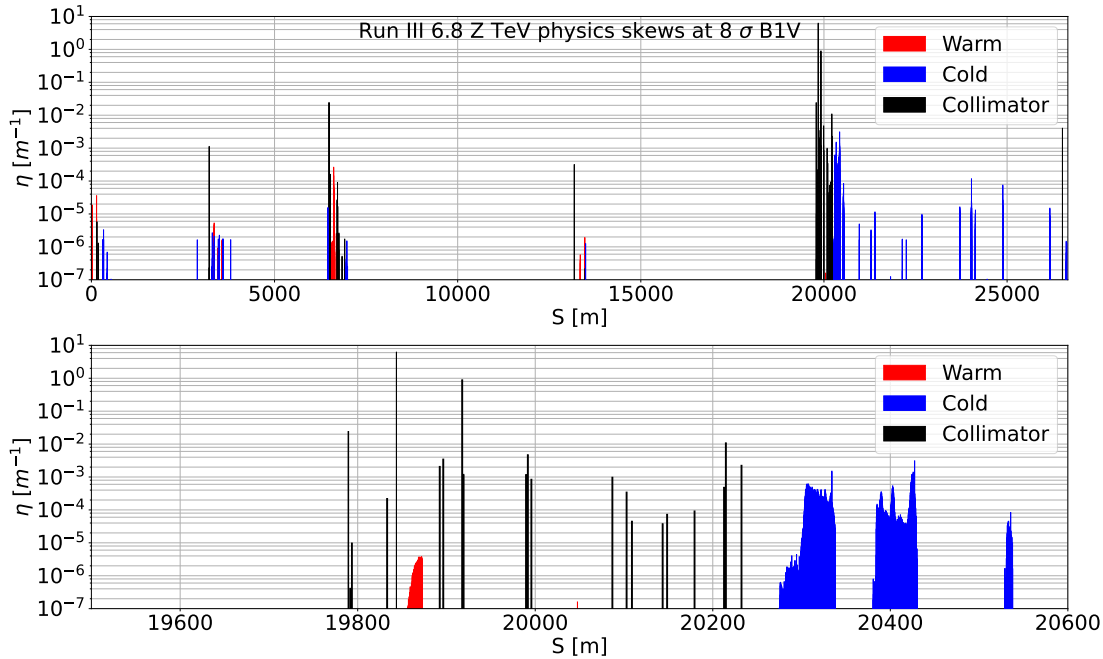


Figure 8.20 – Simulated loss maps of Run 3 B1V with Pb ions at 6.8 Z TeV in the new collimator settings (see Table 8.2) and skew collimators at 8σ with their respective zoomed version in IR7 (bottom).

8.4 Asynchronous dump simulation

The previous studies in this chapter concern the cleaning of beam halo losses in regular operation. The collimation system must protect the machine also in case of fast failures. Since the collimation system must handle also irregular sudden losses [71], in this chapter the effect of the most severe sudden beam loss scenario envisaged, an asynchronous beam dump, is simulated for the first time in the presence of a crystal-based collimation system.

In the LHC, at the end of every cycle, any remaining beam is safely extracted into a beam dump channel and disposed on the beam dump block. Beam dumps may also occur for undesired reasons, such as high beam losses (in which case the BLM system triggers an abort) or equipment failures [149]. The extraction of the beam occurs thanks to 15 horizontal beam kicker modules called MKD in IR6, which should be fired at the same time. No beam is allowed to pass during the rise of the field of the MKDs, and they are hence fired synchronously with a so-called abort gap of $3\mu\text{s}$. No beam is allowed to be injected in the abort gap in the LHC injection schemes. However, certain failure modes exist in which one or several MKDs fire outside of the abort gap, while beam is passing (called *asynchronous* beam dump), or if beam for some reason (e.g. due to RF failures) leak into the abort gap. In those cases, beam particles pass the MKDs when they have an intermediate field and those particles receive intermediate kicks that may not be sufficient to divert them into the extraction channel but large enough to kick them directly onto the aperture or collimators somewhere in the ring [71, 20].

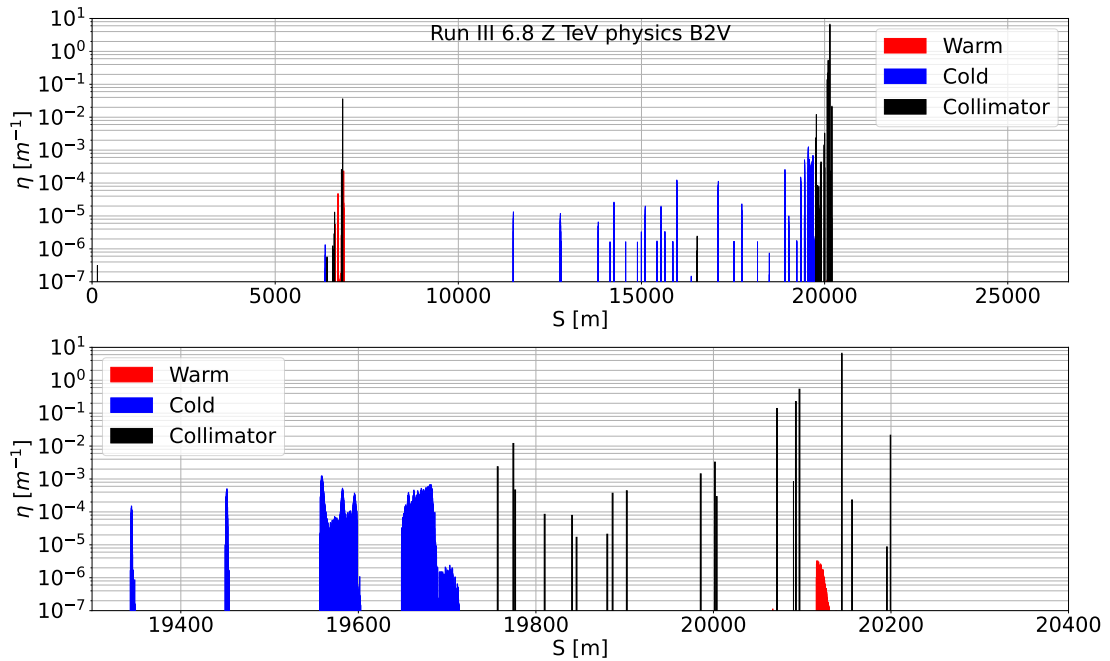


Figure 8.21 – Simulated loss maps of Run 3 B2V with Pb ions at 6.8 Z TeV in the new collimator settings (see Table 8.2) and skew collimators at 6.5σ with their respective zoomed version in IR7 (bottom).

The asynchronous dump mode investigated here is called Single Module Pre-Fire (SMPF), which is the most severe known failure mode. During this process only one of the 15 MKD modules is erroneously fired outside of the abort gap, and a re-triggering system induces the rest to trigger after a delay of around $0.65 \mu\text{s}$. This type of failure has a slower kick strength rise time than if all MKDs fire at once, thus more bunches risk to be kicked with insufficient strengths to be extracted [150]. The SMPF with the slowest kick strength rise time is called SMPF type 2 [151], which is investigated here.

These simulations are very different from other collimation studies, because the full beam core is simulated, and not only the halo as in previous studies. A slow rise of the MKD kicker strength means that each passing bunch will receive a different MKD kick. To reproduce this effect, several simulations are launched, one for each bunch, with different MKD strengths. For each bunch 1.8×10^4 primary particles are simulated using a Gaussian starting distribution. Following the simulation method in [20], using the DYNK (dynamic kick) module in SixTrack [152], all MKD strengths are set to zero on the first simulated machine turn, while on the second turn each MKD is assigned a kick value sampled from the measured time profile of the MKD field during such a failure [151], sampled at the time of each passing bunch. On the third turn, all MKDs are set to full strength, so that any remaining particles are kicked to the location of the extraction channel. For each such simulation, the resulting loss pattern around the ring on collimators and aperture is recorded, and in the post-processing, the losses from each bunch are then summed and weighted by the real expected bunch population in

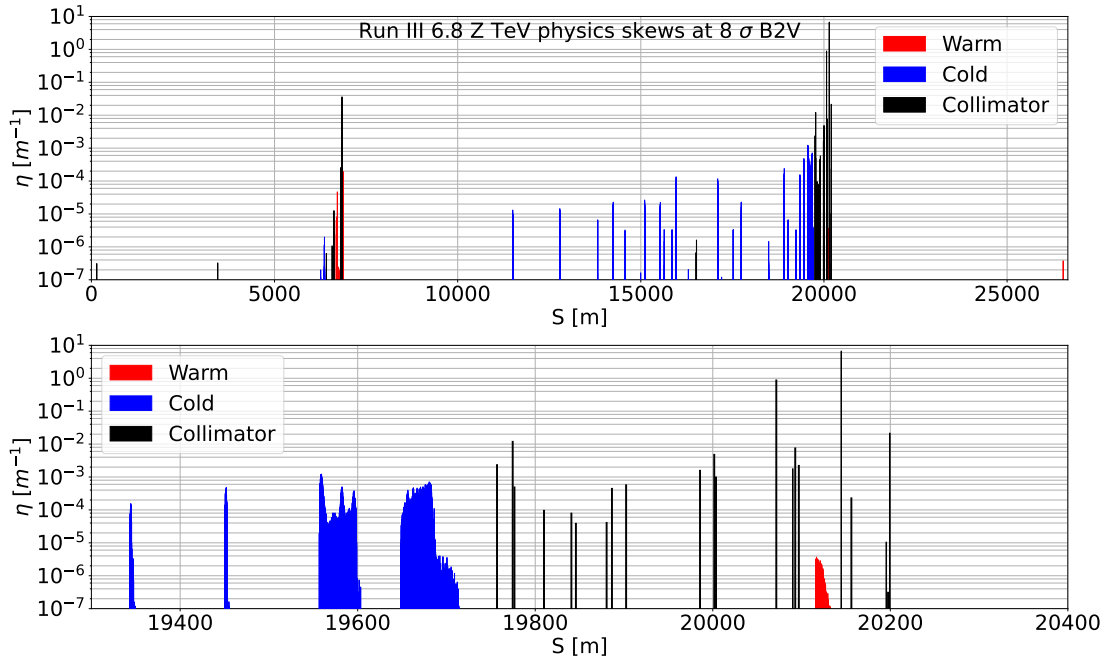


Figure 8.22 – Simulated loss maps of Run 3 B2V with Pb ions at 6.8 Z TeV in the new collimator settings (see Table 8.2) and skew collimators at 8σ with their respective zoomed version in IR7 (bottom).

the LHC. Only a subset of the bunches in the full ring is simulated—31 bunches that either encounter zero MKD kicks, or kicks large enough to reach the extraction channel or the dump septum, do not contribute to the losses around the ring and are hence not simulated. This scenario is simulated for both beams and the effect is only in the horizontal plane.

The simulated machine scenario is one of the proposed setups for Pb-Pb *physics* in Run 3 at 6.8 Z TeV and the collimation settings are listed in Table 8.4. More about the conception of this setup will be presented in the next section.

The summed loss distribution around the ring is shown in Figs 8.27 and 8.28 for B1 and B2 respectively. The result has been normalized by the element length and so that each simulated bunch carries the same energy as a real bunch in the LHC operational scenario, i.e., 1.8×10^8 Pb ions at top energy, meaning that the unit is total energy lost on machine aperture or collimators per unit length. The highest losses in this case are seen in IR6 at about $s \approx 16600$ m, around the extraction channel, which is expected. The warm losses, which are the highest, are in fact made up of particles that would be extracted in the real machine, however, the extraction line is not included in the simulation and there is instead an aperture there which intercepts these losses. There are also high losses on the collimators in IR6. These collimators are the dump protection collimators (TCDQ and TCSP) and they are made to withstand even higher impacting energies that results from similar failures with proton beams. The losses in IR6 are hence expected and not worrying.

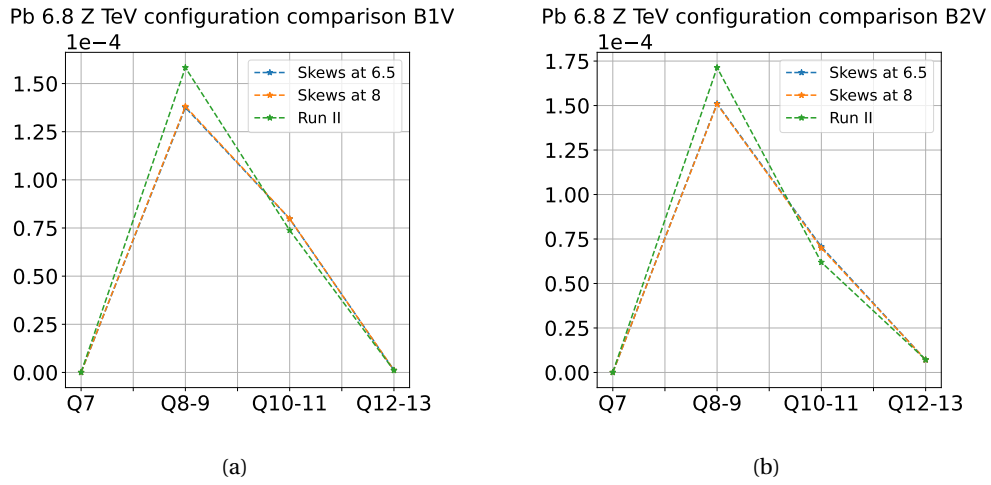


Figure 8.23 – Simulated average inefficiency in the DS for the Run 3 B1V (left) and B2V (right) with Pb ions at 6.8 Z TeV and different collimator setups: new collimation with skew collimators (in Table 8.2) at 6.5 σ (blue), new collimation with skew collimators at 8 σ (orange), and Run 2 *physics* collimation settings in Table 7.8 (green).

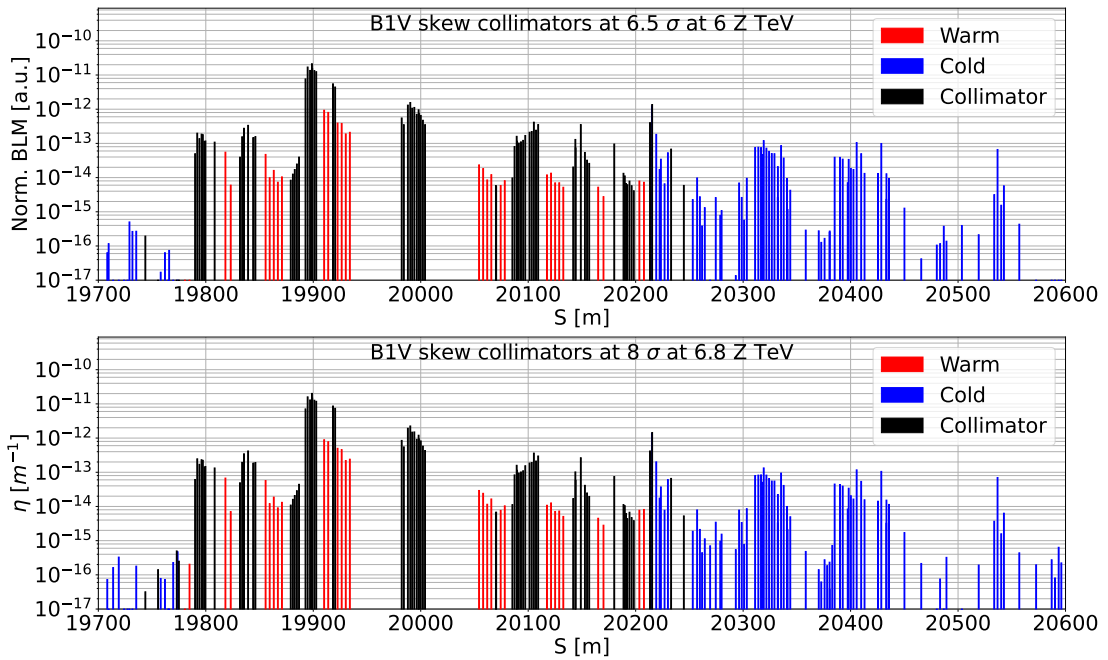


Figure 8.24 – Measured loss map for B1V at 6.8 Z TeV with proposed collimator settings in Table 8.2 and skew collimators (TCSG.[A/B]5L/7.B1) at 6.5 σ (top) and at 8 σ (bottom).

Outside of the beam dump insertion in IR6, the highest total impacting energy per unit length, summed over all bunches, is on the crystal, however, this value has been normalized to the 4 mm length, and in absolute the total deposited energy is around 160 J. On other collimators,

Collimator	IR	Adiabatic settings	Upstream open
		Half gap [σ]	
TCP.D6R7.B2		5	10
TCP.C6R7.B		5	10
TCP.B6R7.B2		5	10
TCSG.A6R7.B2		6.5	10
TCPCV.A6R7.B2			4.75
TCSG.B5R7.B2	7	6.5	10
TCSG.A5R7.B2		6.5	10
TCPCH.A5R7.B2			4.75
other TCSGs			6.5
TCLAs			10
TCPs/TCSGs/TCLAs	3	15.0/18.0/20.0	
TCTs	1/2/5/8	18.0/37.0/18.0/18.0	
TCSPs/TCDQ	6		7.3
TCL	1/5	± 25 mm	

Table 8.3 – Collimator settings for 2022 B2H the 6.8 Z TeV Pb ions with collimators upstream of the crystal closed (adiabatic settings) and open ($\beta^* = 1$ m) [137].

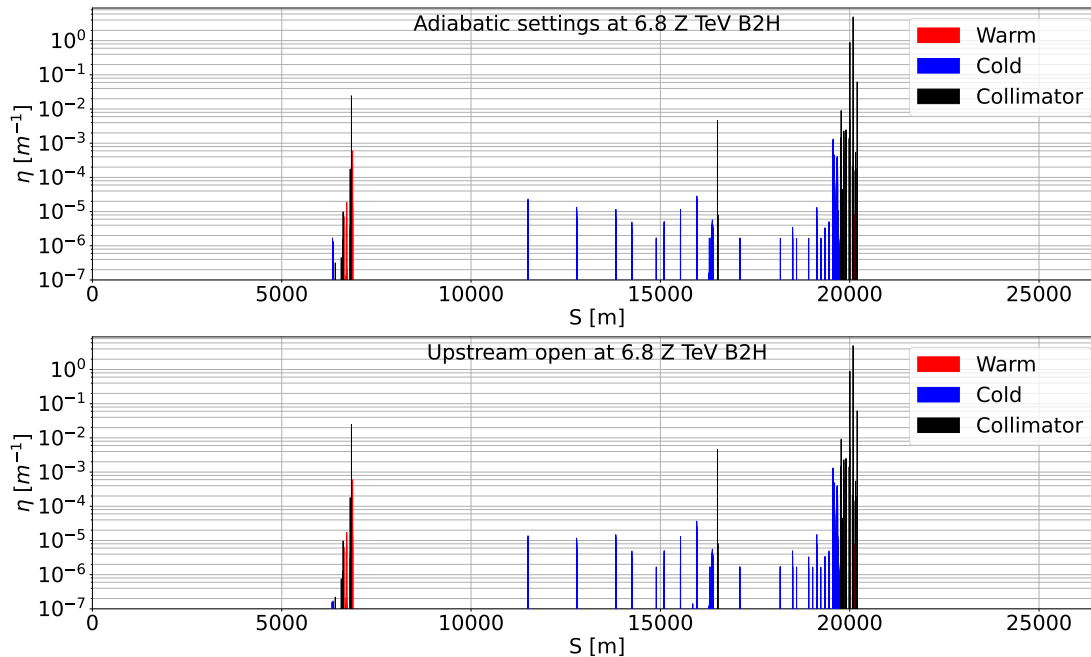


Figure 8.25 – Simulated loss map for the 2022 B2H ion run at 6.8 Z TeV with adiabatic collimator settings (top) and upstream open (bottom).

the total lost energy goes up to around 100 J on carbon collimators and tens of J on tungsten collimators. None of these values are problematic. The most sensitive collimators are the ones

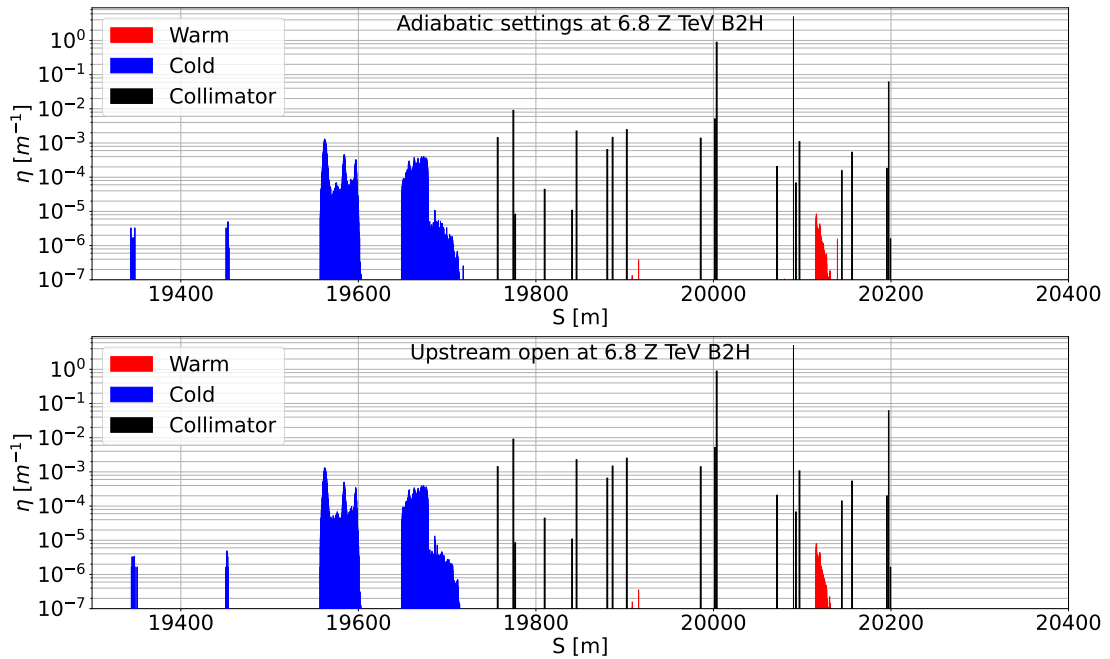


Figure 8.26 – Simulated loss map zoomed in IR7 for the 2022 B2H ion run at 6.8 Z TeV with adiabatic collimator settings (top) and upstream open (bottom).

made of tungsten (TCLAs and TCTs). The onset of plastic deformation for these collimators occurs at an impact of about 5×10^9 protons at 7 TeV [153], which corresponds to about 5.6 kJ impacting energy. The simulated losses are clearly orders of magnitude below this, so there is no risk of damage to these elements in the simulated scenario.

It should be noted that machine imperfections could change the nominal settings used in this simulation, and therefore scans of certain collimator settings have been performed. These scans show also how much the scanned collimator families can be moved in before there is risk of damage and hence how much margin there is in terms of transverse setting.

In Section 8.3.1, different TCLA settings have been tested and a tighter setting seemed to give better cleaning in the DS. With tighter collimator settings the collimators are also more at risk in case of asynchronous dump. With the same simulation setup for the asynchronous dump described above, one simulation has been performed for each TCLA setting. The summed losses over all bunches is shown as a function of the TCLA setting in Fig. 8.29.

As expected, the impacting energy increases with the tightening of the TCLAs for both beam. The most drastic case is for a half-gap of 7σ . The highest total impacting energy, summed over all bunches, is around 300 J/m at 7σ for both beams. Hence, even with the tightest studied setting, the collimators will be safely below the 5.6 kJ damage limit with a very significant margin. Given the risk of orbit drifts over time, it is nevertheless proposed to not go below 8σ setting if the secondary collimators are kept at 6.5σ , due to the risk of hierarchy breakage.

Collimator	IR	Half gap [σ]
TCPs		6.0*
TCSG.A6[L/R]7		7.0
TCPCV.A6[L/R]7		5.0
TCSG.B5[L/R]7		7.0
TCSG.A5[L/R]7		7.0
TCSG.D4[L/R]7	7	6.5
TCPCH.A[4L/5R]7		5.0
other TCSGs		6.5
TCLAs		8.0
TCPs/TCSGs/TCLAs	3	15.0/18.0/20.0
TCTs	1/2/5/8	9.0/9.0/9.0/9.0
TCSPs/TCDQ	6	7.4
TCL 4/5/6	1/5	15.0/15.0/out

Table 8.4 – Proposal 1 of collimator settings for Run 3 Pb ion crystal collimation at 6.8 Z TeV for both beams in *physics* stage. *TCPs for B1 were set to 7σ .

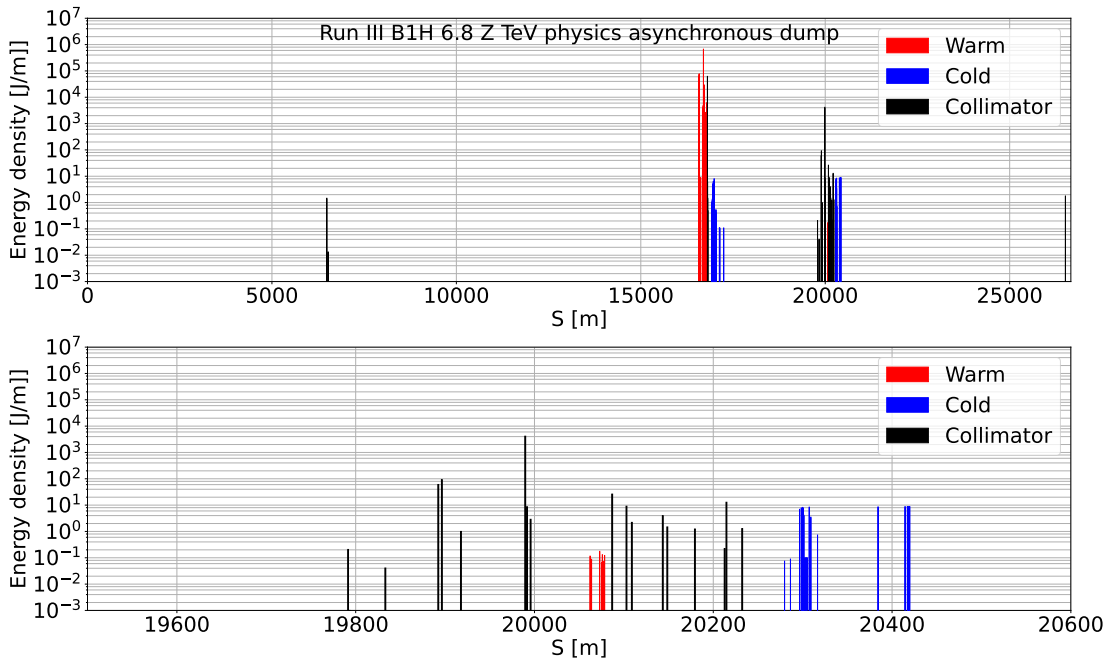


Figure 8.27 – Simulated loss distribution during an asynchronous dump, assuming the scenario of SMPF type 2 for B1, in the machine configuration for Run 3 Pb *physics* at 6.8 Z TeV with Proposal 1 of collimation settings (see Table 8.4).

Lastly, to take into considerations possible damages to the TCTs due to orbit drifts in an asynchronous dump, a similar study as the one done for the TCLAs was carried out. The scanned TCT settings range from 6 to 11 σ . All the other settings are the same as for the TCLAs scan. The total energy deposited as a function of half-gap for the different collimators is shown

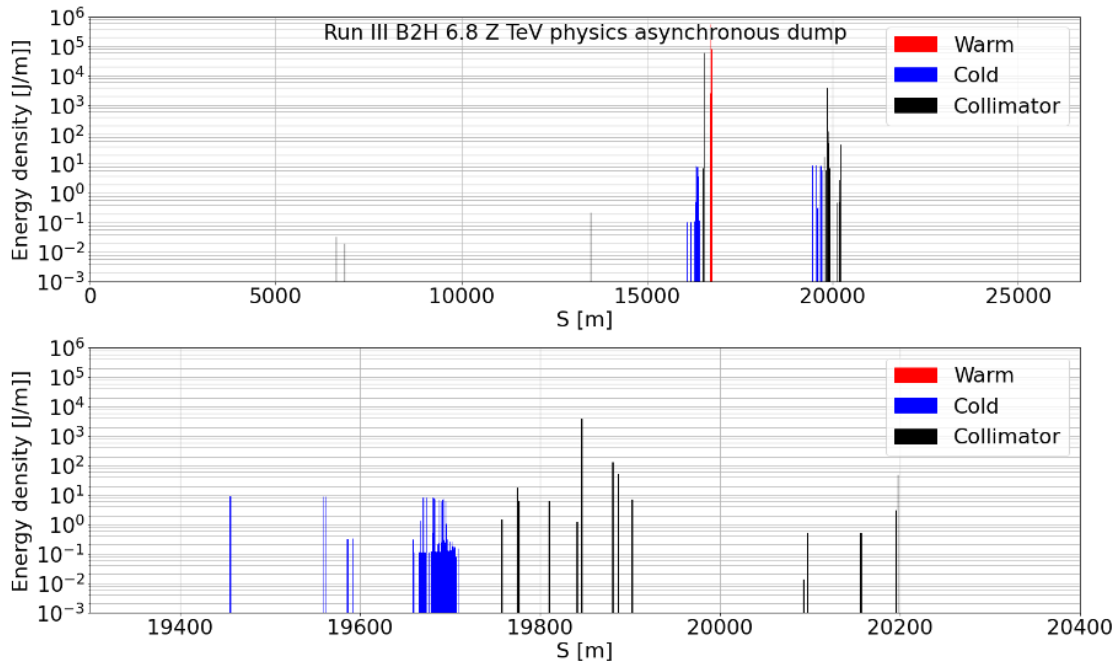


Figure 8.28 – Simulated loss distribution during an asynchronous dump, assuming the scenario of SMPF type 2 for B2, in the machine configuration for Run 3 Pb *physics* at 6.8 Z TeV with Proposal 1 of collimation settings (see Table 8.4).

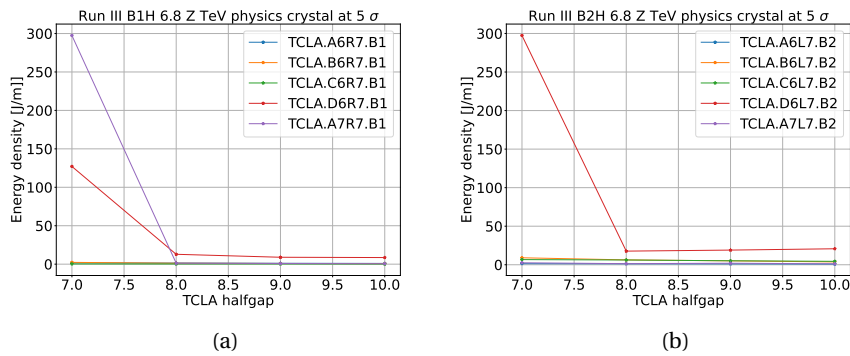


Figure 8.29 – Total energy deposited per meter during an asynchronous beam dump with Pb ions at 6.8 Z TeV on each of the TCLAs, as a function of TCLAs setting for B1 (left) and B2 (right).

in Fig. 8.30. Since the maximum value is around 400 J/m and the damage threshold is the same as for the TCLAs, these losses can also be supported. It is therefore concluded that with the studied collimation settings and optics, there is no risk of collimator damage during an asynchronous beam dump.

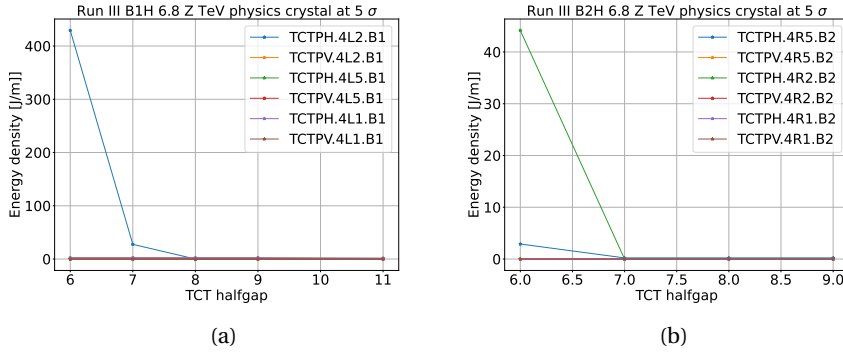


Figure 8.30 – Total energy deposited per metre by all bunches as a function of TCT setting for the B1H (left) and B2H (right) crystal collimation asynchronous dump at 6.8 Z TeV for each TCLA.

8.5 Run 3 Proposed configuration

The final proposed collimation configuration for operation in Run 3 combines the lessons learnt in the previous sections. Starting from the settings used in the 2018 crystal tests, the settings shown in Table 7.8 with the crystal placed adiabatically at 4.75 σ , a few changes are proposed based on the findings in this thesis work and from past experiences. These findings can be summarized as:

- The TCPs are to be set to 6 σ , to minimize the risk of a potential loss of hierarchy, which would mean immediately reverting to the standard collimation.
- The TCLAs can have an opening of 8 σ , as it was seen that with smaller TCLAs half-gaps there is a proportional improvement of the cleaning of the Q8-9 cluster in the DS compared to the previously used 10 σ setting. A half-gap of 7 σ is not proposed in order to leave a margin in the collimator hierarchy.
- The skew TCSGs could be retracted, or kept at 6.5 σ . We choose to keep them at 6.5 σ .

These considerations have led to a proposal for Run 3 settings as defined in Table 8.2.

For the TCTs, it has been considered prudent to keep them as open as possible while still protecting the triplet aperture. They will then intercept less regular and irregular losses, which makes operation more robust and lowers the risk of dumping on the TCT BLMs during lifetime drops. As explained later in this section, more open TCTs also lead to smaller experimental backgrounds. Therefore, it was decided to fix the TCT setting based on the aperture measurements in the beam commissioning. The TCTs in IR2 for Beam 1 were hence opened up to 13 σ to reduce significant losses seen in loss maps. This setting is also beneficial for ALICE experiment background signal (more detail can be found in Section 8.6), the TCTs in IR8 to 15 σ , and the other TCTs to 10.5 σ .

Collimator name	IR	Plane	Half-gap [σ]
TCLs	1/5	H	± 25 mm
TCTs	1/2/5/8	H/V	10.5/13 ^I /10.5/10.5
TDI.4[L/R][2/8].B[1/2]	2/8	V	out
TCLI[A/B].4[L/R][2/8].B[1/2]	2/8	V	out
TCP6[L/R]3.B[1/2]	3	H	15
TCSGs	3	H	18
TCLAs	3	V	20
TCDQ.4[R/L]6.B[1/2]	6	H	7.3
TCSPA4[R/L]6.B[1/2]	6	H	10.3
TCPs	7	S	6
TCPCV.A6[L/R]7.B[1/2]	7	V	5
TCPCH.A[4L/5R]7.B[1/2]	7	H	4.75
TCS[G/PM]s	7	H	6.5
TCLAs	7	V	8
TCLD.A11[R/L]2.B[1/2]	7	H	30

Table 8.5 – Final collimator settings for the 2023 6.8 Z TeV Pb ion run at the stage of *physics*.

Furthermore, based on the commissioning results, the IR6 TCSP was retracted to 10.3σ to reduce losses on the non-critical jaw, which is not needed for protection against asynchronous dumps, similarly to the 2018 configuration.

All the final collimator settings for 2023 operation can be found in Table 8.5.

8.6 Operational experience with crystals in the 2023 Pb ion run

This section gives a short overview of the operational experience gathered with crystal collimation in the 2023 Pb ion run. The commissioning and operational follow-up of the collimation system was based on a team effort, extending beyond this thesis work. Focus is therefore put on the parts for which simulations and studies were carried out as a part of this thesis.

Around the end of September 2023, the ion commissioning was carried out, putting the settings in Table 8.5 in operation. Before high-intensity beams are allowed, loss maps are taken to qualify the cleaning performance. The measured loss maps collected at the *physics* stage were compared to simulations done for this thesis. The Run 3 optics was used, and the collimator settings are as described in Table 8.5. For each plane, 3×10^6 primary $^{208}\text{Pb}^{82+}$ halo particles at 6.8 Z TeV were simulated in a pencil beam. The loss map comparisons between simulations and measurements can be found in Figs 8.31 - 8.38. The level of reproduction by the simulations is comparable to what was observed for the benchmark loss maps in Section 7.3.2.

^I13 only for Beam 1, Beam 2 TCTs set to 10.5σ .

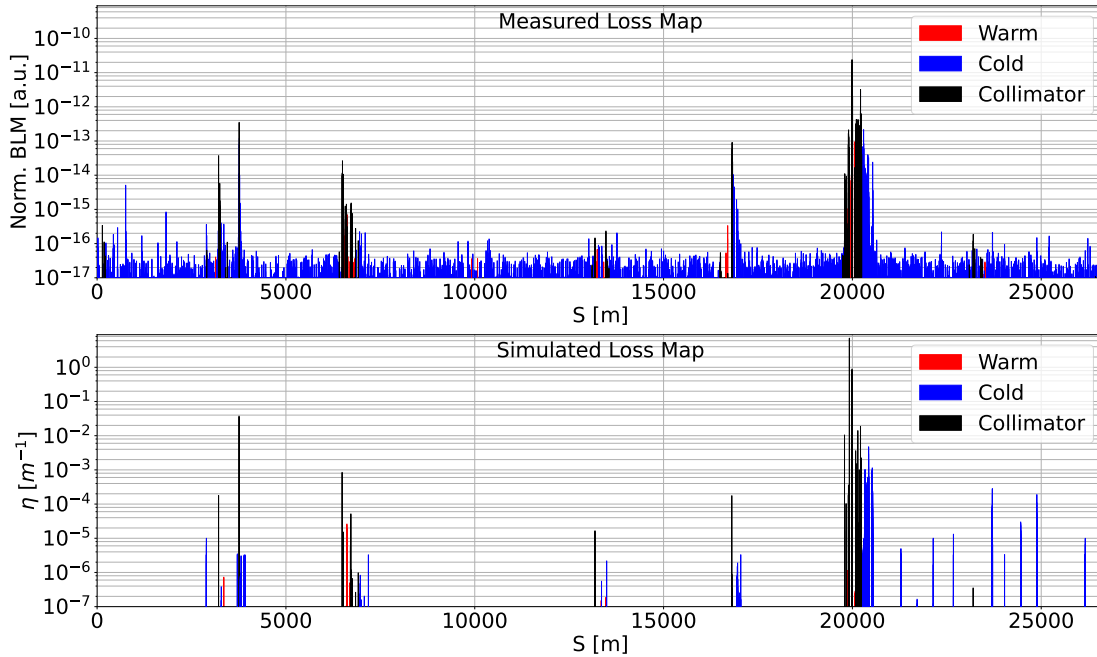


Figure 8.31 – Measured (top) and simulated (bottom) 2023 loss map in B1H with 6.8 Z TeV $^{208}\text{Pb}^{82+}$ and final collision collimation setup (Table 8.5). Measured loss map normalized to total BLM signal can be found in Fig. A.17.

Crystal collimation has demonstrated in the 2023 run a consistent improvement with respect to the standard collimation system, as already observed in the past. This can be seen in loss maps collected at *flat-top*, where both the crystal collimation and the standard collimation setup were tested in the 2023 commissioning. The loss maps at IR7 are shown in Figs 8.39 and 8.40. The cold losses are consistently much lower with crystal collimation for all planes. It appears that for Beam 1 the improvement factors are larger than in Beam 2, with the Beam 2 improvement being more inline with what can be expected from the previous benchmark in Section 7.3.3. This may be due to the fact that the standard collimation for Beam 1 was not optimized in detail during operations in terms of collimator alignment. It should also be mentioned that from Section 7.3.3 we saw that generally speaking improvement factors between crystal and standard system in measurements are not always numerically consistent from one setup to another.

The 2023 ion run has been the first time that crystal collimation was deployed in standard physics operation and at high intensities. In terms of operational stability and global collimation performance, a few events are worth mentioning. During the entire run, heavy losses have been recorded during the energy ramp, especially at the end of the ramp. This limited the increase in intensity at the beginning, but as these losses were not considered dangerous, it was possible to advance and to bypass this issue by changing the threshold of several BLMs, which had correction factors for higher thresholds implemented at flat top but not at lower energies during the ramp.

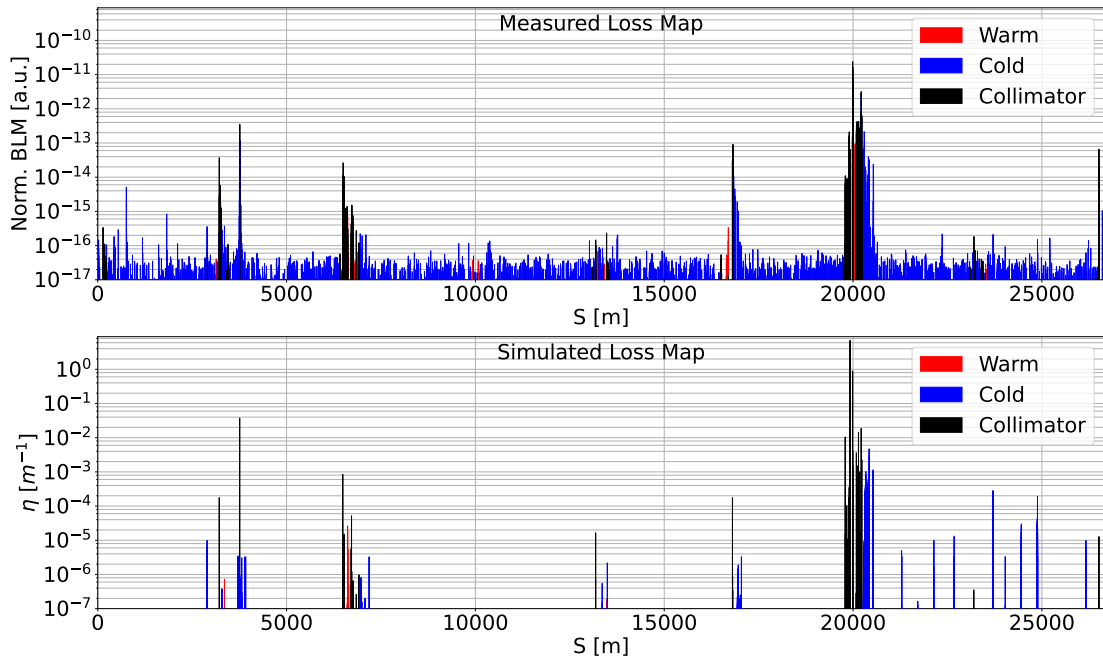


Figure 8.32 – IR7 zoom of measured (top) and simulated (bottom) 2023 loss map in B1H with 6.8 Z TeV $^{208}\text{Pb}^{82+}$ and final collision collimation setup (Table 8.5). Measured loss map normalized to total BLM signal can be found in Fig. A.18.

One of the other problems faced this year was the reappearance of orbit oscillations with growing amplitudes, which would result in fast losses and beam dumps. Since these oscillations have a frequency of around 10 Hz, these special events were dubbed *10 Hz events* [154]. These events were observed also in 2018 [154] and the cause is still not understood in detail, but online analysis by the operation team indicated that they could be induced by vibrations of certain quadrupoles in cells 13L8 and 13L2. It was hoped that with crystal collimation the system would be less sensitive to the 10 Hz events and it is in fact found in offline analysis that crystal collimation was able to withstand larger orbit oscillations and higher losses than the standard system. Nevertheless, 7 beam dumps occurred due to these events. Studies of the cause and mitigations are ongoing beyond the scope of this thesis.

Another problem concerns the stability of the crystal channeling orientation. In the commissioning, the optimal angles were found and programmed into the static functions that the crystal settings follow in every fill. However, the loss patterns observed later in operation seemed to indicate that sometimes beam losses were intercepted in amorphous orientation and not in channeling. The cause of this is not fully understood, as observed drifts of the orbit and angle of the orbit were far below the critical angle. Investigations outside the scope of this thesis indicate that this might be caused by a temperature effect, maybe related to impedance heating. These investigations are still ongoing, but as an intermediate solution, the operations team implemented an automatic feedback that continuously and automatically re-optimized the crystal angle during operation at flat top. This was successfully deployed operationally

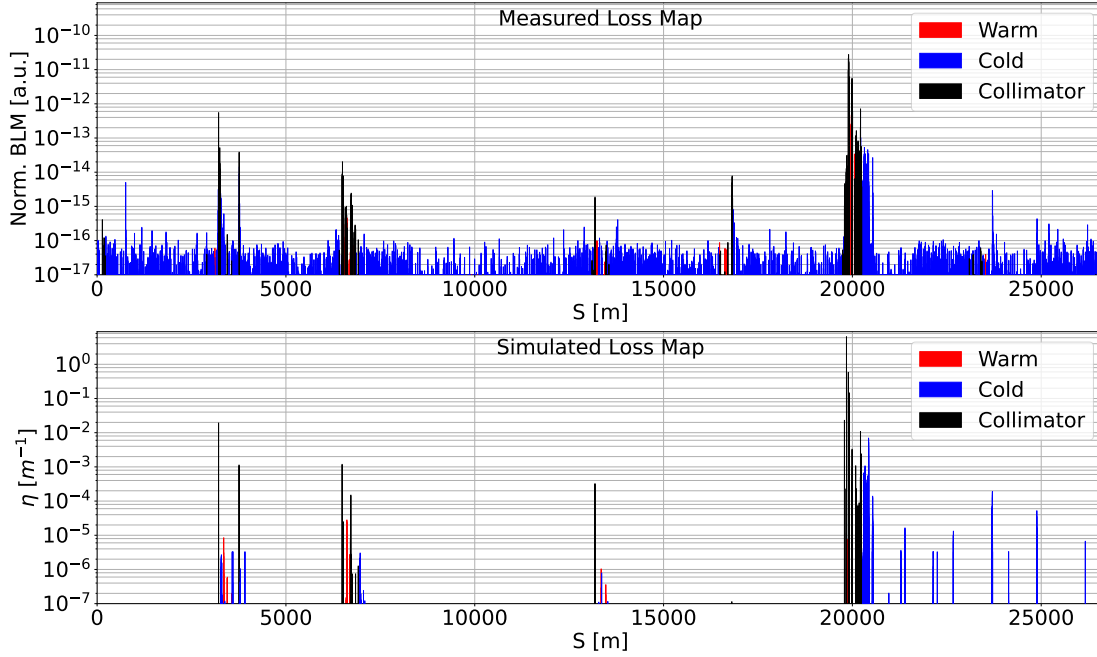


Figure 8.33 – Measured (top) and simulated (bottom) 2023 loss map in B1V with 6.8 Z TeV $^{208}\text{Pb}^{82+}$ and final collision collimation setup (Table 8.5). Measured loss map normalized to total BLM signal can be found in Fig. A.19.

during the second half of the run.

Another problem encountered concerns background at the ALICE experiment. From the start of the physics operation, a strong background signal was detected in the ALICE Inner Tracking System (ITS) and chips in 25% of the acceptance were completely saturated and hence not usable for data taking. This was a serious problem that jeopardized the ALICE physics program and hence needed an urgent solution. Therefore, a campaign of machine studies and simulations was launched, included as a part of this thesis work. Many experimental hours have been dedicated to the identification of the culprit in the losses on ALICE and on finding an appropriate solution. Tests were done by changing some settings while monitoring the background signal online with a low-intensity beam. The tests included among others retracting the TCTs in IR2 gradually, separating the IPs to check if the losses come from the collisions, using collimators in other IRs to observe phase dependency, and more. It was concluded unambiguously that the losses originate mainly from the bottom jaw of the vertical B1 TCT in IR2, TCTPV.4L2.B1, as the background reduced by orders of magnitude when this jaw was opened to parking.

In parallel to the experiments, simulations within this thesis work were run and analyzed. The cleaning simulations indicated that the betatron cleaning of both the horizontal and vertical halo caused significant losses on the bottom jaw of TCTPV.4L2.B1, fully dominated by the isotope $^{207}\text{Pb}^{82+}$, which was created through the loss of a single neutron in interactions with

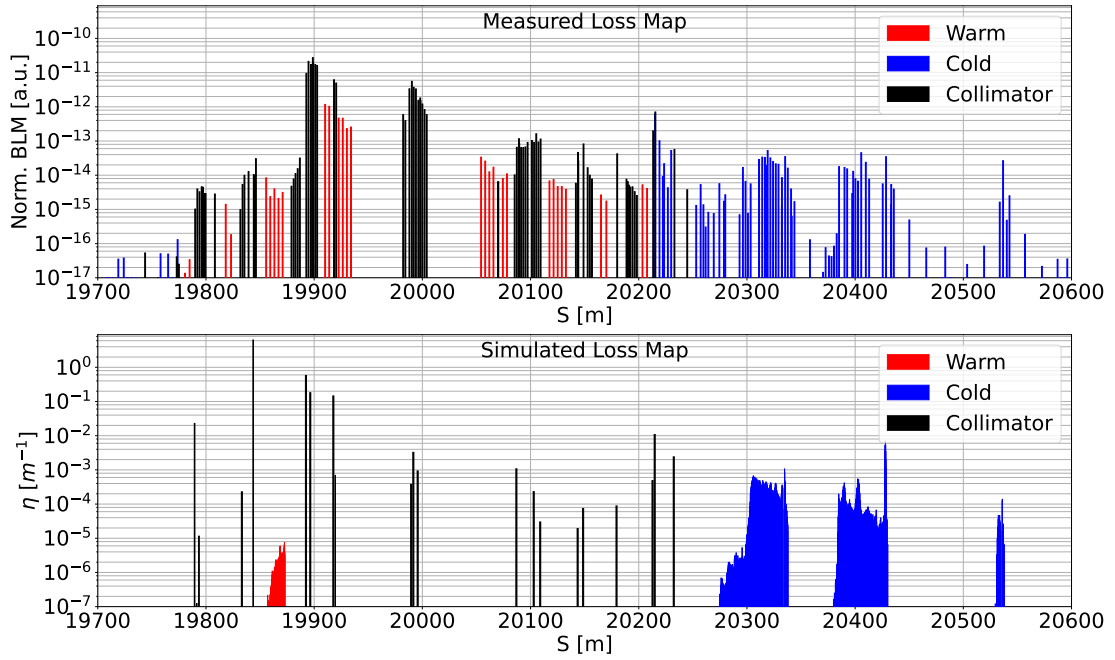


Figure 8.34 – IR7 zoom of measured (top) and simulated (bottom) 2023 loss map in B1V with 6.8 Z TeV $^{208}\text{Pb}^{82+}$ and final collision collimation setup (Table 8.5). Measured loss map normalized to total BLM signal can be found in Fig. A.18.

the crystal collimators. Similar interactions also take place in standard collimators, at an even higher rate since there is no channeling. The dynamics of these ions was further studied using MAD-X. As an example, the trajectory of $^{207}\text{Pb}^{82+}$ exiting the vertical B1 crystal from TCPCVA6L7.B1 to TCPD6L7.B1 is shown in Fig 8.41, while a zoom at IR2 is shown in Fig. 8.42. In fact, there is a phase advance of around 270° which could bring outscattered particles to large amplitudes at the bottom jaw of the TCTPV.4L2.B1.

Once the likely source was identified, a solution could be devised: the excursion of the $^{207}\text{Pb}^{82+}$ trajectory in IR2 could be decreased using vertical orbit bumps in B1 extending through the arcs between IR8, IR1 and IR2. These orbit bumps were designed to reduce vertical spurious dispersion from the crossing angle in IR1 and used in proton operation. The new $^{207}\text{Pb}^{82+}$ trajectory with these orbit bumps activated is plotted in Fig 8.43. From this plot we can see that these particles now escape the TCTPV.4L2.B1. A very strong reduction of losses on this collimator with the bump active was confirmed in measurements. The measurements also confirmed a very strong reduction of the ALICE background in this configuration, which was deemed acceptable for data taking. The bump was therefore deployed in operation for the rest of the run.

It should be noted that with the bump active, the studies showed that the $^{207}\text{Pb}^{82+}$ were instead lost in the horizontal plane on the right jaw of the TCLD downstream of ALICE. An large increase of losses on this collimator was confirmed in measurements. The TCLDs were

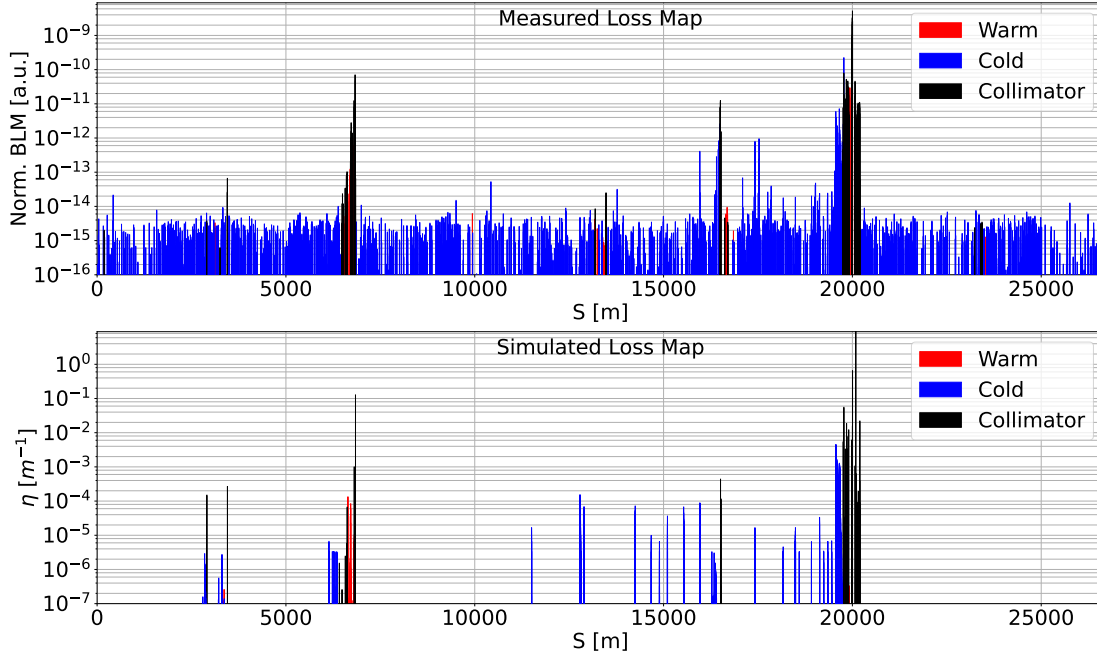


Figure 8.35 – Measured (top) and simulated (bottom) 2023 loss map in B2H with 6.8 Z TeV $^{208}\text{Pb}^{82+}$ and final collision collimation setup (Table 8.5). Measured loss map normalized to total BLM signal can be found in Fig. A.21.

installed to intercept one-electron ions created in bound-free pair production (BFPP) in the collisions, which would otherwise be lost on cold magnets where they would trigger a quench at nominal luminosity [155, 156]. Intercepting the $^{207}\text{Pb}^{82+}$ on the right TCLD jaw was quite problematic, since they instead became the bottleneck for betatron losses and limited the maximum beam loss power tolerable without dump. Since only the left TCLD jaw is used to intercept the BFPP losses, and the right jaw of the TCLD was hit by the $^{207}\text{Pb}^{82+}$ according to the analytical studies in this thesis, it was decided to retract the right jaw only. This proposal was confirmed to be effective in a machine development test on the 18th of October 2023, and successfully implemented in the subsequent operations directly afterwards. In the configuration with the right TCLD jaw open, the $^{207}\text{Pb}^{82+}$ losses are instead intercepted in IR3, where they are not a bottleneck for the cleaning performance.

To conclude, thanks to the simulation framework and the understanding of the source of beam losses, it was possible to solve the problem in a fast and timely manner. This is a further demonstration of the importance for operation of having a well-built simulation framework.

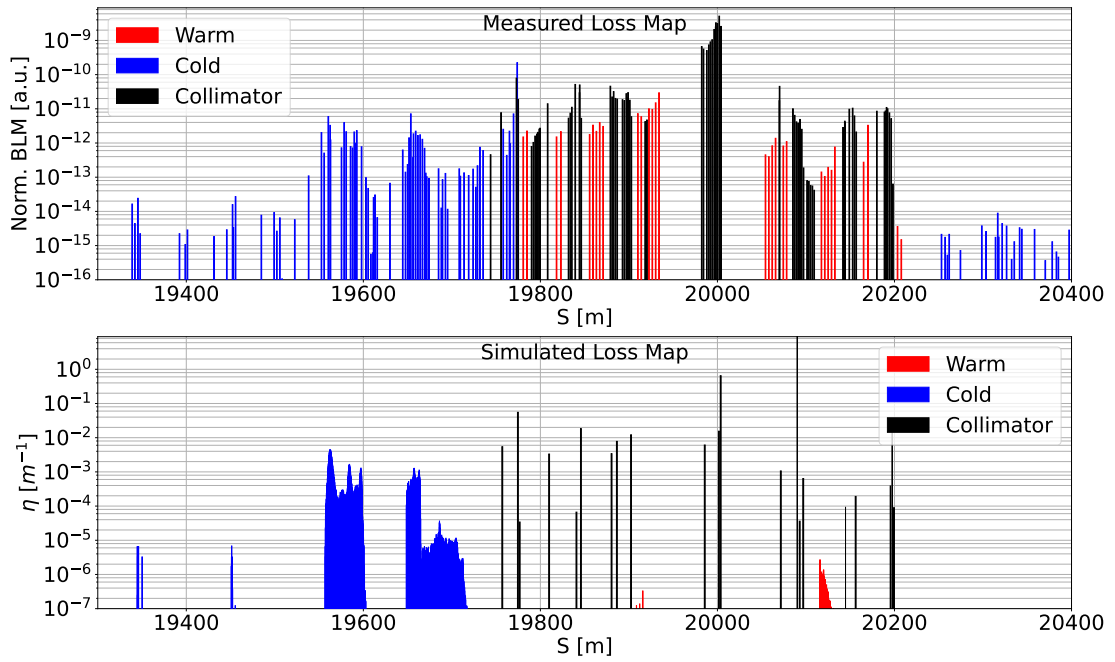


Figure 8.36 – IR7 zoom of measured (top) and simulated (bottom) 2023 loss map in B2H with 6.8 Z TeV $^{208}\text{Pb}^{82+}$ and final collision collimation setup (Table 8.5). Measured loss map normalized to total BLM signal can be found in Fig. A.22.

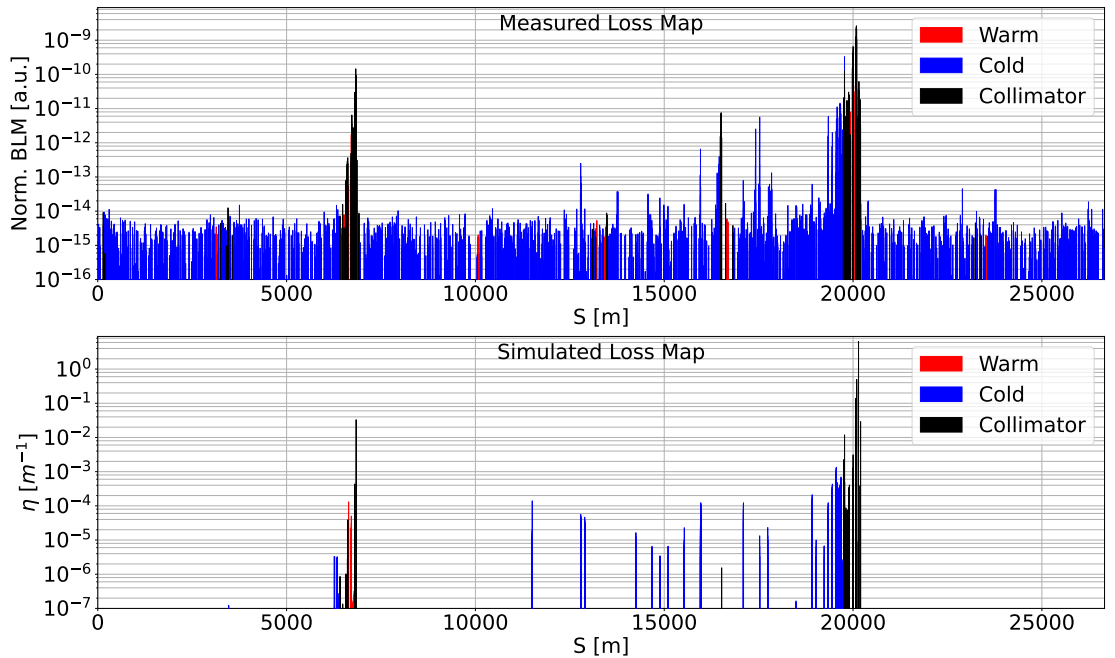


Figure 8.37 – Measured (top) and simulated (bottom) 2023 loss map in B2V with 6.8 Z TeV $^{207}\text{Pb}^{82+}$ and final collision collimation setup (Table 8.5). Measured loss map normalized to total BLM signal can be found in Fig. A.23.

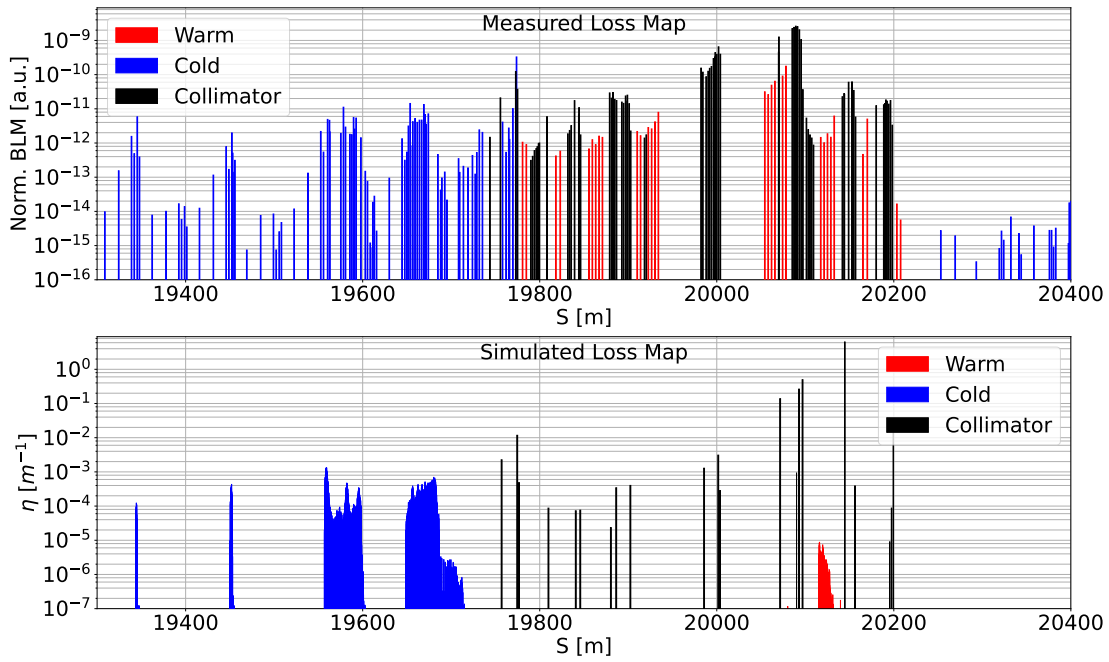
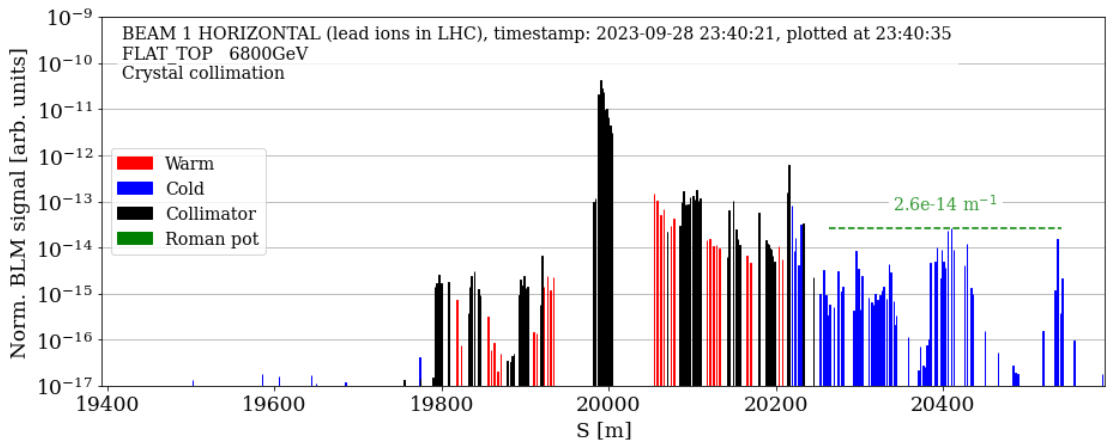
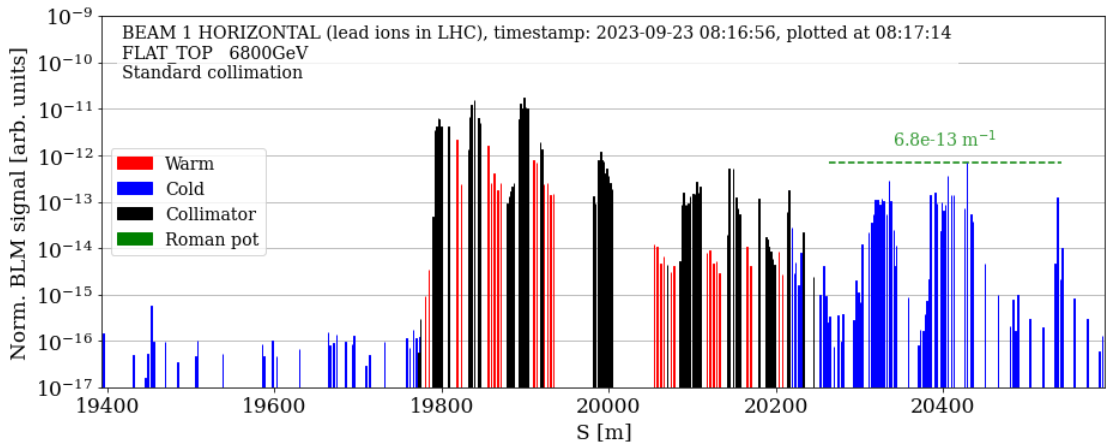


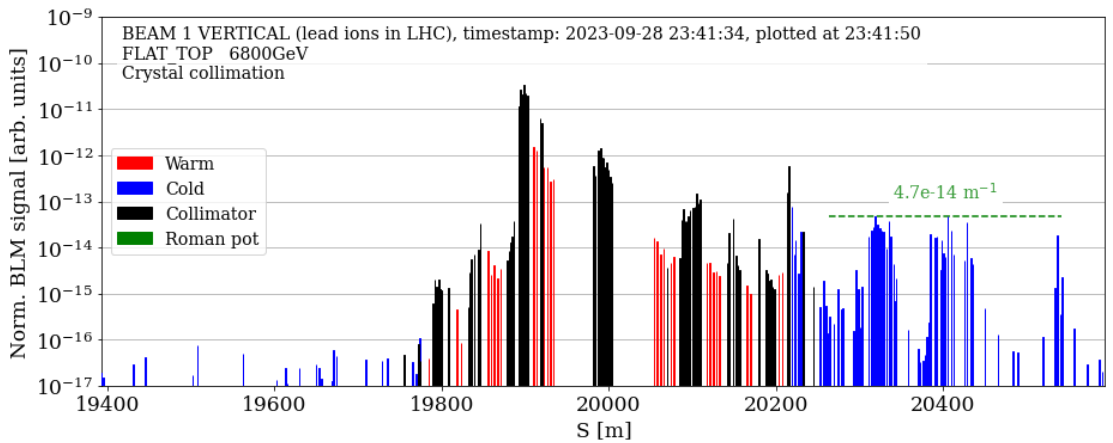
Figure 8.38 – IR7 zoom of measured (top) and simulated (bottom) 2023 loss map in B2V with 6.8 Z TeV $^{207}\text{Pb}^{82+}$ and final collision collimation setup (Table 8.5). Measured loss map normalized to total BLM signal can be found in Fig. A.24.



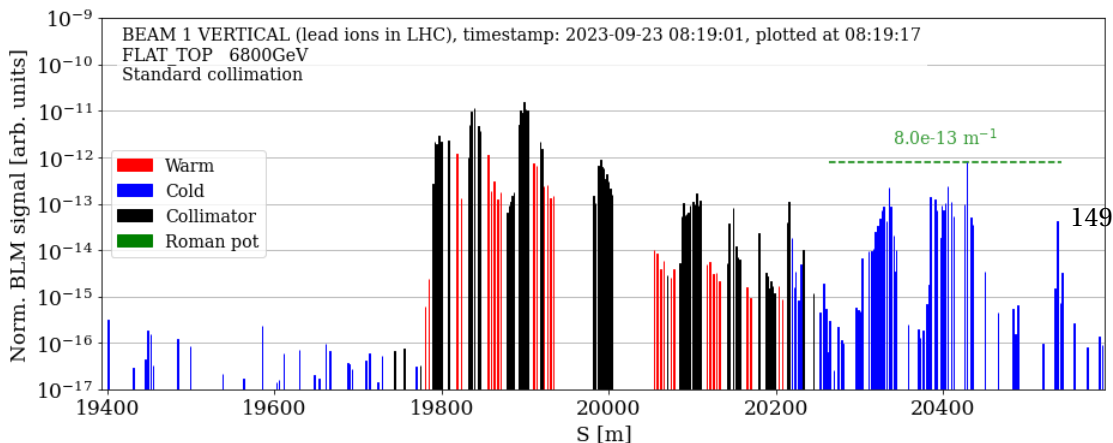
(a)

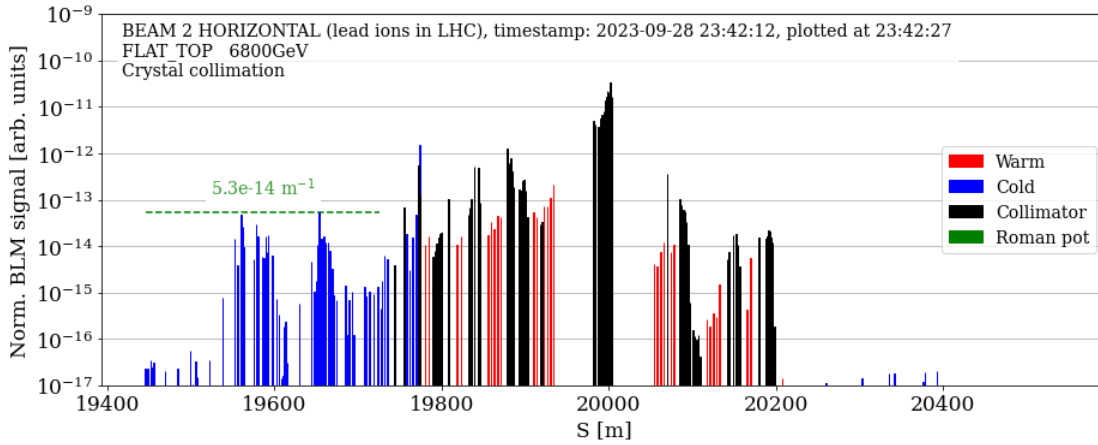


(b)

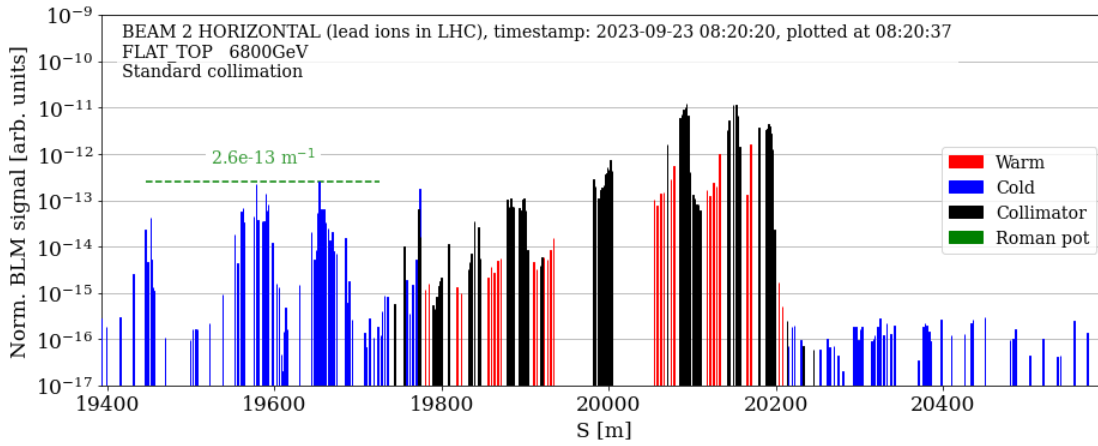


(c)

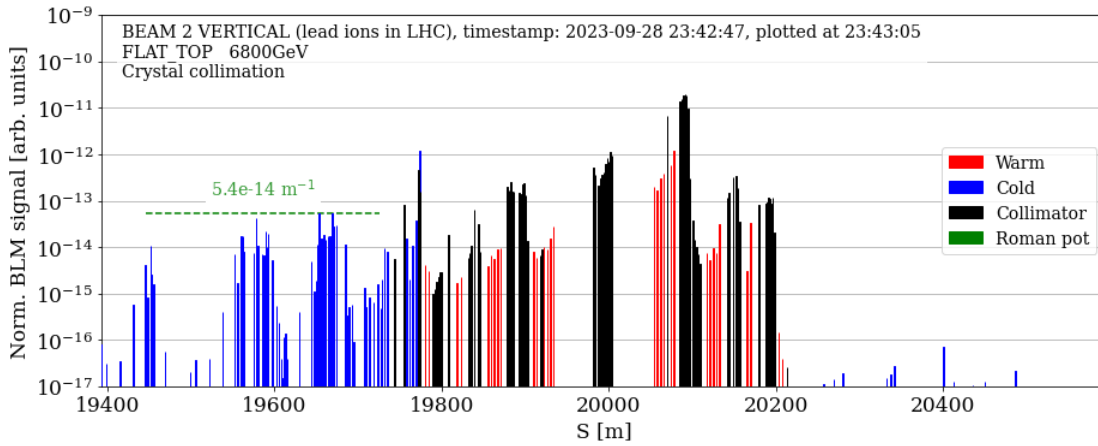




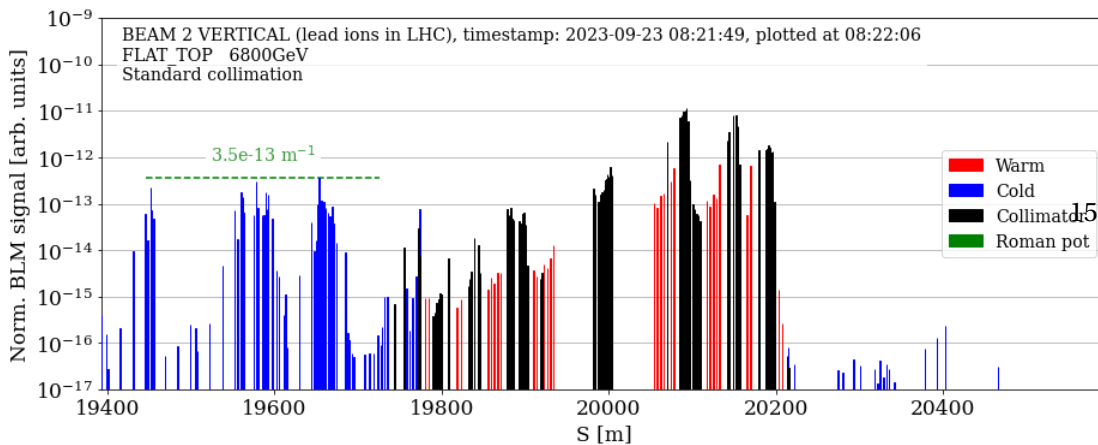
(a)



(b)



(c)



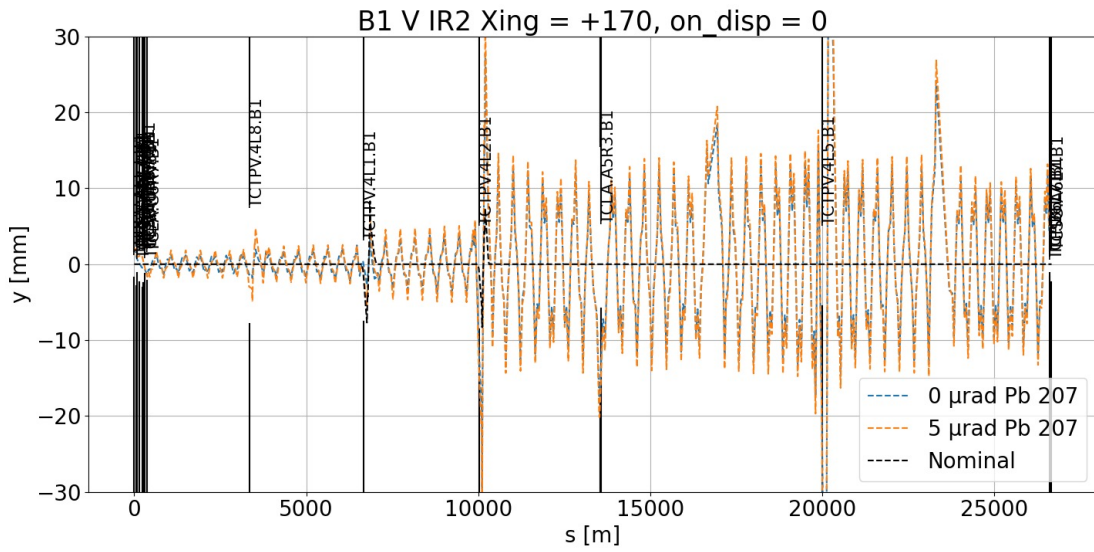


Figure 8.41 – Trajectory in the vertical plane of the B1 nominal particle (black dashed), of $^{207}\text{Pb}^{82+}$ exiting TCPCV.A6L7.B1 with no angular kick (blue dashed), and with an angular kick of $5\ \mu\text{rad}$ (orange dashed). The trajectory ranges from TCPCV.A6L7.B1 to TCP.D6L7.B1. The vertical black bars represent the collimator jaws along the ring.

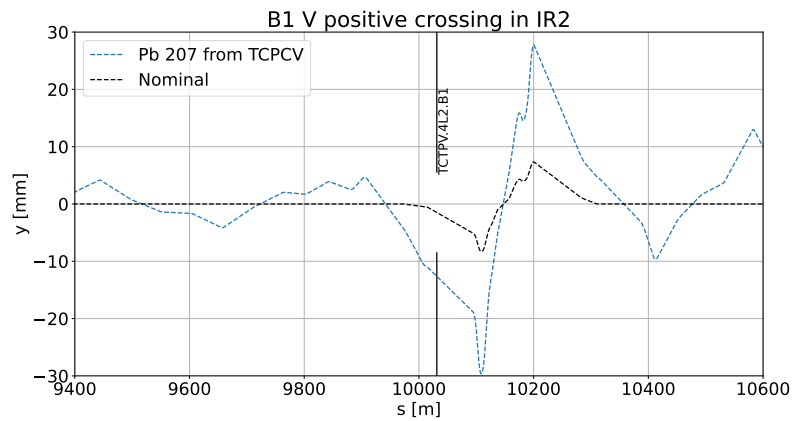


Figure 8.42 – Trajectory of the B1 nominal particle and $^{207}\text{Pb}^{82+}$ in the vertical plane around IR2 exiting TCPCV.A6L7.B1 with no angular kick.

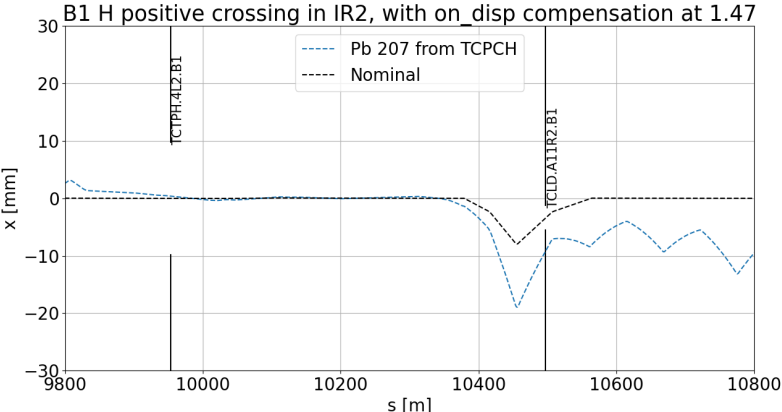


Figure 8.43 – Trajectory of the B1 nominal particle and $^{207}\text{Pb}^{82+}$ in the horizontal plane around IR2 exiting TCPCV.A6L7.B1 with no angular kick.

9 Standard ion collimation optimization

Part of the thesis work is devoted to further studies of the use of the standard collimation system with ion beams. The motivation is to study a backup scenario in case of unexpected problems with the crystal system. This chapter lays out the results of these studies.

9.1 Standard system ion impact parameter scan

An impact parameter scan was done with the standard system as for crystal collimation. This kind of study has already been done for the standard ion collimation system with the HL-LHC configuration in Chapter 8 of [37]. However, it was done for a previous optics and collimation setup, and as a starting point for the subsequent studies it is important to verify the impact parameter dependence and to identify the most critical impact parameter.

The simulation setup uses the 2018 ion optics and the collimation configuration at *physics* stage shown in Table 7.8, which is almost identical to the Run 3 and presumed HL-LHC ion configuration. A pencil beam of 6×10^6 $^{208}\text{Pb}^{82+}$ primary ions was simulated for B2H. The results are reported as average and maximum inefficiencies in the DS in Fig. 9.1.

The overall conclusion is that an impact parameter of $b = 1 \mu\text{m}$ gives the highest leakage of losses to the cold magnets, which is the same result as obtained in the previous study [37]. The reduction in losses with $b > 1 \mu\text{m}$ is due to the fact that the beam is convergent at the collimator and the larger is the impact parameter, the larger is the distance traversed. With a longer path in the material there is a higher chance of multiple interactions including nuclear fragmentation, which may lead to either an absorption in the primary collimator or outscattering of lighter fragments only, with a very large change in magnetic rigidity. Generally, the closer the magnetic rigidity is to that of the main beam, the more likely it is to travel far and escape the downstream collimators to end up in the DS. Therefore, lighter fragments resulting from multiple fragmentations are typically lost in the collimation insertion upstream of the DS and therefore do not contribute to the cleaning inefficiency on the cold magnets.

On the other hand, the reduction in losses with $b < 1 \mu\text{m}$ is due to the fact that an increasing

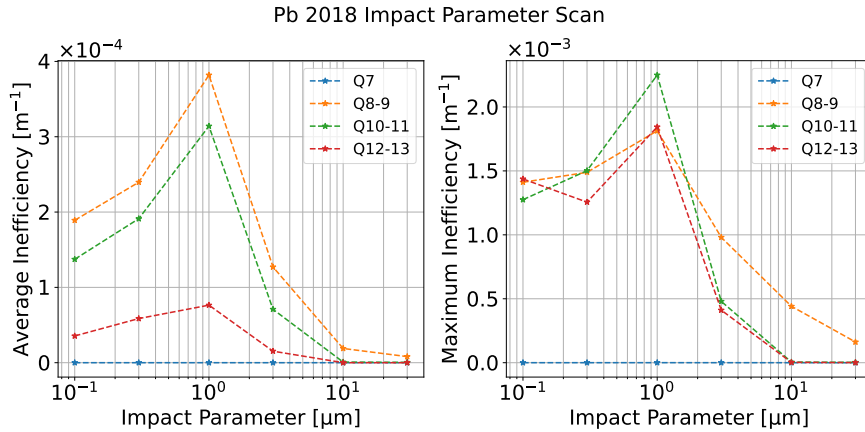


Figure 9.1 – Average and maximum inefficiency in DS for a B2H impact parameter scan of standard collimation without crystal at 6.37 Z TeV.

fraction of ions does not undergo any nuclear fragmentation on the first passage through the collimator, due to the short path length. On the other hand, they are always subject to ionization energy loss and multiple Coulomb scattering, which give small kicks in energy and angle. Therefore, these ions hit deeper in the primary collimator when they come back on a sub-sequent turn, leading to a higher chance of multiple fragmentation events and therefore less leakage to the DS. This explains the local maximum of the cleaning inefficiency at $b = 1 \mu\text{m}$.

It is worth remarking that the level of the standard collimation average loss at Q8-9 with large b (e.g. $b > 1 \mu\text{m}$) is smaller than the average loss at the same cluster with crystal collimation. Hence, it would be best in theory to use crystal collimation for small impact parameters and the standard collimation for large impact parameters, although this is of course not possible in practice.

9.2 Single jaw collimation performance

In the 2018 machine development tests, one of the ideas was to see whether having only one of the two horizontal primary collimator jaw operating would give a better cleaning. This test was done on the 9th of September 2018 with 6.37 Z TeV Pb ion beams. The collimation setup for both beams followed the one for 2018 *physics* (Table 7.8) with one of the two TCP jaws opened to 10 mm at a time. Since an improvement in cleaning was observed in some cases with only one jaw active, a study was proposed to check whether this behavior is also predicted in simulations.

The jaws in the ring are referred to as "left" and "right" with respect to the direction of travel of the beam. The same configuration used in the data taking (i.e. Run 2 optics in *physics* with the collimator settings in Table 7.8) is used in simulation and the initial distribution had 6×10^6

$^{208}\text{Pb}^{82+}$. The loss maps have been plotted for the cold losses only in Figs 9.2 and 9.3. The full measured loss maps are in Figs. 9.4 and 9.5.

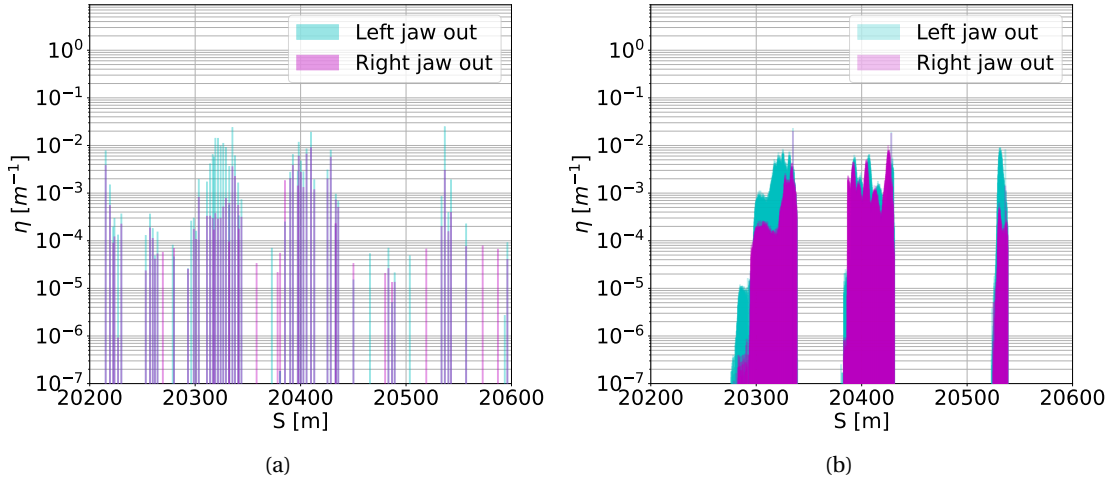


Figure 9.2 – Measured (left) and simulated (right) single jaw (left jaw out – turquoise, right jaw out – fuchsia) standard collimation loss maps at IR7 DS for B1H in the 2018 *physics* configuration with Pb at 6.37 Z TeV.

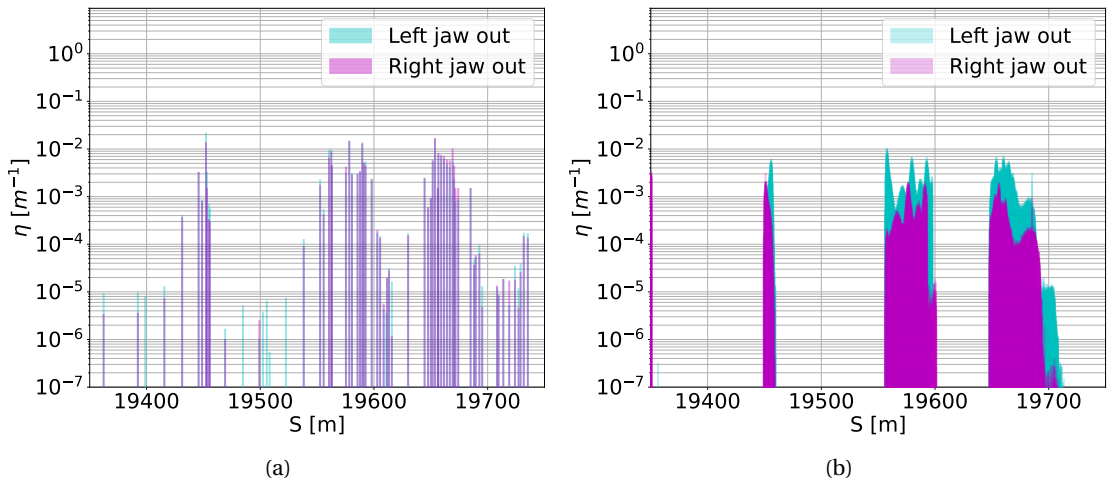


Figure 9.3 – Measured (left) and simulated (right) single TCP jaw (left jaw out – turquoise, right jaw out – fuchsia) standard collimation loss maps at IR7 DS for B2H in the 2018 *physics* configuration with Pb at 6.37 Z TeV.

For B1H there is a clear reduction in the losses in the IR7 DS both from the measured and the simulated loss maps when the right jaw is retracted and the left jaw is left in. The difference in the measured loss maps for B2H between using either of the jaws appears less noticeable. However, the simulated version produces almost a mirror-like result to that of B1H.

It can be concluded that using a single left jaw or having the right jaw more retracted than the

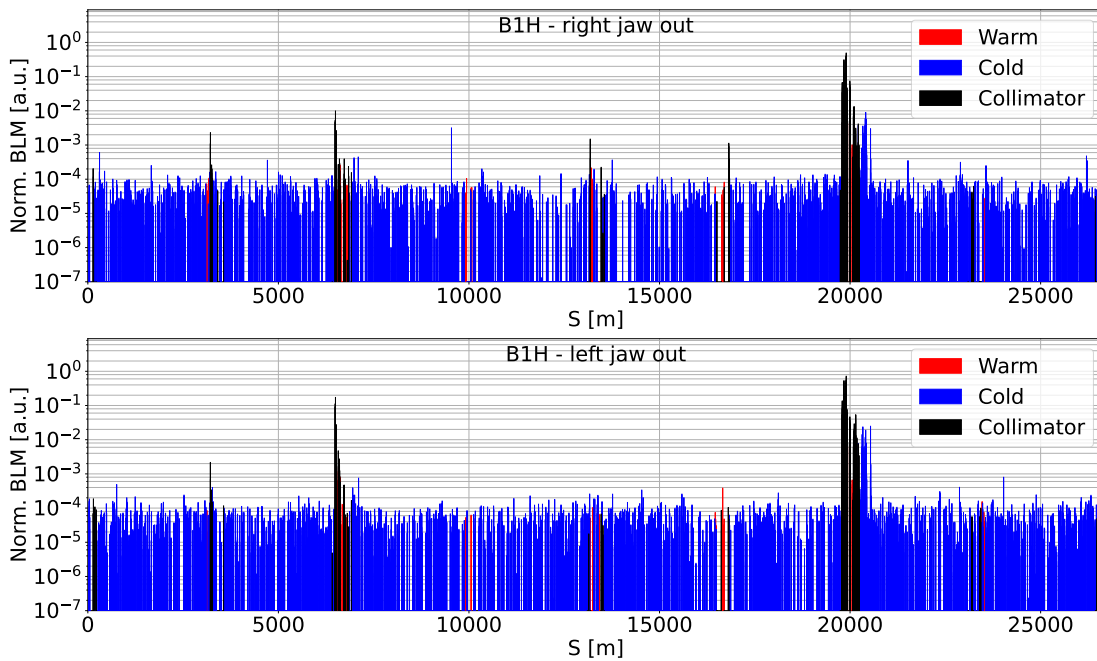


Figure 9.4 – Measured loss map of 6.37 Z TeV Pb ions in B1H with the right jaw (top) or left jaw (bottom) of the TCP.C6L7.B1 collimator retracted.

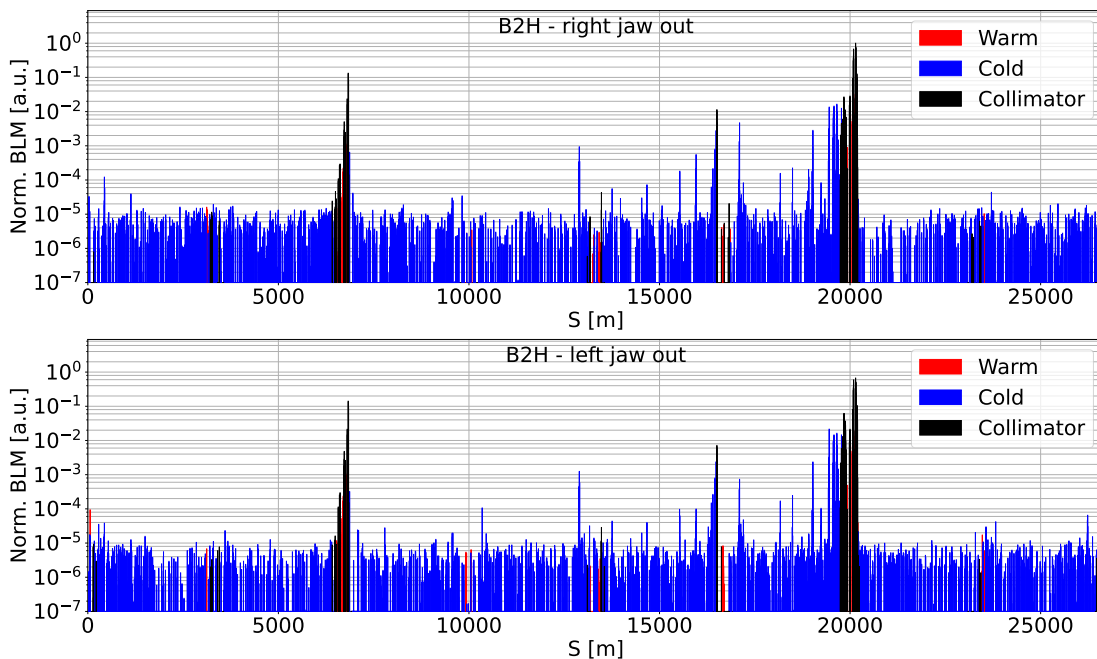


Figure 9.5 – Measured loss map of 6.37 Z TeV Pb ions in B2H with the right jaw (top) or left jaw (bottom) of the TCP.C6R7.B2 collimator retracted.

left jaw may be beneficial for the cleaning in the IR7 DS for the standard collimation systems.

9.3 Collimator jaw tilt study

One of the issues that are difficult to control during operations is the potential tilting of collimator jaws in the longitudinal direction. A study has been carried out to estimate the worsening of the collimation performance due to collimator tilts.

Due to the fact that the beam has a divergence at the primary collimator, it is more accurate to simulate the two tilting jaws separately, such that the same impact parameter can be conserved on both sides, and then combine the two contributions. A schematic illustration is given in Fig 9.6. In order to simulate the same impact parameter, the halo particles simulated must have different x and x' . The statistic of 6×10^6 primary particles is simulated at 6.37 Z TeV. The optics and collimation setup used are the ones for the B2H 2018 *physics* stage [22] with the crystal at 4.75σ . The results are plotted as average inefficiencies in the DS in Fig. 9.7 for each jaw and the two jaws combined.

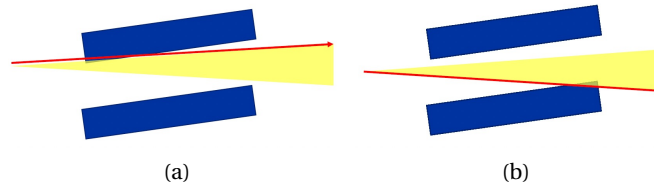


Figure 9.6 – Schematic representation of a diverging beam impacting the two tilted jaws separately.

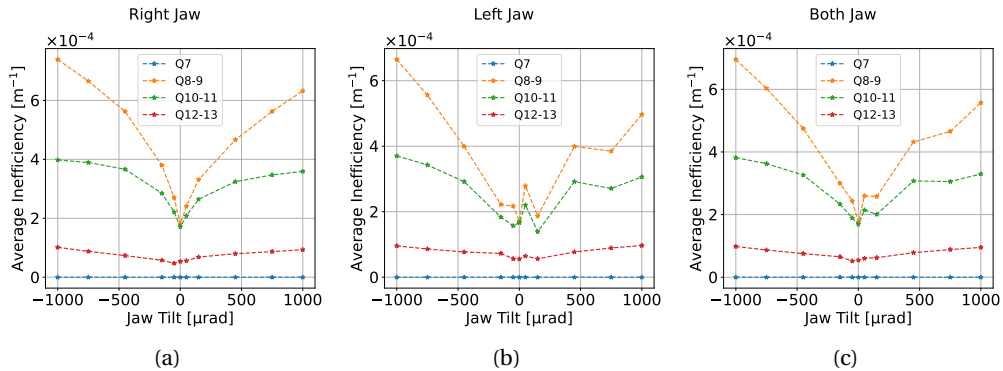


Figure 9.7 – Simulated average inefficiency for the B2H TCP jaws at different tilting angles at 6.37 Z TeV for left jaw (a), right jaw (b), and both (c).

For the left jaw there is a clear dependence of average loss with respect to the tilt angle from both sides. This is also true, albeit noisier, for the right jaw. The cause of the decrease in cleaning performance mostly likely comes from the decrease in the distance travelled by the particle within the material. This is consistent for all clusters in the DS. The worsening is up to a factor of 3.

9.4 Optics improvement

A new optics has recently been developed for the collimation insertion, with the aim of improving the cleaning performance and the impedance for proton collimation using the standard collimation system [157, 158, 159, 160]. The underlying principle for the cleaning improvement is that any particle that scatter out of the primary collimator has typically received some angular kick. If the β -function at the primary is larger, the same angular kick corresponds to a larger normalized amplitude in beam σ , so that a larger oscillation is induced downstream and the particle can be intercepted by the downstream collimation stages for a smaller absolute kick. A further improvement is obtained by introducing a large orbit bump in IR7 that increases the single-pass dispersion from the primary, so that off-momentum particles get larger excursions and therefore potentially can be intercepted by collimators instead of being lost in the DS.

As an attempt to further improve the cleaning of the standard system, this optics has been incorporated in the ion optics with minimal changes (only a small re-matching of the phase advance over IR7 has been done) thanks to [140, 160]. The obtained optical functions in IR7 are shown for the standard optics and the new optics in Fig 9.8. In this section, we investigate the ion cleaning performance for Pb ions with the new optics.

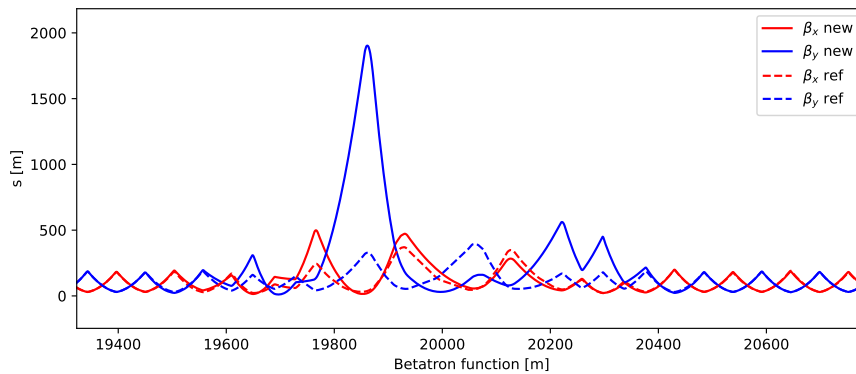


Figure 9.8 – Betatron functions in the two planes for Beam 1 as a function of the s position around IR7 for the modified optics and the reference optics.

Various machine configurations have been compared, each with a statistics of 6×10^6 $^{208}\text{Pb}^{82+}$ at 6.8 Z TeV for B1H. The configurations include:

- Crystal collimation with Run 3 *physics* optics, Run 2 collimation setup in Table 7.8 and the crystal at 4.75σ – ‘Crystal’ in Fig. 9.9.
- Standard collimation with Run 3 *physics* optics without modifications nor crystal and Run 2 collimation configuration (as in Table 7.8 but without asymmetric jaws at TCP) – ‘Std’ in Fig. 9.9.

- Standard collimation with modified Run 3 optics and Run 2 collimation configuration (as in Table 7.8 but without asymmetric jaws at TCP) – ‘Std Opt IR7’ in Fig. 9.9.
- Standard collimation with modified Run 3 optics together with orbit bump, and Run 2 collimation configuration (as in [22] but without asymmetric jaws at TCP) – ‘Std w bump both jaws’ in Fig. 9.9.
- Standard collimation with modified Run 3 optics together with orbit bump, and Run 2 collimation configuration as in [22] but with one TCP jaw only – ‘Right jaw only’ and ‘Left jaw only’ in Fig. 9.9.

The average inefficiencies of each configuration is shown in Fig. 9.9. The worst performing setup is the standard collimation as in Run 2, as expected. The cleaning with the modified optics fares significantly better already. The bump in IR7 brings the losses in Q10-11 down by another 2.5×10^{-4} approximately. With this optics, single jaw setups were investigated. However, with the new optics, using only the left jaw does not bring any further dramatic cleaning improvement. With only the right jaw, the losses in Q8-9 increases, while the losses in Q10-11 slightly decrease. Finally, with crystal collimation, the cleaning in Q10-11 is the best of all studied configurations with a large margin, while the losses in Q8-9 are slightly higher than with standard system and new optics. In terms of the highest loss in any cell in the DS, the crystal system is still the best, while the new optics is shown to significantly improve the performance with the standard system.

This study shows that already by directly taking over optics changes studied for protons we are able to see an improvement in cleaning. For a scenario where crystal collimation cannot be used, this new optics together with the orbit bump can be used. The specific primary jaw settings should be investigated more in detail for each plane. When the improvement with single jaw setups are not prominent, both jaws should be favored for operational safety.

9.5 Tilted TCP configuration and optics improvement

In the Section 9.3, the collimator tilt angles set have been large. However, as seen in the impact parameter scan, the longer is the distance traversed in the active material, the better is the cleaning efficiency. With the existing divergence of the beam envelope and the collimator jaws parallel to the beam trajectory, the distance traversed is usually not the longest possible. To achieve the longest possible particle path inside the primary, both collimator jaws could be tilted to fit the beam envelop and hence be close to parallel to the direction of incoming halo particles. A study with 6×10^6 $^{208}\text{Pb}^{82+}$ at 6.8 Z TeV was carried out for the modified B1H Run 3 optics with orbit bump and the Run 2 collimator settings in Table 7.8 with the horizontal TCP aligned to the beam envelop.

In the modified optics for B1H Run 3, the beam is converging at the TCP.C6L7.B1. This means that a clockwise rotation around the y -axis in the x - z (seen from the positive y) of the left

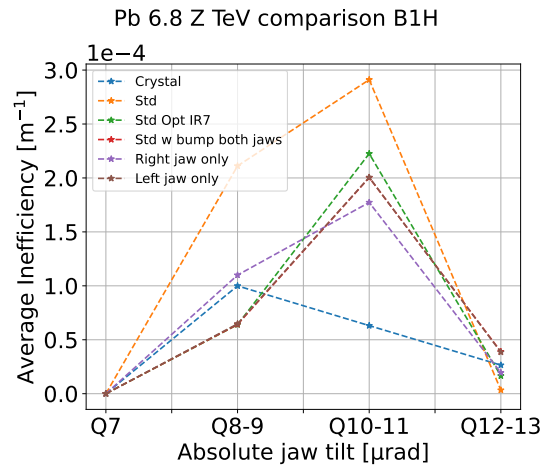


Figure 9.9 – Simulated average inefficiencies of various B1H ion collimation configurations at 6.8 Z TeV. The legend description is in list 9.4.

jaw to match the beam envelop after the jaws have moved to the nominal half-gap will give a different impact parameter and can possibly make the beam intercept on the lateral face. For this reason, after the jaw rotation, the left jaw is translated downwards to maintain the usual impact parameter on the front face. A similar operation is done for the other jaw. The process is illustrated in Fig. 9.10.

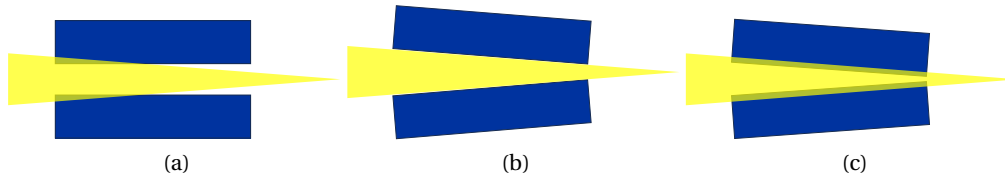


Figure 9.10 – Schematic representation translational and rotational transformations of the TCP.C6L7.B1 jaws to align them to the beam envelop. (a) The collimator jaws are opened to the nominal half-gap. (b) The jaws are rotated to the same angle as the x' of the beam halo. (c) The jaws are moved towards the beam core to intercept the beam halo are $b = 1 \mu\text{rad}$.

The results are shown as loss maps in Fig. 9.11 and 9.12 (zoom in IR7), and are compared to the standard collimator setup without the alignment but with the same optics. It is clear that the improvement of with the TCP aligned angularly with the beam envelope is enormous (up to around 2 orders of magnitude). This improvement is not limited to the IR7 DS region, but is observed in the entire ring. At least theoretically, it proves to provide an even better cleaning than with the use of crystal. The main difficulty lies in accurately keeping the jaws aligned to the beam envelop at all times during operations, since the rotation angle here is of the order of $16.8 \mu\text{rad}$. It should be noted also that the minimum step of the stepping motor at each jaw corner is $5 \mu\text{m}$. Therefore, with a 60 cm collimator length, a single step of one jaw corner would change the tilt angle by about $8 \mu\text{rad}$ which is hence the smallest angular resolution

technically possible with the present hardware. Furthermore, even if this would be possible, the beam-based alignment technique has intrinsic limitations on the precision. It is therefore not possible to exactly align the collimator angle to the angle of the beam envelope.

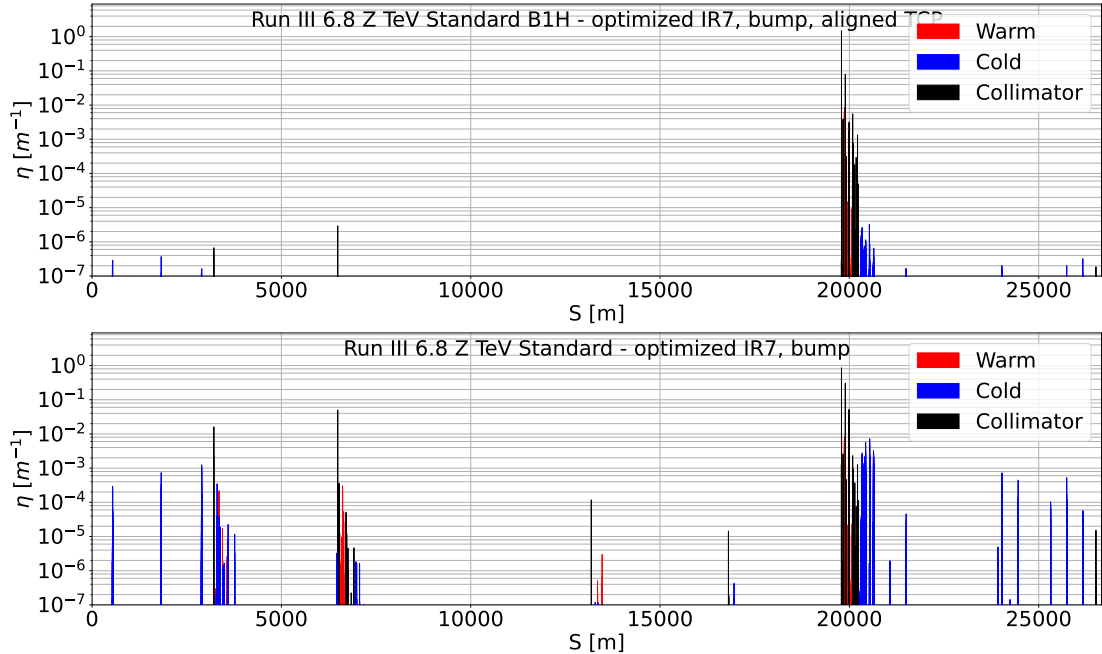


Figure 9.11 – Loss map of B1H standard collimation with (top) and without (bottom) TCP alignment to the beam envelop with 6.8 Z TeV Pb beam Run 3 modified optics with orbit bump in IR7 and Run 2 collimation *physics* settings (Table 7.8).

For the present case, in order to assess sensitivity to variations of the orbit and to the expected alignment error due to the resolution, smaller tilts around the optimum position have been simulated. Tilts bigger than the critical angle have not been considered because it would be equivalent to defining the impact parameter on the outgoing face. The impact parameter would not be exactly the same (thus neither the distance traversed), but it would be close enough that the effects would be similar as investigated in Section 9.3.

The effects of smaller rotation angles are presented as average inefficiencies in Fig. 9.13. We can see that when moving away from the optimum orientation, the observed improvement over the standard zero orientation rapidly degrades. With an error of approx. $10 \mu\text{rad}$, it is still possible to achieve a factor 2–3 in cleaning improvement. This could be possible from the hardware point of view, however, it might be very challenging to achieve this when accounting for also the unavoidable errors in the collimator alignment procedure as well as small orbit drifts over time. It is therefore, with present hardware and alignment, not realistic to reproduce experimentally the huge gain that was shown in Fig. 9.11 simulation for the perfect alignment with the envelope. Nevertheless, the results are considered interesting and could be tested experimentally in machine development, as well as the new optics.

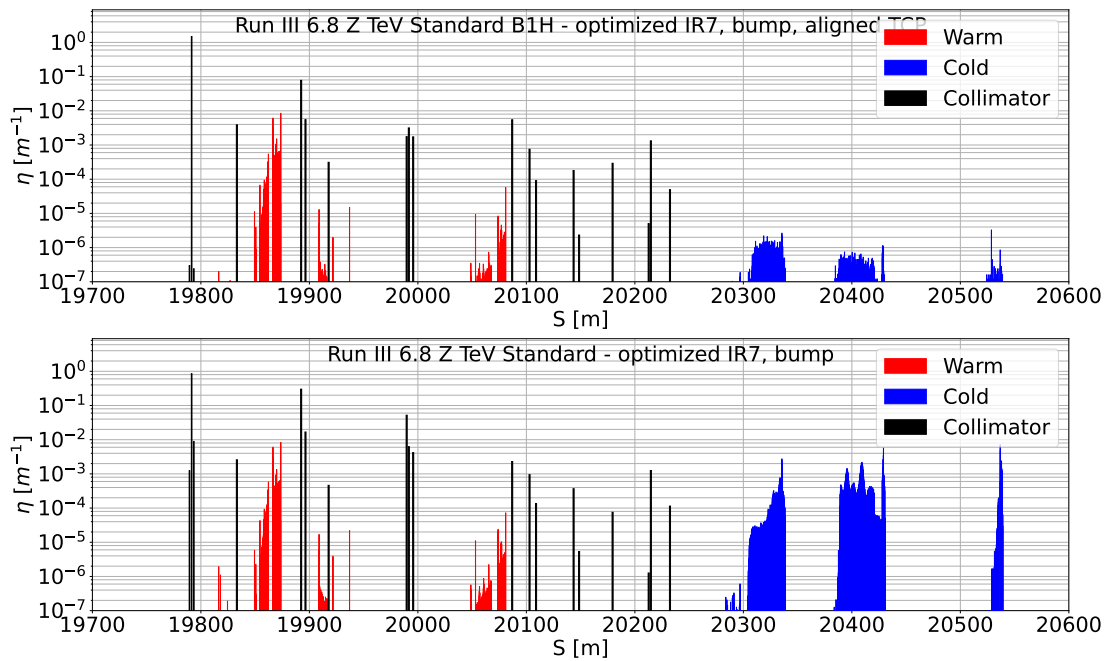


Figure 9.12 – IR7 Loss map of B1H standard collimation with (top) and without (bottom) TCP alignment to the beam envelop with 6.8 Z TeV Pb beam Run 3 modified optics with orbit bump in IR7 and Run 2 collimation *physics* settings (Table 7.8).

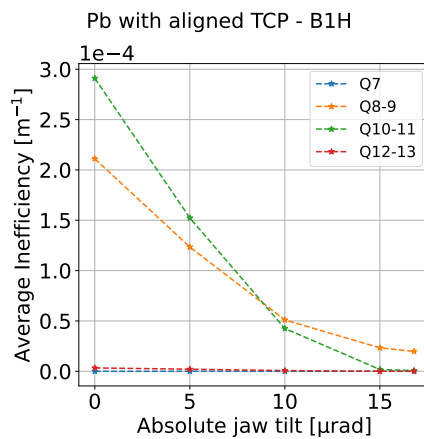


Figure 9.13 – Average inefficiency of DS cluster at TCP jaw tilts smaller than the beam envelop alignment angle for B1H at 6.8 Z TeV.

10 Simulations of future runs

The simulation setup built for crystal ion collimation has been used in this final chapter to predict the cleaning performance in some future scenarios that are planned or under discussion. First scenario seen is the simulations for the HL-LHC at 7 Z TeV, while the second is the operation with other ion species than Pb.

10.1 Simulation at higher energy

So far, the highest achieved energy in the LHC is 6.8 Z TeV, although the LHC design energy is 7 Z TeV. In the future HL-LHC, the assumed energy is also 7 Z TeV. Therefore, the cleaning performance at this higher energy is simulated in this section. It is presently foreseen to use the same optics and collimator settings in HL-LHC as in Run 2 and Run 3 (see Table 7.8), although this may change in the future. Therefore, the aim of this simulation is mostly exploratory to investigate any energy dependence, and the actual performance may differ depending on the entire collimation and optics settings.

In the simulation of the HL-LHC cases, the optics setup for Run 2 has been used but with the energy set to 7 Z TeV. In total, 6×10^6 $^{208}\text{Pb}^{82+}$ ions have been simulated for B1H and B2H. The simulated loss maps are shown in Figs. 10.1 to 10.4, together with Run 2 reference loss maps in the same configuration but with a beam energy of 6.37 Z TeV.

For B1H, we can see that the loss maps at 7 Z TeV are in general rather similar to the ones at 6.37 Z TeV, which can be expected since the particle-matter interaction cross sections have only a weak energy dependence in this regime. It can be seen that the B1H losses in the DS are actually slightly lower for the 7 Z TeV ion beam than for the 6.37 Z TeV. A noticeable increase can be seen at the TCPs around $s = 19890$ m too. An increase in losses is also seen in IR5.

The DS losses in B2H for the two energies are almost identical. However, there is an interesting shift in losses around the TCSGs after the crystal at around $s = 20000$ m. In some other IRs, the losses are more prominent for the 7 Z TeV case, e.g. in IR2 (approx. at $s = 3500$ m), IR3 (approx. at $s = 6800$ m), and IR6 (approx. at $s = 17000$ m). The differences of losses in the other IRs may

be due to the shift in losses around the TCSGs in IR7. This may be explained also by the small offsets in magnetic rigidity.

Overall, the performance in the DS is as expected. This is because from a crystal channeling point of view, the initial beam distribution has an angular spread of approximately 2.5 nrad. On the other hand, the critical angle scales as $\theta_c \propto \sqrt{1/pv}$, so with a value of around 2 μ rad at 7 Z TeV it is slightly reduced compared to 6.37 Z TeV or 6.8 Z TeV. Therefore, nuclear interactions are still heavily suppressed in the crystal [46] and the losses in the DS do not change significantly. However, for any very strong losses with significantly larger impact parameter than the studied 1 μ m the angular spread could risk to bring more particles outside the channeling acceptance which would have a negative impact on the cleaning performance.

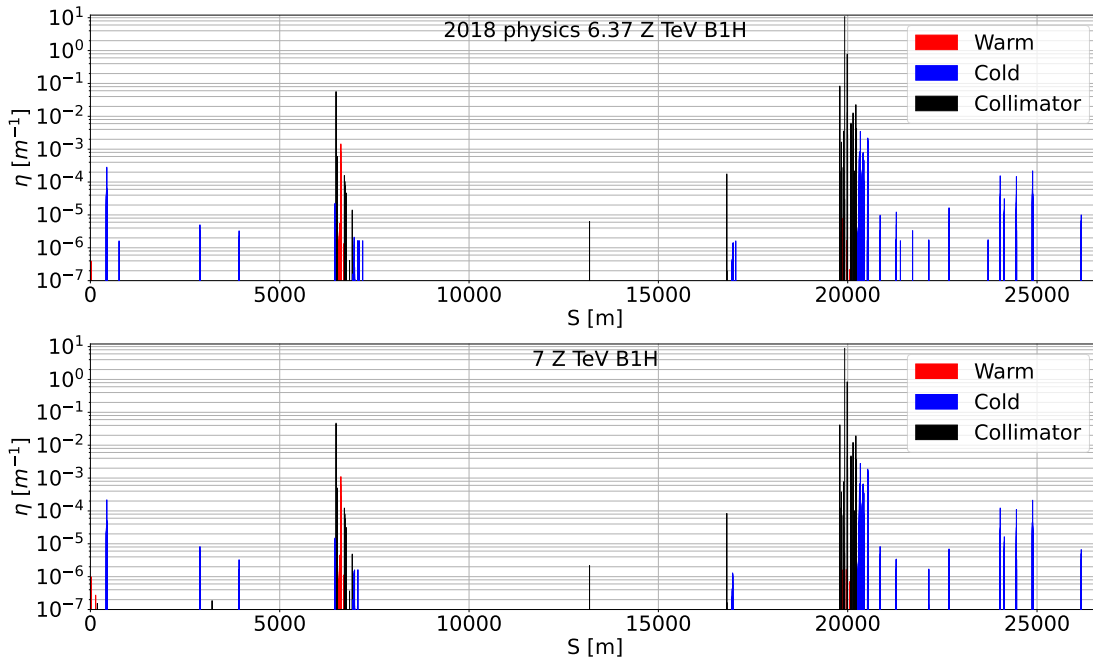


Figure 10.1 – Simulated loss map for the 2018 B1H ion run at 6.37 Z TeV (top) and 7 Z TeV (bottom) with the crystal in adiabatic settings and Run 2 *physics* collimation setup.

10.2 Crystal collimation performance with various ion species

The present LHC heavy-ion program is scheduled to continue until the end of Run 4 (at the time of writing, until for end of 2032) with yearly one-month runs of Pb-Pb or p-Pb collisions. It has been proposed to extend the ion operation further[101], and at the ALICE experiment, a new detector (ALICE3) with higher performance is under study for Run 5 (presently scheduled to start in 2035) [161]. These additional ion runs have the main aim of reaching a significantly higher integrated nucleon-nucleon luminosity than in Run 3–4.

Since many optimizations have already been performed in the injector complex and the

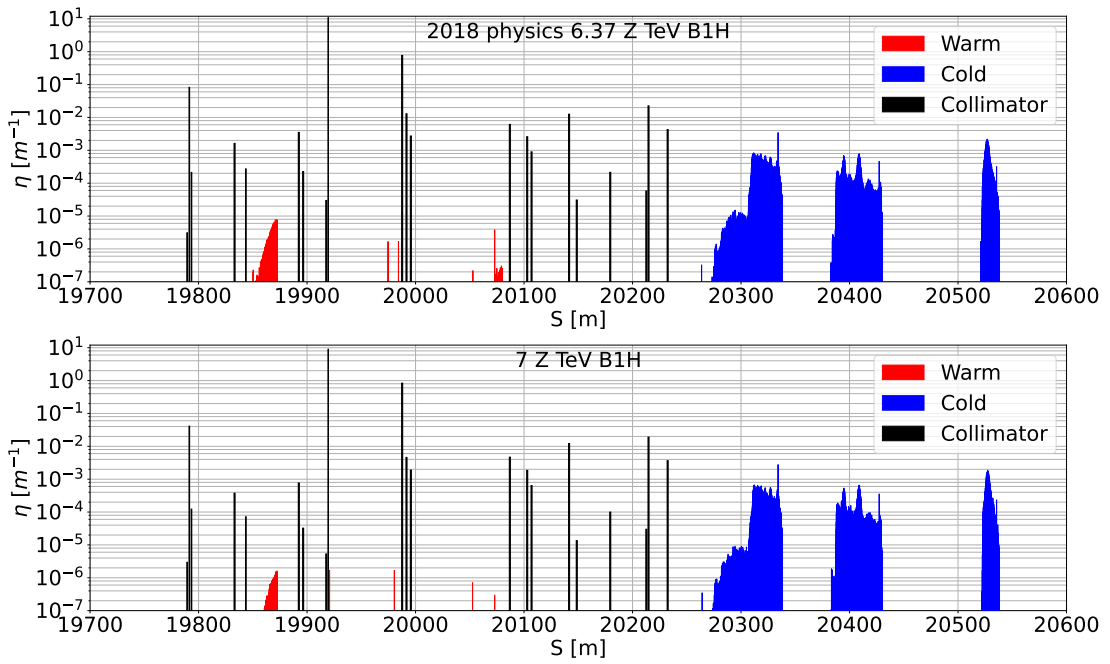


Figure 10.2 – Simulated loss map zoomed in IR7 for the 2018 B1H ion run at 6.37 Z TeV (top) and 7 Z TeV (bottom) with the crystal in adiabatic settings and Run 2 *physics* collimation setup.

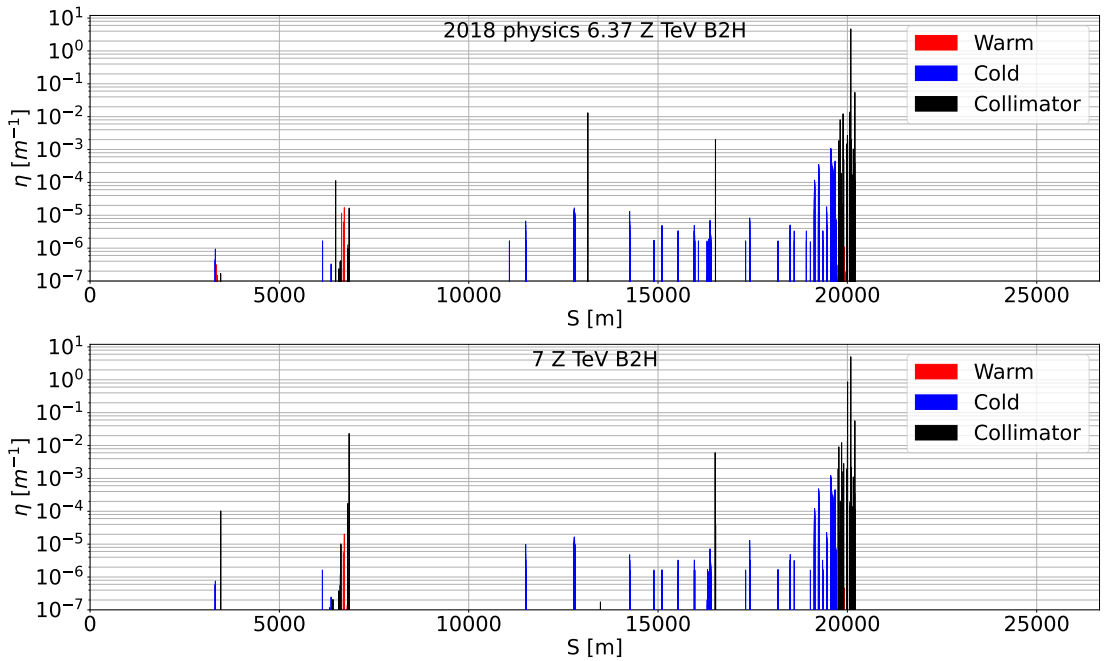


Figure 10.3 – Simulated loss map for the 2018 B2H ion run at 6.37 Z TeV (top) and 7 Z TeV (bottom) with the crystal in adiabatic settings and Run 2 *physics* collimation setup.

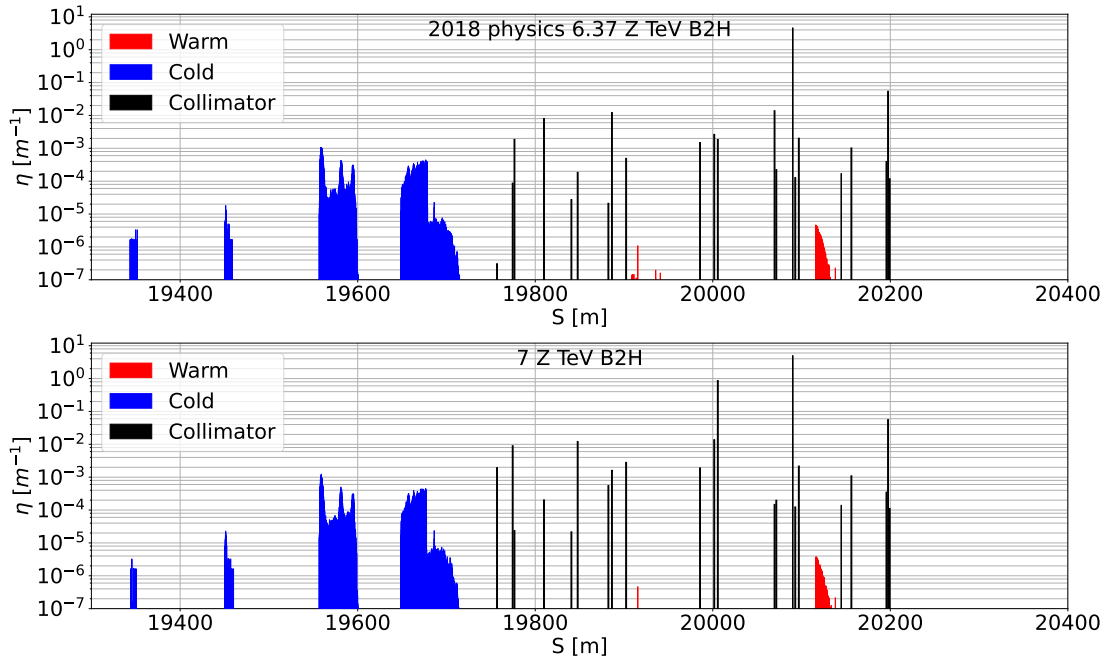


Figure 10.4 – Simulated loss map zoomed in IR7 for the 2018 B2H ion run at 6.37 Z TeV (top) and 7 Z TeV (bottom) with the crystal in adiabatic settings and Run 2 *physics* collimation setup.

LHC to increase the Pb-Pb luminosity [60, 162], no obvious further large gain factors are easily within reach. Therefore collisions of other ion species than Pb are under study, which could potentially be used to create higher bunch charge and hence higher nucleon-nucleon luminosity [101]. With higher bunch charge, collimation becomes even more critical, and it is therefore important to study the collimation of these other ion species at an early stage to identify potential showstoppers, which is the main topic of this section.

It should be noted also that a short LHC pilot run at low intensity with O beams is scheduled for Run 3 [163]. Although collimation will not be critical in this run due to the low intensity, it could give an opportunity to benchmark the simulation tools for collimation with other ion species.

In this study the ions $^{16}\text{O}^{8+}$, $^{40}\text{Ar}^{18+}$, $^{84}\text{Kr}^{36+}$, and $^{129}\text{Xe}^{54+}$ are considered, following the studies in [101]. For these ion species, for which very little or no operational experience exists in the CERN accelerator complex, the emittance cannot be known in detail at present. We therefore assume that the collimator settings used for Pb operation are kept in mm, which with the proton geometric emittance corresponds to a 4.75σ cut. The collimator settings would be identical also in units of beam σ if the geometric emittance is the same, meaning that the normalized emittance at a certain energy per nucleon is the same as that of a proton

beam at equivalent magnetic rigidity:

$$\epsilon_{n,\text{ion}} = \gamma\beta\epsilon_g \quad (10.1)$$

where γ is the relativistic factor, $\beta = v/c$, and ϵ_g is the geometric emittance (i.e. not normalized) of the proton beam at the same magnetic rigidity. With this in mind, the optics used is the B1H Run 3 ion *physics* optics together with the Run 2 *physics* collimation setup in Table 7.8 and the TCPCH.A4L7.B1 (new) crystal in adiabatic position, i.e. at 4.75σ . For each ion species a simulation of 6×10^6 primary ions at 6.8 Z TeV has been carried out. The loss maps are shown in Figs. 10.5 to 10.8. For comparison, the corresponding reference case for Pb ions is shown in Fig. 10.9.

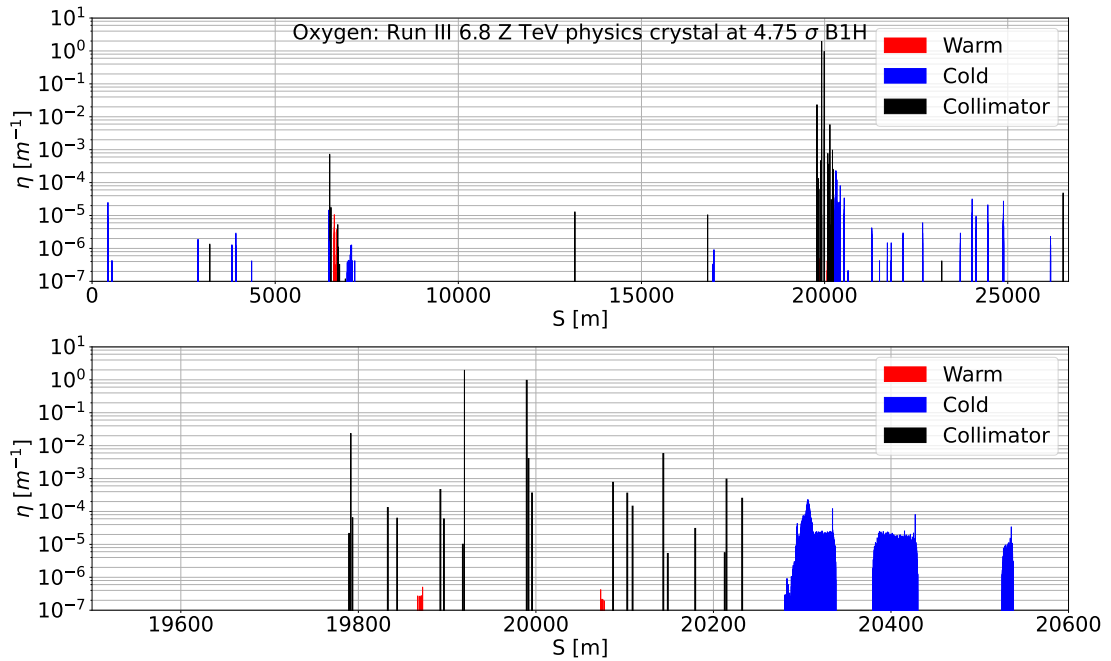
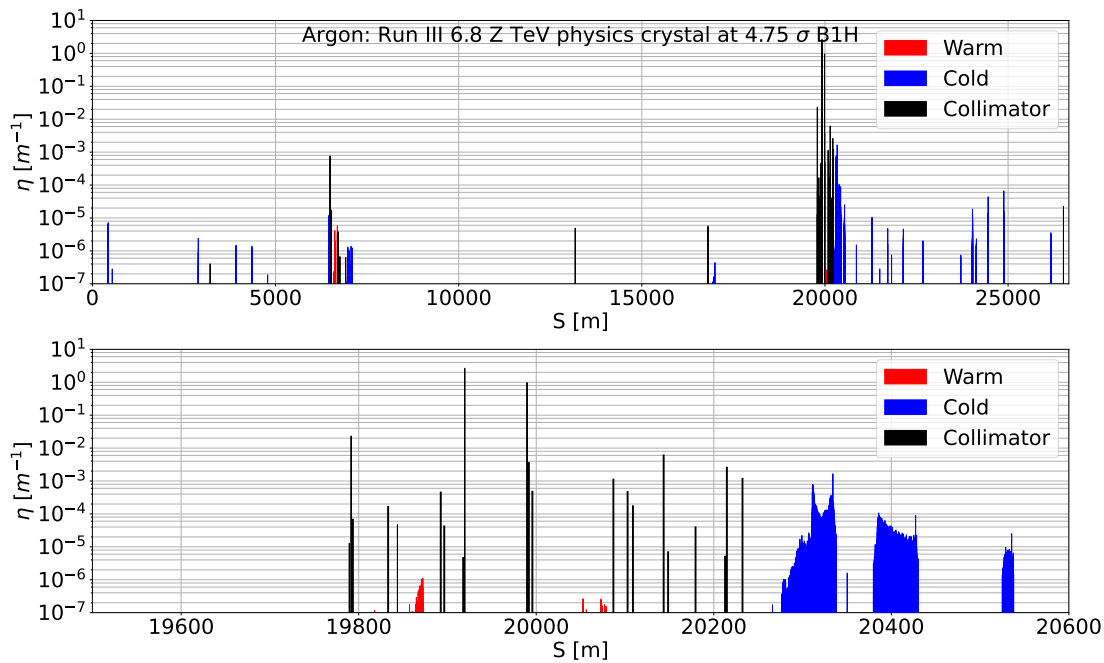
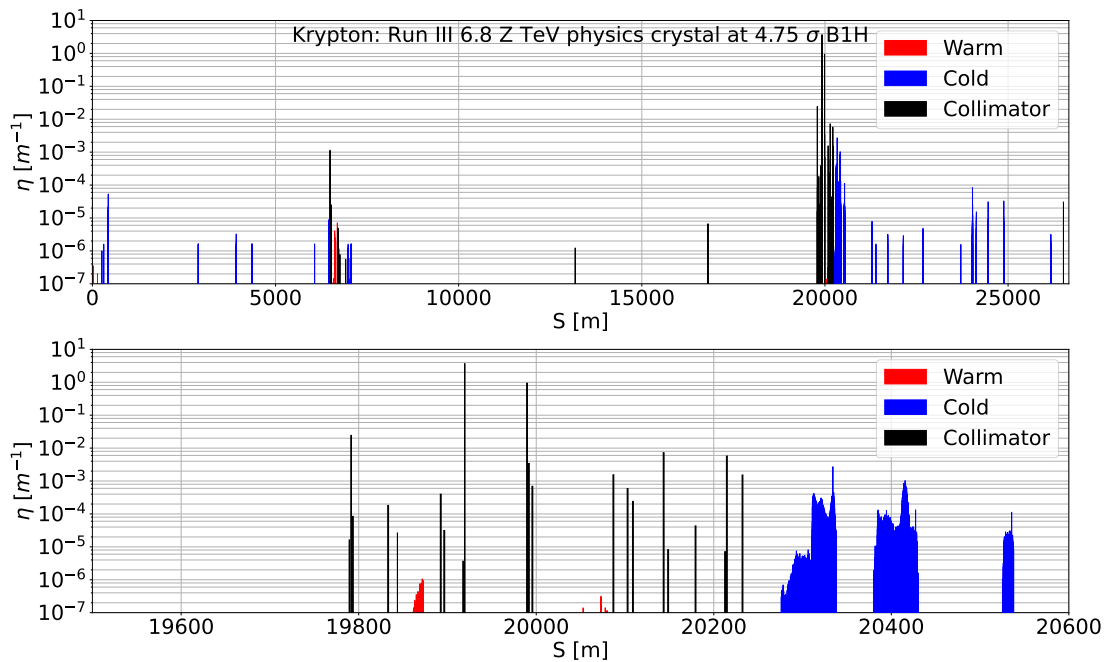


Figure 10.5 – Simulated loss map in B1H of $^{16}\text{O}^{8+}$ beam at 6.8 Z TeV.

It is visible from the loss maps that the local cleaning inefficiency in the cold clusters in the IR7 DS decreases with the atomic number Z . More quantitatively, the average and the maximum inefficiencies are plotted in Fig. 10.10. Here, the general positive slope of the cold losses as function of Z is apparent. Occasional deviations from this dependence, such as for the Q8-9 loss for $^{84}\text{Kr}^{36+}$ can be explained by the fact that the changes in magnetic rigidity due to fragmentation are not continuous, and there are hard thresholds to whether certain isotopes end up in a certain cluster.

This dependence on the Z can be explained by the fact that the EMD cross section increases with Z^2 , as mentioned in Section 4.3. The crystal interactions are mostly (for the exceptions please consult [46]) generated by the scaling of the cross sections of the various physical processes according to how the particle's properties relate to the conditions of channeling (and

Figure 10.6 – Simulated loss map in B1H of $^{40}\text{Ar}^{18+}$ beam at 6.8 Z TeV.Figure 10.7 – Simulated loss map in B1H of $^{84}\text{Kr}^{36+}$ beam at 6.8 Z TeV.

of other coherent effects). Hence, on average, relationship of the interaction rates between the different species within the crystal still holds as for the amorphous material, assuming the same particle distribution in position and momentum. This means that an increase of

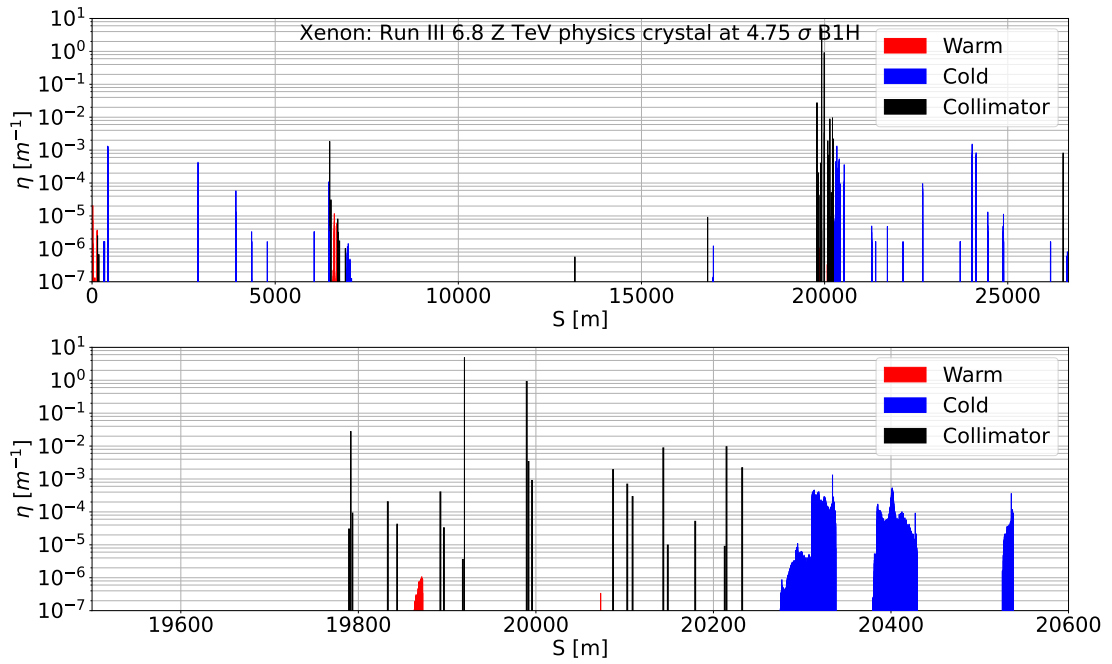


Figure 10.8 – Simulated loss map in B1H of $^{129}\text{Xe}^{54+}$ beam at 6.8 Z TeV.

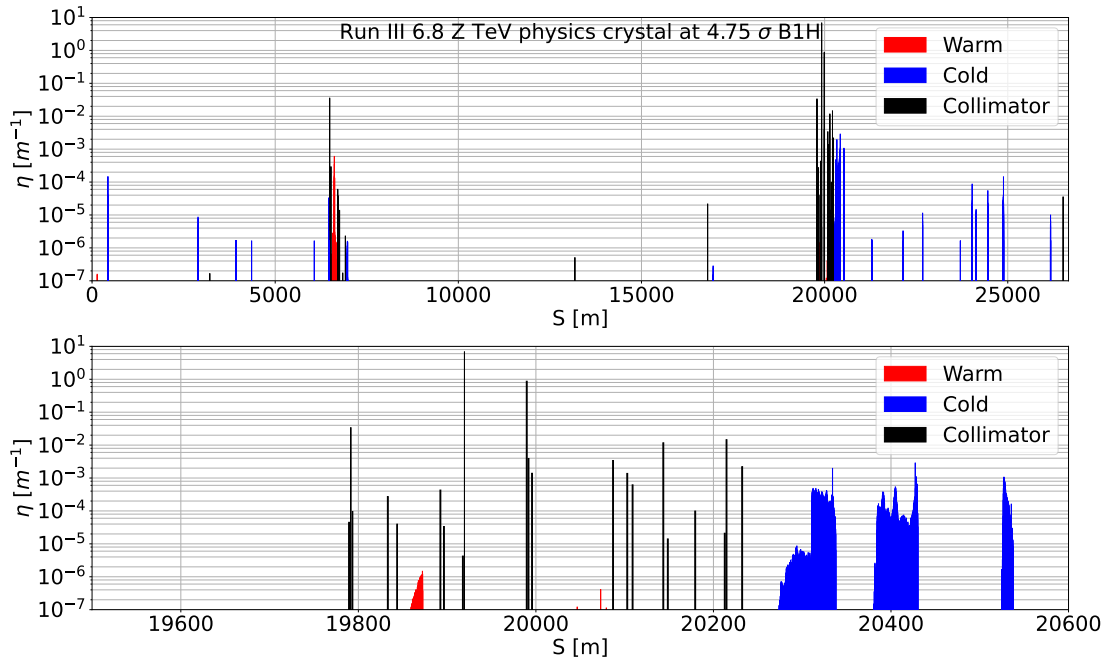


Figure 10.9 – Simulated loss map in B1H of $^{208}\text{Pb}^{82+}$ beam at 6.8 Z TeV.

fragmentation due to higher Z also occurs in crystals. Coupling this information with the finding that most DS losses comes directly from the crystal, an increase in fragmentation and in rigidity deviation from the crystal also implies an increase of losses in the DS.

Another difference between the various ion species is that nuclear fragmentation changes the magnetic rigidity more drastically for ion species with lower A and Z , since each lost nucleon is a larger fraction of the total mass or charge and hence increases the smallest discrete change in magnetic rigidity. Fragments with a large difference in magnetic rigidity from the main beam are much more likely to be intercepted by downstream collimators than those with small rigidity deviations. This is an additional reason as to why the collimation of lighter ions gives in relative less losses leaking to the DS. On the other hand, this effect is counteracted by the fact that certain ion species may fragment into smaller ions with similar charge-to-mass ratio as the initial ion. One example of this is $^{16}\text{O}^{8+}$, which can fragment into, e.g., $^{12}\text{C}^{6+}$ or $^4\text{He}^{2+}$. Such fragments have a very similar magnetic rigidity to the main beam, since the momentum loss in the fragmentation is typically rather small, so they can potentially travel far in the ring.

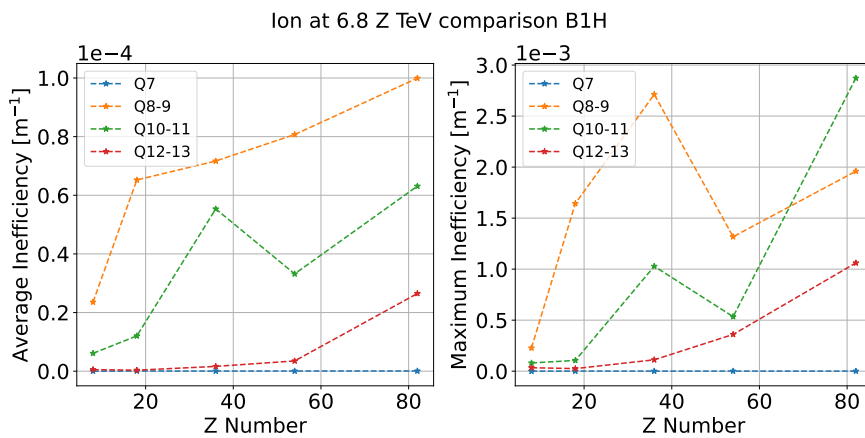


Figure 10.10 – Simulated average and maximum inefficiencies in the cold DS clusters for ions with different atomic number in B2H at 6.8 Z TeV.

In order to investigate which are the most abundant fragments that are lost in the entire IR7 DS range for each ion species, a detailed plot of the 5 most abundant ones is shown in Fig. 10.11.

Starting from $^{16}\text{O}^{8+}$, we can see that the highest losses are from $^{15}\text{N}^{7+}$, which is close to $^{16}\text{O}^{8+}$, and $^4\text{He}^{2+}$, which has the same charge-to-mass ratio as the original beam. For $^{40}\text{Ar}^{18+}$ we can see the peaks in the isotopes of argon with one or two neutrons stripped, and a few isotopes of chlorine. All these are species close in charge-to-mass ratio to the main beam. Finally, for $^{84}\text{Kr}^{36+}$, $^{129}\text{Xe}^{54+}$, and $^{208}\text{Pb}^{82+}$ except for one case ($^{79}\text{Br}^{35+}$) the atomic number stays always the same.

To conclude, when assuming the same physical emittance, crystal collimation works well with lighter ion species. In particular, the performance improves as the atomic number decreases, which is encouraging in view of the potentially larger stored beam energies in future operation with lighter ions. Compared to Pb, a maximum decrease in average cold losses of about a factor 4 is found, with the crystal-based collimation system being the most efficient for O. However, for the maximum recorded loss, the picture is more complicated (see Fig. 10.10), and some of the lighter ion species have a higher maximum inefficiency than Pb.

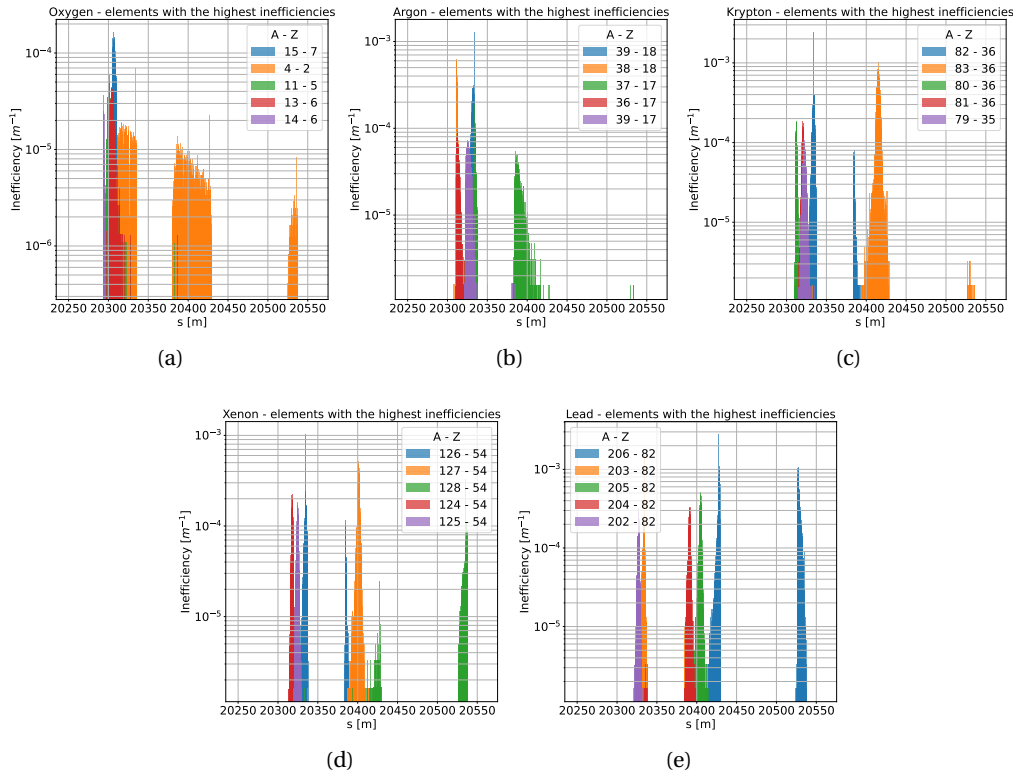


Figure 10.11 – Inefficiency of the 5 most abundant ion species in each ion species simulation at 6.8 Z TeV: (a) $^{16}\text{O}^{8+}$, (b) $^{40}\text{Ar}^{18+}$, (c) $^{84}\text{Kr}^{36+}$, (d) $^{129}\text{Xe}^{54+}$, and (e) $^{208}\text{Pb}^{82+}$.

On the other hand, in [101] an increase of the stored beam energy between 25% (for Xe) and a factor 3 (for O) is envisaged, although it should be noted that more recent studies give lower predicted beam intensities [164]. These studies give therefore a first preliminary indication that the needed cleaning improvement might be within reach if only the average cleaning inefficiency is considered, however, not in terms of the local maximum. This local maximum of particles impacting on the aperture in 10 cm bins is, however, not directly proportional to the maximum energy deposition in the superconducting coils of the impacted magnet. Therefore, to conclude on any limitations on allowed beam loss power that can be handled without quenching magnets or dumping the beam, further studies are needed, including in particular energy deposition. It is likely that ion collimation remains challenging also in future runs.

Conclusions and outlook

The Large Hadron Collider (LHC) at CERN is a particle accelerator that collides protons and heavy ions at unprecedented energies. Its creation has paved the way for important scientific discoveries. While fundamental sciences keep pushing the boundaries of our collected knowledge, the researchers also strive to enhance the performance of the LHC and provide higher statistics and reliability in the experiments. With the upgrade to the High Luminosity LHC (HL-LHC), the total stored beam energy for Pb ions is increased from 13 MJ to around 20 MJ. It is challenging to operate the machine with this amount of stored energy, as even a small fraction of the total energy deposited locally on a sensitive element due to beam losses may cause malfunction or even damage. In particular, the superconducting magnets are kept at a very low temperature of a few K. With enough beam losses hitting these magnets and hence heating them, they may lose their superconducting properties and quench. To protect these and other devices around the ring, a multi-stage collimation system is deployed, which should safely intercept and dispose of beam losses.

The LHC collimation system is very effective with protons. However, the fragmentation of heavy ions makes them much more difficult to stop within the collimation insertion, and the fractional leakage of beam losses out of the collimation system to cold magnets is about two orders of magnitude higher with ions than with protons. Therefore, even though the stored beam energy is about a factor 20–30 lower than for protons, collimation of Pb ion beams remains very challenging. The intensity upgrade requires even better performance of the cleaning of the beam halo. Therefore, thanks to extensive tests and studies in the past, a new collimation scheme using bent crystals as primary collimators has been added to the baseline of Run 3 and HL-LHC for Pb ion operation. Halo particles hitting the crystals are *channeled*, i.e. they are trapped in the potential well between the crystalline planes and forced to follow the bending of the crystal so that they exit the crystal with a large angular kick. The channeled halo is thus separated from the main beam and hits deeply in a downstream collimator, used as absorber, leading to a strong suppression of out-scattered particles.

A systematic and reliable way of studying collimation for heavy ions in simulation is needed, in order to understand how to operate the crystal-based system as efficiently as possible, to identify and mitigate any performance bottlenecks, and to quantify the collimation performance in future machine configurations. This has not been available up to now for ion beams. For this reason, this thesis work has been dedicated to the construction of such a simulation

framework and its applications. The creation of this tool has made it possible to study the physics of ion crystal collimation in a multi-turn accelerator setting, explore possible optimizations, investigate future proposals, and analyse past experiments. In the previous tracking code for crystal collimation, based on a built-in routine in SixTrack, it was only possible to simulate protons. The new simulation tool allows both protons and arbitrary ion species to be simulated, including particle-matter interactions in both crystals and amorphous materials, and more flexibility in the geometry and setup of the crystal.

The simulation framework is built upon an existing coupling between a particle tracking program, SixTrack, and a multi-purpose Monte Carlo simulation software, FLUKA. This coupling is the present state-of-the-art code for ion collimation with the standard amorphous collimation system. SixTrack takes care of the magnetic tracking part, while FLUKA simulates the particle matter interactions in the collimators. The new ion crystal collimation framework exploits the recently added crystal module within FLUKA. In addition to modifications and additions to the inputs and outputs to make it compatible with crystals, several 3D crystal geometries have been created along with their crystal lattice definitions. These elements have been added to the FLUKA database for collimators to facilitate the ease of use. Pre- and post-processing have been added where necessary.

The simulation framework has been benchmarked against proton and Pb ion data, and for protons, against the standalone SixTrack that has a built-in routine for crystal collimation of protons only. Both crystal routines have been benchmarked previously with data at low energy for a single passage through the crystal. In this thesis, a single-pass comparison is done at LHC energy between the two codes, as no experimental data exist at this energy. Then, benchmarks with measured LHC data have been performed for multi-turn dynamics. These are the loss map, angular scan and linear scan comparisons for protons at 6.5 TeV. In the loss map benchmark, the measured particle loss distribution around the ring is compared to the simulation results from the two tools. In the angular scan, the multi-turn loss at the crystal is investigated at different crystal orientations. In the linear scan, the multi-turn channeled beam halo is reconstructed by looking at the measured losses locally at the absorber intercepting the channeled halo. The same studies have been done with Pb ions at 6.37 Z TeV without the comparison to SixTrack. The results from the benchmark are largely positive. Some discrepancies between the FLUKA and SixTrack crystal routines are observed for isolated physics processes, however, they do not have a major impact on the global loss distribution which is the main observable for collimation cleaning. Most of the difference seen between simulated and measured data can be explained by the fact that this kind of benchmark does not include detailed shower propagation, as this has been done separately, as well as various imperfections that are not known in detail and hence not included in the simulation model. Overall, the setup is deemed suitable for deployment.

The new simulation setup has been used to provide valuable insight and expand our knowledge and detailed understanding of crystal collimation, with the goal to devise optimized operational settings for ion crystal collimation in the LHC. Hence, the cleaning performance

for a generic Pb beam halo has been studied for a series of collimation configurations. Firstly, it has been shown that the crystal-based system performs significantly better than the standard amorphous collimation system when the crystals are in channeling orientation, while it performs worse when the crystal is in amorphous orientation. Scans of the settings of various other standard collimators in the crystal-based system have been done in order to find a configuration that minimizes the leakage of losses to cold magnets without introducing significant risks of losing the collimation hierarchy over time. In particular, the cleaning efficiency was shown to improve by tightening some of the downstream collimators (TCLAs). Simulations have been done also of the losses resulting from a very fast beam dump failure case. Here, no risks of material damage have been found with the crystal based system, as long as the alignment of the collimators with respect to the beam stays within tolerances.

By piecing together the lessons learnt from each study, a proposal for operational settings of a crystal-based collimation system for Pb ions has been presented in this thesis. These settings were subsequently put in operation in the 2023 LHC Pb ion run. Simulations of the beam loss patterns with operational settings showed a good agreement with measured loss maps acquired during the 2023 beam commissioning, which further confirms the robustness of the simulation framework. Operational experience from the 2023 run confirms the excellent cleaning with crystals in channeling orientation, however, drifts of the angular orientations over time were observed, which are being followed up beyond the scope of this thesis. An unforeseen problem occurred also in terms of high beam-induced background at the ALICE experiment, which severely impacted the data-taking. Using the simulations in this thesis in combination with a measurement campaign, the background source could be identified as $^{207}\text{Pb}^{82+}$, created through the loss of a neutron from the main $^{208}\text{Pb}^{82+}$ inside the crystal, which impacted on the tertiary collimator upstream of ALICE and caused a shower to the detector. With the background source being understood, a mitigation could be rapidly found and deployed in terms of an orbit bump that made the $^{207}\text{Pb}^{82+}$ miss the tertiary collimator. Without a performing simulation setup, it would have been much more cumbersome, if at all possible, to rapidly solve the problem at the start of the run, which highlights the importance of the new simulation setup.

Furthermore, it has been found through the simulations in this thesis that the crystal collimation performance, in terms of of the average normalised loss in the superconducting magnets, shows a a quasi-linear dependence on the impacting depth of the particle. This may indicate that a crystal-based system is less robust than a conventional collimation system against very fast losses that could lead to very large impact parameters. These studies have also found that the main source of the leakage to cold magnets is the crystal itself, and leakage from other collimators is negligible. Therefore, all future optimizing efforts should be directed to decreasing the inevitable leakage from the crystal, e.g., by improving phase advances, dispersion, and optics in general. Simulations have been carried out also for a series of imperfections. Crystal orientation errors up to approximately $\pm 2\mu\text{rad}$ do not reduce the cleaning efficiency drastically in downstream cold magnet region. This value is directly linked to the characteristic critical angle within which channeling occurs in the deployed crystals. The effect of miscut

angles, which occur when the crystalline planes are not perpendicular to the crystal face, have been investigated up to $\pm 75 \mu\text{rad}$, as this is a typical maximum miscut measured from on previously examined crystals. No negative impact on the losses on the superconducting magnets has been detected within this range. This is mainly due to the absorber being positioned close to the crystal transversely in the collimation hierarchy, so that a big fraction of the partially channeled particles can anyway be captured. Another imperfection study done involves the standard collimators. Imperfections have been added to their transverse position and tilt. For the studied parameters, the cleaning performance is impacted to a level of around 20% with respect to the perfect system.

Another part of this thesis work is the exploration of possible backup plans with the standard collimation system for heavy-ion operation. Here, several options have been tested to increase the collimation performance: asymmetric openings of the primary, collimator jaw tilts, and change of optics in the collimation insertion. A study of the influence of the depth of impacting beam on the primary collimator has also been repeated from previous studies. One important takeaway point is that the cleaning performance generally improves with the increasing depth of the impacting beam, while this is not true for crystal collimation. The cleaning performance has been studied with only one of the two jaws of the primary collimator in the horizontal plane at the beam and it has been found that one jaw performs better than the other. Collimator jaw tilt studies also gave the promising result that a collimator aligned longitudinally to the beam envelope would be able to give a major decrease in losses in the superconducting magnet region. However, these risks will be very difficult to implement operationally due to the required angular precision. Finally, the cleaning performance with standard collimation and a new optics in IR7 has been explored in simulation, and an improvement of around a factor of two with respect to the traditional ion optics has been found. Future work might include studies of a new optics for a crystal-based system. A final collimation configuration has not been proposed for this run with the standard collimation, although the findings outlined here may prove to be useful for the design of future configurations.

On the subject of future Pb runs in Run 4, the simulation setup has been used to give predictions on the cleaning performance at the High-Luminosity LHC energy. The simulation predicts that the current crystal setup should give a similar performance at 7 Z TeV, as the channeling efficiency does not change greatly from 6.8 Z TeV.

Finally, exploratory studies have been done of the crystal collimation performance with other ion species than Pb, which are under consideration for operation if the LHC ion physics program would be extended beyond Run 4. A series of ion species have been investigated. It has been found that the collimation performance improves with decreasing atomic number, however, the stored beam energy will also increase. Future energy deposition studies are needed for each specific case in order to say with certainty if the cleaning performance will be sufficient for the considered ion beams. The detailed isotopic composition has also been retrieved for major contributors of the superconducting region.

In summary, by the conclusion of this PhD project, a complete ion crystal simulation framework has been built for particle accelerators. The setup has been extensively tested and benchmarked against measured LHC data yielding generally good results. The simulation tool has been used to explore the characteristics of ion crystal collimation and to probe methods of configuration optimization. The results gathered thanks to these studies were a major contributor to the collimation in the 2023 Pb ion run, which is the first time in history that crystal collimation is used regularly in LHC operation in high-intensity physics fills, as well as during an extended time period of several weeks. Finally, the thesis ends with the studies done for alternative scenarios to heavy-ion crystal collimation including standard collimation and crystal collimation for other ion species than Pb, which provide important inputs to the design of the future LHC ion physics program.

A Appendix

This Chapter provides a series of measured loss maps comparisons presented in previous chapters normalized to the total BLM energy lost in the ring instead of dI/dt as described in Eq. 4.17.

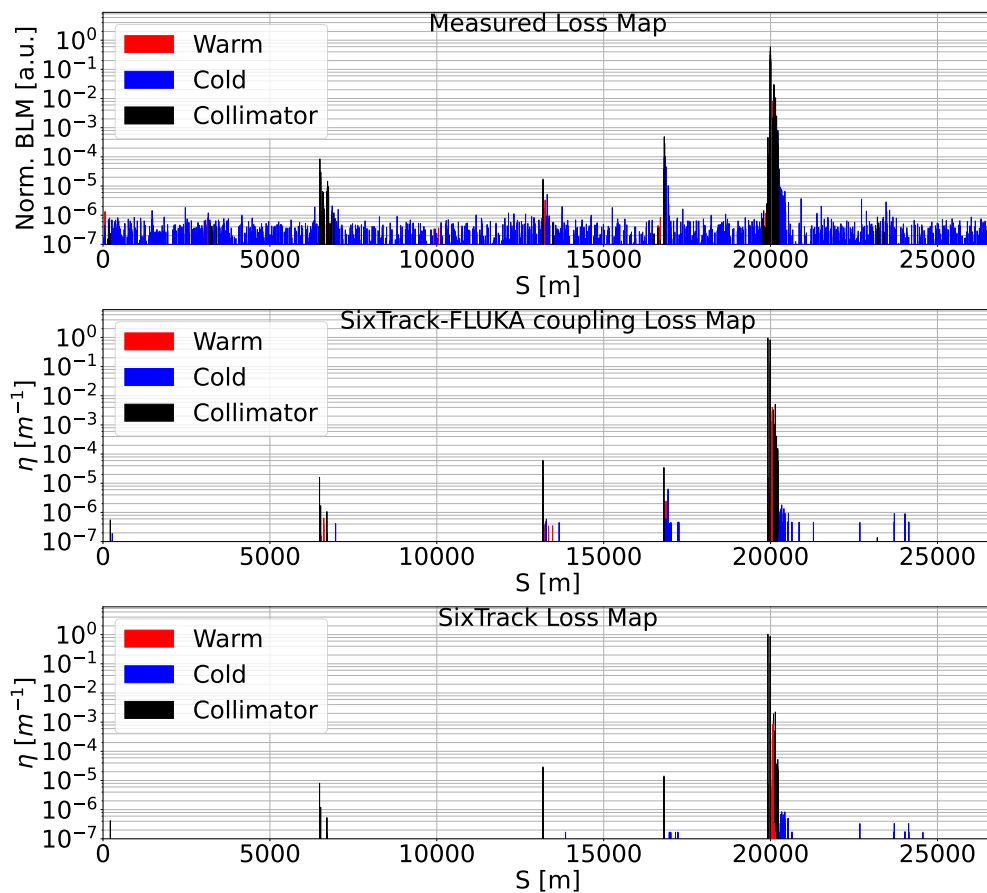


Figure A.1 – Measured (top), SixTrack-FLUKA coupling simulated (middle) and SixTrack simulated (bottom) loss map from the B1H 2018 proton test at 6.5 TeV ($\beta^* = 1$ m).

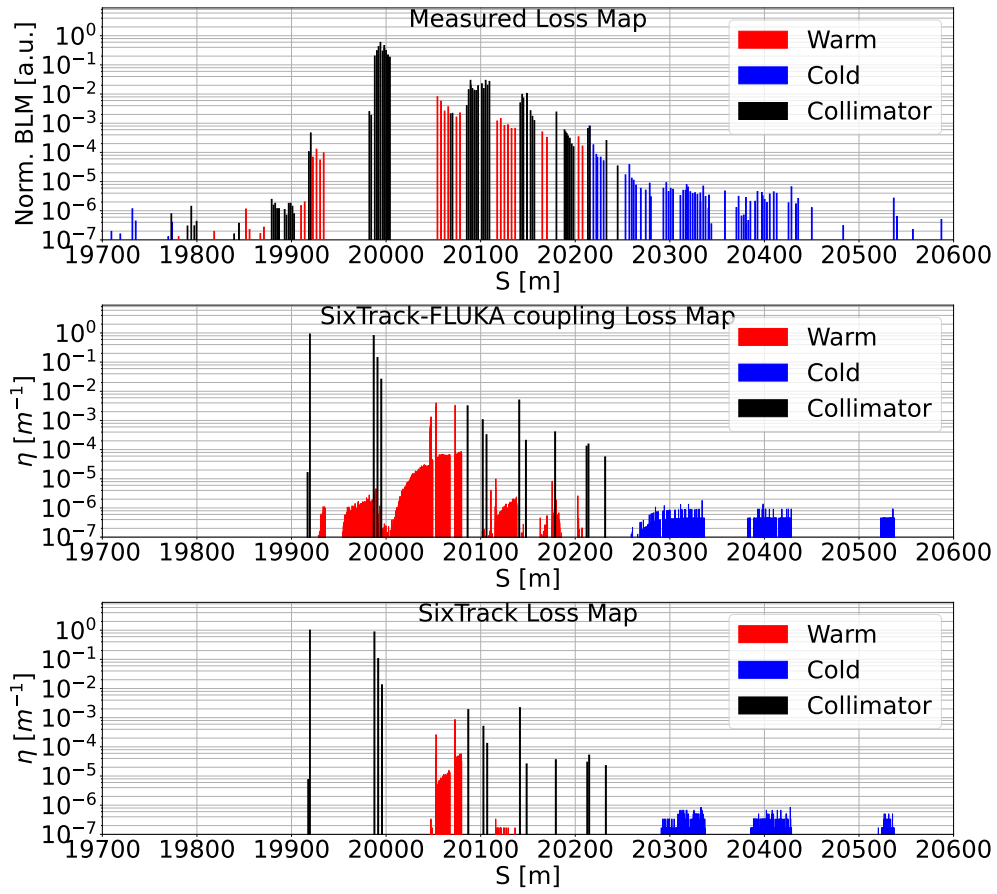


Figure A.2 – Measured (top), SixTrack-FLUKA coupling simulated (middle) and SixTrack simulated (bottom) loss map from the 2018 proton test at 6.5 TeV, as in Fig. 7.6 but zoomed around IR7. The crystal can be found at 19919.5 m and the absorber at 19987 m.

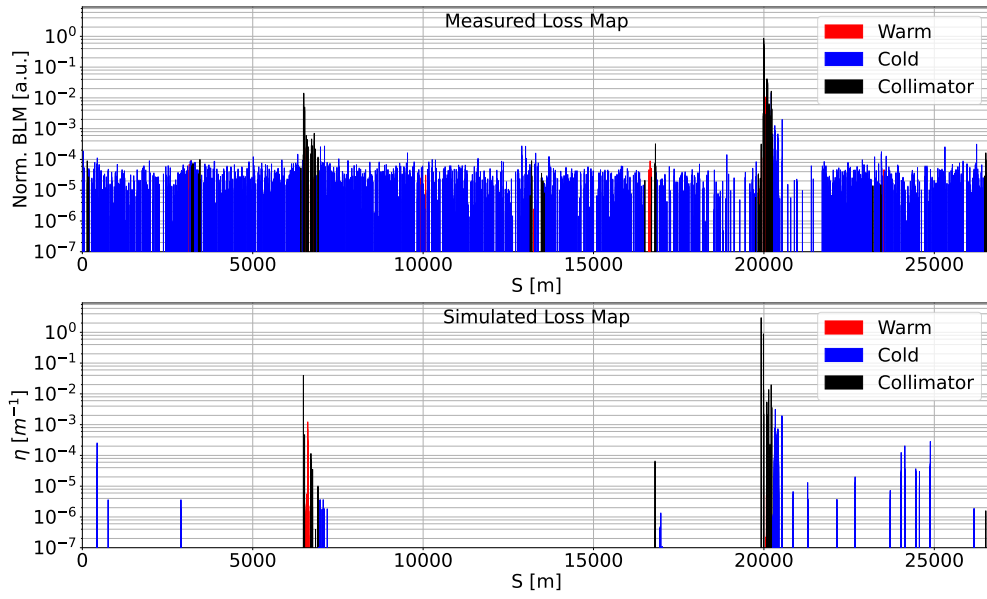


Figure A.3 – Measured (top) and simulated (bottom) loss map for B1H 2018 Pb run at 6.37 Z TeV.

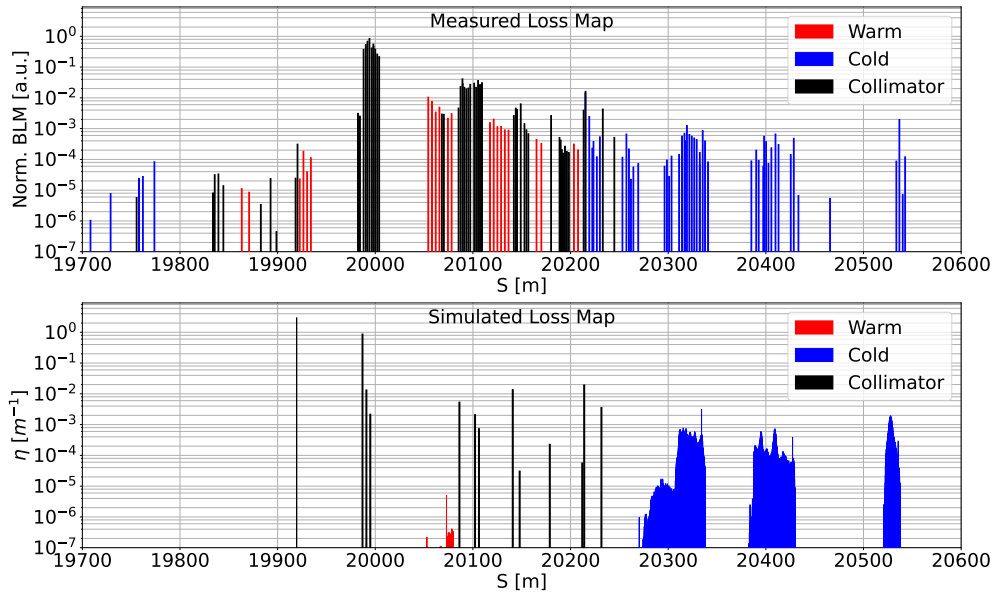


Figure A.4 – Measured (top) and simulated (bottom) loss map around IR7 for 2018 Pb run at 6.37 Z TeV.

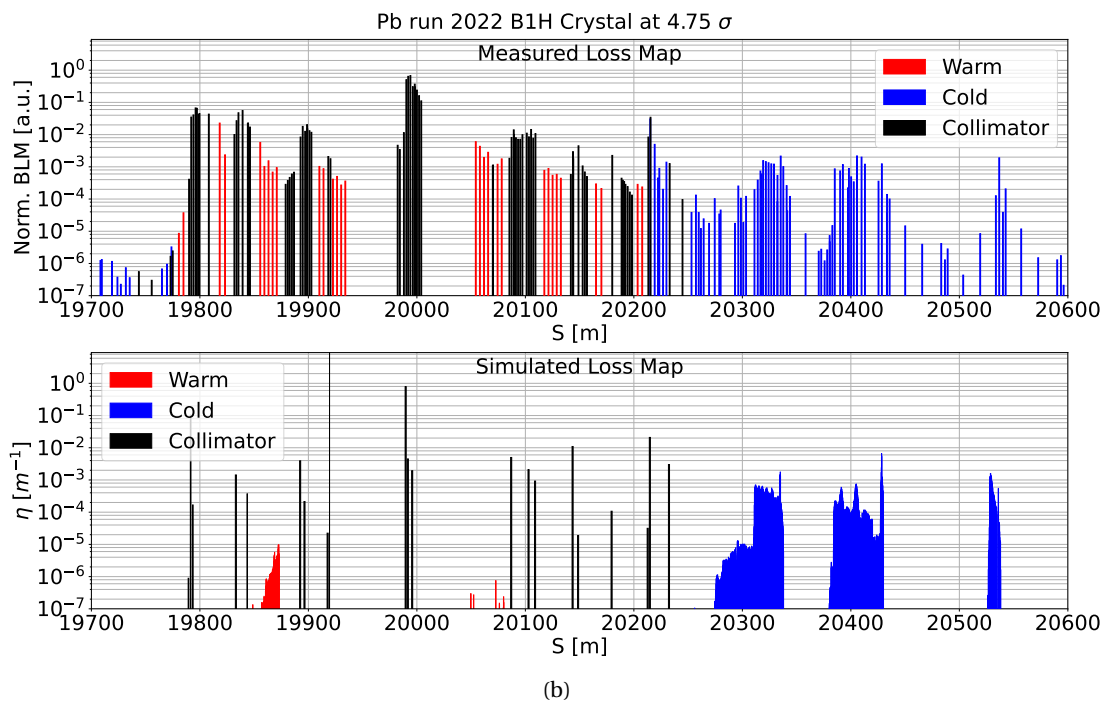
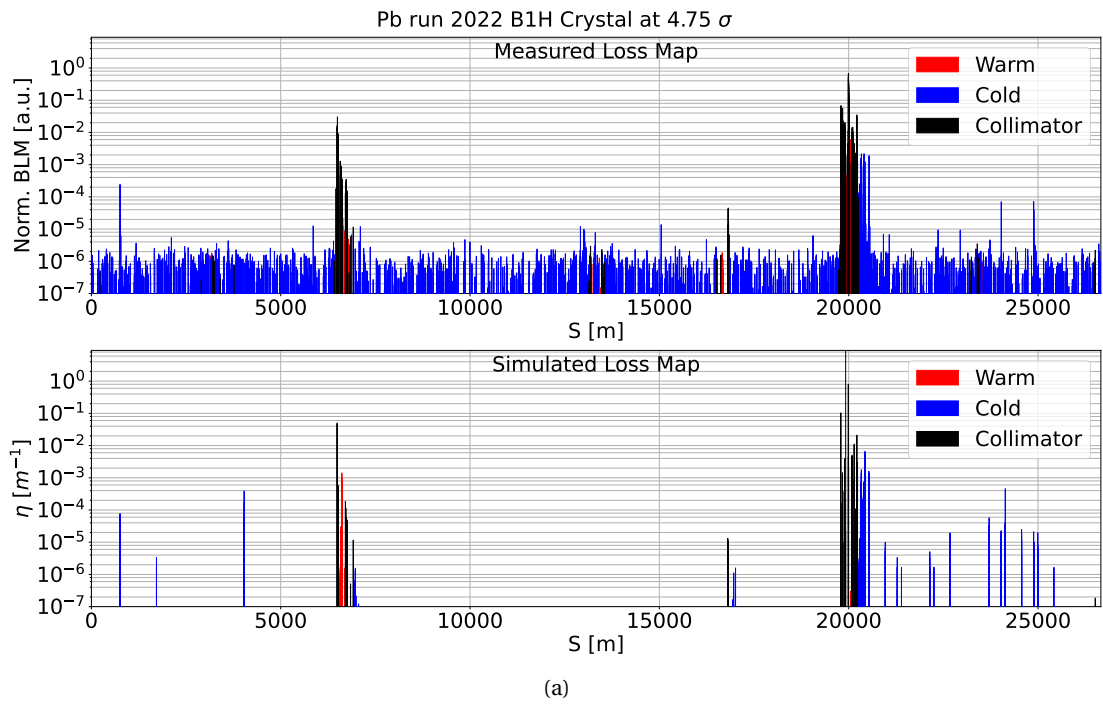


Figure A.5 – (a): Measured (top) and simulated (bottom) loss map for B1H 2022 Pb test crystal collimation in channeling at $6.8 Z$ TeV *physics*. (b): zoom in IR7.

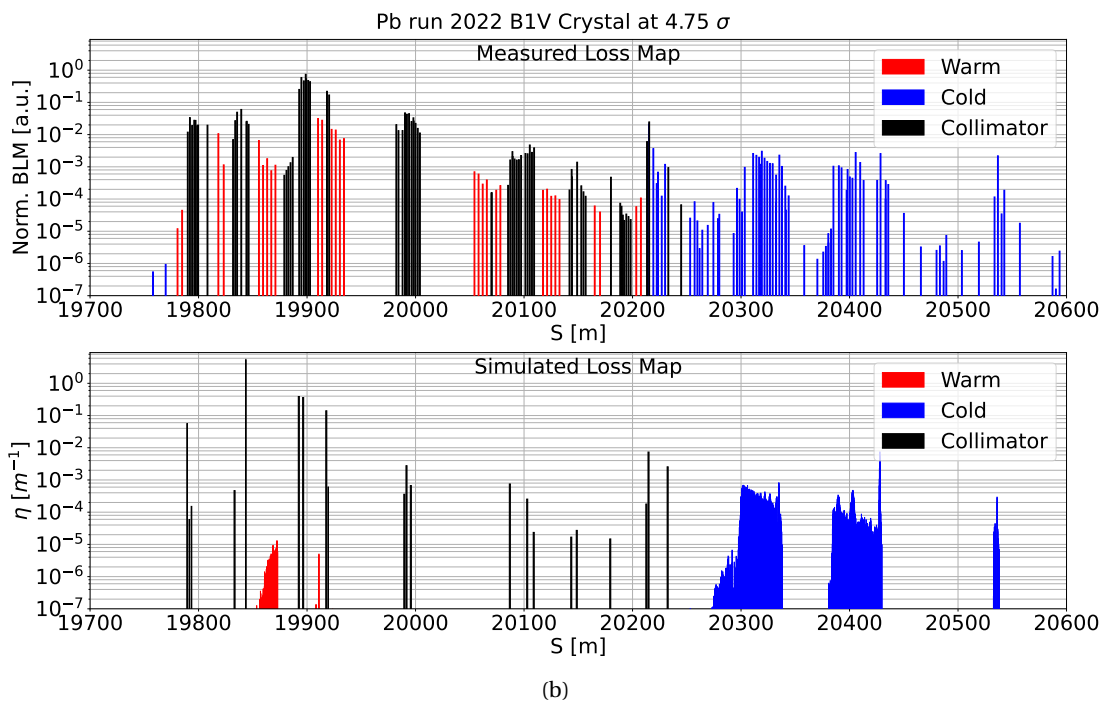
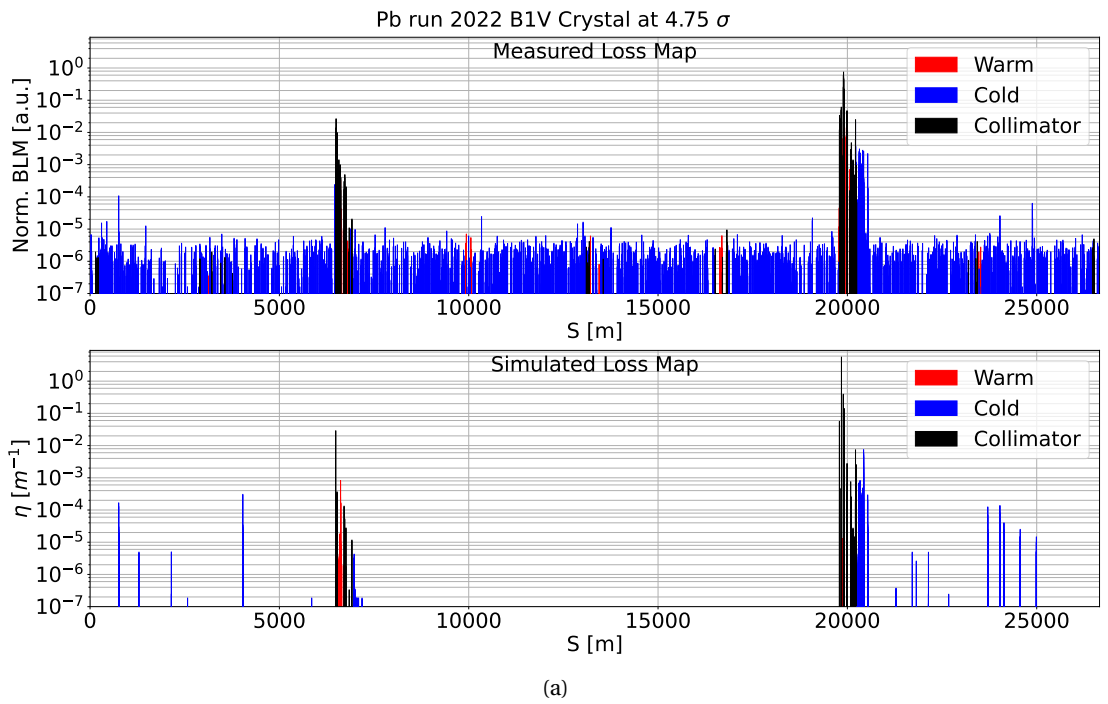


Figure A.6 – (a): Measured (top) and simulated (bottom) loss map for B1V 2022 Pb test crystal collimation in channeling at 6.8 Z TeV *physics*. (b): zoom in IR7.

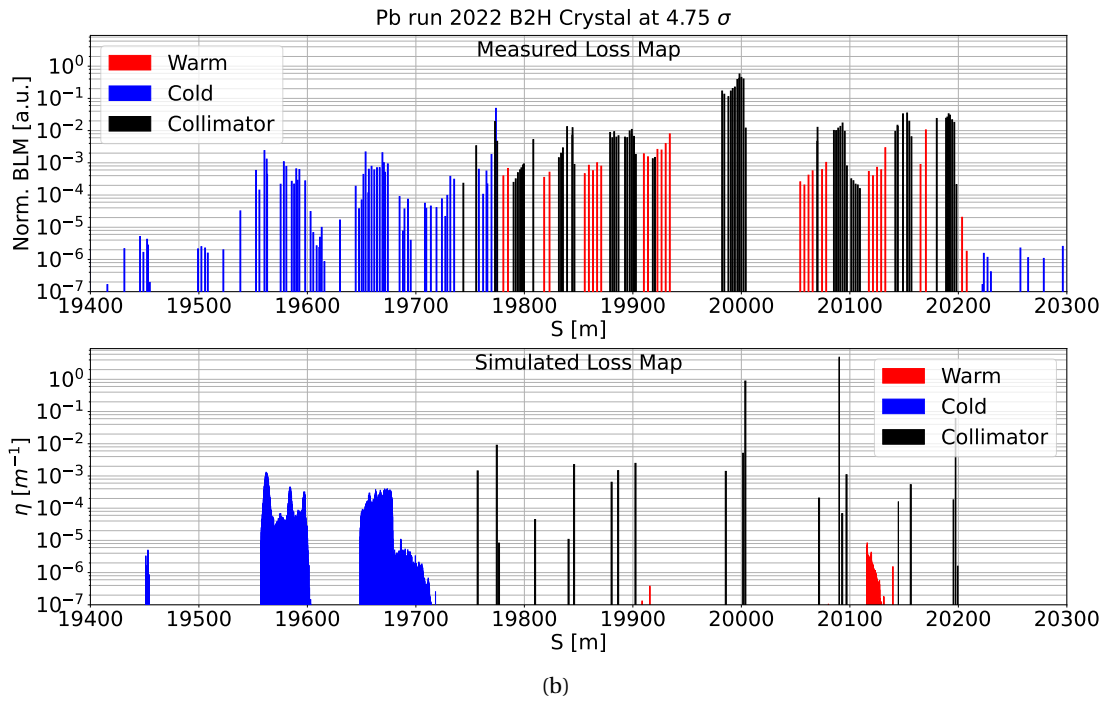
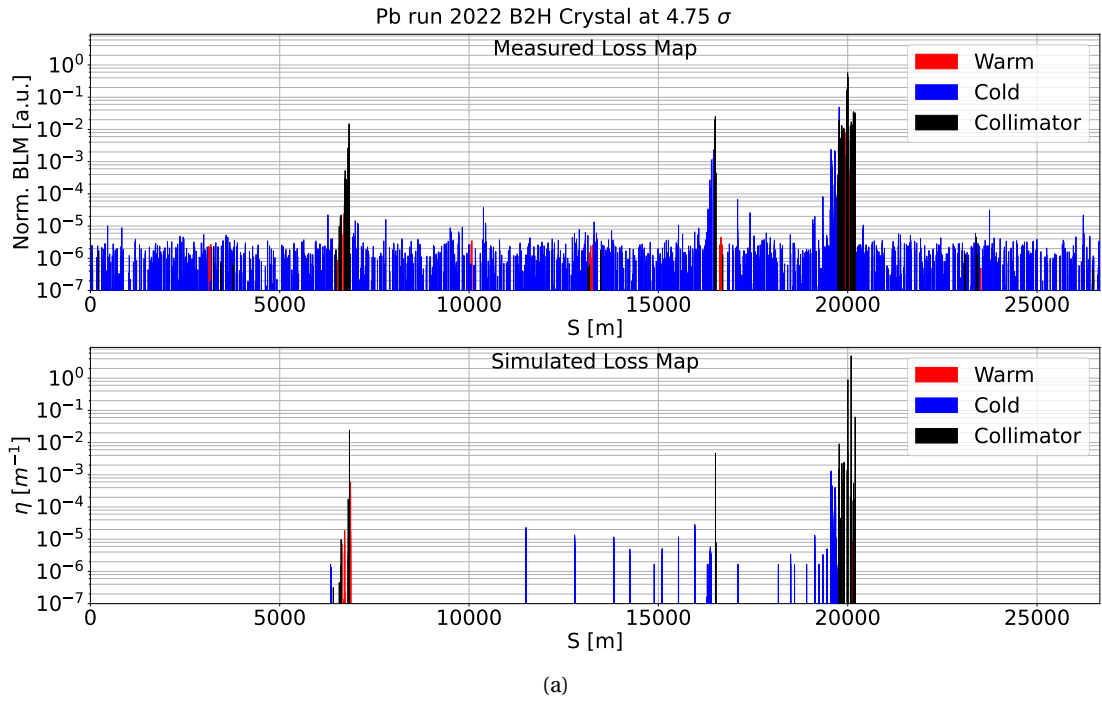


Figure A.7 – (a): Measured (top) and simulated (bottom) loss map for B2H 2022 Pb test crystal collimation in channeling at $6.8 Z$ TeV *physics*. (b): zoom in IR7.

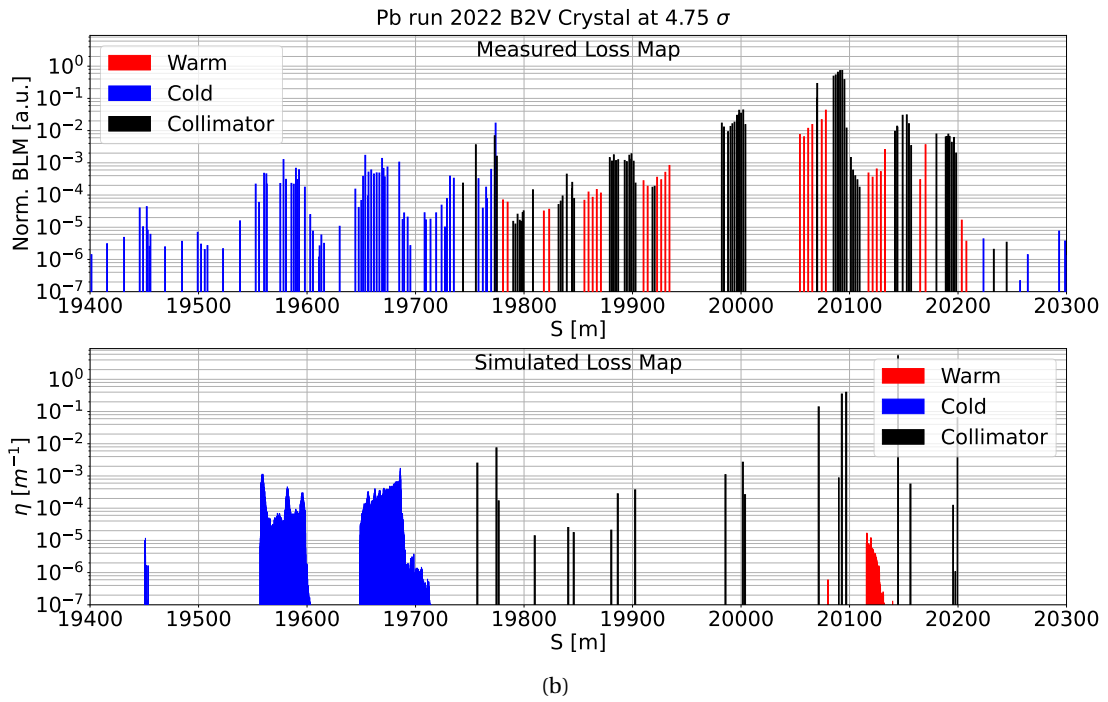
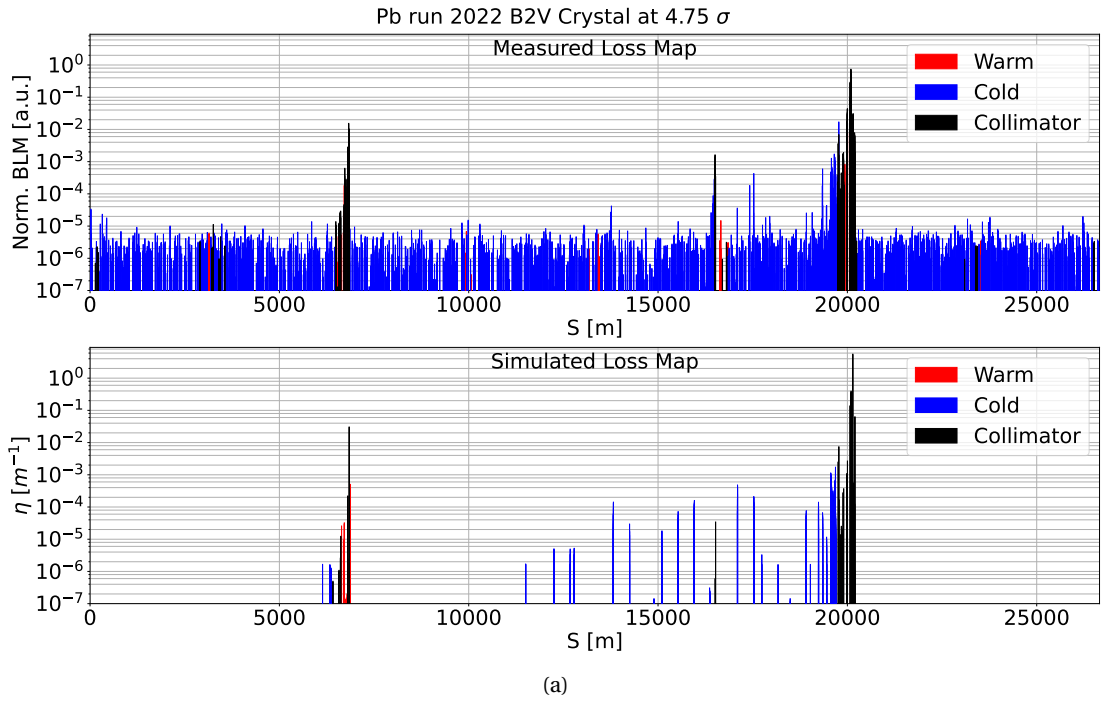
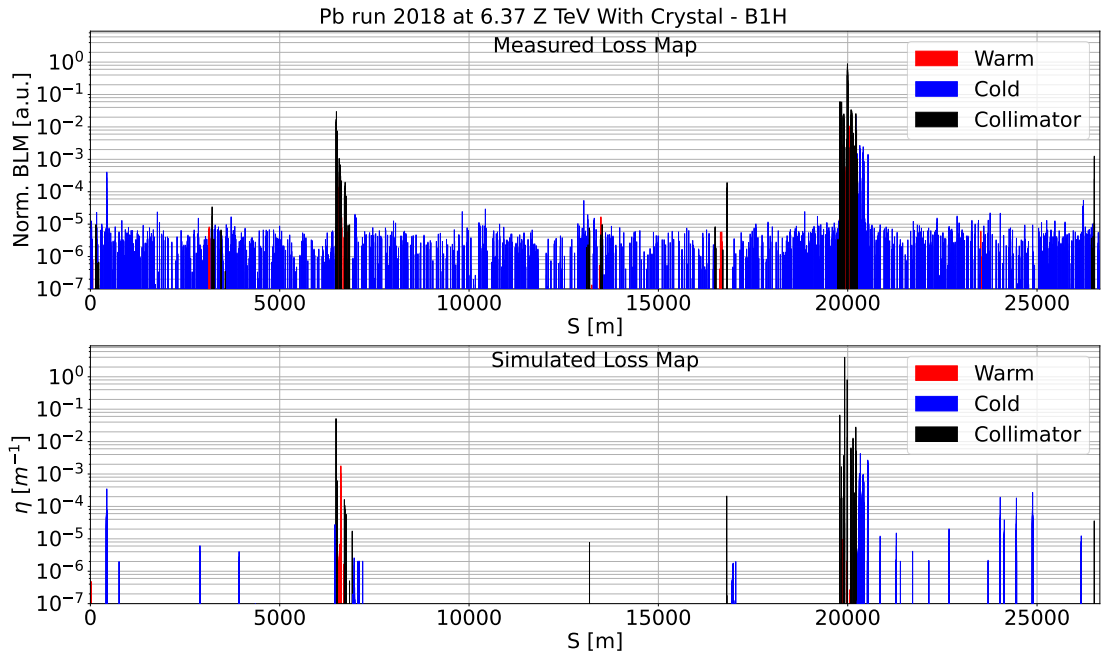
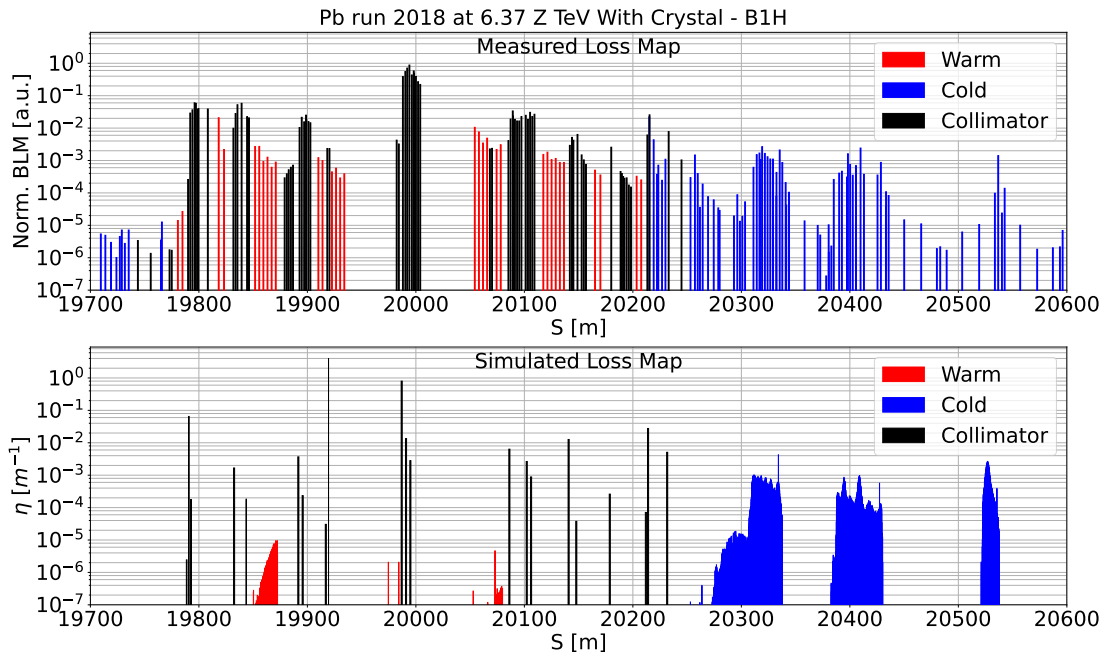


Figure A.8 – (a): Measured (top) and simulated (bottom) loss map for B2V 2022 Pb test crystal collimation in channeling at 6.8 Z TeV *physics*. (b): zoom in IR7.



(a)



(b)

Figure A.9 – Measured (top) and simulated (bottom) loss map comparison for 2018 B1H crystal collimation in channeling at 6.37 Z TeV *physics*. (a): full ring; (b): zoom in IR7.

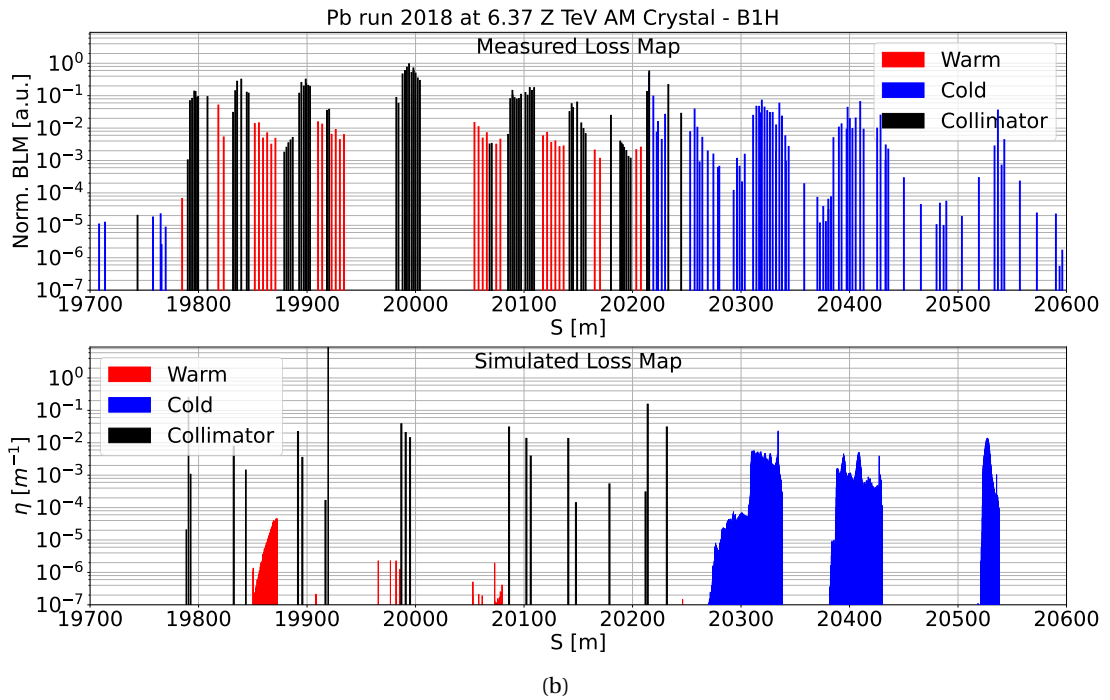
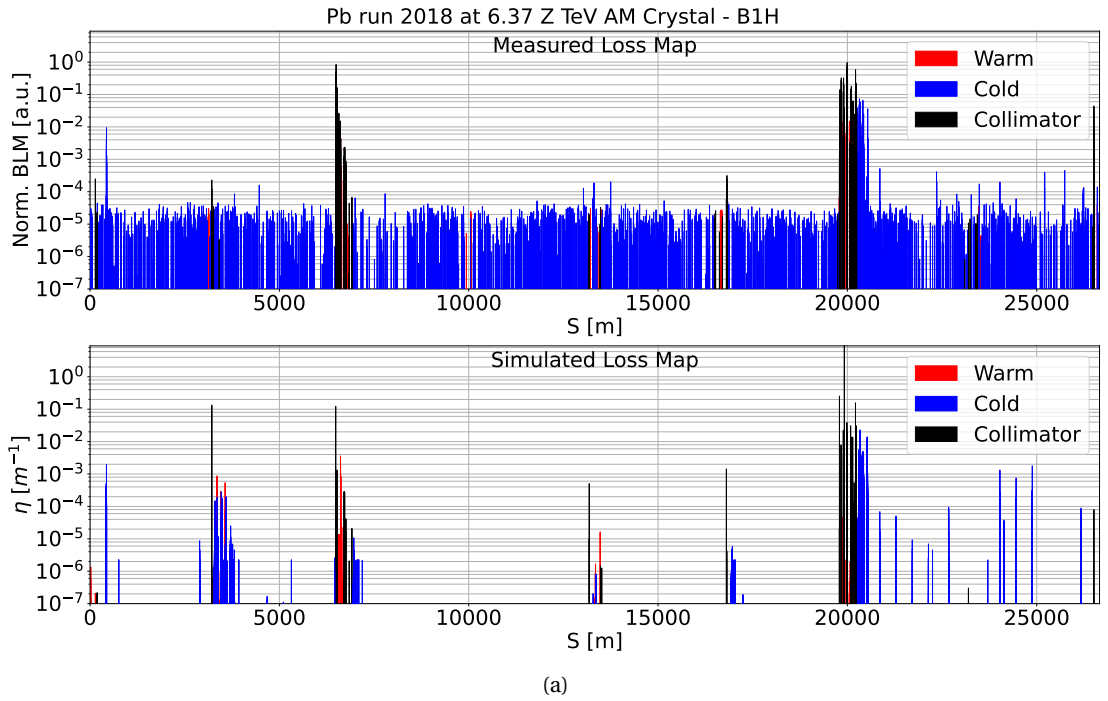


Figure A.10 – Measured (top) and simulated (bottom) loss map comparison for 2018 B1H crystal collimation in amorphous at 6.37 Z TeV *physics*. (a): full ring; (b): zoom in IR7.

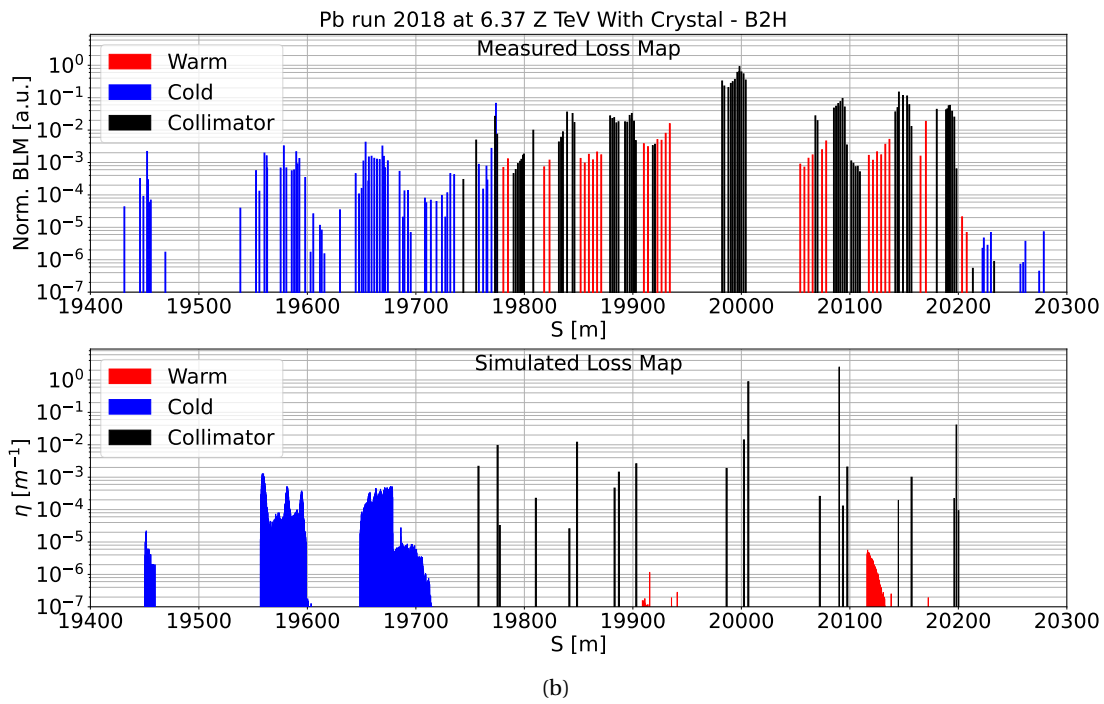
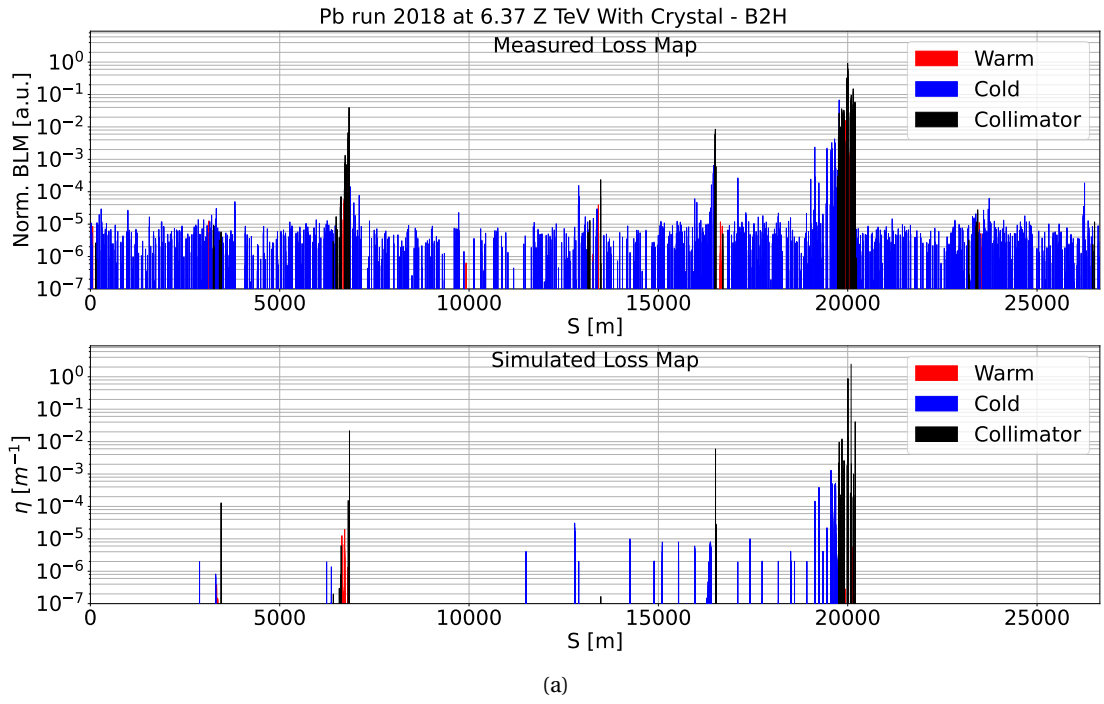


Figure A.11 – Measured (top) and simulated (bottom) loss map comparison for 2018 B2H crystal collimation in channeling at 6.37 Z TeV *physics*. (a): full ring; (b): zoom in IR7.

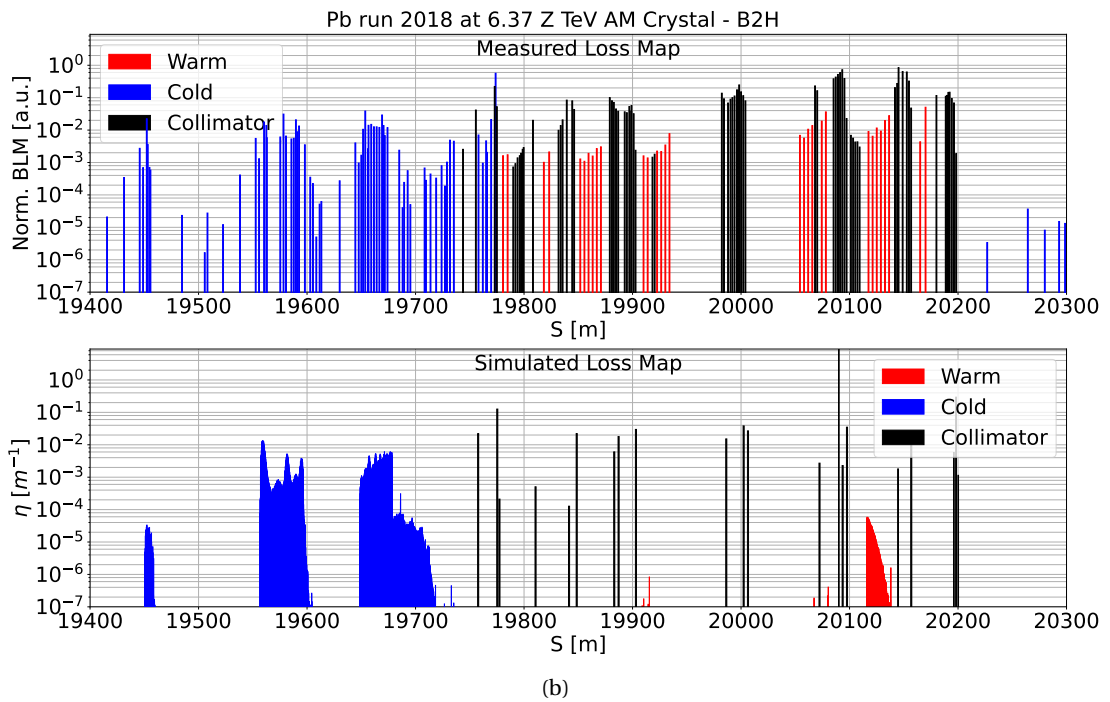
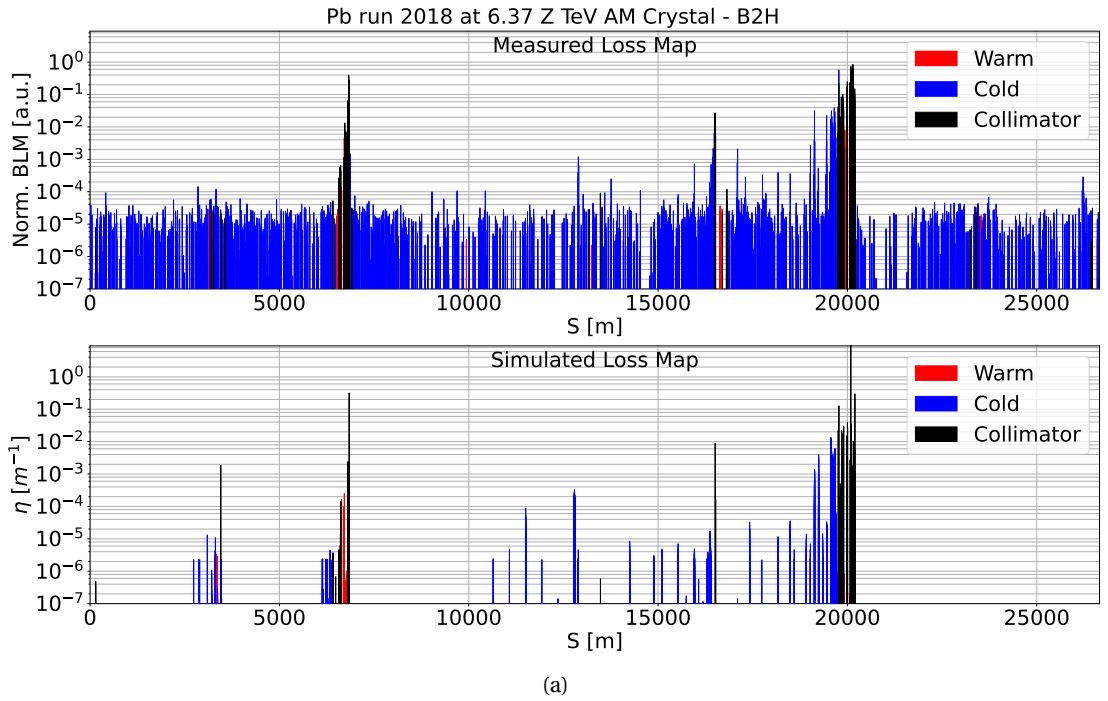


Figure A.12 – Measured (top) and simulated (bottom) loss map comparison for 2018 B2H crystal collimation in channeling at 6.37 Z TeV *physics*. (a): full ring; (b): zoom in IR7.

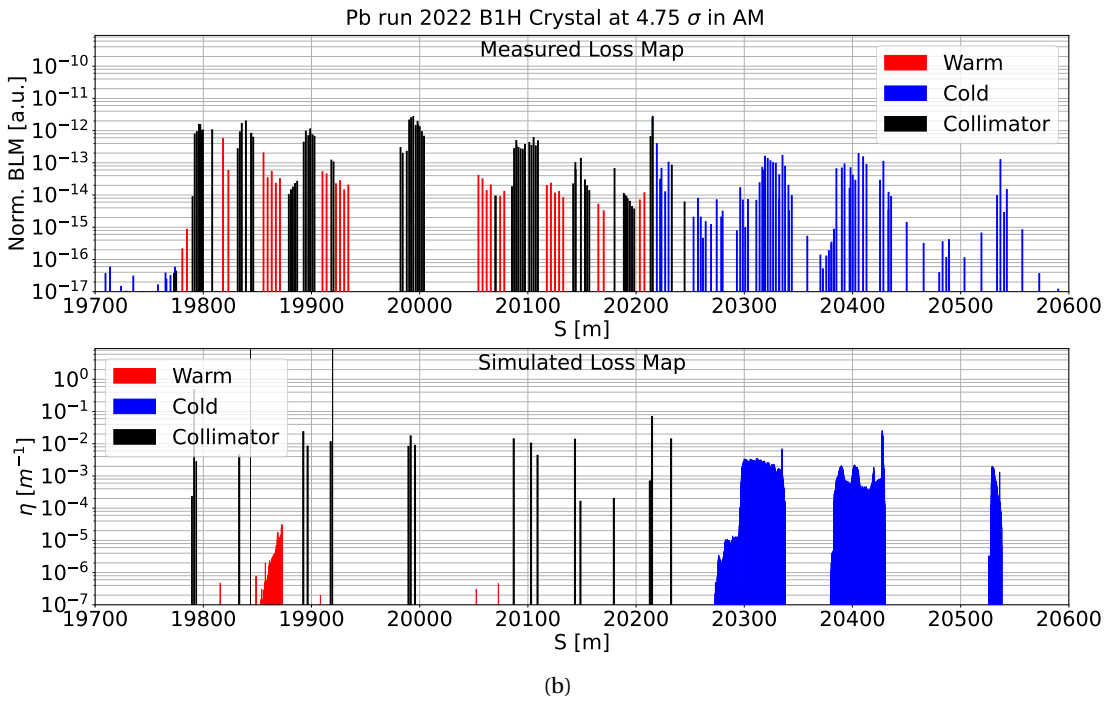
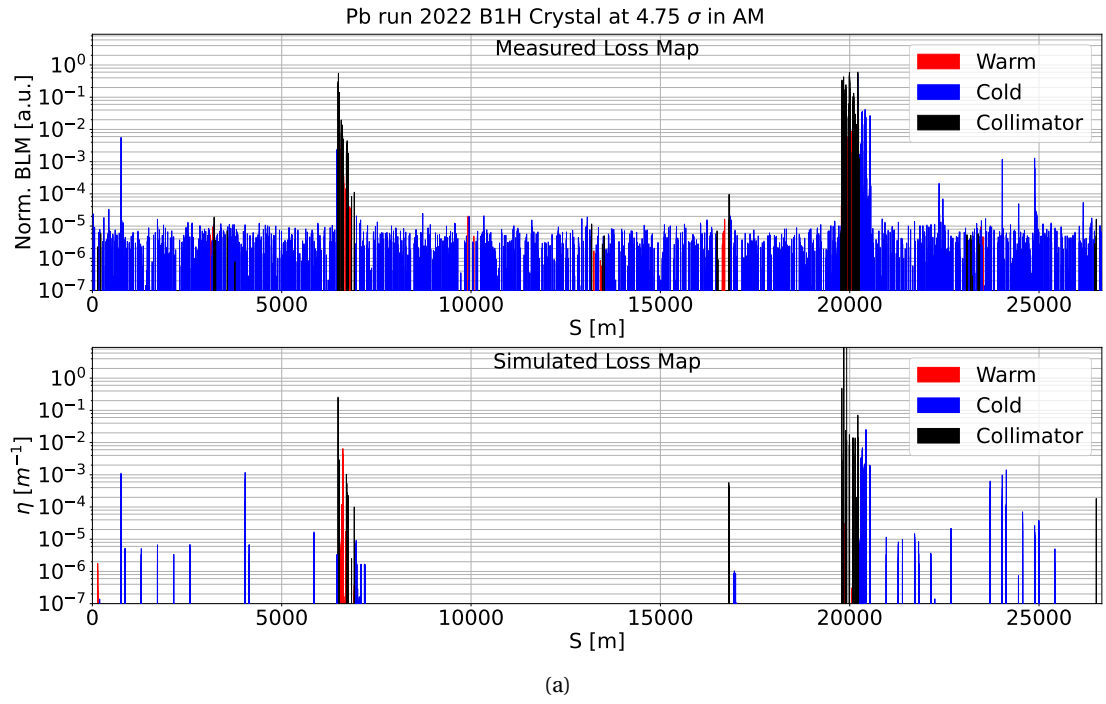


Figure A.13 – (a): Measured (top) and simulated (bottom) loss map for B1H 2022 Pb test crystal collimation in amorphous at 6.8 Z TeV *flat-top*. (b): zoom in IR7.

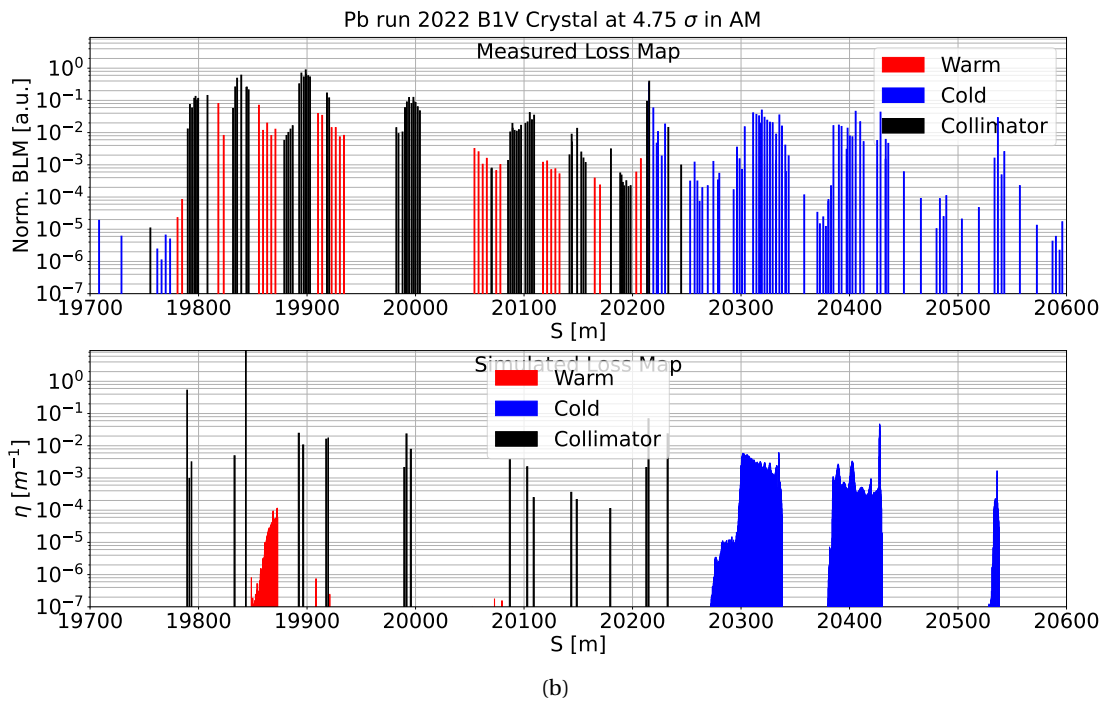
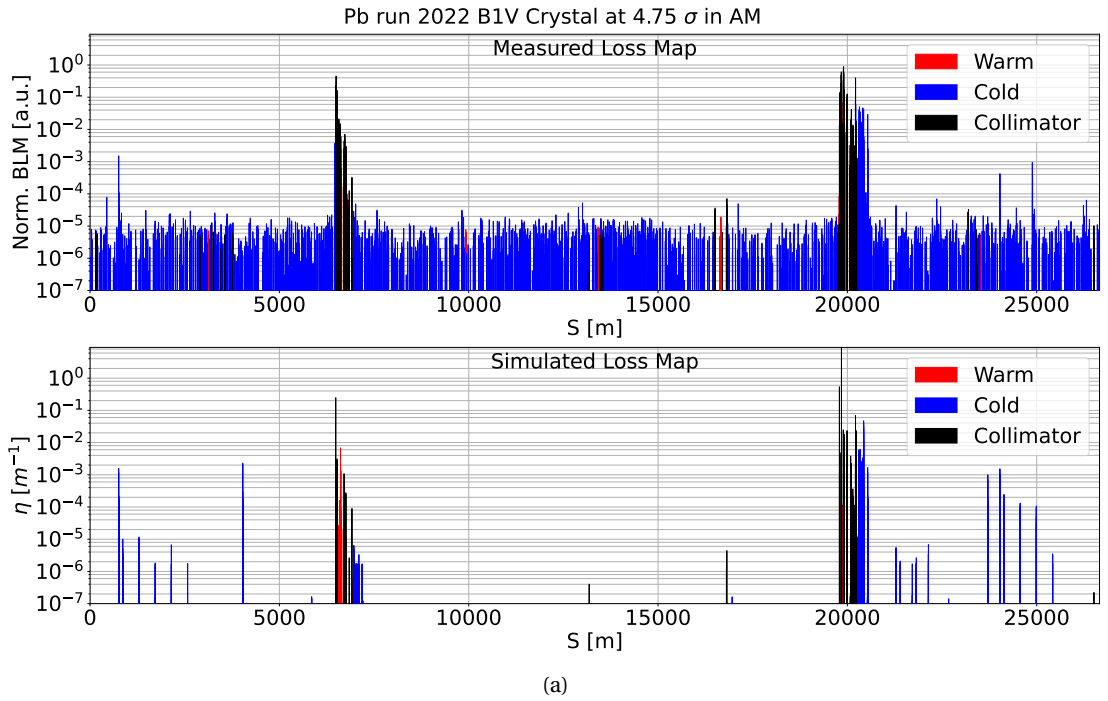


Figure A.14 – (a): Measured (top) and simulated (bottom) loss map for B1V 2022 Pb test crystal collimation in amorphous at 6.8 Z TeV flat-top. (b): zoom in IR7.

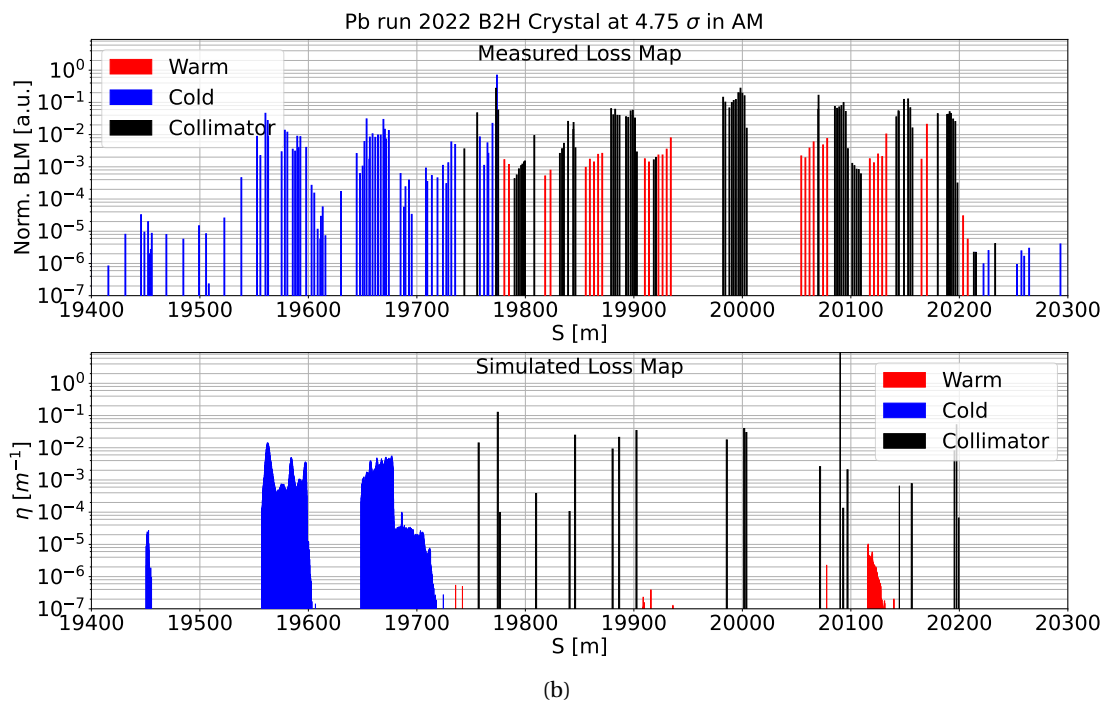
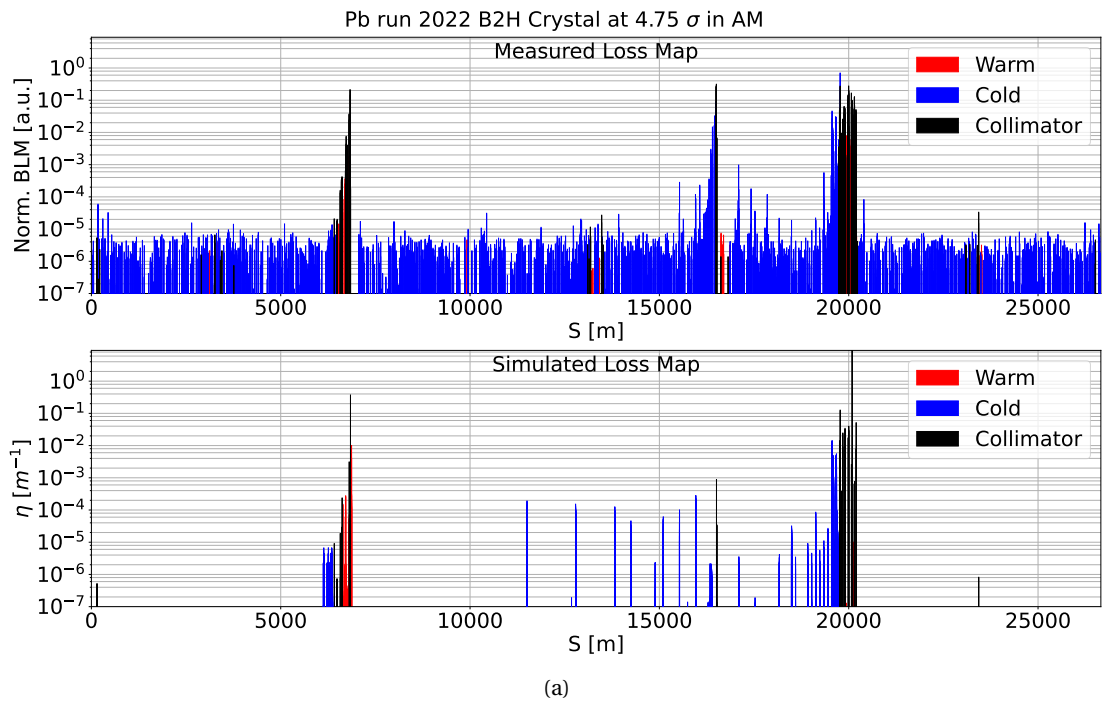


Figure A.15 – (a): Measured (top) and simulated (bottom) loss map for B2H 2022 Pb test crystal collimation in amorphous at 6.8 Z TeV flat-top. (b): zoom in IR7.

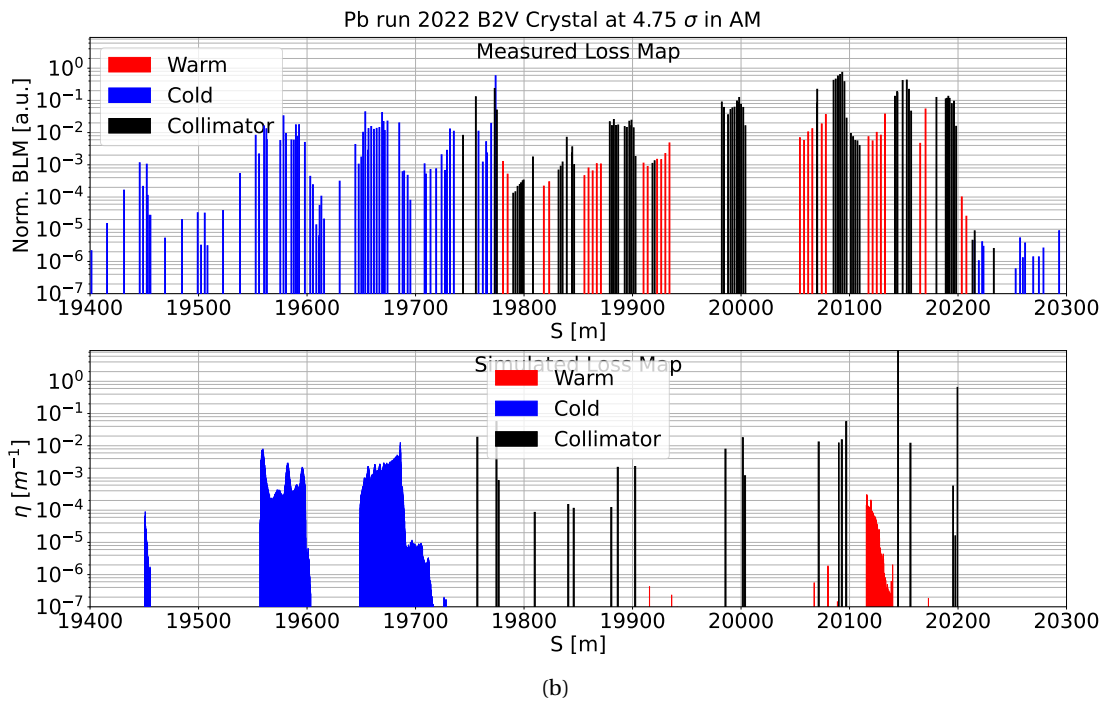
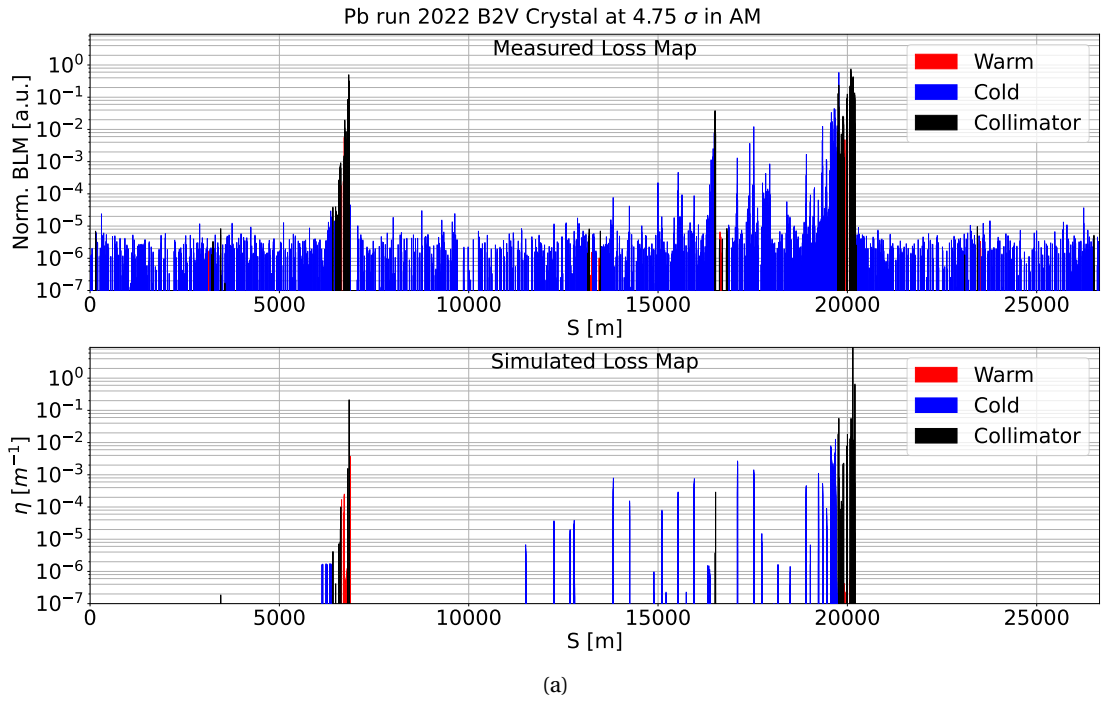


Figure A.16 – (a): Measured (top) and simulated (bottom) loss map for B2V 2022 Pb test crystal collimation in amorphous at 6.8 Z TeV flat-top. (b): zoom in IR7.

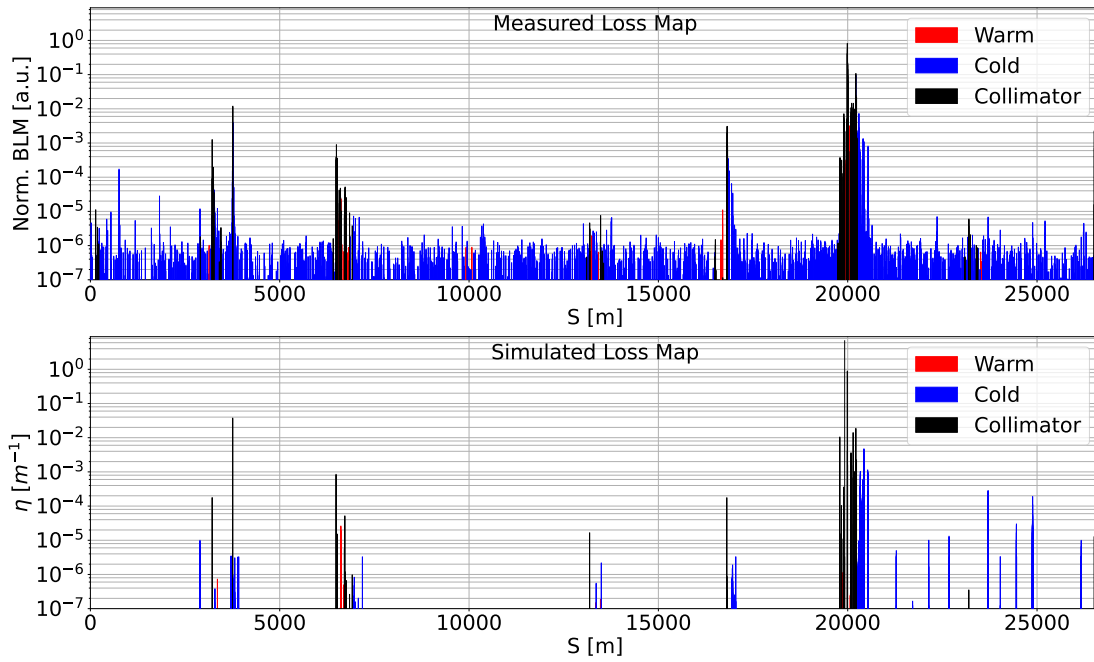


Figure A.17 – Measured (top) and simulated (bottom) 2023 loss map in B1H with 6.8 Z TeV $^{208}\text{Pb}^{82+}$ and final collision collimation setup (Table 8.5).

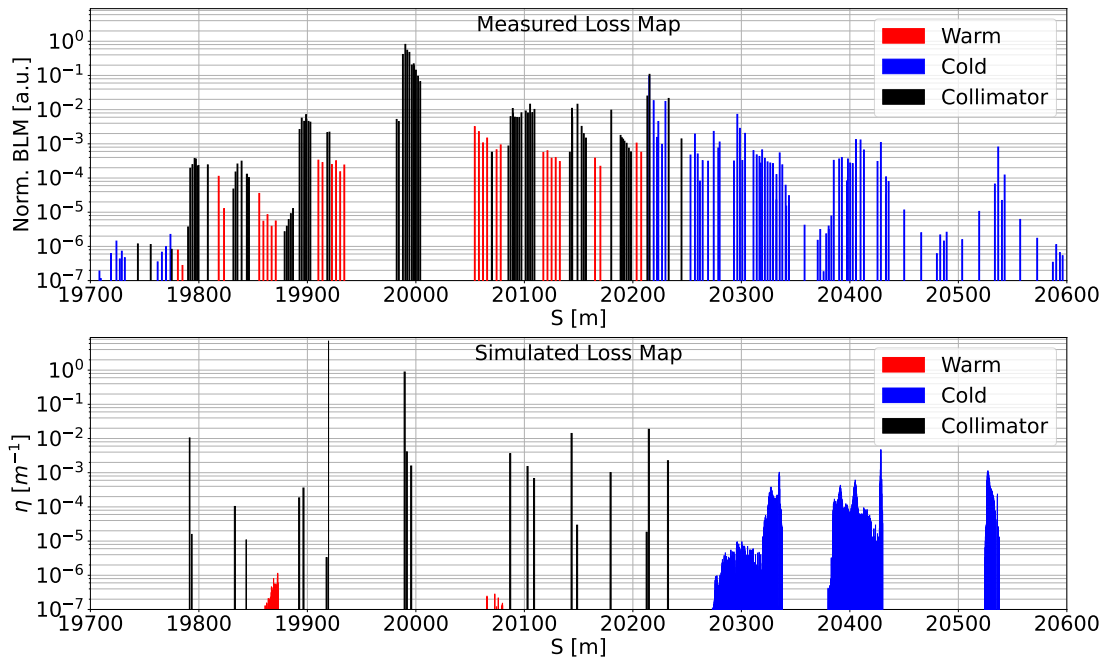


Figure A.18 – IR7 zoom of measured (top) and simulated (bottom) 2023 loss map in B1H with 6.8 Z TeV $^{208}\text{Pb}^{82+}$ and final collision collimation setup (Table 8.5).

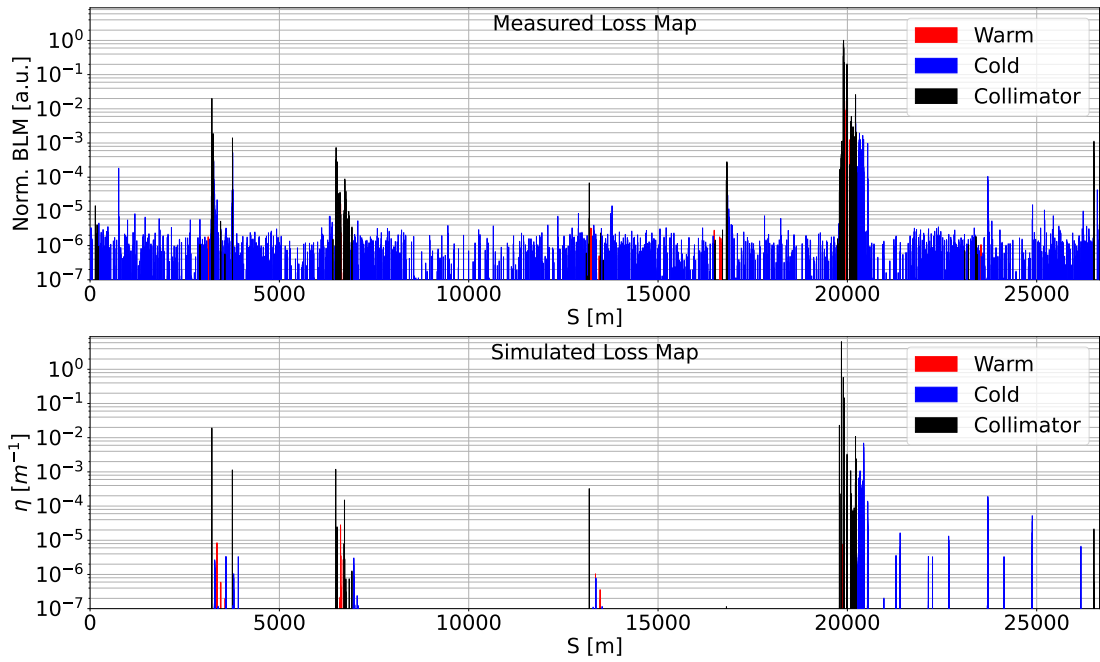


Figure A.19 – Measured (top) and simulated (bottom) 2023 loss map in BIV with 6.8 Z TeV $^{208}\text{Pb}^{82+}$ and final collision collimation setup (Table 8.5).

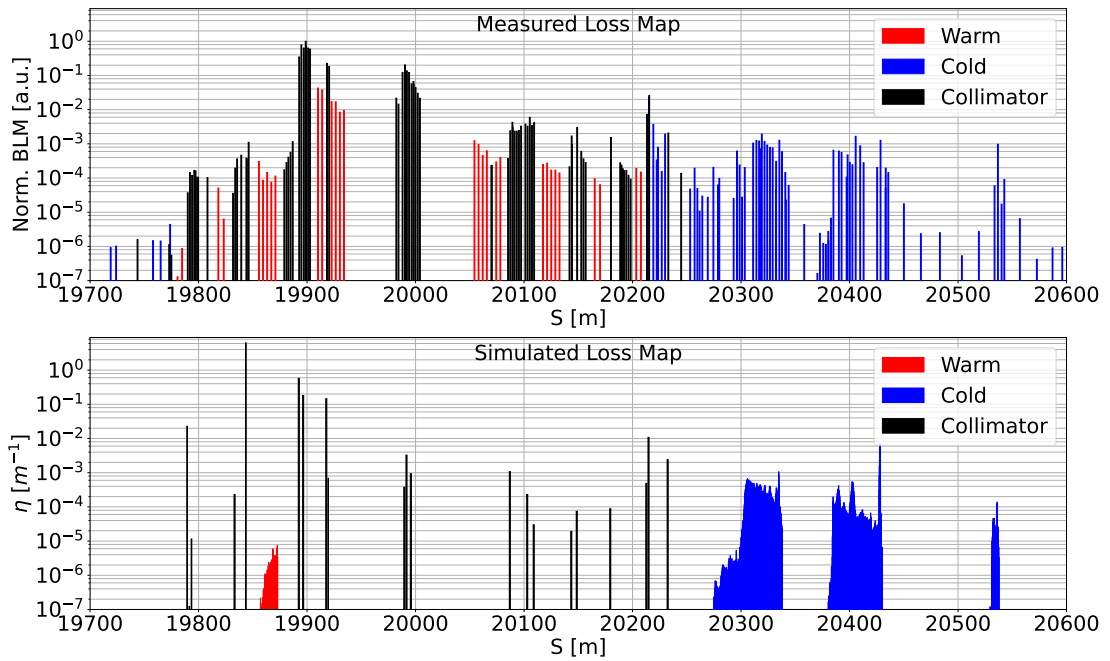


Figure A.20 – IR7 zoom of measured (top) and simulated (bottom) 2023 loss map in BIV with 6.8 Z TeV $^{208}\text{Pb}^{82+}$ and final collision collimation setup (Table 8.5).

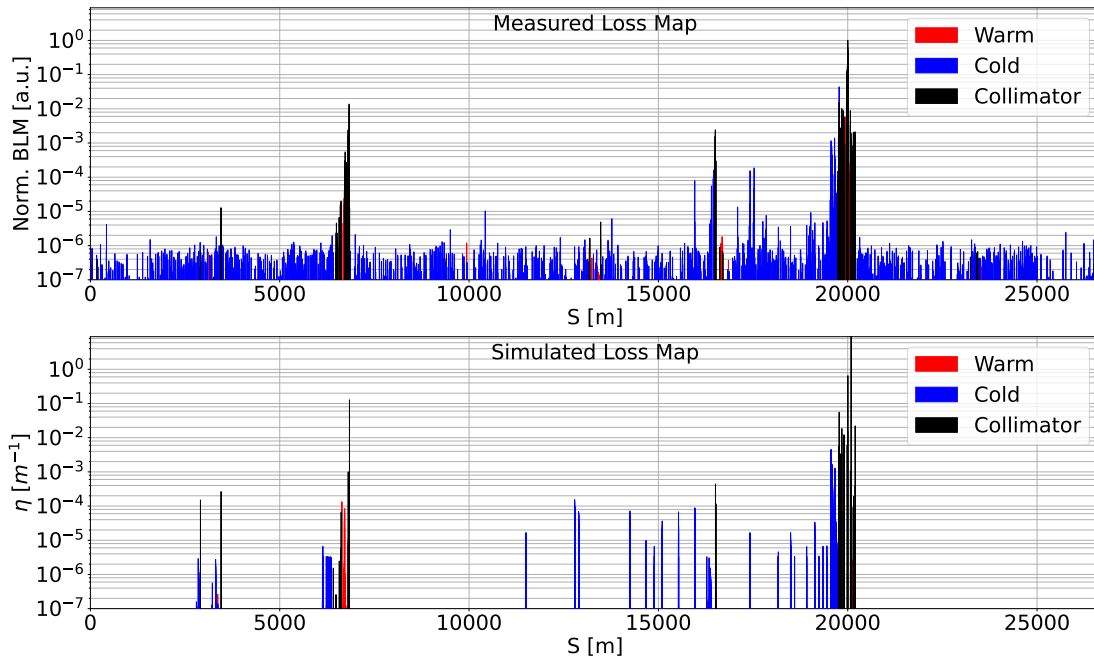


Figure A.21 – Measured (top) and simulated (bottom) 2023 loss map in B2H with 6.8 Z TeV $^{208}\text{Pb}^{82+}$ and final collision collimation setup (Table 8.5).

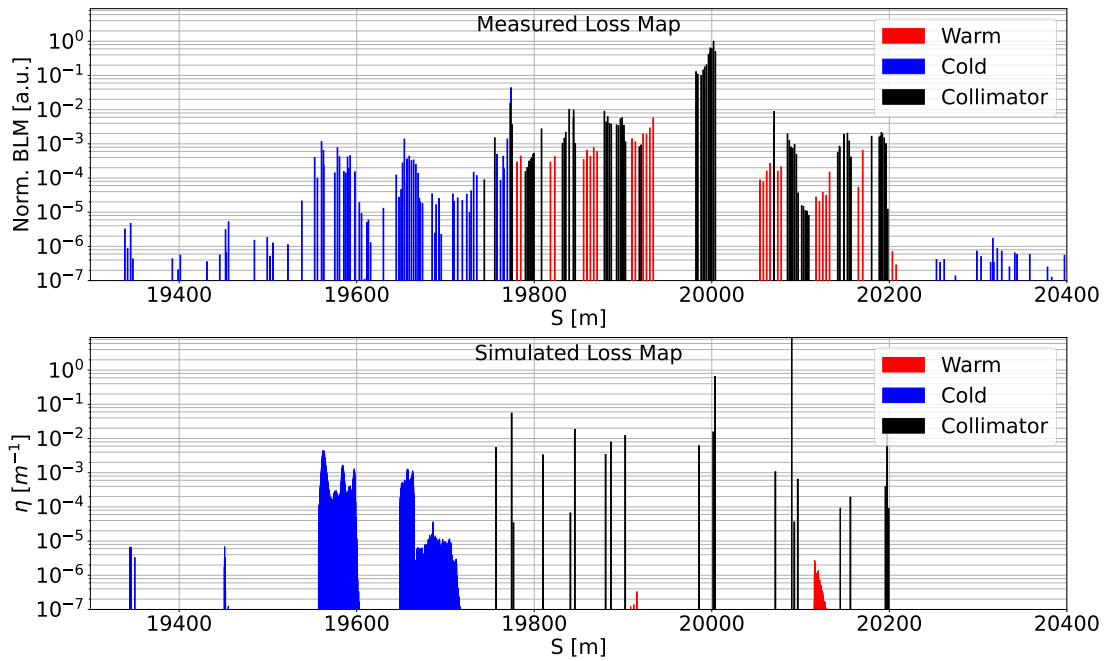


Figure A.22 – IR7 zoom of measured (top) and simulated (bottom) 2023 loss map in B2H with 6.8 Z TeV $^{208}\text{Pb}^{82+}$ and final collision collimation setup (Table 8.5).

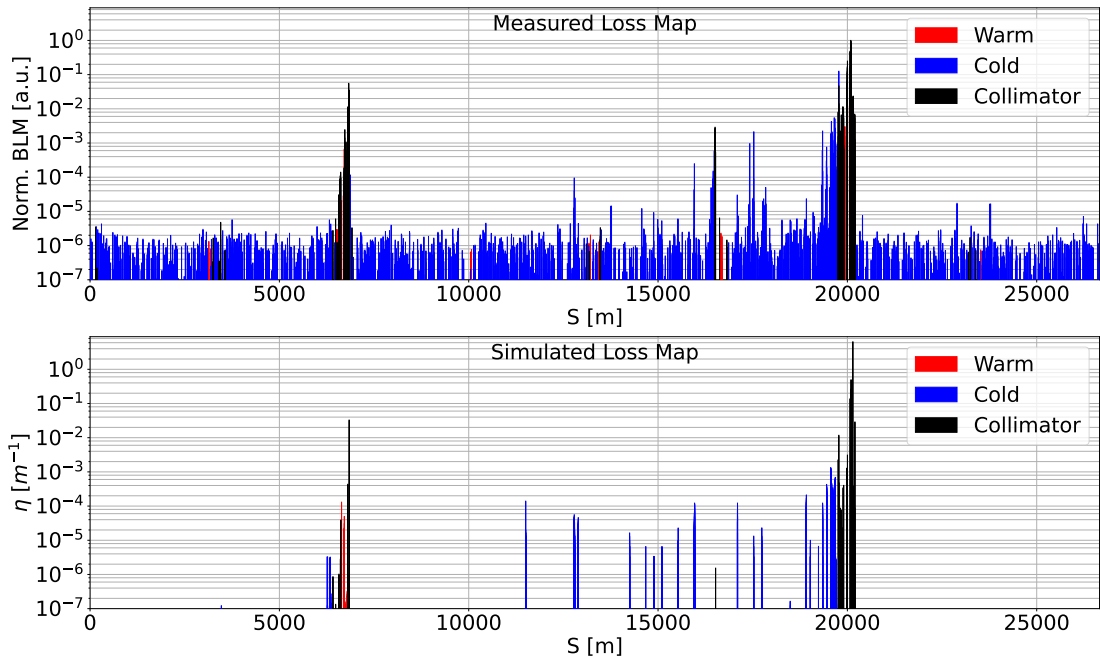


Figure A.23 – Measured (top) and simulated (bottom) 2023 loss map in B2V with 6.8 Z TeV $^{207}\text{Pb}^{82+}$ and final collision collimation setup (Table 8.5).

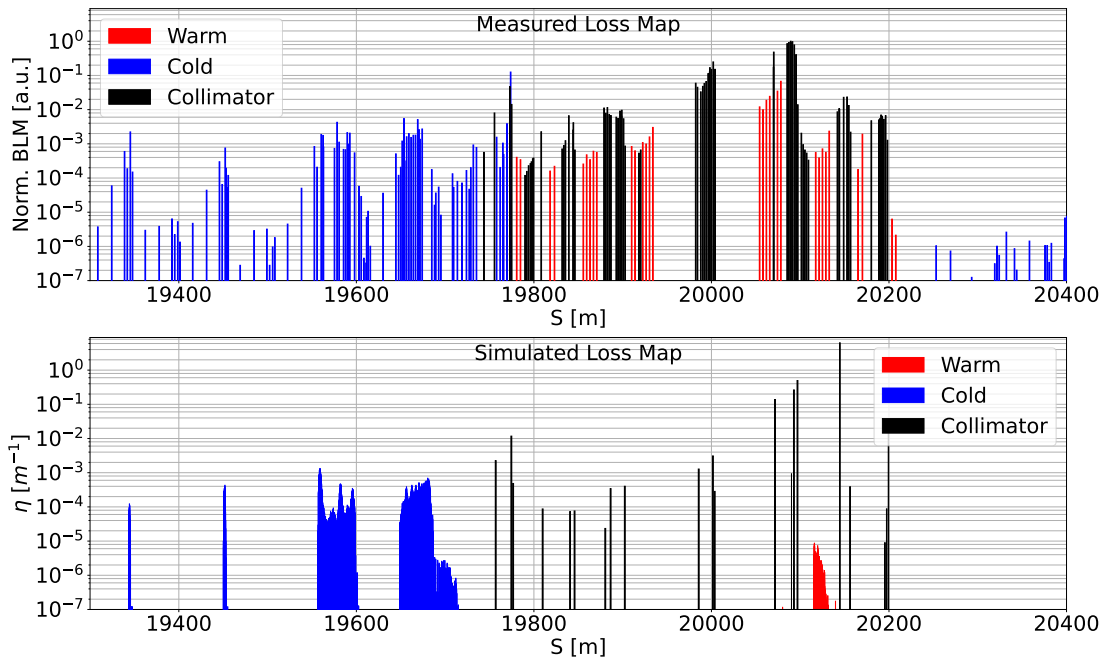


Figure A.24 – IR7 zoom of measured (top) and simulated (bottom) 2023 loss map in B2V with 6.8 Z TeV $^{207}\text{Pb}^{82+}$ and final collision collimation setup (Table 8.5).

List of Figures

1.1	Illustration of the Frenet-Serret coordinate system [39].	5
2.1	Example of simple planes and their Miller indices for a cubic unit cell [41]. . . .	13
2.2	Interplanar potential for Si crystals for a) (110) planes and b) (111) planes . . .	14
2.3	Reference system of a positively charged particle in planar channeling.	15
2.4	Debye temperature Θ_D in Silicon as a function of the absolute temperature T . .	17
2.5	Planar potential of a Si crystal at different temperatures.	18
2.6	Illustration of the working principle of a bent crystal.	19
2.7	Effective potential of channeling well of a Si crystal.	20
2.8	Schematic illustration of the volume reflection process in a bent planar crystal.	21
2.9	Schematic illustration of the dechanneling process in a bent planar crystal. . .	22
2.10	Schematic illustration of the volume capture process in a bent planar crystal. .	23
3.1	Schematic illustration of the CERN complex [52].	26
3.2	LHC layout.	27
3.3	Schematic layout and optical functions of an experimental IR.	28
4.1	Representation of the impact parameter, b , on a collimator jaw [37].	34
4.2	Schematic layout of all collimators in the LHC.	34
4.3	Illustration of the collimation cleaning hierarchy from [37] adapted from [76]. .	35

4.4	Primary and secondary collimator normalized angular kick in normalized phase-space.	38
4.5	Working principle of crystal collimation [24].	45
4.6	Left – Schematic drawing of a goniometer. Right – (110) crystal in its holder [25].	45
5.1	Working principle schematic of the SixTrack-FLUKA Coupling	52
5.2	Transverse projection in the x-z plane of the a collimator lattice.	53
6.1	Illustration of the crystal inserted in the LHC.	58
6.2	Illustration of FLUKA CRYSTAL card positional vectors.	60
6.3	Illustration of the crystal's lattice rotations and translations.	63
7.1	Example of annular halo in the phase space.	67
7.2	Proton crystal channeling single pass angular kick distribution.	69
7.3	The blue line is the SixTrack simulated BIH crystal angular kick distribution in VR range with 6.5 TeV protons. The black dashed line is the Gaussian fit of the VR peak. The incoming angle range is from 2 μ rad to 65 μ rad.	71
7.4	Simulated VR and DC distribution comparison for protons.	72
7.5	Crystal process summary for 6.5 TeV protons.	73
7.6	Proton full loss map benchmark at 6.5 TeV.	75
7.7	Proton IR7 loss map benchmark at 6.5 TeV.	76
7.8	Angular scan illustration.	76
7.9	Proton angular scan benchmark at 6.5 TeV protons.	77
7.10	Linear scan illustration: Beam travels from left to right. The beam halo (light blue) hits the crystal (grey) and the particles exiting the crystal can have channeled (green), dechanneled (yellow), or interacted with the amorphous material (red). They can then hit the absorber depending on the position of the absorber. In a linear scan the absorber moved downwards until it reaches the beam core. The BLM signal (right blue curve) recorded as a function of its transverse position and the corresponding beam distribution (left blue curve) are illustrated schematically.	79

7.11 Measured and simulated 2022 B2V crystal linear scan for 6.8 TeV proton.	80
7.12 Pb crystal channeling single pass angular kick distribution.	81
7.13 Crystal process efficiency summary for the SixTrack-Coupling with protons and Pb ions.	82
7.14 Measured (top) and simulated (bottom) loss map for B1H 2018 Pb run at 6.37 Z TeV. Measured loss map normalized to total BLM signal can be found in Fig. A.3. . .	83
7.15 Measured (top) and simulated (bottom) loss map around IR7 for 2018 Pb run at 6.37 Z TeV. Measured loss map normalized to total BLM signal can be found in Fig. A.4.	84
7.16 Figure from [134] showing simulated and experimental BLM signals for crystal-based 6.37 Z TeV Pb collimation in IR7 and the downstream DS region for B1H 2018 machine development test. The beam direction is from left to right. The BLM signals are given per ion lost in the collimation system. The acronyms MB, MQ represent the dipoles, and quadrupoles respectively.	85
7.17 Benchmark of 2022 B1H crystal collimation in channeling at 6.8 Z TeV.	86
7.18 Benchmark of 2022 B1V crystal collimation in channeling at 6.8 Z TeV.	87
7.19 Benchmark of 2022 B2H crystal collimation in channeling at 6.8 Z TeV.	88
7.20 Benchmark of 2022 B2V crystal collimation in channeling at 6.8 Z TeV.	89
7.21 Illustration of cold loss clustering in DS region.	90
7.22 Benchmark of 2018 B1H standard collimation at 6.37 Z TeV.	92
7.23 Benchmark of 2018 B1H crystal collimation in channeling at 6.37 Z TeV.	93
7.24 Benchmark of 2018 B1H crystal collimation in amorphous at 6.37 Z TeV.	94
7.25 Benchmark of 2018 B2H standard collimation at 6.37 Z TeV.	95
7.26 Benchmark of 2018 B2H crystal collimation in channeling at 6.37 Z TeV.	96
7.27 Benchmark of 2018 B2H crystal collimation in amorphous at 6.37 Z TeV.	97
7.28 B1H DS inefficiencies for different crystal orientations.	98
7.29 B2H DS inefficiencies for different crystal orientations.	98
7.30 Benchmark of 2022 B1H crystal collimation in amorphous at 6.8 Z TeV.	100
7.31 Benchmark of 2022 B1V crystal collimation in amorphous at 6.8 Z TeV.	101

7.32 Benchmark of 2022 B2H crystal collimation in amorphous at 6.8 Z TeV.	102
7.33 Benchmark of 2022 B2V crystal collimation in amorphous at 6.8 Z TeV.	103
7.34 Benchmark of 2022 B1H standard collimation at 6.8 Z TeV.	104
7.35 Benchmark of 2022 B1V standard collimation at 6.8 Z TeV.	105
7.36 Benchmark of 2022 B2H standard collimation at 6.8 Z TeV.	106
7.37 Benchmark of 2022 B2V standard collimation at 6.8 Z TeV.	107
7.38 2022 B1H DS inefficiencies for different crystal orientations.	108
7.39 2022 B1V DS inefficiencies for different crystal orientations.	108
7.40 2022 B2H DS inefficiencies for different crystal orientations.	109
7.41 2022 B2V DS inefficiencies for different crystal orientations.	109
7.42 Pb ion angular scan.	110
7.43 Measured and simulated 2022 B2V crystal linear scan for 6.8 Z TeV Pb ions. . .	111
8.1 Front view of a collimator set as black absorber.	115
8.2 Black absorber study full loss map.	115
8.3 Black absorber study loss map in IR7.	116
8.4 Collimator particle leakage count in traceback study.	117
8.5 Count of crystal interaction and loss turn number in traceback study.	118
8.6 Schematic representation of impact parameter change in crystals with miscut. .	119
8.7 Average inefficiencies of cold loss clusters in the DS region for different crystal miscut values in B2H at 6.37 Z TeV.	120
8.8 Schematic representation of the particle path length within a miscut crystal. . .	121
8.9 Bending angle of crystals with different miscut at constant impact parameter. .	121
8.10 DS inefficiency as a function of optimal crystal orientation (ϕ) offset.	122
8.11 DS inefficiency in machine imperfection study for different random seeds. . . .	123
8.12 DS inefficiency in machine imperfection study for different random seeds. . . .	124
8.13 DS inefficiency in impact parameter study.	125

8.14 B1H DS inefficiencies for different TCLA settings.	127
8.15 B1V DS inefficiencies for different TCLA settings.	127
8.16 B2H DS inefficiencies for different TCLA settings.	128
8.17 B2V DS inefficiencies for different TCLA settings.	128
8.18 Simulated trajectory of a particle channeled by vertical crystals intercepting skew collimators.	130
8.19 Simulated B1V loss map for skew collimator setting comparison.	131
8.20 Simulated B1V loss map for skew collimator setting comparison.	132
8.21 Simulated B1V loss map for skew collimator setting comparison.	133
8.22 Simulated B1V loss map for skew collimator setting comparison.	134
8.23 DS inefficiency for different setups for Run 3 B1V.	135
8.24 Measured B1V loss map for skew collimator comparison.	135
8.25 Simulated loss map for adiabatic settings at 6.8 Z TeV.	136
8.26 Simulated loss map for adiabatic settings at 6.8 Z TeV (IR7).	137
8.27 Asynchronous dump with ion crystal collimation loss map.	138
8.28 Asynchronous dump with ion crystal collimation loss map.	139
8.29 Asynchronous dump total energy deposition for different TCLA settings.	139
8.30 Asynchronous dump total energy deposition for different TCT settings.	140
8.31 Measured and simulated B1H 2023 loss map.	142
8.32 Measured and simulated B1H 2023 loss map in IR7.	143
8.33 Measured and simulated B1V 2023 loss map.	144
8.34 Measured and simulated B1V 2023 loss map in IR7.	145
8.35 Measured and simulated B2H 2023 loss map.	146
8.36 Measured and simulated B2H 2023 loss map in IR7.	147
8.37 Measured and simulated B2V 2023 loss map.	147
8.38 Measured and simulated B2V 2023 loss map in B2V.	148

8.39 Measured loss map at <i>flat-top</i> with 6.8 Z TeV $^{208}\text{Pb}^{82+}$ for B1.	149
8.40 Measured loss map at <i>flat-top</i> with 6.8 Z TeV $^{208}\text{Pb}^{82+}$ for B2.	150
8.41 B1 trajectory in vertical plane of $^{207}\text{Pb}^{82+}$ from TCPCV.A6L7.B1 without orbit bump.	151
8.42 B1 trajectory in vertical plane of $^{207}\text{Pb}^{82+}$ from TCPCV.A6L7.B1 without orbit bump.	151
8.43 B1 trajectory in horizontal plane of $^{207}\text{Pb}^{82+}$ from TCPCV.A6L7.B1 with orbit bump.	152
9.1 Impact parameter scan inefficiency in DS.	154
9.2 Single jaw standard cold loss comparison for B1H.	155
9.3 Single jaw standard cold loss comparison for B2H.	155
9.4 Measured loss map of B1H single jaw configurations.	156
9.5 Measured loss map of B2H single jaw configurations.	156
9.6 Schematic representation of a diverging beam impacting the two tilted jaws separately.	157
9.7 Standard collimation jaw tilt study DS inefficiencies for B2H.	157
9.8 Betatron functions in the two planes for Beam 1 as a function of the s position around IR7 for the modified optics and the reference optics.	158
9.9 DS inefficiencies for B1H standard collimation with updated optics.	160
9.10 Illustration of jaw alignment to beam envelop.	160
9.11 Full loss map of B1H standard collimation with TCP aligned to beam envelop.	161
9.12 IR7 loss map of B1H standard collimation with TCP aligned to beam envelop.	162
9.13 DS inefficiency for TCP jaw tilts smaller than the beam envelop alignment angle for B1H.	162
10.1 B1H full loss map at 7 Z TeV.	164
10.2 B1H loss map at 7 Z TeV in IR7.	165
10.3 B2H full loss map at 7 Z TeV.	165

10.4	B2H loss map at 7 Z TeV in IR7.	166
10.5	Simulated loss map in B1H of $^{16}\text{O}^{8+}$ beam at 6.8 Z TeV.	167
10.6	Simulated loss map in B1H of $^{40}\text{Ar}^{18+}$ beam at 6.8 Z TeV.	168
10.7	Simulated loss map in B1H of $^{84}\text{Kr}^{36+}$ beam at 6.8 Z TeV.	168
10.8	Simulated loss map in B1H of $^{129}\text{Xe}^{54+}$ beam at 6.8 Z TeV.	169
10.9	Simulated loss map in B1H of $^{208}\text{Pb}^{82+}$ beam at 6.8 Z TeV.	169
10.10	Inefficiencies in the cold DS clusters for different Z number.	170
10.11	Inefficiency of the 5 most abundant ion species in each light-ion simulation.	171
A.1	Proton full loss map benchmark at 6.5 TeV.	179
A.2	Proton IR7 loss map benchmark at 6.5 TeV.	180
A.3	Measured (top) and simulated (bottom) loss map for B1H 2018 Pb run at 6.37 Z TeV.	181
A.4	Measured (top) and simulated (bottom) loss map around IR7 for 2018 Pb run at 6.37 Z TeV.	181
A.5	Benchmark of 2022 B1H crystal collimation in channeling at 6.8 Z TeV.	182
A.6	Benchmark of 2022 B1V crystal collimation in channeling at 6.8 Z TeV.	183
A.7	Benchmark of 2022 B2H crystal collimation in channeling at 6.8 Z TeV.	184
A.8	Benchmark of 2022 B2V crystal collimation in channeling at 6.8 Z TeV.	185
A.9	Benchmark of 2018 B1H crystal collimation in channeling at 6.37 Z TeV.	186
A.10	Benchmark of 2018 B1H crystal collimation in amorphous at 6.37 Z TeV.	187
A.11	Benchmark of 2018 B2H crystal collimation in channeling at 6.37 Z TeV.	188
A.12	Benchmark of 2018 B2H crystal collimation in amorphous at 6.37 Z TeV.	189
A.13	Benchmark of 2022 B1H crystal collimation in amorphous at 6.8 Z TeV.	190
A.14	Benchmark of 2022 B1V crystal collimation in amorphous at 6.8 Z TeV.	191
A.15	Benchmark of 2022 B2H crystal collimation in amorphous at 6.8 Z TeV.	192
A.16	Benchmark of 2022 B2V crystal collimation in amorphous at 6.8 Z TeV.	193
A.17	Measured and simulated B1H 2023 loss map.	194

A.18 Measured and simulated B1H 2023 loss map in IR7. 194

A.19 Measured and simulated B1V 2023 loss map. 195

A.20 Measured and simulated B1V 2023 loss map in IR7. 195

A.21 Measured and simulated B2H 2023 loss map. 196

A.22 Measured and simulated B2H 2023 loss map in IR7. 196

A.23 Measured and simulated B2V 2023 loss map. 197

A.24 Measured and simulated B2V 2023 loss map in B2V. 197

List of Tables

2.1	Interplanar spacing of silicon for different planes.	12
3.1	LHC beam parameters.	30
4.1	LHC collimator characteristics for 2022 and 2023 runs.	37
4.2	Specifications of crystals featuring in this thesis work.	46
7.1	SixTrack crystal process classification codes.	70
7.2	FLUKA crystal process classification codes.	71
7.3	Crystal single pass study incoming angle boundary division for protons.	72
7.4	Collimator settings for 2018 B1H proton angular scan benchmark.	74
7.5	Collimator settings for 6.8 TeV proton and 6.8 Z TeV Pb linear scan benchmark.	80
7.6	Collimator settings for 2018 B1H Pb ion crystal benchmark at 6.37 Z TeV.	83
7.7	Collimator settings for 2022 6.8 Z TeV Pb loss map benchmark.	85
7.8	2018 $^{208}\text{Pb}^{82+}$ ion runs collimator settings for $\epsilon_N^P=3.5 \mu\text{m}$ from [22]. L and R indicates the left and right jaw, respectively. H and V correspond to horizontal and vertical planes, respectively.	91
8.1	Miscut study collimator settings.	119
8.2	Proposed Run 3 collimator settings.	130
8.3	Upstream open collimator settings.	136
8.4	Proposal 1 of collimator settings for Run 3.	138

8.5 Final collimator settings for the 2023 6.8 Z TeV Pb ion run at the stage of *physics*. 141

Bibliography

- [1] LHC Design Report Vol.1: The LHC Main Ring. 6 2004. doi: 10.5170/CERN-2004-003-V-1.
- [2] J. M. Jowett *et al.* Ions in the lhc ring. *Proceedings of the LHC Performance Workshop, Chamonix XII*, 2003.
- [3] J. M. Jowett. LHC operation for heavy ions. *Proceedings of the LHC Performance Workshop, Chamonix XIV*, page 88, 2005.
- [4] ATLAS Collaboration. The ATLAS experiment at the CERN Large Hadron Collider. *JINST*, 3:S08003, 2008.
- [5] The ALICE Collaboration. The ALICE experiment at the CERN LHC. *Journal of Instrumentation*, 3(08):S08002, 2008. doi: 10.1088/1748-0221/3/08/S08002.
- [6] CMS Collaboration. The CMS experiment at the CERN LHC. *JINST*, 3:S08004, 2008.
- [7] LHCb technical proposal. *CERN/LHCC 98-4, LHCC/P4*, 1998.
- [8] The LHCb Collaboration. The LHCb Detector at the LHC. *Journal of Instrumentation*, 3(08):S08005, 2008.
- [9] W Fischer and J M Jowett. Ion Colliders. *Rev. Accel. Sci. Technol.*, 7:49–76, 2014. doi: 10.1142/S1793626814300047. URL <https://cds.cern.ch/record/1983191>.
- [10] P. Foka. Experimental Overview of Heavy-Ion Physics at the SPS and Rhic. In *Quark Confinement and the Hadron Spectrum V*, pages 23–41, August 2003. doi: 10.1142/9789812704269_0003.
- [11] H. Hahn, E. Forsyth, H. Foelsche, M. Harrison, J. Kewisch, G. Parzen, S. Peggs, E. Raka, A. Ruggiero, A. Stevens, S. Tepikian, P. Thieberger, D. Trbojevic, J. Wei, E. Willen, S. Ozaki, and S. Y. Lee. The rhic design overview. *Nucl. Instrum. Methods Phys. Res., Sect. A*, 499(2-3):245 – 263, 2003.
- [12] A. Accardi, J.L. Albacete, M. Anselmino, N. Armesto, E.C. Aschenauer, A. Bacchetta, D. Boer, W.K. Brooks, T. Burton, N.B. Chang, W.T. Deng, A. Deshpande, M. Diehl, A. Dumitru, R. Dupré, R. Ent, S. Fazio, H. Gao, V. Guzey, H. Hakobyan, Y. Hao, D. Hasch,

- R. Holt, T. Horn, M. Huang, A. Hutton, C. Hyde, J. Jalilian-Marian, S. Klein, B. Kopelevich, Y. Kovchegov, K. Kumar, K. Kumerički, M.A.C. Lamont, T. Lappi, J.H. Lee, Y. Lee, E.M. Levin, F.L. Lin, V. Litvinenko, T.W. Ludlam, C. Marquet, Z.E. Meziani, R. McKeown, A. Metz, R. Milner, V.S. Morozov, A.H. Mueller, B. Müller, Dieter Müller, P. Nadel-Turonski, H. Paukkunen, A. Prokudin, V. Ptitsyn, X. Qian, J.W. Qiu, M. Ramsey-Musolf, T. Roser, F. Sabatié, R. Sassot, G. Schnell, P. Schweitzer, E. Sichtermann, M. Stratmann, M. Strikman, M. Sullivan, S. Taneja, T. Toll, D. Trbojevic, T. Ullrich, R. Venugopalan, S. Vigdor, W. Vogelsang, C. Weiss, B.W. Xiao, F. Yuan, Y.H. Zhang, and L. Zheng. Electron Ion Collider: The Next QCD Frontier - Understanding the glue that binds us all. *Eur. Phys. J. A*, 52(9):268, 2016. doi: 10.1140/epja/i2016-16268-9. URL <https://cds.cern.ch/record/1498519>. Comments: The Second Edition, 164 pages.
- [13] E. C. Aschenauer, M. D. Baker, A. Bazilevsky, K. Boyle, S. Belomestnykh, I. Ben-Zvi, S. Brooks, C. Brutus, T. Burton, S. Fazio, A. Fedotov, D. Gassner, Y. Hao, Y. Jing, D. Kayran, A. Kiselev, M. A. C. Lamont, J. H. Lee, V. N. Litvinenko, C. Liu, T. Ludlam, G. Mahler, G. McIntyre, W. Meng, F. Meot, T. Miller, M. Minty, B. Parker, R. Petti, I. Pinayev, V. Ptitsyn, T. Roser, M. Stratmann, E. Sichtermann, J. Skaritka, O. Tchoubar, P. Thieberger, T. Toll, D. Trbojevic, N. Tsoupas, J. Tuozzolo, T. Ullrich, E. Wang, G. Wang, Q. Wu, W. Xu, and L. Zheng. erhic design study: An electron-ion collider at bnl, 2014.
- [14] Lucio Rossi and Oliver Brüning. *The High Luminosity Large Hadron Collider: the new machine for illuminating the mysteries of Universe*. Advanced series on directions in high energy physics. World Scientific, Hackensack, NJ, 2015. doi: 10.1142/9581. URL <https://cds.cern.ch/record/1995532>.
- [15] R.W. Assmann. Collimators and Beam Absorbers for Cleaning and Machine Protection. *Proceedings of the LHC Project Workshop - Chamonix XIV, Chamonix, France*, page 261, 2005.
- [16] R.W. Assmann *et al.* The Final Collimation System for the LHC. *Proc. of the European Particle Accelerator Conference 2006, Edinburgh, Scotland*, page 986, 2006.
- [17] G. Robert-Demolaize. *Design and Performance Optimization of the LHC Collimation System*. PhD thesis, Université Joseph Fourier, Grenoble, 2006. URL <http://cdsweb.cern.ch/record/1004869/files/thesis-2006-069.pdf>.
- [18] C. Bracco. *Commissioning Scenarios and Tests for the LHC Collimation System*. PhD thesis, EPFL Lausanne, 2008.
- [19] R. Bruce, R. W. Assmann, V. Boccone, C. Bracco, M. Brugger, M. Cauchi, F. Cerutti, D. Deboy, A. Ferrari, L. Lari, A. Marsili, A. Mereghetti, D. Mirarchi, E. Quaranta, S. Redaelli, G. Robert-Demolaize, A. Rossi, B. Salvachua, E. Skordis, C. Tambasco, G. Valentino, T. Weiler, V. Vlachoudis, and D. Wollmann. Simulations and measurements of beam loss patterns at the CERN Large Hadron Collider. *Phys. Rev. ST Accel. Beams*, 17:081004, 2014. doi: 10.1103/PhysRevSTAB.17.081004. URL <http://link.aps.org/doi/10.1103/PhysRevSTAB.17.081004>.

- [20] R. Bruce, C. Bracco, R. De Maria, M. Giovannozzi, A. Mereghetti, D. Mirarchi, S. Redaelli, E. Quaranta, and B. Salvachua. Reaching record-low β^* at the CERN Large Hadron Collider using a novel scheme of collimator settings and optics. *Nucl. Instrum. Methods Phys. Res. A*, 848:19 – 30, Jan 2017. doi: <http://dx.doi.org/10.1016/j.nima.2016.12.039>. URL <http://www.sciencedirect.com/science/article/pii/S0168900216313092>.
- [21] P.D. Hermes, R. Bruce, J.M. Jowett, S. Redaelli, B. Salvachua Ferrando, G. Valentino, and D. Wollmann. Measured and simulated heavy-ion beam loss patterns at the CERN Large Hadron Collider. *Nucl. Instrum. Methods Phys. Res. A*, 819:73 – 83, Feb 2016. doi: <http://dx.doi.org/10.1016/j.nima.2016.02.050>. URL <https://www.sciencedirect.com/science/article/pii/S0168900216002175?via%3Dihub>.
- [22] N. Fuster-Martínez, R. Bruce, F. Cerutti, R. De Maria, P. Hermes, A. Lechner, A. Mereghetti, J. Molson, S. Redaelli, E. Skordis, A. Abramov, and L. Nevay. Simulations of heavy-ion halo collimation at the cern large hadron collider: Benchmark with measurements and cleaning performance evaluation. *Phys. Rev. Accel. Beams*, 23:111002, Nov 2020. doi: 10.1103/PhysRevAccelBeams.23.111002. URL <https://link.aps.org/doi/10.1103/PhysRevAccelBeams.23.111002>.
- [23] N. Fuster Martinez, A. Abramov, G. Azzopardi, A. Gorzawski, E. Belli, C. Boscolo-Meneguolo, R. Bruce, M. D’Andrea, M. Di Castro, M. Fiassaris, A. Fomin, P. D. Hermes, H. Garcia-Morales, R. Kwee-Hinzmann, D. Kodjaandreev, A. Mereghetti, D. Mirarchi, J. Molson, L. Nevay, E. Quaranta, M. Patecki, S. Redaelli, A. Rossi, R. Rossi, B. Salvachua, M. Solfaroli Camillocci, G. Valentino, A. Valloni, and J. Wagner. Run 2 collimation overview. *Proceedings of the 9th LHC Operations Evian Workshop, Evian, France*, 2019. URL <http://cds.cern.ch/record/2750291?ln=en>.
- [24] D. Mirarchi. *Crystal Collimation for LHC*. PhD thesis, Imperial College, London, 08 2015. URL <http://cds.cern.ch/record/2036210>.
- [25] Roberto Rossi. *Experimental Assessment of Crystal Collimation at the Large Hadron Collider*. PhD thesis, 2017. URL <https://cds.cern.ch/record/2644175>. Presented 26 Jan 2018.
- [26] D. Mirarchi, G. Hall, S. Redaelli, and W. Scandale. Design and implementation of a crystal collimation test stand at the large hadron collider. *The European Physical Journal C*, 77(6):424, Jun 2017. ISSN 1434-6052. doi: 10.1140/epjc/s10052-017-4985-4. URL <https://doi.org/10.1140/epjc/s10052-017-4985-4>.
- [27] Marco D’Andrea. *Applications of Crystal Collimation to the CERN Large Hadron Collider (LHC) and its High Luminosity Upgrade Project (HL-LHC)*. PhD thesis, University of Padova, Feb 2021. URL <http://cds.cern.ch/record/2758839>. Presented 23 Feb 2021.
- [28] Roberto Rossi, Stefano Redaelli, Francesca Galluccio, Alessandro Masi, Daniele Mirarchi, Simone Montesano, Gianluca Valentino, and Walter Scandale. Crystal Collimation with protons at flat top energy. 2017. URL <https://cds.cern.ch/record/2257957>.

- [29] R. Rossi, F. Galluccio, A. Masi, D. Mirarchi, S. Montesano, S. Redaelli, G. Valentino, and W. Scandale. Crystal Collimation with protons at injection energy. *CERN-ACC-NOTE-2016-0035*, 2016.
- [30] Roberto Rossi, Oliver Aberle, Odd Oyvind Andreassen, Mark Butcher, Cristovao Andre Dionisio Barreto, Alessandro Masi, Daniele Mirarchi, Simone Montesano, Inigo Lamas Garcia, Stefano Redaelli, Walter Scandale, Pablo Serrano Galvez, Adriaan Rijllart, Gianluca Valentino, and Francesca Galluccio. Beam 2 Crystal Characterization Measurements with Proton Beams in the LHC. 2018. URL <https://cds.cern.ch/record/2643353>.
- [31] Roberto Rossi, Oliver Aberle, Odd Oyvind Andreassen, Mark Butcher, Cristovao Andre Dionisio Barreto, Alessandro Masi, Daniele Mirarchi, Simone Montesano, Inigo Lamas Garcia, Stefano Redaelli, Walter Scandale, Pablo Serrano Galvez, Adriaan Rijllart, and Gianluca Valentino. Crystal Collimation Cleaning Measurements with Proton Beams in LHC. 2016. URL <https://cds.cern.ch/record/2306605>.
- [32] Marco D'Andrea, Daniele Mirarchi, Stefano Redaelli, Belen Maria Salvachua Ferrando, Laurence James Nevay, Roberto Rossi, Walter Scandale, Simone Montesano, Francesca Galluccio, Pablo Serrano Galvez, Cristovao Andre Dionisio Barreto, Mark Butcher, and Inigo Lamas Garcia. Crystal Collimation Tests with Proton Beams. 2019. URL <https://cds.cern.ch/record/2678779>.
- [33] Marco D'Andrea, Daniele Mirarchi, Stefano Redaelli, Belen Maria Salvachua Ferrando, Laurence James Nevay, Roberto Rossi, Walter Scandale, Simone Montesano, Francesca Galluccio, Pablo Serrano Galvez, Cristovao Andre Dionisio Barreto, Mark Butcher, and Inigo Lamas Garcia. Operational Aspects of Crystal Collimation with Proton Beams. 2019. URL <https://cds.cern.ch/record/2678780>.
- [34] M. D'Andrea, V. Avati, R. Bruce, M. Butcher, M. Di Castro, M. Deile, B. Dziedzic, H. Garcia Morales, Y. Gavrikov, K. Hiller, S. Jakobsen, J. Kaspar, K. Korcyl, I. Lamas Garcia, A. Masi, A. Mereghetti, D. Mirarchi, S. Redaelli, B. Salvachua Ferrando, P. Serrano Galvez, M. Solfaroli Camillocci, and N. Turini. First Experience of Crystal Collimators During LHC Special Runs and Plans for the Future. *Proceedings of the 64th ICFA Advanced Beam Dynamics Workshop on High-Intensity and High-Brightness Hadron Beams*, HB2021: MOCC3, 2022. doi: 10.18429/JACoW-HB2021-MOCC3.
- [35] M. D'Andrea, D. Mirarchi, S. Redaelli, A. Fomin, E. Belli, B. Salvachua Ferrando, L. Nevay, R. Rossi, W. Scandale, S. Montesano, F. Galluccio, P. Serrano Galvez, C. Dionisio Barreto, M. Butcher, and I. Lamas Garcia. Crystal Collimation Tests with Pb Ion Beams. *CERN-ACC-NOTE-2019-0024*, Jun 2019. URL <http://cds.cern.ch/record/2678781>.
- [36] M. D'Andrea, R. Bruce, M. Di Castro, I. Lamas Garcia, A. Masi, D. Mirarchi, S. Redaelli, R. Rossi, B. Salvachua, W. Scandale, F. Galluccio, and L.J. Nevay. Crystal collimation of 20 mj heavy-ion beams at the hl-lhc. *Proceedings of the 12th International Particle Accelerator Conference (IPAC'21): Campinas, Brazil, May 2021*, pages 2644–2647, May

2021. doi: doi:10.18429/JACoW-IPAC2021-WEPAB023. URL <https://jacow.org/ipac2021/papers/WEPAB023.pdf>. <https://doi.org/10.18429/JACoW-IPAC2021-WEPAB023>.
- [37] P. Hermes. *Heavy-Ion Collimation at the Large Hadron Collider : Simulations and Measurements*. PhD thesis, University of Munster, 2016.
- [38] H. Wiedemann. *Particle Accelerator Physics*. Springer, third edition, 2007.
- [39] Sixtrack physics manual. http://sixtrack.web.cern.ch/SixTrack/docs/physics_manual.pdf, .
- [40] James D. Patterson and Bernard C. Bailey. *Crystal Binding and Structure*, pages 1–45. Springer International Publishing, Cham, 2018. ISBN 978-3-319-75322-5. doi: 10.1007/978-3-319-75322-5_1. URL https://doi.org/10.1007/978-3-319-75322-5_1.
- [41] V. M. Biryukov, Yu. A. Chesnokov, and V. I. Kotov. *Crystal channeling and its application at high-energy accelerators*. 1997. ISBN 978-3-642-08238-2.
- [42] Gert Moliere. Theorie der streuung schneller geladener teilchen i. einzelstreuung am abgeschirmten coulomb-feld. *Zeitschrift für Naturforschung A*, 2(3):133–145, 1947. doi: doi:10.1515/zna-1947-0302. URL <https://doi.org/10.1515/zna-1947-0302>.
- [43] J Lindhard. Influence of crystal lattice on motion of energetic charged particles. *Kongel. Dan. Vidensk. Selsk., Mat.-Fys. Medd.*, Vol: 34: No. 14, 1 1965. URL <https://www.osti.gov/biblio/4536390>.
- [44] GIORDANO DIAMBRINI PALAZZI. High-energy bremsstrahlung and electron pair production in thin crystals. *Rev. Mod. Phys.*, 40:611–631, Jul 1968. doi: 10.1103/RevModPhys.40.611. URL <https://link.aps.org/doi/10.1103/RevModPhys.40.611>.
- [45] P. Flubacher, A. J. Leadbetter, and J. A. Morrison. The heat capacity of pure silicon and germanium and properties of their vibrational frequency spectra. *The Philosophical Magazine: A Journal of Theoretical Experimental and Applied Physics*, 4 (39):273–294, 1959. doi: 10.1080/14786435908233340. URL <https://doi.org/10.1080/14786435908233340>.
- [46] Philippe Schoofs. *Monte Carlo Modeling of Crystal Channeling at High Energies*. PhD thesis, EPFL Lausanne, Feb 2014. URL <https://cds.cern.ch/record/1950908>. Presented 18 Mar 2014.
- [47] Walter Scandale, Dean A. Still, Alberto Carnera, Gianantonio Della Mea, Davide De Salvador, Riccardo Milan, Alberto Vomiero, Stefano Baricordi, Pietro Dalpiaz, Massimiliano Fiorini, Vincenzo Guidi, Giuliano Martinelli, Andrea Mazzolari, Emiliano Milan, Giovanni Ambrosi, Philipp Azzarello, Roberto Battiston, Bruna Bertucci, William J. Burger, Maria Ionica, Paolo Zuccon, Gianluca Cavoto, Roberta Santacesaria, Paolo Valente, Erik Vallazza, Alexander G. Afonin, Vladimir T. Baranov, Yury A. Chesnokov, Vladilen I. Kotov,

- Vladimir A. Maisheev, Igor A. Yaznin, Sergey V. Afansiev, Alexander D. Kovalenko, Alexander M. Taratin, Alexander S. Denisov, Yury A. Gavrikov, Yuri M. Ivanov, Vladimir G. Ivochkin, Sergey V. Kosyanenko, Anatoli A. Petrunin, Vyacheslav V. Skorobogatov, Vsevolod M. Suvorov, Davide Bolognini, Luca Foggetta, Said Hasan, and Michela Prest. High-efficiency volume reflection of an ultrarelativistic proton beam with a bent silicon crystal. *Phys. Rev. Lett.*, 98:154801, Apr 2007. doi: 10.1103/PhysRevLett.98.154801. URL <https://link.aps.org/doi/10.1103/PhysRevLett.98.154801>.
- [48] W. Scandale, A. Vomiero, S. Baricordi, P. Dalpiaz, M. Fiorini, V. Guidi, A. Mazzolari, R. Milan, Gianantonio Della Mea, G. Ambrosi, B. Bertucci, W. J. Burger, M. Duranti, P. Zuccon, G. Cavoto, F. Iacoangeli, C. Luci, S. Pisano, R. Santacesaria, P. Valente, E. Vallazza, A. G. Afonin, Yu. A. Chesnokov, V. I. Kotov, V. A. Maisheev, I. A. Yazynin, A. D. Kovalenko, A. M. Taratin, A. S. Denisov, Yu. A. Gavrikov, Yu. M. Ivanov, L. P. Lapina, L. G. Malyarenko, V. V. Skorobogatov, V. M. Suvorov, S. A. Vavilov, D. Bolognini, S. Hasan, D. Lietti, A. Mozzanica, and M. Prest. Volume reflection dependence of 400 GeV/c protons on the bent crystal curvature. *Phys. Rev. Lett.*, 101:234801, Dec 2008. doi: 10.1103/PhysRevLett.101.234801. URL <https://link.aps.org/doi/10.1103/PhysRevLett.101.234801>.
- [49] W. Scandale, G. Arduini, M. Butcher, F. Cerutti, M. Garattini, S. Gilardoni, L. Lari, A. Lechner, R. Losito, A. Masi, A. Mereghetti, E. Metral, D. Mirarchi, S. Montesano, S. Redaelli, R. Rossi, P. Schoofs, G. Smirnov, E. Bagli, L. Bandiera, S. Baricordi, P. Dalpiaz, G. Germogli, V. Guidi, A. Mazzolari, D. Vincenzi, G. Claps, S. Dabagov, D. Hampai, F. Murtas, G. Cavoto, F. Iacoangeli, L. Ludovici, R. Santacesaria, P. Valente, F. Galluccio, A.G. Afonin, Yu.A. Chesnokov, V.A. Maisheev, Yu.E. Sandomirskiy, A.A. Yanovich, I.A. Yazynin, A.D. Kovalenko, A.M. Taratin, Yu.A. Gavrikov, Yu.M. Ivanov, L.P. Lapina, W. Ferguson, J. Fulcher, G. Hall, M. Pesaresi, M. Raymond, D. Bolognini, S. Hasan, M. Prest, and E. Vallazza. Observation of nuclear dechanneling length reduction for high energy protons in a short bent crystal. *Physics Letters B*, 743:440–443, 2015. ISSN 0370-2693. doi: <https://doi.org/10.1016/j.physletb.2015.02.072>. URL <https://www.sciencedirect.com/science/article/pii/S037026931500163X>.
- [50] W. Scandale, A. Vomiero, S. Baricordi, P. Dalpiaz, M. Fiorini, V. Guidi, A. Mazzolari, R. Milan, Gianantonio Della Mea, G. Ambrosi, B. Bertucci, W.J. Burger, P. Zuccon, G. Cavoto, R. Santacesaria, P. Valente, E. Vallazza, A.G. Afonin, Yu.A. Chesnokov, V.A. Maisheev, I.A. Yazynin, A.D. Kovalenko, A.M. Taratin, A.S. Denisov, Yu.A. Gavrikov, Yu.M. Ivanov, L.P. Lapina, L.G. Malyarenko, V.V. Skorobogatov, V.M. Suvorov, S.A. Vavilov, D. Bolognini, S. Hasan, and M. Prest. Observation of nuclear dechanneling for high-energy protons in crystals. *Physics Letters B*, 680(2):129–132, 2009. ISSN 0370-2693. doi: <https://doi.org/10.1016/j.physletb.2009.08.046>. URL <https://www.sciencedirect.com/science/article/pii/S0370269309010089>.
- [51] O. S. Brüning, P. Collier, P. Lebrun, S. Myers, R. Ostojic, J. Poole, and P. Proudlock (editors). LHC design report v.1 : The LHC main ring. *CERN-2004-003-V1*, CERN, Geneva, Switzerland, 2004.

- [52] Christiane Lefèvre. The CERN accelerator complex. Complexe des accélérateurs du CERN. 2008. URL <https://cds.cern.ch/record/1260465>.
- [53] LHC Modes. URL <https://lhc-commissioning.web.cern.ch/systems/data-exchange/doc/LHC-OP-ES-0005-10-00.pdf>.
- [54] RHIC design manual. http://www.agsrhichome.bnl.gov/NT-share/rhicdm/00_toc1i.htm.
- [55] J.M. Jowett, G. Arduini, R. Assmann, P. Baudrengnien, C. Carli, M. Lamont, M. Solfaroli Camillocci, J. Uythoven, W. Venturini, and J. Wenninger. First run of the LHC as a heavy-ion collider. *Proceedings of IPAC11, San Sebastian, Spain*, page 1837, 2011. URL <http://accelconf.web.cern.ch/AccelConf/IPAC2011/papers/tupz016.pdf>.
- [56] J.M. Jowett, R. Alemany-Fernandez, P. Baudrengnien, D. Jacquet, M. Lamont, D. Manglunki, S. Redaelli, M. Sapinski, M. Schaumann, M. Solfaroli Camillocci, R. Tomas, J.A. Uythoven, D. Valuch, R. Versteegen, and J. Wenninger. Proton-nucleus Collisions in the LHC. *Proceedings of IPAC13, Shanghai, China*, page 49, 2013. URL <https://cds.cern.ch/record/1572994?ln=en>.
- [57] J.M. Jowett. Colliding heavy ions in the LHC. *Proceedings of the International Particle Accelerator Conference 2018, Vancouver, Canada*, page 584, 2018. URL <https://accelconf.web.cern.ch/ipac2018/papers/tuxgbd2.pdf>.
- [58] J.M. Jowett *et al.* Overview of ion runs during Run 2. *Proceedings of the 9th LHC Operations Evian Workshop, Evian, France*, 2019. URL <https://indico.cern.ch/event/751857/timetable/#20190130.detailed>.
- [59] G. Apollinari, I. Bejar Alonso, O. Bruning, P. Fessia, M. Lamont, L. Rossi, and L. Tavian (editors). *High-Luminosity Large Hadron Collider (HL-LHC): Technical Design Report V. 0.1*. CERN Yellow Reports: Monographs. CERN-2017-007-M. CERN, Geneva, Switzerland, 2017. doi: <http://dx.doi.org/10.23731/CYRM-2017-004>. URL <https://cds.cern.ch/record/2284929>.
- [60] J. Coupard, H. Damerau, A. Funken, R. Garoby, S. Gilardoni, B. Goddard, K. Hanke, D. Manglunki, M. Meddahi, G. Rumolo, R. Scrivens, and E. Chapirochnikova. LHC Injectors Upgrade, Technical Design Report, Vol. II: Ions. Technical Report CERN-ACC-2016-0041, CERN, Geneva, Apr 2016. URL <https://cds.cern.ch/record/2153863>.
- [61] R. Bruce, T. Argyropoulos, H. Bartosik, R. De Maria, N. Fuster-Martinez, M.A. Jebramcik, J.M. Jowett, N. Mounet, S. Redaelli, G. Rumolo, M. Schaumann, and H. Timko. HL-LHC operational scenario for Pb-Pb and p-Pb operation. *CERN-ACC-2020-0011*, 2020. URL <https://cds.cern.ch/record/2722753>.
- [62] J.M. Jowett, C. Bahamonde Castro, W. Bartmann, C. Bracco, R. Bruce, J. Dilly, S. Fartoukh, A. Garcia-Tabares, M. Hofer, M.A. Jebramcik, J. Keintzel, A. Lechner, E.H. Maclean,

- L. Malina, T. Medvedeva, D. Mirarchi, T. Persson, B. Petersen, S. Redaelli, M. Schaumann, M. Solfaroli, R. Tomas, J. Wenninger, J. Coello, E. Fol, N. Fuster-Martinez, E.B. Holzer, A. Mereghetti, B. Salvachua, C. Schwick, M. Spitznagel, H. Timko, A. Wegscheider, and D. Wollmann. The 2018 Heavy-Ion Run of the LHC. *Proceedings of the 10th International Particle Accelerator Conference (IPAC2019): Melbourne, Australia, May 19-24, 2019*, page 2258, 2019. doi: <https://doi.org/10.18429/JACoW-IPAC2019-WEYYPLM2>.
- [63] J.M. Jowett, R. Alemany, Michaela Schaumann, P. Hermes, and T. Mertens. HL-LHC beam parameters and performance with heavy ions—an update. *Presentation in the LHC Performance Workshop (Chamonix 2017), Chamonix, France, 2017*. URL <https://indico.cern.ch/event/580313/timetable/>.
- [64] Michael Tinkham. *Introduction to Superconductivity*. Dover Publications, 2 edition, June 2004. ISBN 0486435032. URL <http://www.worldcat.org/isbn/0486435032>.
- [65] B. Auchmann, T. Baer, M. Bednarek, G. Bellodi, C. Bracco, R. Bruce, F. Cerutti, V. Chetvertkova, B. Dehning, P. P. Granieri, W. Hofle, E. B. Holzer, A. Lechner, E. Nebot Del Busto, A. Priebe, S. Redaelli, B. Salvachua, M. Sapinski, R. Schmidt, N. Shetty, E. Skordis, M. Solfaroli, J. Steckert, D. Valuch, A. Verweij, J. Wenninger, D. Wollmann, and M. Zerlauth. Testing beam-induced quench levels of lhc superconducting magnets. *Phys. Rev. ST Accel. Beams*, 18:061002, Jun 2015. doi: 10.1103/PhysRevSTAB.18.061002. URL <https://link.aps.org/doi/10.1103/PhysRevSTAB.18.061002>.
- [66] S Redaelli. Beam Cleaning and Collimation Systems. 2014. URL <https://cds.cern.ch/record/1970915>.
- [67] M Lamont. Estimates of Annual Proton Doses in the LHC. Technical report, CERN, Geneva, 2005. URL <https://cds.cern.ch/record/893060>.
- [68] A Piwinski. Intra-beam-scattering. 1974. doi: 10.5170/CERN-1992-001.226. URL <https://cds.cern.ch/record/400720>.
- [69] Michel Martini, Fanouria Antoniou, and Yannis Papaphilippou. Intrabeam Scattering. *ICFA Beam Dyn. Newsl.*, 69:38–59, 2016. URL <https://cds.cern.ch/record/2266030>.
- [70] R Schmidt, Ralph Wolfgang Assmann, E Carlier, B Dehning, R Denz, B Goddard, E B Holzer, V Kain, B Puccio, B Todd, J Uythoven, J Wenninger, and M Zerlauth. LHC Machine Protection. 2007. doi: 10.1109/PAC.2007.4441111. URL <https://cds.cern.ch/record/1076302>.
- [71] R.W. Assmann, B. Goddard, E. Vossenber, and E. Weisse. The consequences of abnormal beam dump actions on the LHC collimation system. *LHC Project Note 293, CERN*, 1996.
- [72] Mike Seidel. The Proton collimation system of HERA. Other thesis, 6 1994.

- [73] R W Assmann, F Schmidt, Frank Zimmermann, and M P Zorzano-Mier. Equilibrium Beam Distribution and Halo in the LHC. 2002. URL <https://cds.cern.ch/record/569470>. Same report as LHC-Project-Report-597.
- [74] S. Redaelli, S. Antipov, N. Biancacci, A. Bertarelli, R. Bruce, F. Carra, G. Gobbi, A. Lechner, A. Mereghetti, and E. Metral. Staged implementation of low-impedance collimation in IR7: plans for LS2. *CERN-ACC-NOTE-2019-0001*, Jan 2019. URL <https://cds.cern.ch/record/2654779>.
- [75] S Redaelli, C Alabau Pons, R Assmann, R Bruce, M Giovannozzi, G Muller, and J Wenninger. Aperture measurements in the LHC interaction regions. *Conf. Proc.*, C1205201: MOPPD062, 2012. URL <https://cds.cern.ch/record/1459455>.
- [76] The collimation system: defence against beam loss. *CERN Courier*, 53(7):37–39, 2013. URL <https://cds.cern.ch/record/1734984>.
- [77] R.W. Assmann, R. Bruce, F. Burkart, M. Cauchi, D. Deboy, L. Lari, E. Metral, N. Mounet, S. Redaelli, A. Rossi, B. Salvant, G. Valentino, and D. Wollmann. Summary of MD on nominal collimator settings. *CERN-ATS-Note-2011-036 MD*, 2011. URL <http://cdsweb.cern.ch/record/1353517>.
- [78] S. Redaelli. Beam cleaning and collimation systems. *CERN Yellow Reports*, page Vol 2 (2016): Proceedings of the 2014 Joint International Accelerator School: Beam Loss and Accelerator Protection, 2016. doi: 10.5170/CERN-2016-002.403. URL <https://e-publishing.cern.ch/index.php/CYR/article/view/243>.
- [79] Particle Data Group, R L Workman, V D Burkert, V Crede, E Klempt, U Thoma, L Tiator, K Agashe, G Aielli, B C Allanach, C Amsler, M Antonelli, E C Aschenauer, D M Asner, H Baer, Sw Banerjee, R M Barnett, L Baudis, C W Bauer, J J Beatty, V I Belousov, J Beringer, A Bettini, O Biebel, K M Black, E Blucher, R Bonventre, V V Bryzgalov, O Buchmuller, M A Bychkov, R N Cahn, M Carena, A Ceccucci, A Cerri, R Sekhar Chivukula, G Cowan, K Cranmer, O Cremonesi, G D’Ambrosio, T Damour, D de Florian, A de Gouvêa, T DeGrand, P de Jong, S Demers, B A Dobrescu, M D’Onofrio, M Doser, H K Dreiner, P Eerola, U Egede, S Eidelman, A X El-Khadra, J Ellis, S C Eno, J Erler, V V Ezhela, W Fetscher, B D Fields, A Freitas, H Gallagher, Y Gershtein, T Gherghetta, M C Gonzalez-Garcia, M Goodman, C Grab, A V Gribsan, C Grojean, D E Groom, M Grünewald, A Gurtu, T Gutsche, H E Haber, Matthieu Hamel, C Hanhart, S Hashimoto, Y Hayato, A Hebecker, S Heinemeyer, J J Hernández-Rey, K Hikasa, J Hisano, A Höcker, J Holder, L Hsu, J Huston, T Hyodo, Al Ianni, M Kado, M Karliner, U F Katz, M Kenzie, V A Khoze, S R Klein, F Krauss, M Kreps, P Križan, B Krusche, Y Kwon, O Lahav, J Laiho, L P Lellouch, J Lesgourgues, A R Liddle, Z Ligeti, C-J Lin, C Lippmann, T M Liss, L Littenberg, C Lourenço, K S Lugovsky, S B Lugovsky, A Lusiani, Y Makida, F Maltoni, T Mannel, A V Manohar, W J Marciano, A Masoni, J Matthews, U-G Meißner, I-A Melzer-Pellmann, M Mikhasenko, D J Miller, D Milstead, R E Mitchell, K Mönig, P Molaro, F Moortgat, M Moskvic, K Nakamura,

- M Narain, P Nason, S Navas, A Nelles, M Neubert, P Nevski, Y Nir, K A Olive, C Patrignani, J A Peacock, V A Petrov, E Pianori, A Pich, A Piepke, F Pietropaolo, A Pomarol, S Pordes, S Profumo, A Quadt, K Rabbertz, J Rademacker, G Raffelt, M Ramsey-Musolf, B N Ratcliff, P Richardson, A Ringwald, D J Robinson, S Roesler, S Rolli, A Romaniouk, L J Rosenberg, J L Rosner, G Rybka, M G Ryskin, R A Ryutin, Y Sakai, S Sarkar, F Sauli, O Schneider, S Schönert, K Scholberg, A J Schwartz, J Schwiening, D Scott, F Sefkow, U Seljak, V Sharma, S R Sharpe, V Shiltsev, G Signorelli, M Silari, F Simon, T Sjöstrand, P Skands, T Skwarnicki, G F Smoot, A Soffer, M S Sozzi, S Spanier, C Spiering, A Stahl, S L Stone, Y Sumino, M J Syphers, F Takahashi, M Tanabashi, J Tanaka, M Taševský, K Terao, K Terashi, J Terning, R S Thorne, M Titov, N P Tkachenko, D R Tovey, K Trabelsi, P Urquijo, G Valencia, R Van de Water, N Varelas, G Venanzoni, L Verde, I Vivarelli, P Vogel, W Vogelsang, V Vorobyev, S P Wakely, W Walkowiak, C W Walter, D Wands, D H Weinberg, E J Weinberg, N Wermes, M White, L R Wiencke, S Willocq, C G Wohl, C L Woody, W-M Yao, M Yokoyama, R Yoshida, G Zanderighi, G P Zeller, O V Zenin, R-Y Zhu, Shi-Lin Zhu, F Zimmermann, and P A Zyla. Review of Particle Physics. *Progress of Theoretical and Experimental Physics*, 2022(8):083C01, 08 2022. ISSN 2050-3911. doi: 10.1093/ptep/ptac097. URL <https://doi.org/10.1093/ptep/ptac097>.
- [80] H. H. Braun, A. Fassò, A. Ferrari, J. M. Jowett, P. R. Sala, and G. I. Smirnov. Hadronic and electromagnetic fragmentation of ultrarelativistic heavy ions at LHC. *Phys. Rev. ST Accel. Beams*, 17:021006, Feb 2014. doi: 10.1103/PhysRevSTAB.17.021006. URL <https://link.aps.org/doi/10.1103/PhysRevSTAB.17.021006>.
- [81] A. Aste. Bound-free pair production cross-section in heavy-ion colliders from the equivalent photon approach. *EPL (Europhysics Letters)*, 81(6):61001, feb 2008. doi: 10.1209/0295-5075/81/61001. URL <https://doi.org/10.1209/0295-5075/81/61001>.
- [82] Helmar Meier, Zlatko Halabuka, Kai Hencken, Dirk Trautmann, and Gerhard Baur. Bound-free electron-positron pair production in relativistic heavy-ion collisions. *Phys. Rev. A*, 63:032713, Feb 2001. doi: 10.1103/PhysRevA.63.032713. URL <https://link.aps.org/doi/10.1103/PhysRevA.63.032713>.
- [83] R. Anholt and U. Becker. Atomic collisions with relativistic heavy ions. ix. ultrarelativistic collisions. *Phys. Rev. A*, 36:4628–4636, Nov 1987. doi: 10.1103/PhysRevA.36.4628. URL <https://link.aps.org/doi/10.1103/PhysRevA.36.4628>.
- [84] Maurizio Serluca, Robert B. Appleby, James Molson, Roger J. Barlow, Haroon Rafique, and Adina Toader. Hi-Lumi LHC Collimation Studies with MERLIN Code. In *5th International Particle Accelerator Conference*, page MOPRI077, 7 2014. doi: 10.18429/JACoW-IPAC2014-MOPRI077.
- [85] Jerzy Bartke. *Introduction to relativistic heavy ion physics*. 2009.
- [86] *ALICE: Technical proposal for a Large Ion collider Experiment at the CERN LHC*. LHC technical proposal. CERN, Geneva, 1995. URL <https://cds.cern.ch/record/293391>.

- [87] A. Fasso et al. The Physics models of FLUKA: Status and recent developments. *eConf*, C0303241:MOMT005, 2003.
- [88] B.V. Carlson, R. Donangelo, S.R. Souza, W.G. Lynch, A.W. Steiner, and M.B. Tsang. Fermi breakup and the statistical multifragmentation model. *Nuclear Physics A*, 876:77–92, 2012. ISSN 0375-9474. doi: <https://doi.org/10.1016/j.nuclphysa.2011.12.009>. URL <https://www.sciencedirect.com/science/article/pii/S0375947411006993>.
- [89] H.H. Braun et al. Collimation of Heavy Ion Beams in the LHC. *Proc. of the European Particle Accelerator Conf. 2004, Lucerne, Switzerland*, page 551, 2004.
- [90] E.B. Holzer, B. Dehning, E. Effinger, J. Emery, G. Ferioli, J.L. Gonzalez, E. Gschwendtner, G. Guaglio, M. Hodgson, D. Kramer, R. Leitner, L. Ponce, V. Prieto, M. Stockner, and C. Zamantzas. Beam Loss Monitoring System for the LHC. *IEEE Nuclear Science Symposium Conference Record*, 2:1052, 2005. doi: 10.1109/NSSMIC.2005.1596433.
- [91] E. B. Holzer et al. Development, production and testing of 4500 beam loss monitors. *Proc. of the European Particle Accelerator Conf. 2008, Genoa, Italy*, page 1134, 2008.
- [92] R W Assmann. Collimators and Cleaning, Could this Limit the LHC Performance? 2003. URL <https://cds.cern.ch/record/642461>.
- [93] W. Scandale, G. Arduini, M. Butcher, F. Cerutti, M. Garattini, S. Gilardoni, A. Lechner, R. Losito, A. Masi, D. Mirarchi, S. Montesano, S. Redaelli, R. Rossi, P. Schoofs, G. Smirnov, G. Valentino, D. Breton, L. Burmistrov, V. Chaumat, S. Dubos, J. Maalmi, V. Puill, A. Stocchi, E. Bagli, L. Bandiera, G. Germogli, V. Guidi, A. Mazzolari, S. Dabagov, F. Murtas, F. Addesa, G. Cavoto, F. Iacoangeli, L. Ludovici, R. Santacesaria, P. Valente, F. Galluccio, A.G. Afonin, Yu.A. Chesnokov, A.A. Durum, V.A. Maisheev, Yu.E. Sandomirskiy, A.A. Yanovich, A.D. Kovalenko, A.M. Taratin, A.S. Denisov, Yu.A. Gavrikov, Yu.M. Ivanov, L.P. Lapina, L.G. Malyarenko, V.V. Skorobogatov, T. James, G. Hall, M. Pesaresi, and M. Raymond. Observation of channeling for 6500 GeV/c protons in the crystal assisted collimation setup for LHC. *Physics Letters B*, 758:129 – 133, 2016. ISSN 0370-2693. doi: <https://doi.org/10.1016/j.physletb.2016.05.004>. URL <http://www.sciencedirect.com/science/article/pii/S0370269316301514>.
- [94] Q. Demassieux and R. Seidenbinder. Update on TCPCH-B1: NC report, refurbishment and TS1 report. Presentation at the LHC Collimation Upgrade Specification Meeting, CERN, Geneva, Switzerland, 2023. URL <https://indico.cern.ch/event/1285838/>.
- [95] M. D’Andrea and R. Cai. LHC beam measurement 2023 and MD plans. Presentation at the LHC Collimation Upgrade Specification Meeting, CERN, Geneva, Switzerland, 2023. URL <https://indico.cern.ch/event/1285838/>.
- [96] Q. Demassieux. TCPCs YETS 2021 installation. Presentation at the LHC Collimation Upgrade Specification Meeting, CERN, Geneva, Switzerland, 2021. URL <https://indico.cern.ch/event/1094761/>.

- [97] M. D'Andrea, A. Abramov, R. Bruce, R. Cai, K. Dewhurst, M. Di Castro, H. Hermes, B. Lindström, E. Matheson, D. Mirarchi, S. Redaelli, G. Ricci, and S. Solis Paiva. Results of crystal collimation measurements with proton beams in 2022. Presentation at the LHC Collimation Upgrade Specification Meeting, CERN, Geneva, Switzerland, 2022. URL <https://indico.cern.ch/event/1212179/>.
- [98] R. Seidenbinder. Feedback on TCPC installation. Presentation at the LHC Collimation Upgrade Specification Meeting, CERN, Geneva, Switzerland, 2023. URL <https://indico.cern.ch/event/1255430/>.
- [99] M. D'Andrea, O. Aberle, A. Abramov, L. Bandiera, R. Bruce, R. Cai, M. Calviani, Q. Demassieux, K. A. Dewhurst, M. Di Castro, L. S. Esposito, Y. Gavrikov, S. Gilardoni, V. Guidi, P. D. Hermes, Y. Ivanov, B. H. F. Lindström, A. Lechner, A. Mazzolari, E. Matheson, D. Mirarchi, J. B. Potoine, S. Redaelli, G. Ricci, M. Romagnoni, R. Seidenbinder, S. Solis Paiva, and M. Tamisari. Characterization of bent crystals for beam collimation with 6.8 TeV proton beams at the LHC. *Nuclear Instruments and Methods in Physics Research Section A: Accelerators, Spectrometers, Detectors and Associated Equipment*.
- [100] P.D. Hermes, B. Auchmann, R. Bruce, W. Hofle, E. B. Holzer, M. Kalliokoski, G. Kotzian, A. Mereghetti, D. Mirarchi, E. Quaranta, S. Redaelli, B. Salvachua Ferrando, G. Valentino, D. Valuch, D. Wollmann, and M. Zerlauth. LHC Heavy-Ion Collimation Quench Test at 6.37Z TeV. *CERN-ACC-NOTE-2016-0031*, Mar 2016. URL <http://cds.cern.ch/record/2136828>.
- [101] Z. Citron et al. Future physics opportunities for high-density QCD at the LHC with heavy-ion and proton beams. *HL/HE-LHC Workshop: Workshop on the Physics of HL-LHC, and Perspectives at HE-LHC Geneva, Switzerland, June 18-20, 2018, CERN-LPCC-2018-07*, 2018. URL <https://cds.cern.ch/record/2650176?ln=en>.
- [102] R. Bruce, A. Marsili, and S. Redaelli. Cleaning Performance with 11T Dipoles and Local Dispersion Suppressor Collimation at the LHC. *Proceedings of the International Particle Accelerator Conference 2014, Dresden, Germany*, page 170, 2014. URL <http://accelconf.web.cern.ch/AccelConf/IPAC2014/papers/mopro042.pdf>.
- [103] A. Lechner, B. Auchmann, R. Bruce, F. Cerutti, P.P. Granieri, A. Marsili, S. Redaelli, N.V. Shetty, E. Skordis, G.E. Steele, and A.P. Verwei. Power Deposition in LHC Magnets With and Without Dispersion Suppressor Collimators Downstream of the Betatron Cleaning Insertion. *Proceedings of the International Particle Accelerator Conference 2014, Dresden, Germany*, page 112, 2014. URL <http://accelconf.web.cern.ch/AccelConf/IPAC2014/papers/mopro021.pdf>.
- [104] A. Waets et al. Update on power deposition studies for IR7 DS. Presentation at the LHC Collimation Upgrade Specification Meeting 138, CERN, Geneva, Switzerland, 2021. URL https://indico.cern.ch/event/1012710/contributions/4250374/attachments/2199331/3719359/ColUSM137_AW.pdf.

- [105] MAD-X program. <http://cern.ch/mad/> CERN, Geneva, Switzerland.
- [106] <http://www.fluka.org>, .
- [107] G. Battistoni et al. Overview of the FLUKA code. *Annals Nucl. Energy*, 82:10–18, 2015. doi: 10.1016/j.anucene.2014.11.007.
- [108] C. Ahdida, D. Bozzato, D. Calzolari, F. Cerutti, N. Charitonidis, A. Cimmino, A. Coronetti, G. L. D'Alessandro, A. Donadon Servelle, L. S. Esposito, R. Froeschl, R. Garcia Alia, A. Gerbershagen, S. Gilardoni, D. Horvath, G. Hugo, A. Infantino, V. Kouskoura, A. Lechner, B. Lefebvre, G. Lerner, M. Magistris, A. Manousos, G. Moryc, F. Ogalzar Ruiz, F. Pozzi, D. Prelipcean, S. Roesler, R. Rossi, M. Sabate Gilarte, F. Salvat Pujol, P. Schoofs, V. Stransky, C. Theis, A. Tsinganis, R. Versaci, V. Vlachoudis, A. Waets, and M. Widorski. New capabilities of the FLUKA multi-purpose code. *Frontiers in Physics*, 9, 2022. ISSN 2296-424X. doi: 10.3389/fphy.2021.788253. URL <https://www.frontiersin.org/article/10.3389/fphy.2021.788253>.
- [109] S. Roesler, R. Engel, and J. Ranft. The Monte Carlo Event Generator DPMJET-III. *SLAC Report SLAC-PUB-8740*, 2000.
- [110] P. Schoofs, F. Cerutti, A. Ferrari, and G. Smirnov. Monte carlo modeling of crystal channeling at high energies. *Nuclear Instruments and Methods in Physics Research Section B: Beam Interactions with Materials and Atoms*, 309:115–119, 2013. ISSN 0168-583X. doi: <https://doi.org/10.1016/j.nimb.2013.02.027>. URL <https://www.sciencedirect.com/science/article/pii/S0168583X1300284X>. The 5th International Conference "Channeling 2012", "Charged & Neutral Particles Channeling Phenomena" September 23-28,2012, Alghero (Sardinia), Italy.
- [111] Riccardo De Maria, Joel Andersson, Barbara Dalena, Laurence Field, Massimo Giovannozzi, Pascal Hermes, Nils Hoimyr, Giovanni Iadarola, Sofia Kostoglou, Ewen Maclean, Eric McIntosh, Alessio Mereghetti, James Molson, Veronica Olsen, Dario Pellegrini, Tobias Persson, Thomas Pognat, Martin Schwinzerl, Kyrre Sjobak, and Igor Zacharov. SixTrack Version 5: Status and New Developments. In *Proceedings of the 10th Int. Particle Accelerator Conf. (IPAC 2019)*, pages 3200–3203, Melbourne, Australia, 2019. doi: 10.18429/JACOW-IPAC2019-WEPTS043. URL <http://jacow.org/ipac2019/doi/JACoW-IPAC2019-WEPTS043.html>. paper WEPTS043.
- [112] Sixtrack web site. <http://sixtrack.web.cern.ch/SixTrack/>, .
- [113] T. Trenkler and J.B. Jeanneret. K2, a software package evaluating collimation systems in circular colliders (manual). *CERN SL/94105 (AP)*, 1994.
- [114] G. Robert-Demolaize, R. W. Assmann, S. Redaelli, and F. Schmidt. A New Version of SixTrack with Collimation and Aperture Interface. In *Proc. PAC'05*, pages 4084–4086. JACoW Publishing, Geneva, Switzerland. URL <https://jacow.org/p05/papers/FPAT081.pdf>.

- [115] C. Tambasco. An improved scattering routine for collimation tracking studies at LHC. Master's thesis, Università di Roma, Italy, 2014.
- [116] P.D. Hermes, R. Bruce, and R. De Maria. Symplectic tracking of multi-isotopic heavy-ion beams in SixTrack. *Proceedings of the International Particle Accelerator Conference 2016, Busan, Korea*, page 1450, 2016. URL <http://accelconf.web.cern.ch/AccelConf/ipac2016/papers/tupmw015.pdf>.
- [117] Valentina Previtali. *Performance evaluation of a crystal-enhanced collimation system for the LHC*. PhD thesis, Ecole Polytechnique, Lausanne, 2010.
- [118] A. Mereghetti et al. SixTrack-Fluka Active Coupling for the Upgrade of the SPS Scrapers. In *Proc. IPAC'13*, pages 2657–2659. JACoW Publishing, Geneva, Switzerland. URL <https://jacow.org/IPAC2013/papers/WEPEA064.pdf>.
- [119] <https://twiki.cern.ch/twiki/bin/view/FlukaTeam/FlukaIO>, .
- [120] N Holden. Development of the ICOSIM Program and Application to Magnetised Collimators in the LHC. Technical report, CERN, Geneva, 2008. URL <https://cds.cern.ch/record/1151294>.
- [121] E. Skordis, V. Vlachoudis, R. Bruce, F. Cerutti, A. Ferrari, A. Lechner, A. Mereghetti, P.G. Ortega, S. Redaelli, and D. Sinuela Pastor. FLUKA coupling to Sixtrack. In *Proc. of the ICFA Mini-Workshop on Tracking for Collimation*, pages 17–25, 2018. doi: 10.23732/CYRCP-2018-002.17. URL <https://cds.cern.ch/record/2694313>.
- [122] D Mirarchi, G Hall, S Redaelli, and W Scandale. A crystal routine for collimation studies in circular proton accelerators. *Nucl. Instrum. Methods Phys. Res., B*, 355:378–382. 5 p, 2015. doi: 10.1016/j.nimb.2015.03.026. URL <https://cds.cern.ch/record/2159102>.
- [123] D Mirarchi, V Avati, R Bruce, M Butcher, M D'Andrea, M Di Castro, M Deile, B Dziedzic, K Hiller, S Jakobsen, J Kašpar, K Korcyl, I Lamas, A Masi, A Mereghetti, H Garcia Morales, Y Gavrikov, S Redaelli, B Salvachua Ferrando, P Serrano, M Solfaroli Camillocci, and N Turini. Reducing Beam-Related Background on Forward Physics Detectors Using Crystal Collimation at the Large Hadron Collider. *Phys. Rev. Applied*, 14:064066. 20 p, 2020. doi: 10.1103/PhysRevApplied.14.064066. URL <https://cds.cern.ch/record/2750007>.
- [124] S. Abdel Khalek, B. Allongue, F. Anghinolfi, P. Barrillon, G. Blanchot, S. Blin-Bondil, A. Braem, L. Chytka, P. Conde Muñío, M. Düren, P. Fassnacht, S. Franz, L. Gurriana, P. P. Grafström, M. Heller, M. Haguenaue, W. Hain, P. Hamal, K. Hiller, W. Iwanski, S. Jakobsen, C. Joram, U. Kötz, K. Korcyl, K. Kreutzfeldt, T. Lohse, A. Maio, M.J.P. Maneira, A. Mapelli, D. Notz, L. Nozka, A. Palma, D. Petschull, X. Pons, P. Puzo, S. Ravat, T. Schneider, L. Seabra, T. Sykora, R. Staszewski, H. Stenzel, M. Trzebinski, S. Valkar, M. Viti, V. Vorobel, and A. Wemans. The alfa roman pot detectors of atlas. *Journal of Instrumentation*, 11(11):P11013, nov 2016. doi: 10.1088/1748-0221/11/11/P11013. URL <https://dx.doi.org/10.1088/1748-0221/11/11/P11013>.

- [125] The TOTEM Collaboration, G Anelli, G Antchev, P Aspell, V Avati, M G Bagliesi, V Berardi, M Berretti, V Boccone, U Bottigli, M Bozzo, E Brücken, A Buzzo, F Cafagna, M Calicchio, F Capurro, M G Catanesi, P L Catastini, R Cecchi, S Cerchi, R Cereseto, M A Ciocci, S Cuneo, C Da Vià, E David, M Deile, E Dimovasili, M Doubrava, K Eggert, V Eremin, F Ferro, A Foussat, M Galuška, F Garcia, F Gherarducci, S Giani, V Greco, J Hasi, F Haug, J Heino, T Hilden, P Jarron, C Joram, J Kalliopuska, J Kaplon, J Kašpar, V Kandrát, K Kurvinen, J M Lacroix, S Lami, G Latino, R Lauhakangas, E Lippmaa, M Lokajíček, M Lo Vetere, F Lucas Rodriguez, D Macina, M Macrí, C Magazzù, G Magazzù, A Magri, G Maire, A Manco, M Meucci, S Minutoli, A Morelli, P Musico, M Negri, H Niewiadomski, E Noschis, G Notarnicola, E Oliveri, F Oljemark, R Orava, M Oriunno, A-L Perrot, K Österberg, R Paoletti, E Pedreschi, J Petäjajarvi, P Pollovio, M Quinto, E Radermacher, E Radicioni, S Rangod, F Ravotti, G Rella, E Robutti, L Ropelewski, G Ruggiero, A Rummel, H Saarikko, G Sanguinetti, A Santroni, A Scribano, G Sette, W Snoeys, F Spinella, P Squillacioti, A Ster, C Taylor, A Tazzioli, D Torazza, A Trovato, A Trummal, N Turini, V Vacek, N Van Remortel, V Vinš, S Watts, J Whitmore, and J Wu. The totem experiment at the cern large hadron collider. *Journal of Instrumentation*, 3(08):S08007, aug 2008. doi: 10.1088/1748-0221/3/08/S08007. URL <https://dx.doi.org/10.1088/1748-0221/3/08/S08007>.
- [126] P. Schoofs, F. Cerutti, A. Ferrari, and G. Smirnov. Benchmark of the FLUKA model of crystal channeling against the ua9-h8 experiment. *Nuclear Instruments and Methods in Physics Research Section B: Beam Interactions with Materials and Atoms*, 355:374–377, 2015. ISSN 0168-583X. doi: <https://doi.org/10.1016/j.nimb.2015.03.074>. URL <https://www.sciencedirect.com/science/article/pii/S0168583X15003092>. Proceedings of the 6th International Conference Channeling 2014: “Charged & Neutral Particles Channeling Phenomena” October 5-10, 2014, Capri, Italy.
- [127] R. Rossi, L. S. Esposito, F. Cerutti, F. Salvat-Pujol, and W. Scandale. First benchmarking of the FLUKA crystal model with ion beams. *presentation in the LHC Collimation Upgrade Specification Meeting 132*, 2020.
- [128] R. Assmann, F. Schmidt, and F. Zimmermann. Equilibrium beam distribution and halo in the LHC. *Proc. of the European Particle Accelerator Conf. 2002, Paris, France*, page 1326, 2002. URL <http://accelconf.web.cern.ch/e02/PAPERS/WEPLE048.pdf>.
- [129] G. Valentino, R. Aßmann, R. Bruce, F. Burkart, V. Previtali, S. Redaelli, B. Salvachua, G. Stancari, and A. Valishev. Beam diffusion measurements using collimator scans in the LHC. *Phys. Rev. ST Accel. Beams*, 16:021003, 2013. doi: 10.1103/PhysRevSTAB.16.021003.
- [130] A. Gorzawski, R.B. Appleby, M. Giovannozzi, A. Mereghetti, D. Mirarchi, S. Redaelli, et al. Probing LHC halo dynamics using collimator loss rates at 6.5 TeV. *Phys. Rev. ST Accel. Beams*, 23:044802, 2020.
- [131] D. Mirarchi, S. Redaelli, and W. Scandale. Crystal implementation in SixTrack for proton

- beams. In *Proc. of the ICFA Mini-Workshop on Tracking for Collimation*, pages 91–108, 2018. doi: 10.23732/CYRCP-2018-002.91. URL <https://cds.cern.ch/record/2694336>.
- [132] *ICFA Mini-Workshop on Tracking for Collimation in Particle Accelerators: CERN, Geneva, Switzerland 30 Oct 2015*, Geneva, Dec 2018. CERN, CERN. doi: 10.23732/CYRCP-2018-002. URL <http://cds.cern.ch/record/2646800>.
- [133] T Persson, F Carlier, J Coello, J Dilly, S Fartoukh, E Fol, A Garcia-Tabares, M Giovannozzi, M Hofer, E H Maclean, L Malina, P K Skowronski, M L Spitznagel, R Tomás, A Wegscheider, and J Wenninger. LHC Optics Corrections in Run 2. pages 59–66, 2019. URL <https://cds.cern.ch/record/2750277>.
- [134] J. B. Potoine, R. Bruce, R. Cai, F. Cerutti, M. D’Andrea, L. Esposito, P. D. Hermes, A. Lechner, D. Mirarchi, S. Redaelli, V. Rodin, F. Salvat Pujó, P. Schoofs, A. Waets, and F. Wrobel. Power deposition studies for standard and crystal-assisted heavy ion collimation in the CERN Large Hadron Collider. *Phys. Rev. Accel. Beams*, 26:093001, Sep 2023. doi: 10.1103/PhysRevAccelBeams.26.093001. URL <https://link.aps.org/doi/10.1103/PhysRevAccelBeams.26.093001>.
- [135] A. Lechner, B. Auchmann, T. Baer, C. Bahamonde Castro, R. Bruce, F. Cerutti, L. S. Esposito, A. Ferrari, J. M. Jowett, A. Mereghetti, F. Pietropaolo, S. Redaelli, B. Salvachua, M. Sapinski, M. Schaumann, N. V. Shetty, V. Vlachoudis, and E. Skordis. Validation of energy deposition simulations for proton and heavy ion losses in the CERN Large Hadron Collider. *Phys. Rev. Accel. Beams*, 22:071003, Jul 2019. doi: 10.1103/PhysRevAccelBeams.22.071003. URL <https://link.aps.org/doi/10.1103/PhysRevAccelBeams.22.071003>.
- [136] S. Fartoukh et al. LHC Configuration and Operational Scenario for Run 3. *CERN-ACC-2021-0007*. URL <http://cds.cern.ch/record/2790409>.
- [137] D. Mirarchi, R. Bruce, S. Redaelli, M. Solfaroli Camillocci, and F. Van Der Veken. Review of operational cycles and their collimator settings. Presentation at the 31st ABP-NDC section meeting, CERN, Geneva, Switzerland, 2022. URL https://indico.cern.ch/event/1148933/contributions/4821135/attachments/2436971/4186879/ReviewOPcycles_DM.pdf.
- [138] Potoine, Jean-Baptiste and Bruce, Roderik and Cai, Rongrong and Esposito, Luigi Salvatore and Hermes, Pascal and Lechner, Anton and Redaelli, Stefano and Waets, Andreas and Wrobel, Frederic. Power Deposition Studies for Crystal-Based Heavy Ion Collimation in the LHC. *JACoW, IPAC2022:1726–1729*, 2022. doi: 10.18429/JACoW-IPAC2022-WEPOST018.
- [139] R. Bruce, R. Alemany Fernandez, T. Argyropoulos, H. Bartosik, C. Bracco, R. Cai, M. D’Andrea, A. Frasca, P. Hermes, J.M. Jowett, D. Mirarchi, S. Redaelli, M. Solfaroli, N. Triantafyllou, and J. Wenninger. First results of running the LHC with lead ions at a beam energy of 6.8 Z TeV. *Proceedings of the International Particle Accelerator Conference 2023, Venice, Italy, 2023*.

- [140] B. Lindström. private communication.
- [141] LHC Optics Source. URL <https://proj-lhc-optics-web.web.cern.ch/proj-lhc-optics-web/OpticsSourceAllVersions.link/>.
- [142] E. Matheson *et al.* TCPC – Crystal Choice for YETS22-23 Installation, 2022. URL <https://indico.cern.ch/event/1197008/>.
- [143] E. Matheson, S. A. Solis Paiva, and M. di Castro. LHC Crystal Goniometers: Crystal X-Ray Measurements. Presentation at the LHC Collimation Upgrade Specification Meeting, CERN, Geneva, Switzerland, 2021. URL <https://indico.cern.ch/event/1061692/contributions/4462062>.
- [144] M. di Castro and E. Matheson. Results of x-ray measurement campaigns on crystals for beam collimation. Presentation at the LHC Collimation Upgrade Specification Meeting, CERN, Geneva, Switzerland, 2021. URL <https://indico.cern.ch/event/1042417/>.
- [145] D. Mirarchi, O. Andreassen, R. Bruce, R. Cai, M. Di Castro, M. D’Andrea, M. Hostettler, D. Jacquet, A. Masi, E. Matheson, S. Redaelli, G. Ricci, M. Solfaroli, S. Solis, J. Tagg, and J. Wenninger. Operational handling of crystal collimation at the LHC. *Proceedings of the International Particle Accelerator Conference 2023, Venice, Italy*, 2023.
- [146] G. Valentino, G. Baud, R. Bruce, M. Gasior, A. Mereghetti, D. Mirarchi, J. Olexa, S. Redaelli, S. Salvachua, A. Valloni, and J. Wenninger. Final implementation, commissioning, and performance of embedded collimator beam position monitors in the large hadron collider. *Phys. Rev. Accel. Beams*, 20:081002, Aug 2017. doi: 10.1103/PhysRevAccelBeams.20.081002. URL <https://link.aps.org/doi/10.1103/PhysRevAccelBeams.20.081002>.
- [147] A. Mereghetti, N. Biancacci, R. Bruce, L. R. Carver, R. Kwee-Hinzmann, E. Metral, D. Mirarchi, E. Quaranta, S. Redaelli, A. Rossi, R. Rossi, B. Salvachua-Ferrando, B. Salvant, G. Valentino, and A. Valloni. β^* -reach – IR7 collimation hierarchy limit and impedance. *CERN-ACC-NOTE-2016-0007*, 2016. URL <https://cds.cern.ch/record/2120132?ln=en>.
- [148] D. Mirarchi, M. D’Andrea, R. Cai, K. Dewhurst, A. Vella, G. Ricci, S. Redaelli, D. Veres, and E. Matheson. Overview MD7007. Presentation at the 59th ABP-NDC section meeting, CERN, Geneva, Switzerland, 2023. URL <https://indico.cern.ch/event/1296930/>.
- [149] T. Kramer. *LHC Beam Dump System: Analysis of beam commissioning, performance and the consequences of abnormal operation*. PhD thesis, TU Graz, 2008.
- [150] R. Bruce, C. Bracco, R. De Maria, M. Giovannozzi, S. Redaelli, R. Tomas, F. Velotti, and J. Wenninger. Updated parameters for hl-lhc aperture calculations for proton beams. *CERN-ACC-2017-0051*, 2017. URL <https://cds.cern.ch/record/2274330?ln=en>.
- [151] M.A. Fraser, W. Bartmann, C. Bracco, E. Carlier, B. Goddard, V. Kain, N. Magnin, J. Uythoven, and F.M. Velotti. A beam-based measurement of the LHC beam dump kicker waveform. *Proceedings of the International Particle Accelerator Conference 2016, Busan, Korea*, page 3911, 2016.

- [152] K. Sjobak, H. Burkhardt, R. De Maria, A. Mereghetti, and A. Santamaria Garcia. General functionality for turn-dependent element properties in SixTrack. *Proceedings of the International Particle Accelerator Conference 2015, Richmond, VA, USA*, page 468, 2015.
- [153] E. Quaranta, A. Bertarelli, R. Bruce, F. Carra, F. Cerutti, A. Lechner, S. Redaelli, E. Skordis, and P. Gradassi. Modeling of beam-induced damage of the LHC tertiary collimators. *Phys. Rev. Accel. Beams*, 20:091002, Sep 2017. doi: 10.1103/PhysRevAccelBeams.20.091002. URL <https://link.aps.org/doi/10.1103/PhysRevAccelBeams.20.091002>.
- [154] D Mirarchi, G Arduini, M Giovanozzi, A Lechner, S Redaelli, and J Wenninger. Special Losses during LHC Run 2. pages 213–220, 2019. URL <https://cds.cern.ch/record/2750296>.
- [155] R. Bruce, D. Bocian, S. Gilardoni, and J. M. Jowett. Beam losses from ultraperipheral nuclear collisions between Pb ions in the Large Hadron Collider and their alleviation. *Phys. Rev. ST Accel. Beams*, 12(7):071002, Jul 2009. doi: 10.1103/PhysRevSTAB.12.071002.
- [156] M. Schaumann, J. M. Jowett, C. Bahamonde Castro, R. Bruce, A. Lechner, and T. Mertens. Bound-free pair production from nuclear collisions and the steady-state quench limit of the main dipole magnets of the CERN Large Hadron Collider. *Phys. Rev. Accel. Beams*, 23:121003, Dec 2020. doi: 10.1103/PhysRevAccelBeams.23.121003. URL <https://link.aps.org/doi/10.1103/PhysRevAccelBeams.23.121003>.
- [157] R. Bruce, R. De Maria, M. Giovanozzi, N. Mounet, and S. Redaelli. Optics configurations for improved machine impedance and cleaning performance of a multi-stage collimation insertion. *Proceedings of the 12th International Particle Accelerator Conference (IPAC'21): Campinas, Brazil, May 2021*, pages 57–60, May 2021. doi: doi:10.18429/JACoW-IPAC2021-MOPAB006. URL <https://jacow.org/ipac2021/papers/MOPAB006.pdf>.
- [158] B. Lindstrom, A. Abramov, R. Bruce, R. De Maria, P. Hermes, J. Molson, and F. Van der Veken S. Redaelli. Settings for Improved Betatron Collimation in the First Run of the High Luminosity LHC. In *Proc. IPAC'22*, number 13 in International Particle Accelerator Conference, pages 1366–1369. JACoW Publishing, Geneva, Switzerland, 7 2022. ISBN 978-3-95-450227-1. doi: 10.18429/JACoW-IPAC2022-TUPOTK062. URL <https://jacow.org/IPAC2022/papers/TUPOTK062.pdf>.
- [159] Bjorn Lindstrom, Roderik Bruce, Pascal Hermes, and Stefano Redaelli. Update on the High Luminosity LHC collimation performance with proton beams. In *Proceedings of the 14th Int. Particle Accelerator Conf. (IPAC 2023)*, page 4, Venice, Italy, May 2023. paper MOPA126, this conference.
- [160] B. Lindström, R. Bruce, X. Buffat, R. de Maria, L. Giacometti, N. Mounet, and title = "Updates on IR7 design Redaelli, S.", 2023. URL <https://indico.cern.ch/event/1320306/>.

- [161] Letter of intent for ALICE 3: A next generation heavy-ion experiment at the LHC. Technical report, CERN, Geneva, 2022. URL <https://cds.cern.ch/record/2803563>. 202 pages, 103 captioned figures, 19 tables.
- [162] I. Bejar Alonso, O. Bruning, P. Fessia, M. Lamont, L. Rossi, L. Taviani, and M. Zerlauth (editors). *High-Luminosity Large Hadron Collider (HL-LHC): Technical design report*. CERN Yellow Reports: Monographs, CERN-2020-0010. CERN, Geneva, 2020. doi: 10.23731/CYRM-2020-0010. URL <http://cds.cern.ch/record/2749422?ln=en>.
- [163] R. Bruce, R. Alemany-Fernández, H. Bartosik, M. Jebramcik, J.M. Jowett, and M. Schumann. Studies for an LHC Pilot Run with Oxygen Beams. *Proceedings of the 12th International Particle Accelerator Conference (IPAC'21): Campinas, Brazil, May 2021*, pages 53–56, 2021. doi: 10.18429/JACoW-IPAC2021-MOPAB005.
- [164] R. Bruce, R. Alemany Fernandez, H. Bartosik, and J.M. Jowett. Preliminary LHC light-ion scenarios for Run 5 and beyond. Presentation at LIU-Ions PS injectors Performance Coordination Meeting, CERN, Geneva, Switzerland, 2021. URL <https://indico.cern.ch/event/1085343/>.

Acronyms

ADT Active Transverse Damper. 67, 75, 78

AM Amorphous. 64, 70, 72, 85, 109

B1H Beam 1 horizontal plane. 67, 71, 76, 77, 83, 85, 86, 90–94, 98–100, 104, 108, 114, 116, 127, 140, 142, 143, 149, 155, 156, 158–165, 167–169, 182, 186, 187, 190, 194, 201–207

B1V Beam 2 vertical plane. 67, 87, 101, 105, 108, 127, 129–132, 135, 144, 145, 149, 183, 191, 195, 201–203, 205, 206

B2H Beam 2 horizontal plane. 45, 67, 88, 90, 91, 95–98, 102, 106, 109, 115, 119, 120, 122–125, 127, 128, 131, 136, 137, 140, 146, 147, 150, 153–157, 163, 165, 166, 170, 184, 188, 189, 192, 196, 201–206

B2V Beam 2 vertical plane. 45, 67, 89, 103, 107, 109, 110, 127–130, 133–135, 147, 148, 150, 185, 193, 197, 201–203, 205, 206

BFPP Bound-Free Pair Production. 40, 41

BLM Beam Loss Monitor. 42, 44, 67, 73–79, 83–89, 93, 94, 96, 97, 99–103, 118, 140, 142–148, 179, 200, 201

BPM Beam Position Monitor. 123

CH Channeling. 21, 69, 72, 78, 85

DC Dechanneling. 21, 22, 70, 72, 200

DS Dispersion Suppressor. 27, 28, 31, 35, 43, 74, 85, 90, 91, 98, 108, 109, 113–122, 124–128, 130, 135, 137, 140, 153–157, 160, 162–164, 167, 169, 170, 201–205

EMD Electromagnetic Dissociation. 39, 40, 64, 66, 116, 167

FEDB FLUKA elements database. 52, 56, 57, 62

HL-LHC High Luminosity LHC. 1, 3, 29, 46, 57, 153, 163

- IP** Interaction Point. 27, 28, 32, 35, 40, 41, 144
- IR** Insertion Region. 26–28, 33–37, 43, 67, 73, 82, 84–89, 92–97, 100–107, 110, 113, 114, 116–118, 122, 123, 127, 128, 131–134, 137, 140–152, 155, 156, 158–167, 170, 182–197, 199–206
- ISR** Intersecting Storage Rings. 25
- LEP** Large Electron-Positron Collider. 25
- LHC** Large Hadron Collider. 5, 26, 31, 32, 34, 42, 58, 199, 200
- MAD-X** Methodical Accelerator Design. 49, 55, 56, 61, 62
- MCS** Multiple Coulomb Scattering. 38
- PS** Proton Synchrotron. 26
- PSB** Proton Synchrotron Booster. 26
- RHIC** Relativistic Heavy-Ion Collider. 25
- SD** Single Diffractive Scattering. 40, 43
- SMPF** Single Module Pre-Fire. 133, 138, 139
- SPS** Super Proton Synchrotron. 26
- TCDQ** Target Collimator Dump Quadruple. 33, 36, 134
- TCL** Target Collimator Long. 35
- TCLA** Target Collimator Long Absorber. 35, 91, 116, 126–129, 137–140, 175, 203
- TCLD** Target Collimator Long Dispersion. 36, 46, 145, 146
- TCLI** Target Collimator Long Injection Protection. 36
- TCP** Target Collimator Primary. 34, 35, 41, 42, 116, 129–131, 138, 140, 154, 155, 157–163, 204
- TCPC** Target Collimator Primary Crystal. 45
- TCSG** Target Collimator Secondary Graphite. 35, 41, 126, 129, 140, 163, 164
- TCSP** Target Collimator Secondary with Pick-up. 36, 134, 141
- TCT** Target Collimator Tertiary. 35, 53, 137, 138, 140, 141, 144, 203
- TDI** Target Dump Injection. 36
- VC** Volume Capture. 22, 70, 72
- VR** Volume Reflection. 21, 64, 69–72, 78, 109, 200



RONGRONG CAI

rongrong.cai@epfl.ch

+41 79 862 98 69 | EU Citizen (Italy) | 19.06.1996
Rue Alcide-Jentzer, 8; 1205 Geneva, Switzerland

Education

EPFL – Switzerland	2.2021 – 5.2024
PhD in Physics: “Studies of crystal collimation for heavy-ion operation at the LHC”	
Imperial College London EPFL CERN – UK Switzerland	10.2016 – 8.2020
MSci in Physics with Year in Europe (combined BA+MSc): Upper-second Class Honours (69.4, approx. 3.9 GPA)	
Liceo E. Majorana di Desio Liceo Leonardo da Vinci Milano – Italy	9.2011 – 7.2016
High school diploma (scientific): 100/100	

Work Experience

Doctoral Researcher Teaching assistant at CERN EPFL - Switzerland	2.2021– 2.2024
<ul style="list-style-type: none"> Build and benchmark simulation setup for heavy-ion crystal collimation at the LHC with SixTrack-FLUKA Coupling. Study ion crystal collimation: <ul style="list-style-type: none"> Characterize key features of heavy-ion crystal collimation. Optimize collimation system for Pb ion Run 3. Simulate machine imperfections and failure backup plan. Investigate HiLumi energies and light ion collimation (Ar, O, Xe, Kr). 	<ul style="list-style-type: none"> Participate in crystal beam tests and perform related data analysis. Contribute to beam commissioning. Give regular presentations within CERN. Write scientific papers. Teaching assistant to master’s course at EFPL.
Trainee at CERN - Switzerland	7.2019 – 10.2019
<ul style="list-style-type: none"> Simulations of e-lens and non-linearities particle loss for the HL-LHC. Presentation and report writing. 	
Vacation Student at National Physical Laboratory - UK	7.2017 – 9.2017
<ul style="list-style-type: none"> Entire production process of an apparatus for thermal stabilisation of optical fibre-based time distribution hardware including the apparatus design, material procurement, component design (Solidworks) and assembly. Reach internal thermal stability of 0.1 K. Post-production performance verification through mathematical modelling, experiment design, data acquisition and model-data benchmarking. Optimization and control automatization via a proportional control (PI) system on LabVIEW. 	

Further Experience

Member at SOS EAU Giteranyi - Switzerland	9.2018 – 6.2019
<ul style="list-style-type: none"> Draft and edit surveys and documents; organise workshops and showcases. 	
Treasurer Project Manager at E.quinox - UK	8.2017 – 8.2018
<ul style="list-style-type: none"> In charge of the society’s funding (> 50k GBP). Annual budgeting and report. Approve expenses and proposals. Liaise with external organisations. Organise outreach and social events. Part of the off-grid electrification of rural Ruanda project. 	<ul style="list-style-type: none"> Recruit and manage members (~10) for a laundry project using recycled rainwater (Rwanda and Kenya). Set goals, roles, and tasks. Organise weekly meetings, keep minutes, and report progress. Finalists in the CleanTech Challenge.
Volunteer at Victoria and Albert Museum - UK	7.2017 – 4.2018
<ul style="list-style-type: none"> Welcome visitors, enhance visiting experience and provide general assistance. 	
Volunteer at Red Cross – Comitato di Desio - Italy	08/2014 - 06/2016
<ul style="list-style-type: none"> Non-urgent ambulance service and switchboard. 	

Technical Skills

Windows, Linux, MacOS,
Microsoft Office Package,
Python, Bash, Latex, (Git, C++, Fortran)
SixTrack, FLUKA, MADX, Origin, LabVIEW, Solidworks

Languages

English: C2
Italian: Bilingual
Chinese: Bilingual
French: B2

Conferences and Workshops

Joint Accelerator Performance Workshop 2023 - Presentation	12.2023
Channeling 2023 - Presentation	6.2023
International Particle Accelerator Conference 2023 - Poster	5.2023
12th HL-LHC Meeting - Presentation	9.2022
International Particle Accelerator Conference 2022 - Poster (poster award finalist)	6.2022

Awards

Best Young Researcher at Channeling 2023	2023
Concorso Enrico Deponi (Scholarship for academic excellence)	2016
Borsa di Studio Andrea Lozza (Scholarship for academic excellence)	2012

Publications

Main author:

R. Cai et al. *Simulation framework and measurements of crystal collimation of proton beams at the Large Hadron Collider*. Nuclear Inst. and Methods in Physics Research, A

R. Cai et al. *Crystal collimation tests with Pb beams at 6.8 Z TeV at the LHC*. Proceedings of the International Particle Accelerator Conference 2023, Venice, Italy, 2023.

R. Cai et al. *Simulation of Heavy-Ion Beam Losses with Crystal Collimation*. Proceedings of the International Particle Accelerator Conference 2022, Bangkok, Thailand, 2022.

R. Cai et al. Simulations of particle loss due to hollow e-lens and non-linearities for the HL-LHC. 2020. URL: <https://cds.cern.ch/record/2732000>

Contributing author:

P. Schoofs et al. *Recent developments of the FLUKA channeling model and benchmarking of LHC and SPS crystal-related activities*. Nuclear Inst. and Methods in Physics Research, A (under review)

M. D'Andrea et al. *Characterization of bent crystals for beam collimation with 6.8 TeV proton beams at the LHC*. Nuclear Inst. and Methods in Physics Research, A

M. D'Andrea et al. *Operational performance of crystal collimation with 6.37 Z TeV Pb ion beams at the LHC*. Phys. Rev. Accel. Beams

J. B. Potoine et al. *Power deposition studies for standard and crystal-assisted heavy ion collimation in the CERN Large Hadron Collider*. Phys. Rev. Accel. Beams, 26:093001, Sep 2023.

F.F. Van der Veken et al. *Collimation performance of the 400MJ LHC beam at 6.8 TeV*. Proceedings of the International Particle Accelerator Conference 2023, Venice, Italy, 2023.

M. D'Andrea et al. *Crystal collimation performance at the LHC with a 6.8 TeV proton beam*. Proceedings of the International Particle Accelerator Conference 2023, Venice, Italy, 2023.

R. Bruce et al. *First results of running the LHC with lead ions at a beam energy of 6.8 Z TeV*. Proceedings of the International Particle Accelerator Conference 2023, Venice, Italy, 2023.

D. Mirarchi et al. *Operational handling of crystal collimation at the LHC*. Proceedings of the International Particle Accelerator Conference 2023, Venice, Italy, 2023.

A. Frasca et al. *Simulations and measurements of collisional losses with Pb beams at the LHC*. Proceedings of the International Particle Accelerator Conference 2023, Venice, Italy, 2023.

J.B. Potoine et al. *Benchmarks of Energy Deposition Studies for Heavy-Ion Collimation Losses at the LHC*. Proceedings of the International Particle Accelerator Conference 2022, Bangkok, Thailand, 2022.

J.B. Potoine et al. *Power Deposition Studies for Crystal-Based Heavy Ion Collimation in the LHC*. Proceedings of the International Particle Accelerator Conference 2022, Bangkok, Thailand, 2022.